2018-08-30

# Mechanistic Model for Ultraviolet Degradation of Light Hydrocarbons in Waste Gas

Asili, Vahid

UNIVERSITY OF CALGARY

# Mechanistic Model for Ultraviolet Degradation of Light Hydrocarbons in Waste Gas

by

Vahid Asili

A THESIS

SUBMITTED TO THE FACULTY OF GRADUATE STUDIES

IN PARTIAL FULFILMENT OF THE REQUIREMENTS FOR THE

DEGREE OF DOCTOR OF PHILOSOPHY

GRADUATE PROGRAM IN CHEMICAL AND PETROLEUM ENGINEERING

CALGARY, ALBERTA

AUGUST, 2018

## Abstract

A mechanistic simulation model was developed to describe ultraviolet waste gas treatment of the light hydrocarbons methane, ethane, and ethylene. The presented model can be used in both environmental and chemical engineering applications. Efforts were made to include all the possible chemical and photochemical reactions between air components and each hydrocarbon. The most comprehensive model consists of 199 reactions (165 chemical reactions, and 34 photochemical reactions) with 69 reactive species.

Trials indicated that most of the computation time was spent on calculating reactions that have insignificant effects on the effluent concentration. Hence, model variants were developed that include only the most relevant chemical and photochemical reactions, without loss of accuracy, while maintaining the lowest possible run-time. $NO_x$ is included in one model version as well. This work may benefit Eulerian air quality models, where most of the computation time is spent resolving the complicated chemistry.

Simulation results confirmed that removal efficiency (i.e., conversion) of ethylene is significantly higher than ethane, followed by methane, as expected. Sensitivity analysis of the models indicated that the water content, ozone premixing, and reactor cross-section are the main contributing factors affecting the removal efficiency, while changing the temperature and flow pattern do not influence the conversions by much.

The proposed model is able to predict the reaction products of the photolysis process in the gas phase. The predicted effluent has a composition in general agreement with literature research.

COMSOL simulations of the photoreactor showed that the assumptions made in the original model development were justified, since the simulated flow pattern was consistent with the fully-developed laminar assumption in the base model. Also, thermal analysis indicated a noticeable temperature gradient in the gas phase photoreactor, but removal efficiencies are not impacted meaningfully by the temperature rise. Hence it can be concluded that the gas phase UV photolysis is mostly photon-limited, kinetically- and diffusion-controlled. This research reverses the conventional wisdom of waste gas photolysis where it is believed that turbulent flow is essential, a thin gap between lamp and wall is preferred, sophisticated light field modeling is essential, and detailed chemical modeling is unnecessary.

*Keywords*: Photolysis; Waste Gas; Simulation; Methane, Ethane, and Ethylene; Chemical and Photochemical Reactions; Optimum Reaction Network; Simulation Runtime; Removal Efficiency; Sensitivity Analysis; Hydrocarbon Mixture; Reaction Products; Flow Pattern; CFD Simulation

## Acknowledgements

This journey would not have been possible without the support of my parents, my wife, friends, and professors.

To my parents and siblings! Thank you for encouraging me in all my pursuits; your support has always been with me in my life. I am especially thankful to my parents; without their faith in me, I could not have made it this far.

To my lovely wife, Behnoosh! You should know that your support and encouragement is worth more than I can express on paper; but I would like to say, “thank you” for your patience, understanding, and invaluable source of unconditional love and support. You scarified many opportunities to be with me all these years, and inspired me to finish this journey. Without your patience and love, I would not have been able to complete this work. Thank you for giving me the most precious gift, our lovely daughter, Kimia. But most of all, thank you for being my best friend. I owe you everything.

In addition, some special words of gratitude go to my friends who have always been supported me through this entire process: Ehsan, Milad, Kamran, Kavan, Zainab, and Mehrshad. Thanks guys for always being there for me.

Now, I would like to express my utter gratitude to my supervisor, Dr. Alex De Visscher, for his continuous support throughout my graduate studies. His fruitful advice has always helped and encouraged me through different stages of this work. His continuous support, especially the long-distance supervision in the last two years of this work, helped me to get the right direction finish this journey.

Furthermore, I am thankful to my co-supervisor, Dr. Jalel Azaiez, and members of my supervisory committee, Dr. Edward (Ted) Roberts, and Dr. Abdulmajeed Mohamad. Part of the research findings are due to their constructive comments. Their support is greatly acknowledged and appreciated.

I am also grateful to my internal examiner, Dr. Dennis Salahub (Department of Chemistry, University of Calgary), and my external examiner, Dr. Mita Ray (Department of Chemical and Biochemical Engineering, University of Western Ontario), for their participation in the assessment of my thesis.

## Dedication

TO MY FAMILY

## Table of Contents

## List of Tables

## List of Figures and Illustrations

# Chapter 1: Introduction

Industrial developments impact air quality significantly. In upstream oil and gas operations and most downstream chemical processes, considerable amounts of hydrocarbons are emitted every year in Canada (NPRI, 2017), representing more than 30% of the overall air pollution emission. Waste gas polluted with hydrocarbons can be very harmful to the people exposed during their daily activities such as work and school, and there is an increased risk of cancer, skin damage due to oxygen deficient blood, liver and kidneys (Alberta Environment, 2008).

Alkanes and alkenes are two major classes of petroleum hydrocarbon components. These compounds enter the environment as a result of stationary and mobile sources and comprise a significant portion of the contaminant mixture found in the polluted atmosphere (Berry & Brammer, 1977; Singh & Zimmerman, 1992). Light hydrocarbons are usually known to be dangerous due to flammability whereas heavier and aromatic hydrocarbons are known to be hazardous due to health impacts on people, so the investigation of conversion or removal of them is an important research area.

Introducing new hydrocarbon elimination techniques can benefit the industry by achieving present and future emission standards. Since these emissions are coming from thousands of big and small sources, any technology to reduce these emissions needs to be cheap and easy to operate to accomplish wide use in industry. Using ultraviolet light to break molecules, *Photolysis*, is an effective technique that could fall into this category.

Wavelength is a key variable in the application of UV photolysis. Classically, ultraviolet light is categorized as near UV, middle UV and far UV. For near UV, the characteristic wavelength is 350 nm, which requires a catalyst to be effective. A common catalyst used is titanium dioxide or

$TiO_2$ (Demeestere et al., 2007). For middle UV, the typical wavelength is 254 nm and it can break ozone and some organic hydrocarbon molecules, but not oxygen or water. The representative wavelength for far UV is 185 nm, which can break oxygen molecules and water vapor (Mahmoudkhani, 2012).

Other than direct photolysis, chemical species can be degraded by oxidation at low temperature (200 – 300 K) in the atmosphere. The chemical pathways for initiating the oxidation reactions of hydrocarbons are generally reactions involved with ozone ($O_3$), hydroxyl radical (·OH), and oxygen atoms ($O(^1D)$ and $O(^3P)$) in the lower atmosphere (Calvert et al., 2008), where these radicals are generated by the photolysis of oxygen and water vapor.

In this study, the possibility of using photolysis for the conversion (or degradation) of alkanes (methane and ethane) and an alkene (ethylene) from waste gas originating from the oil and gas industry (or any other usual sources) has been studied. Light hydrocarbons were used in this study because they occur in natural gas, but also as proxy for higher hydrocarbons. The importance of this project is to overcome two main issues in the "Waste gas photolysis" area. On the one hand, lack of a comprehensive sophisticated model for photolysis waste gas removal (except for a few of them that will be discussed later) to cover all the aspects of the waste gas treatment modeling; and on the other hand, neglecting the effect of interactions between pollutants (pollutants may have different impacts when they are combined) are the main gaps in this research area.

An additional gap stems from the fact that our process engineering knowledge of photolysis for pollution control is based on experience with the water phase, where the UV absorption is orders of magnitude larger, and the diffusivity is orders of magnitude smaller than in the gas phase.

Hence, conventional wisdom dictates that an effective photolysis process is only possible in turbulent flow, with a narrow gap between the lamp and the wall, and that computational fluid dynamics (CFD) calculations are required to adequately model the process. In addition, the volumetric heat capacity of a water phase is orders of magnitude larger than of a gas phase, so that the temperature rise of a photolysis process is usually considered negligible. None of these process guidelines have been systematically tested in the gas phase.

This research study can be applicable for two main areas: one in environmental engineering as the modeled system can be used to convert natural gas condensate emissions to more easily removable products without degrading its main content; and the other in chemical process engineering as the model results can be used to simulate the conversion of the condensate to more valuable products. Both areas could overlap, as an example of a "pollutants to products" process.

Photolysis could potentially become a key process in a future sustainable chemical industry. As fossil fuels are phased out in future decades, and replaced by electricity from solar and wind energy, it may no longer make sense to add energy to process streams by heating them. Adding energy more directly, by photons capable of exciting electrons, may be a more effective way.

The economics of photolysis as a feasible process depends heavily on future technological development, as some sample calculations demonstrate. For instance, the lamp that was represented in the models in this thesis produces 2.74 einstein (i.e., mol) of photons per kWh of electricity input (8 % of the electrical power input as 185 nm light and 30 % as 254 nm light). Hence, in a jurisdiction where electricity is expensive (20 cents per kWh), one dollar produces 13.7 mol of photons. Assuming 100 % photon efficiency, and one photon needed to react a 50

g/mol molecule, a photolytic process would add $1460 per tonne to the cost, which is uneconomical for most products. In jurisdictions where electricity is cheap (8 cents per kWh), one dollar produces over 34 mol of photons, and the cost declines to $580 per tonne. Solar and wind projects are increasingly becoming profitable at 5 cents per kWh, and further decreases of the price are anticipated. Particularly in intermittent processes that run only when there is an oversupply of electricity, prices as low as 1 cent per kWh may be feasible in the future. In that case, a dollar would buy 274 mol of photons and the price drops to $73 per tonne, feasible in many processes.

In a future world based on renewable energy, there will still be a need for liquid fuels and carbon-based feedstocks for polymer production. Ideally, these products should be made out of $CO_2$. A useful source of this $CO_2$ would be the cement industry. As cement slowly reabsorbs $CO_2$ from the air, a process may be a closed cycle to some extent. In such a future, reverse water gas shift followed by Fischer-Tropsch synthesis may be used to produce hydrocarbon fuels from $CO_2$. This process produces a lot of light alkanes and alkenes that have limited value because their supply exceeds the demand. These produced alkanes and alkenes can be processed by the proposed research method in this study to convert them to value-added products, such as alcoholic and aldehyde materials.

Another application where this research can be beneficial is in the field of air quality modeling with Eulerian air quality models, where computation times can be excessive, and 50-90% of the computation time is usually spent resolving the complicated chemistry (Byun & Ching, 1999). There are two main types of numerical models are being used in the atmospheric dispersion: Lagrangian, where the framework is moving with the air parcel (i.e., plume); and Eulerian,

where the framework is fixed, and parameters are calculated based on inlet/outlet in a defined stationary frame. Eulerian air quality models can handle more complex chemistry than Lagrangian models, but at the cost of large computation times to resolve the chemistry (50-90 % of the overall run time). The latter is very similar to a modeling of a reactor, and for this reason the importance of time-reduction in this study is comparable with the Eulerian dispersion model.

The objectives of this research study can be summarized as follows:

- To develop a mechanistic model for the ultraviolet degradation of methane, ethane, and ethylene in waste gas where the water vapor and air species are provided for oxidation (as the model is not meant to be used as a direct photolysis).

- To determine the dependency of the removal efficiency for each individual hydrocarbon that modeled in this study (i.e., $CH_4$, $C_2H_6$, or $C_2H_4$) on various factors.

- To propose the dominant reaction pathways for the degradation of each of methane, ethane, and ethylene.

- To include comprehensive reaction networks that contain all the known reactions and species, either in the presence or the absence of $NO_x$.

- To optimize the reaction networks for each of methane, ethane, and ethylene kinetic model to achieve the most accurate results with the lowest possible model run-time.

- To test the hypothesis that it is possible to degrade higher alkanes in natural gas without significantly degrading methane.

- To study the thermal behavior in a photoreactor, and test if the model results are dependent on the temperature variation.

- To simulate the behaviour of flow in the photoreactor, by CFD, and by assuming either a laminar flow velocity profile or plug flow; and test if model results are independent of gas flow pattern.

This research builds on an initial model for benzene degradation (Mahmoudkhani et al., 2016) and the mechanistic first-principles model for $H_2S$ and $NO_x$ (Asili & De Visscher, 2014) which have the same methodology as the present model. Both models were validated with experimental data. The benzene model (Mahmoudkhani et al., 2016) was validated with the experimental data obtained with the same photoreactor that is the basis of proposed reactor in this research. The $H_2S$ model (Asili & De Visscher, 2014), however, was validated with some experimental data obtained from a different type of reactor by a different group of researchers (Xia et al., 2008). The methodology of the model devolvement in both models are consistent, but the operational conditions and reactor properties are different. Table 1-1 shows the operational conditions and reactor properties for the experiments that the models were validated.

**Table 1-1: Comparison of experimental condition for the validation of $H_2S$ and benzene models in the previous studies**

| Operational condition | $H_2S$ experiment (Xia et al., 2008) | Benzene experiment (Mahmoudkhani et al., 2016) |
|---|---|---|
| UV lamp electrical power (W) | 80 | 40 |
| Irradiation power | 4.8 W @ 185 nm<br>33.6 W @ 254 nm | 3.2 W @ 185 nm<br>12 W @ 254 nm |
| Reactor material | Quartz | Stainless steel |
| Light reflection at the reactor wall | 1% | 99% |

| Operational condition | $H_2S$ experiment (Xia et al., 2008) | Benzene experiment (Mahmoudkhani et al., 2016) |
|---|---|---|
| Reactor length (cm) | 90 | 50 |
| Reactor radius (cm) | 1.8 (Tube-A)<br>2.3 (Tube-B) | 2.10 |
| UV lamp radius (cm) | 1.0 | 1.25 |
| Pressure (kPa) | 101.325 | 89 |
| Temperature (K) | 300 | 300 |
| Relative humidity (RH%) | 40 % | 80 % |
| Initial concentration ($mg/m^3$) | 0.6 – 25 of $H_2S$ | 300 – 24000 of benzene |
| Volumetric flow rate ($cm^3/s$) | 140 – 420 (Tube-A)<br>269 – 808 (Tube-B) | 7 – 37 |

The model results for both $H_2S$ and benzene are in a great agreement (less than 10% difference) when the removal efficiency values from the model are compared with the experimental data. Hence, since it was shown that the methodology to develop these detailed kinetic models for the photolysis of waste gas was sound, the presented model is expected to be accurate and the results can be used to establish a feasible process.

Waste gas photolysis is a fairly new field (about 30 years of research) where some experimental data is available, but no other researchers have attempted to model photochemical waste gas treatment techniques at the level of chemical detail of this research. Although no experimental analysis was carried out to validate the presented model; the $H_2S$ and benzene model both were successfully validated with experimental data. Therefore, it gives a confidence that the model results in this study are valid.

Overall, for a model like this presented research, lack of experimental data is not a significant obstacle in finding meaningful trends and presentable data. In addition of saving money for an ineffective experiment or prediction purpose only, one of the added values of doing modeling is

to gain insights that would be difficult to obtain experimentally. Modeling is beneficial for determination of what factors control the process. In this study some of the advantages of modeling, such as changing the process conditions (e.g., temperature, inlet concentration, reactor specification, etc.) and reaction sensitivity, are discussed in-depth later in Chapter 4.

The research questions for the current study can be summarized in the following hypotheses:

- Can photochemical modeling be more efficient by modeling only the most relevant reactions?

- Can non-methane hydrocarbons be converted to value-added products in a photoreactor while leaving the methane intact? (in the current industry: natural gas; in a future industry: the gas fraction of the Fischer-Tropsch products).

- Are existing recommendations for optimizing a photolytic waste gas treatment system based on water-phase photolysis are misleading due to the vastly different properties of air versus water (e.g., $10^4$ times larger diffusion coefficient, lower UV absorption, lower heat capacity)?

This thesis tries to answer the above-discussed questions, concerns, and objectives with the following contributions and novelties:

- Level of detail in modeling of a photoreactor for waste gas treatment.
- Determination of essential steps in a reaction network.
- Conventional wisdom in photochemical waste gas treatment until now was based on waste water treatment. As a result, researchers believed that turbulent flow was essential, a thin gap between lamp and wall were preferred, sophisticated light field modeling was

essential, and detailed chemical modeling was unnecessary. This study shows that all these recommendations need to be reversed.

The research outcomes of the proposed study can benefit the current and the future industry, if some of the research findings transfer to a bigger scale. The main applications and transferability are included but not limited to:

- Convert pollutants into products.
- Treat the gas fraction of Fischer-Tropsch products.
- Use pure oxygen instead of air. (As $H_2$ production from electrolysis also produces pure $O_2$ as a side product, this oxygen can be used instead of air. If the oxygen is dosed so that it is all consumed in the photolysis, it does not need to be separated).

This thesis contains five chapters which are organized as follows:

- Chapter 1 addresses the importance of the work, as well as the application, objectives, and contributions of this research project.

- In Chapter 2, a comprehensive literature review is given to cover the significance of other research works in the area of waste gas photolysis, as well as extensive literature review on the chemical and photochemical reaction rate values. Also, some brief introduction of alkanes and alkenes is presented to emphasize the role of these components in health effects and effects on environment.

- Chapter 3 deals with the model development of the system as the main part of the thesis. In this chapter all mathematical formulations, and reaction rates used in the model are

clearly described. Also, the model of thermal behaviour of the reactor and COMSOL assessment are stated in this chapter.

- In Chapter 4, the simulation results and model predictions are presented. The results are arranged in different categories to show the model strength, and to cover different types of the model including the main model, thermal model and COMSOL simulation. Besides, the model was implemented as a software by introducing *PhotoSim*1.4 (the current version of the software that is developed based on the model).

- Chapter 5 summarizes the significant points of this study. As well, some recommendations and future works, to maximize the quality of the upcoming research in this area, are highlighted.

# Chapter 2: Literature Review

## 2.1 A Brief Introduction to Alkanes and Alkenes

### *2.1.1 Structure and properties*

Alkanes are hydrocarbons with the general formula of $C_nH_{2n+2}$, in the case of noncyclic structures. They are the simplest organic molecules, consisting of only carbon and hydrogen and with only single bonds between carbon atoms. They make up a major component of the trace gas composition of the atmosphere. Alkanes can be linear, branched (due to isomer structures), cyclic (cycloalkane) or halogen substituted (haloalkane). They can be in the form of a gas ($n < 5$), liquid ($5 \leq n \leq 17$) and solid ($n > 17$) at standard conditions (Perry et al., 1997). Generally speaking, while the increasing number of carbon atoms in an alkane increases its boiling point temperature and number of isomers exponentially, it causes decreasing vapor pressure of the alkanes (Calvert et al., 2008).

The alkenes are also chains of carbon atoms with attached hydrogen atoms, but the chains contain carbon–carbon double bonds with the general formula of $C_nH_{2n}$, for the case of a noncyclic structure with one double bond. They are usually known as unsaturated hydrocarbons in relation to the total possible number of attached hydrogen atoms, compared to an alkane of similar carbon chain length (Perry et al., 1997). Alkenes also can be found as linear alkene, cycloalkane, or haloalkene. They can be in the form of a gas ($n < 5$), liquid ($5 \leq n \leq 14$) and solid ($n > 14$) at standard conditions (Perry et al., 1997). The double bonds cause the alkene to form a planar configuration of *cis*- or *trans*- isomers. Alkenes are relatively stable compounds, but are commonly more reactive than alkanes owing to the double bond (Wade Jr, 2006). The physical properties of the linear alkenes are very similar to the linear alkanes.

### *2.1.2 Health effects*

Air pollution takes a great toll on human health and the environment. Although alkanes are generally not of much toxicological concern related to environmental toxicology, they may potentially affect the central nervous system (CNS) (Patnaik, 2007) or acts as general asphyxiants or irritants (Irwin et al., 1997). At low concentrations, alkanes are simple irritants. By themselves, they can cause inflammation, itching, redness, and swelling of the skin, mucous membranes, nose, trachea, and bronchioles. At high concentrations, severe eczema of the skin and respiratory edema may develop (Yu, 2001). Also, breathing vapors of hydrocarbons in gasoline can result in sudden death due to irregular heartbeats (Cockerham & Shane, 1993). Methane and ethane, exclusively, are simple asphyxiants, which means that air containing high levels of these gases (more than 33%volume of air) does not contain adequate oxygen to support respiration (Manahan, 2002). Overall, alkanes are considered to be virtually nontoxic, nonetheless many of them are central nervous system depressants, they may interfere with metabolic processes (Irwin et al., 1997; Patnaik, 2007; Yu, 2001).

For alkenes, especially the lower-molecular-mass compounds, the most likely mode of exposure is inhalation (Manahan, 2002). Exposure to the *cis*- isomers of alkanes may result in weakness, nausea, and vomiting, and tremor and cramps due to their effects on the CNS (Yu, 2001). Exclusively, ethylene, a widely used colorless gas with a somewhat sweet odor, behaves as a simple asphyxiant and anesthetic to animals and is toxic to plants; however, the reaction product of ethylene with oxygen (ethylene oxide) is extremely reactive, and inhalation may cause pulmonary edema, irritated eyes and lung mucous membrane tissue (Manahan, 2002).

### *2.1.3 Role of alkanes and alkenes in ozone formation*

The hydrocarbons, and in particular VOCs (Volatile Organic Compounds), have a dual role in ozone formation in the atmosphere. First, they react with hydroxyl radicals (OH) and form hydroperoxy ($HO_2$) and organic peroxy radicals ($RO_2$). Second, increasing supply of $HO_2$ radicals stimulates the formation of nitrogen dioxide $NO_2$ from nitric oxide NO (Calvert et al., 2008). The mechanism of ozone formation in the atmosphere and in the presence of VOCs was identified by (Blacet, 1952), and quantified by (Leighton, 2012) completely. The main reactions are as follows:

$$\cdot RO_2 + NO \rightarrow \cdot RO + NO_2 \quad (2.1)$$

$$\cdot HO_2 + NO \rightarrow \cdot OH + NO_2 \quad (2.2)$$

$$NO_2 + h\nu \rightarrow NO + O(^3P) \quad (2.3)$$

$$O(^3P) + O_2 \rightarrow O_3 \quad (2.4)$$

The radicals involved in these pathways have a short lifetime, so the ozone forms when the OH radical attacks the VOCs. Thus, oxidation of VOCs by the hydroxyl radical is the rate-determining step for ozone formation and is a competitive process between the VOC species (Calvert et al., 2008).

Very often, in the presence of $NO_x$, the initial reaction products will form more $NO_2$ (Reactions (2.1) and (2.2)); and hence, the production of ozone is increasing (Reactions (2.3) and (2.4)). It is worth mentioning that the percentage of ·OH reactivity to form ozone with the above reactions is around 15% in the presence of alkane, while this value is more than 27% for alkenes (Calvert et al., 2008).

### *2.1.4 Emissions*

Methane is known as the second most important greenhouse gas (GHG) after $CO_2$, and it is continuously being emitted to the environment, mostly due to upstream/downstream oil and gas production. In 2015, more than 722 million tonnes ($CO_2$-equivalent) of GHG emission was reported from all sources, in Canada; where Alberta contributed more than 38% of this value (Canada GHG Emissions, 2017). The importance of studying emission of alkanes and alkenes is that they can act as a global warming agent (Collins et al., 2002). It means, in addition to the effect of radiative forcing, they can also contribute to changes of the distribution of methane and ozone in the troposphere, if the emission of alkanes in the atmosphere is increasing. If the oxidation reactions cause excessive production of peroxy radicals, more $NO_2$ will form which leads to increasing $O_3$ concentration (Reactions (2.1) – (2.4)). Increasing ozone concentration in the troposphere acts as a positive radiative forcing agent which leads to climate change (IPCC, 2005). Moreover, if the reactions of alkanes and alkenes with water vapor do not recycle hydroxyl radicals effectively, the concentration of tropospheric hydroxyl radical concentration decreases and consequently methane concentration increases due to diminished methane oxidation by hydroxyl radicals (Calvert et al., 2008).

Most references report the hydrocarbon emission data as methane ($CH_4$) – due to greenhouse gas (GHG) emission and non-methane VOCs – due to health and environmental health. Significant amounts of methane and non-methane VOCs are emitted each year in Canada from oil and gas production. Although current regulations generally restrict the oil and gas production sectors to release total hydrocarbon to the atmosphere, some emissions still occur in these industries due to equipment leaks (37.4 %), process vents (34.4%), storage tanks (16.7%), combustion equipment

(6.7%), accident and equipment failure (4.3%) and loading/unloading losses (0.5%) (CAPP, 1999).

Statistical data showed that more than 65% of VOCs and methane emitted in Canadian upstream oil and gas operations has been produced in Alberta. Table 2-1 shows the quantity of VOCs and $CH_4$ released only from the oil and gas industry in Canada and Alberta for a comparison. All these data were obtained in the year 2000.

**Table 2-1: VOC and $CH_4$ emission from oil and gas operation sectors in 2000 (CAPP, 2005)**

| Sector | VOC emission (tonnes/year) | | $CH_4$ emission (tonnes/year) | |
|---|---|---|---|---|
| | Canada | Alberta | Canada | Alberta |
| Oil and gas well drilling | 1,554 | 1,076 | 466 | 267 |
| Oil and gas well servicing | 2,163 | 1,764 | 10,520 | 9,002 |
| Well testing | 1,154 | 1,050 | 4,932 | 4,805 |
| Natural gas production | 128,320 | 112,894 | 509,943 | 438,723 |
| Conventional oil production | 274,390 | 181,342 | 244,965 | 193,466 |
| Heavy oil/Bitumen production | 176,386 | 116,872 | 776,841 | 355,493 |
| Thermal operations | 12,171 | 7,668 | 39,693 | 20,354 |
| Natural gas processing | 31,134 | 28,765 | 62,392 | 57,224 |
| Liquid product transportation | 12,235 | 8,782 | 1,234 | 781 |
| Accident and equipment failure | 149,107 | 89,815 | 198,015 | 126,688 |
| **Total** | **788,614** | **550,028** | **1,849,001** | **1,206,803** |

Nonetheless, oil and gas operation sectors are not the only sources to emit hydrocarbons to the environment; lots of other sources emit hydrocarbons as well, such as motor vehicle transportation (mobile sources), wood industries, garbage disposal and other manufacturing industries. According to the historical data of NPRI (National Pollutant Release Inventory) – a division of Environment Canada – the emission share of oil and gas operations in all years is about 25–40% of the total hydrocarbon emission (NPRI, 2017). As shown in Table 2-2, methane

and non-methane VOCs have a larger impact on the environment. Nevertheless, Alberta is a significant contributor.

**Table 2-2: VOC and $CH_4$ emission to air from all reported sources in 2015 (APEI, 2017; NPRI, 2017)**

| Hydrocarbon Pollution | Emission (tonnes $CO_2$ equivalent /year) | |
|---|---|---|
| | Canada | Alberta |
| VOCs | 1,858,662 | 619,727 |
| $CH_4$ | 11,580,944 | 3,772,159 |

In Canada, the release of ethylene ($C_2H_4$) in air is mostly attributed to the combustion of fossil fuels. Although the industrial releases have dropped by over 50 % due largely to the amount of ethylene being recycled (Environment Canada, 2016), still a noteworthy amount of ethylene is emitted every year, and especially in Alberta. Table 2-3 shows the total amount of ethylene released in air by all sources, in Canada and Alberta, for the years of 2000 and 2016.

**Table 2-3: Emission of ethylene in Canada and Alberta (Environment Canada, 2016)**

| Year | Emission of ethylene (tonnes /year) | |
|---|---|---|
| | Canada | Alberta |
| 2000 | 2,710 | 1,238 |
| 2016 | 1,472 | 1,019 |

## 2.2 Atmospheric Reactions

Atmospheric chemistry is a mature field that contains gas phase reactions in two main categories of photochemical and chemical reactions. In any UV process (photochemical reactions), the energy of the photon absorbed should be higher than the bond dissociation energy in order to break the bond (Luo, 2007). UV radiation alone may not be sufficient to degrade recalcitrant compounds such as polymers or VOC's. Hence, it has to be combined with auxiliary oxidants in order to produce more powerful oxidants like hydroxyl radicals (Barrera, 2011). One mole of

photons emitted at 254 nm releases 471 kJ, while one mole of photons, at 185 nm contains 647 kJ based on Planck's relation: (Topudurtir et al., 1998)

$$E = h \cdot \frac{c}{\lambda} \tag{2.5}$$

where $E$ (J) is the energy of one photon at the given $\lambda$ (m), $c$ is the universal constant for light speed in vacuum with the value of 299,792,458 m/s, and $h$ is Planck's constant with the value of $6.626\times10^{-34}$ (J·s). The water molecule starts absorbing radiation from 498 kJ and higher, which corresponds to 240 nm (Oppenländer, 2003). However, hydroxyl (·OH) and hydrogen (H·) radicals are mainly generated at wavelength of 190 nm or shorter (Topudurtir et al., 1998), as primary species because the light absorption is low at higher wavelengths.

For the atmospheric chemical reactions, most of the degradation is caused by the reaction of ·OH radicals due to their high reactivity. Other than the hydroxyl radicals, hydrocarbons undergo reactions with ozone ($O_3$), nitrate radicals ($NO_3$), and oxygen atoms ($O(^3P)$). Table 2-4 shows a qualitative comparison of the reaction rates of alkanes and alkenes with these species. Clearly, reaction of alkenes with these species are potentially important, as alkenes react quickly and decay rapidly following their emission to the atmosphere (Calvert et al., 2008). So, it is expected that ethylene will be degraded faster than methane and ethane, provided that hydroxyl radicals are present in the reaction area.

**Table 2-4: Qualitative assessment of the reaction rates for VOCs in the atmosphere (Atkinson, 1994)**

| VOCs | ·OH | $O_3$ | $NO_3$ | $O(^3P)$ |
|---|---|---|---|---|
| Alkanes | Slow to medium | Extremely slow | | |
| Alkenes | Medium to fast | Fast | Medium to fast | Fast |

As mentioned, the H-OH bond strength in water vapor is 498 kJ/mol (Topudurtir et al., 1998). The value of the C-H bond dissociation energy for methane ($H\text{-}CH_3$), ethane ($H\text{-}CH_2CH_3$), and ethene ($H\text{-}CH{=}CH_2$) are 438 kJ/mol, 423 kJ/mol, and 464 kJ/mol, respectively (Blanksby & Ellison, 2003). Consequently, hydrogen abstraction by ·OH with these molecules is always thermodynamically possible. The reactions of these molecules with other species are not affected as much as reactions with the hydroxyl radical. On the whole, the reaction rates of alkanes and alkenes with OH radicals are 200-1000 times higher than with $O(^3P)$, 4-5 orders of magnitude higher than with $NO_3$, and 7-9 orders of magnitude higher than with $O_3$ (Calvert et al., 2008).

It is also worth mentioning that, for alkanes, the reactivity increases with increasing number of carbon atoms, since tertiary C-atoms (carbon atoms that attach to other three carbon atoms) are more reactive than primary C-atoms (e.g., $-CH_3$ group) (Calvert et al., 2008); while for alkenes, the reactivity is generally based on the π-bond (electron-rich bond) and thus, alkenes are commonly more reactive than alkanes (McMurry, 2006).

In this research, studying and including the reactions, both chemical and photochemical, are one of the biggest challenges. For any contributing species, all the reactions should be searched in the atmospheric reactions studies and the corresponding chemical or photochemical reaction variables (rate constants, quantum yields, and absorption cross-sections) must be presented in the model. In many cases, the data are available in the literature; however, for some cases the reaction products and rate constants must be assumed or estimated based on similarity with known reactions. The chemical and photochemical values along with the reactions for methane, ethane, and ethylene used in the proposed model, are given in Chapter 3, Tables 3-1 to 3-8.

## 2.3 Waste Gas Photolysis

There are several studies on wastewater photolysis, which has been successfully used in wastewater treatment. Photolysis for removing several pollutants in aqueous phase has been modeled for a long time. Some of these models are included but not limited to: the kinetic model of Yue (Yue, 1993) for elimination of low levels of organics in water production plants, the photochemical annulus reactor design of Sallemi et al. (Sellami et al., 2003), the kinetic modelling of Pereira et al. (Pereira et al., 2007) to remove pharmaceutical compounds in water, the detailed mathematical model of Kralik et al. (Kralik et al., 2010) for prediction of chlorinated hydrocarbon pollutants in water, and the model of Sanches et al. (Sanches et al., 2011) for the elimination of polycyclic aromatic hydrocarbons in drinking water. In all of these studies, the reaction mechanisms were very limited, and the effects of kinetic behaviour were neglected typically.

In the gas phase, photolysis has not been studied as much, especially in the modeling area, as only a few studies proposed simulation models for waste gas photolysis. The kinetics of gas phase photo-dissociation of VOC's has been evaluated using a low-pressure mercury UV lamp (Wang & Ray, 2000). Based on this work, it was found that photolysis at 185 nm and 254 nm, followed by oxidation, is a dominant way for an almost complete degradation of all VOCs after 20 minutes and a light intensity of 80 $W/m^2$. The destruction of chlorobenzene ($C_6H_5Cl$) as a chlorinated aromatic compound was examined by modeling of UV photolysis with and without the presence of $O_3$ for potential use in air emissions treatment (Zhang & Anderson, 2013). This model estimated the effective quantum yield and photonic efficiency for the photochemical decomposition of chlorobenzene ($C_6H_5Cl$) in air. It was concluded that ozone increased the degradation efficiency as well as humidity and oxygen. Additionally, ozone enhanced the

effective quantum yield of chlorobenzene since it can strongly absorb UV photons and promote radical reactions.

A reactor model has been developed for carbon tetrachloride ($CCl_4$) and chloroform ($CHCl_3$) photolysis in the gas phase by Chen et al. (Chen et al., 2004). Their model consists of a kinetic model of UV photo-oxidation of chloroform and carbon tetrachloride using a low-pressure mercury UV lamp. They included 14 reactions in their model in order to predict the outlet concentration of the pollutant, and they were able to predict a simple equation for the outlet concentration when the initial concentration of VOCs was low. They concluded, based on a good agreement between the simulated and experimental data, that a sound basis for the design of large-scale reactors had been established. However, they were aware that their approach would be difficult to accomplish for complex photochemical processes involving multiple reactions.

A refined mechanistic simulation model was developed to describe the ultraviolet degradation of $H_2S$ in waste gas (Asili & De Visscher, 2014). The photochemical reactor was simulated with a model that includes 47 reactions (39 chemical reactions and 8 photochemical reactions) involving 19 chemical species, material balances for each species in the model as well as the gas flow pattern. This model showed that the UV degradation of $H_2S$ in waste gas is a highly efficient process. This model was validated by comparing with experimental data of Xia et al. (Xia et al., 2008) with a reactor totally different from their modeled reactor. Comparable trends were found in two different reactors studied, confirming that the model was sound and can be used for feasibility studies. In addition to the $H_2S$ photolysis removal efficiency, the model was also able to predict the photolysis products in both cases of low and high inlet concentration of $H_2S$. In the same platform, this model was extended to include the photochemical degradation of

NO and $H_2S$ + NO mixtures. The extended model included 75 chemical reactions (36 additional reactions), 16 photochemical reactions (8 additional reactions), and 30 chemical species (11 additional species compared with $H_2S$ model alone). The model predicted that the ultraviolet degradation of $H_2S$ + $NO_x$ mixtures was more efficient than the degradation of either of the compounds in isolation, indicating that there was a synergism between $H_2S$ degradation and $NO_x$ degradation.

Lately, a sophisticated simulation model for benzene photolysis in waste gas was developed which was validated with experimental data (Mahmoudkhani et al., 2016). This model contained 59 reactions and 47 species, and included all independent reaction rates, photochemical reaction data. The close agreement between the model predictions and experimental studies showed that the gas phase photolysis system is dominated by a kinetic-control mechanism. Also, it was predicted that the ozone premixing can greatly increase the efficiency of UV degradation of BTEX (Benzene, Toluene, Ethylbenzene and Xylene) removal from waste gas. In addition, it was confirmed that a combination of condensation, ozone pre-mixing and UV photolysis is economically feasible.

### 2.4 Flow Simulation of a Photoreactor

Computational Fluid dynamics (CFD) has been used widely to predict the reactor performance in the area of waste water treatment. In the gas however, only few studies investigated to measure and predict the reactor performance when integration of reaction and mass transfer mechanisms. Most of these studies included photocatalytic processes in a non-homogenous reactor. It has been explored that the geometry of the photoreactor such as configuration, internal baffling (mostly used in water purification systems to make agitation), and inlet pattern have the most influence

on the flow regime in the annulus space (Sozzi & Taghipour, 2006). Later, Duran et al. (Duran et al., 2009) showed that low Reynolds *k-ε* models predicted flow behaviour more accurately, with the experimental validation, at Reynolds number less than 1500, especially, when there was a radial mass transfer occurring in the annulus photoreactor. Also, it was confirmed that simulation results with this model showed flow regimes in excellent agreement with the predictions by the laminar model. Alpert et al. (Alpert et al., 2010) used CFD modeling to predict photoreactor behaviour of UV/$H_2O_2$ advanced oxidation process, including 9 reactions occurring in the system, and compared the results with the experimental data in the pilot scale of an annulus photoreactor. They concluded that the selection of different flow model did not have a significant impact on the prediction of removal containment in the photoreactor.

In the gas phase, a CFD model has been developed to describe the interaction between the fluid dynamics of a VOCs (formaldehyde and methanol) loaded gas stream and the photochemical processes occurring within a photolytic reactor (Mallery & Heinsohn, 1996). This model included the reaction pathways and rates for these species. It was found that the destruction of formaldehyde in the photolytic annulus reactor (with two UV lamps) was more dependent on the light intensity distribution, gas residence time, and combination of ozone with pollutant, rather than selection of flow regime type. Also, Taghipour and Mohseni (Taghipour & Mohseni, 2005) investigated CFD simulation of UV photocatalytic reactors, and they concluded that the removal of a specific VOC (trichloroethylene, TEC) was not dependent on the choice of flow regime, and mostly dependent on concentration and flow rate. Moreover, Vincent et al. (Vincent et al., 2011) showed that for a photocatalytic degradation of gas phase acetone, in an annular UV reactor, the removal efficiency for an ideal plug flow analytical model was in close agreement with the CFD

simulation of the gas in the reactor, which can be concluded as independency of flow behavior in the degradation process.

### 2.5 Temperature in a Photoreactor

The maximum efficiency of commercial UV lamps in terms of their total input electrical power is 20% (Gutierrez et al., 2006). That means only a small portion of light irradiated is absorbed by the reactive medium, and a significant amount of the energy is released to the reactive area by heat loss. In the aqueous phase, this amount of lost energy does not affect the temperature of the aqueous medium, and the temperature variation is small. This is the reason that thermal effects of the photoreactors are normally ignored in the aqueous phase. For the gas phase however, even a small heat source can potentially make a large temperature gradient in the reaction area of a photoreactor.

Measuring temperature dependency of the absorption cross-section of formaldehyde (HCHO) at 254 nm showed that this value is fairly independent of temperature variations (Meller & Moortgat, 2000). Also, experimental photolysis of monochlorobenzene to measure the quantum yield at the wavelengths of 184.9 and 253.7 nm showed that the quantum yield values for this VOC are relatively temperature independent (Ichimura & Mori, 1973). Moreover, experimental and modeling gas phase oxidation kinetics of some chlorinated VOCs showed that the values of removal efficiency are almost independent of temperature variation (Feiyan et al., 2002). Furthermore, the review paper of Ray (Ray, 2000) for the photodegradation of the VOCS in gas phase showed that there might be a temperature variation in the degradation process, but the whole process and degradation efficiency for the majority of VOCS are independent of temperature variations, and other factors such as humidity have further strong impacts on the degradation removal efficiency.

# Chapter 3: Modeling and Simulation

## 3.1 Model Development

A refined mathematical model for the ultraviolet degradation of methane, ethane, and ethylene in waste gas is proposed. The modeled UV reactor is assumed to be tubular, with continuous flow mode, in which the UV lamp is assumed in the reactor and along with the reactor axis. Hence, the gas flows between two nested concentric pipes. The effective length is 50 cm and the inside diameter is 4.2 cm, and a lamp diameter of 2.5 cm. The UV lamp emits light rays at two different wavelengths 185 nm and 254 nm. Figure 3-1 shows a schematic diagram of the simulated photoreactor.

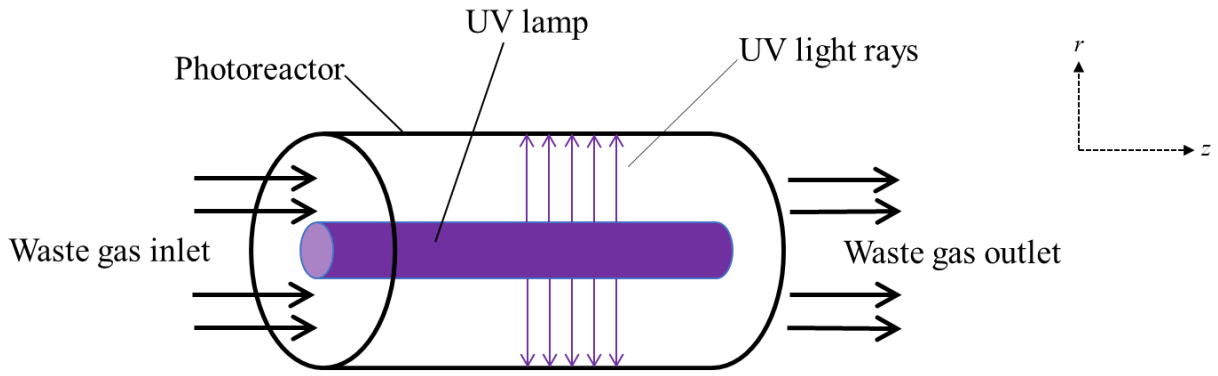


**Figure 3-1: Schematic diagram of the simulated photoreactor**

### *3.1.1 Model assumptions*

The corresponding model assumptions and justifications can be summarized as follows:

- Steady state conditions: The flow condition was also assessed with COMSOL in a time-dependent mode, and it is found that it can quickly (~ 2 minutes) establish the steady state condition.

- 2D model simulation: The reactor has a rotational cylindrical symmetry around the longitudinal (z) axis.

- Laminar flow regime: The Reynolds number is less than 2,100 for all modeled conditions. This assumption was confirmed with CFD calculations.

- Negligible hydrodynamic entrance length: It will be discussed that the flow regime does not have significant influence in the model results. This assumption was confirmed with CFD calculations.

- Newtonian fluid: The hydrocarbons (1%) are diluted with 99% pure moist air (i.e., 97% dry air and 2% water vapor).

- No mechanical dispersion: As the model assumes laminar flow. This assumption was also confirmed with CFD calculations. In addition, it is assumed that the molecular diffusion causes negligible axial dispersion. This was confirmed by calculating the Peclet number in Section 3.1.3.

- Insignificant effect of light scattering: The light model is dominantly led by absorption, as the absorption is at least 5 orders of magnitude stronger than scattering.

To develop a comprehensive model for the first-time simulation of the UV degradation of $CH_4$, $C_2H_6$, and $C_2H_4$ in the gas phase, all the four modeling parts which contribute to the simulation – the velocity profile, material balances, UV radiation field and a chemical kinetics model – should be considered, making the above assumptions. The principle of the model is based on the actual photoreactor for which the set up was described by Mahmoudkhani et al. (Mahmoudkhani et al., 2016).

### *3.1.2 Flow pattern model (velocity profile)*

To find the flow regime, the Reynolds number should be calculated for this reactor with a known value of mean flow velocity ($U$), kinematic viscosity ($\nu$), and pipe hydraulic diameter ($d_h$) as: (White, 2003)

$$Re = \frac{U \cdot d_h}{\nu} \tag{3.1}$$

Since the modeled reactor does not have a circular cross-section, the hydraulic diameter ($d_h$) is used. With $R_0$ = 1.25 cm (outer lamp diameter) and $R_1$ = 2.1 cm (inner reactor wall diameter), and based on its definition (Bansal, 2010), the calculation of hydraulic diameter ($d_h$) is as follows:

$$d_h = \frac{4A}{\mathrm{P}} = \frac{4 \times \text{area}}{\text{wetted perimeter}} = \frac{4\pi(R_1^2 - R_0^2)}{2\pi(R_1 + R_0)} = 2(R_1 - R_0) = 2(2.1\text{ cm} - 1.25\text{ cm}) = 1.7\text{ cm} \tag{3.2}$$

The mean velocity for the reactor can be found by dividing the volumetric flow rate ($Q$) to the cross-section area, such that:

$$U = \frac{Q}{\pi(R_1^2 - R_0^2)} \tag{3.3}$$

Knowing the fact that the assumed volumetric flow rates ($Q$) in the model are variable between 500 – 5000 $cm^3$/min, the mean velocity in the range of 0.93 – 9.32 cm/s is obtained. Considering pure air with kinematic viscosity, $\nu$ = 0.15 $cm^2$/s (Bansal, 2010), the Reynolds number is calculated to be 10.5 – 105 respectively. As the value is significantly less than the laminar region threshold ($Re$<2,100 (White, 2003)), a laminar flow velocity profile is a sensible assumption for this model. This conclusion will be confirmed by CFD simulations in Chapter 4.

Also, it is assumed that laminar flow is established immediately at the reactor entrance. However, because the effect of flow regime on the model results is small, the model is not sensitive to this assumption (this also will be discussed later in Chapter 3 and 4). Furthermore,

the Hydrodynamic Entrance Length ($L_{hy}$) was also calculated based on its formulation: (Atkinson et al., 1969)

$$\frac{L_{hy}}{d_h} = 0.59 + 0.056Re \tag{3.4}$$

With the maximum Reynolds number at worst case scenario ($Re$ = 105), yields to $L_{hy}$ = 11.0 cm; which is less than 22% of the total reactor length. Nevertheless, it will be discussed in Chapter 4 that the higher volumetric flow rate is not desirable as it causes decreasing removal efficiency of the process. The hydrodynamic entrance length calculated here is in general agreement with CFD calculations made in Chapter 4.

In view of all the above-mentioned information, the laminar velocity profile in an annular space can be derived with the force balance applied on a cylindrical element (Figure 3-2), using Newton's viscosity law, as follows:

*Force = (Pressure or stress) × Area* (3.5a)

*Pressure + Shear stress forward = Pressure + Shear stress backward* (3.5b)

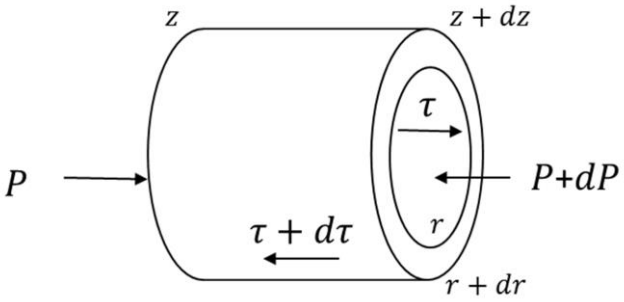


**Figure 3-2: Force balance on an annular element**

Considering $P$ (pressure), $\tau$ (shear stress), $z$ (the length coordinate), and $r$ (the radial coordinate), the local gas velocity for an annular space was attained as: (Bird et al., 2002; Mahmoudkhani, 2012)

$$V = \frac{\frac{2U(R_1^2 - R_0^2)}{\ln \frac{R_1}{R_0}} \ln \frac{r}{R_0} - 2U(r^2 - R_0^2)}{R_1^2 + R_0^2 - \frac{R_1^2 - R_0^2}{\ln \frac{R_1}{R_0}}} \tag{3.5}$$

Where $U$ is the mean flow velocity, and $r$ is the radial coordinate, which has a value between $R_0$ and $R_1$ in the annular space.

Model predictions were previously compared at two different velocity profiles, laminar (using Equation (3.5)) and plug flow (using constant $V=U$), and the results differed by only 1%–2% (Mahmoudkhani et al., 2016). This calculation will be confirmed by a sensitivity analysis in Chapter 4. Thus, the velocity pattern is not critical in the model development. However, for the reason that using Equation (3.5) did not meaningfully lengthen the simulation run-time, Equation (3.5) was used as the velocity profile in all simulations.

### *3.1.3 Model material balance*

As an important factor, the diffusivity of the gas mixture should be calculated. The most accurate calculation of multicomponent diffusion is by applying the Maxwell-Stefan equation for the multicomponent system. However, in a very dilute system, the Maxwell-Stefan equation approaches Fickian diffusion with a binary diffusion coefficient (Treybal, 1980). Hence, as the model assumes that the gas stream contains less than 1% hydrocarbons, using Fick's law with the binary diffusion coefficient as an air-compound binary mixture (i.e. $D_{\text{compound } i\ -\ \text{air}}$) is a valid practical approach. To calculate this value, the empirical formulation of Fuller (Fuller et al., 1969) is used:

$$D_{AB} = \frac{0.00143\ T^{1.75}}{PM_{AB}^{1/2}[(\sum_V)_A^{1/3} + (\sum_V)_B^{1/3}]^2} \tag{3.6a}$$

Where $D_{AB}$ is in $cm^2/s$, $P$ is in atm, $T$ is in Kelvin, $\Sigma_v$ is the summation of structural diffusion volumes. Also, $M_{AB}$ is defined based on each molecular weight:

$$M_{AB} = \frac{2}{(1/M_A) + (1/M_B)} \tag{3.6b}$$

$M_{Air}$ and $(\Sigma_v)_{Air}$ have the value of 28.97 g/mol and 19.7 $cm^3$, respectively. For all other components in the model, the values of molecular weight ($M_A$) and $(\Sigma_v)_B$ were taken from the information of Seader et al. (Seader et al., 2011). Using this information, the model is able to calculate the diffusivity value for each component (69 species) in the model, at a given temperature and pressure. The average value for all the components is found to be $D_{AB}$ = 0.23 $cm^2/s$.

To find the mass transfer mechanism, the Peclet number, $Pe_L$, which is flow velocity divided by diffusion velocity, should be calculated as: (Cussler, 2009)

$$Pe_L = \frac{U \cdot L}{D} \tag{3.7}$$

Where $U$ is the gas mean velocity, $L$ is the reactor length, and $D$ is the gas diffusivity. Considering the minimum value of mean velocity ($U$ = 0.93 cm/s), length ($L$ = 50 cm) and average value of gas diffusivity in the model ($D$ = 0.23 $cm^2/s$), the minimum value of the Peclet number is found to be $Pe_L$ = 202.18. Therefore, as this number is greater than 40, advection can be assumed to be the dominant mass transfer mechanism in the flow direction (Froment et al., 1990). On the other side, the flow regime was assumed laminar previously; thus, diffusion is the dominant mass transfer mechanism in the radial direction. Subsequently, a laminar flow model with radial diffusion limitation and no mechanical dispersion effects was used in the simulation.

Accordingly, in the proposed model, the material balance equation without consideration of mechanical dispersion effects (*Flow in + Diffusion in + Reaction = Flow out + Diffusion out*) can be derived to the assumed annular element (Figure 3-3) with the subsequent variable definitions as follows:

$C_i$ is the concentration of compound *i* (molecules/cm$^3$),

$D_i$ is the molecular diffusivity of compound *i* (cm$^2$/s),

$r_i$ is the reaction rate of *i* (molecules/cm$^3$ s) and

*V* is the local gas velocity (cm/s).

$$Flow\ in\ =\ C_i\big|_z \cdot V \cdot 2\pi r \cdot \mathrm{d}r \tag{3.8a}$$

$$Flow\ out\ =\ (C_i\big|_{z+\mathrm{d}z}) \cdot V \cdot 2\pi r \cdot \mathrm{d}r \tag{3.8b}$$

$$Diffusion\ in\ = -D_i \left.\frac{\partial C_i}{\partial r}\right|_r \cdot 2\pi r \cdot \mathrm{d}z \tag{3.8c}$$

$$Diffusion\ out\ =\ -D_i \left.\frac{\partial C_i}{\partial r}\right|_{r+\mathrm{d}r} \cdot 2\pi (r+\mathrm{d}r) \cdot \mathrm{d}z \tag{3.8d}$$

$$reaction\ =\ r_i \cdot 2\pi r \cdot \mathrm{d}r \cdot \mathrm{d}z \tag{3.8e}$$

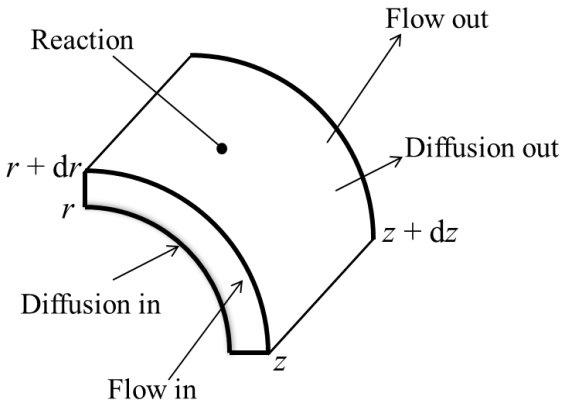


**Figure 3-3: Material balance on an annular element**

Substituting all the above terms to the material balance equation, and dividing all the terms by $2\pi r \cdot \mathrm{d}r \cdot \mathrm{d}z$ leads to:

$$r_i = \frac{V}{\mathrm{d}z} \cdot \left( C_i\big|_{z+\mathrm{d}z} - C_i\big|_z \right) - \frac{D_i}{\mathrm{d}r} \left( \left. \frac{\partial C_i}{\partial r} \right|_{r+\mathrm{d}r} - \left. \frac{\partial C_i}{\partial r} \right|_r \right) - \frac{D_i}{r} \cdot \left. \frac{\partial C_i}{\partial r} \right|_{r+\mathrm{d}r} \tag{3.9}$$

At the limit to d$r \rightarrow 0$ and d$z \rightarrow 0$, the terms between brackets divided by their respective differentials, form second partial derivatives.

All in all:

$$V \cdot \frac{\partial C_i}{\partial z} = D_i \cdot \frac{\partial^2 C_i}{\partial r^2} + \frac{D_i}{r} \cdot \frac{\partial C_i}{\partial r} + r_i \tag{3.10}$$

This is one material balance partial differential equation per compound, which has the unknown value of the concentration. The boundary condition of the concentration at the reactor inlet (i.e., $z = 0$) is assumed to be a known concentration of the feed stream. For the radial derivatives, boundary conditions at $r = R_0$ (UV lamp outer radius) and $r = R_1$ (reactor wall inner radius) are needed. The no-flux condition (i.e. zero radial concentration gradient) is assumed, which means:

$$\frac{\partial C_i}{\partial r} = 0 \qquad @ \qquad r = R_0 \ \text{ and } \ r = R_1 \tag{3.11}$$

Another way to show the Equation (3.10) is to make it non-dimensional. To do this, the following dimensionless variables can be defined:

$$C^* = C \big/ C_0 \tag{3.12a}$$

$$z^* = z \big/ L_0 \tag{3.12b}$$

$$r^* = r \big/ R_0 \tag{3.12c}$$

$$\delta = \frac{L_0}{R_0} \tag{3.12d}$$

So, the Equation (3.10) can be re-arranged in the form of the dimensionless equation:

$$\frac{\partial C_i^*}{\partial z^*} = \frac{\delta^2}{Pe} \cdot \frac{\partial^2 C_i^*}{\partial r^{*2}} + \frac{\delta^2}{r^*} \cdot \frac{1}{Pe} \frac{\partial C_i^*}{\partial r^*} + (\frac{L_0}{C_0 \cdot V}) r_i \quad (3.13)$$

In the above equation, all terms are written in the non-dimensional format. Here, the *Pe* number is defined based on local velocity (*V*) and not the mean velocity (*U*). Also, $\delta$ can be interpreted as the aspect ratio. Since the rate of reaction ($r_i$) can have a different functionality of concentration ($C_i$), the last term can be dimensionless as the different concentration values for each species applied. Although the use of Equation (3.13) can be beneficial for characterization purposes, the model was completely developed with the use of mass balance in the original format (Equation (3.10)).

Dimensional analysis indicates that the solution of Equation (3.13) depends on $\delta^2/Pe$, which is equals to $\frac{L_0 D_i}{R_0^2 V}$, as well as on the inlet concentration of each species, and on the kinetics of each species. However, the latter is itself a function of many variables (temperature, light intensity, geometry of light field, and concentrations), the number of variables affecting the results remains large.

### *3.1.4 Radiation field model*

The proposed model assumes that the lamp can be approximated by a line source of light that sends out light rays perpendicular to the lamp. Previous studies (Asili & De Visscher, 2014; Mahmoudkhani et al., 2016) indicated that this assumption might underestimate the real light absorption, as it only considers the light with the shortest path length. The radial distribution of light intensity is uneven to some extent, with a higher intensity found near the lamp, but because of the narrow gap size, diffusion largely compensates for this effect, and the radial concentration

variation is on the order of 2% (Mahmoudkhani et al., 2016). Moreover, Mahmoudkhani (Mahmoudkhani, 2012) developed a refined and complicated model of light irradiance in which all of the light rays moving at different angles were considered in an extensive iterative process. Although this complicated light field model slightly overestimated the experimental results, it did not have a noticeable effect on the simulated conversion, as the results were different by less than 10%, but the simulation run times were increased by a factor 20. All things considered, the presented model for the light field is a practical approach, since the exact path of light does not play a noteworthy role in the model, due to a degree of reflection of the light back and forth between the lamp and the outside cylinder.

To calculate the values of the light intensity at each location in the reactor, an annular element of the reactor is considered for the photon balance, as shown in Figure 3-4.

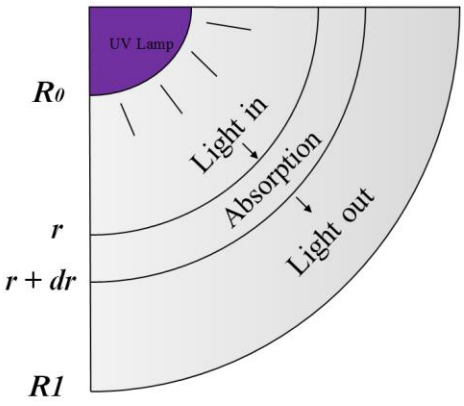


**Figure 3-4: Photon balance on an annular element of the reactor**

The general photon balance equation is:

Light out = Light in – Absorption (3.14a)

In the above equation, the light scattering is neglected, since it has a value of $5.1\times10^{-27}$ $cm^2$ at 532 nm, and its wavelength dependence is proportional to $\lambda^{-4}$ (Sneep & Ubachs, 2005). By a

quick calculation, the scattering wavelength is found to be at least 5 orders of magnitude lower than the absorption cross-section for 185 nm in the system studied.

So, with the following variable definitions and principal equations, the photon balance equation for an annular element of the reactor (Figure 3-4) can be derived as follows:

$E_p$ is irradiance (photons/cm$^2$ s),

$C_i$ is the concentration of compound $i$ (molecules/cm$^3$) and

$\sigma_i$ is the absorption cross-section of compound $i$ (cm$^2$)

$\alpha_i$ is the molecular extinction coefficient of compound $i$ ($\alpha_i = C_i\,\sigma_i$).

Light in = $E_p\big|_r \cdot 2\pi r \cdot z$ (3.14b)

Light out = $E_p\big|_{r+\mathrm{d}r} \cdot 2\pi(r+\mathrm{d}r)\cdot z = E_p\big|_{r+\mathrm{d}r}\, 2\pi r\cdot z + E_p\big|_{r+\mathrm{d}r} \cdot 2\pi\cdot \mathrm{d}r\cdot z$ (3.14c)

Absorption = $\sum_i \alpha_i E_p \cdot 2\pi r\cdot \mathrm{d}r\cdot z$ (3.14d)

Substituting the terms into Equation (3.14) leads to:

$$E_p\big|_{r+\mathrm{d}r}\, 2\pi r\cdot z + E_p\big|_{r+\mathrm{d}r} \cdot 2\pi\cdot \mathrm{d}r\cdot z = E_p\big|_r \cdot 2\pi r\cdot z - \sum_i C_i\sigma_i E_p \cdot 2\pi r\cdot \mathrm{d}r\cdot z \tag{3.14e}$$

Rearranging and dividing the whole equation to $2\pi r\cdot \mathrm{d}r\cdot z$ yields:

$$\left(\frac{E_p\big|_{r+\mathrm{d}r}\cdot 2\pi r\cdot z - E_p\big|_r\cdot 2\pi r\cdot z}{2\pi r\cdot \mathrm{d}r\cdot z}\right) = \frac{-E_p\big|_{r+dr}\cdot 2\pi\cdot \mathrm{d}r\cdot z}{2\pi r\cdot \mathrm{d}r\cdot z} - \frac{\sum_i C_i\sigma_i E_p\cdot 2\pi r\cdot \mathrm{d}r\cdot z}{2\pi r\cdot \mathrm{d}r\cdot z} \tag{3.14f}$$

By taking the limit, and approaching $\mathrm{d}r \to 0$, Equation (3.14f) will be:

$$\frac{\mathrm{d}E_p}{\mathrm{d}r} = -\frac{E_p}{r} - \sum_i C_i\sigma_i E_p \tag{3.15}$$

This equation stands for one differential equation for each wavelength, at each location along the length of the reactor, which has an unknown value of concentration and irradiance. As the direction of the light is substantial for solving this equation, the photon fluence rate is assumed to be the sum of the irradiance of the outgoing light and the reflected light. Also, a separate equation was used for wavelengths 185 nm and 254 nm (as the two lines in the mercury (Hg) UV lamp spectrum in this study).

The boundary condition for Equation (3.15) is the photon irradiance ($E_p$) at the lamp surface. This value can be calculated as emitted light power of the lamp, divided by the surface area of the lamp, and then divided by the energy of one photon. Moreover, The UV reactor provider pointed out that 99 % of the photons reaching the reactor outer wall are reflected, which means if one light ray is traced, once it reached the reactor internal wall, 99% of the energy at that position will be reflected ($E_{p,\text{ forward-wall}} = -0.99\, E_{p,\text{ backward-wall}}$). The light returning to the lamp is either absorbed by the mercury vapor, or re-emitted. The fraction of photons re-emitted is unknown. This fraction can be obtained by comparing the light irradiance at the wall by model predictions with experimental measurements. Mahmoudkhani et. al (Mahmoudkhani et al., 2016) measured this value for pure air, and reported that 60.3 % of the light returning to the lamp is re-emitted, for the lamp that generated 55 mW/cm$^2$ of light irradiance as measured at the outside wall. However, for a newer lamp assumed is in this study (which can generate 65 mW/cm$^2$ of light irradiance), taking 70% of the lamp reflection is a sensible assumption. Which means, by tracing a light ray, once the light ray comes back to the lamp, 30% of its energy is absorbed by the lamp, while the rest (70%) will be re-emitted. Hence, these two values (reflection at the wall, and re-emission of the lamp) should be taken into consideration in the solution of Equation (3.15).

### *3.1.5 Reaction model*

One of the primary focus of this research is to originate a comprehensive reaction network. An extensive effort was made to include all the possible reactions and chemical species in the model, comprehensively. However, this area of research in atmospheric chemistry often suffers from some challenges, such as missing the relevant reaction rate values, or lack of prediction/measurement of the reaction products. To overcome this, some assumptions, justifications and calculations might be required, and for these cases, all of them will be addressed in this research as necessary. In addition, modeling of the reaction process is similar to a trade-off process; the more reactions included to get the greatest accuracy, the longer computational time is needed.

In agreement with atmospheric chemistry, all the reactions in this model can be categorized in two main subject areas: *Chemical Reactions*, and *Photochemical Reactions*.

- ***Chemical Reactions***

The rate of reaction, $-r_i$, is "the number of moles of *i* reacting per unit time, per unit volume" (Fogler, 2016). This rate has a unit of "molecules/cm$^3$·s" in gas phase atmospheric chemistry. For a typical reaction ($A+B \rightarrow Products$), the reaction kinetics is usually described as:

$$-r_i = k_i C_A^{n_{i,A}} C_B^{n_{i,B}} \tag{3.16a}$$

Where $k_i$ is the reaction rate constant, $C$ represents the concentration of reactant and the power, $n$, represents the order of the reaction for its reactant.

The reaction rate constant in the gas phase, $k_i$, is expressed by the Arrhenius equation as follows:

$$k_i = A\exp(-\frac{E_a}{RT}) \tag{3.16b}$$

Where $A$ is known as the frequency factor, $E_a$ is the activation energy, and $R$ is the universal gas constant. In this area of research, very often in the literature $E_a/R$ is presented instead of $E_a$. Not all rate constants must be a function of temperature; in some cases, they are presented only as a constant number, especially when there is a radical in the reaction. However, combining the above equations yield the general reaction rate for a typical chemical reaction ($A+B \rightarrow Products$) in gaseous phase:

$$-r_i = A\exp(-\frac{E}{RT})\, C_A^{n_{i,A}} C_B^{n_{i,B}} \tag{3.16c}$$

In addition, in most cases, there is no pressure dependence for gas phase reaction rate constants. However, some combination reactions have an order of three at low pressure, and two at high pressure. So, there is an intermediate pressure range to describe the kinetics which is known as falloff (Troe, 1979). Typically, the mechanism of these reactions is shown as follows: (Sander et al., 2011)

$$A + B \leftrightarrow AB^* \tag{3.17a}$$

$$AB^* + M \rightarrow AB + M \tag{3.17b}$$

In this case, AB* decomposes at low pressure, and the overall reaction rate is proportional to the concentration of M which can be either $N_2$ or $O_2$; at high pressure, the concentration of M is sufficiently high that every produced intermediate reacts to yield AB, irrespective of the actual concentration of M (De Visscher, 2013).

Two different methods for the calculation of the rate constant in the falloff range can be found in the literature. Both methods are used in the proposed model. One way, Atkinson et al. (Atkinson

et al., 2006) and Atkinson et al. (Atkinson et al., 2004) use Troe's model (Troe, 1979) with the following equations:

$$k_i = \frac{k_0 k_\infty}{k_0 + k_\infty} F \tag{3.18a}$$

$$\log F = \frac{\log F_c}{1 + \left( \frac{\log(k_0 / k_\infty)}{0.75 - 1.27 \log F_c} \right)^2} \tag{3.18b}$$

In which, $k_0$ is the second order rate constant in the low-pressure limit (which is actually a third order constant as multiplied by the concentration of M), $k_\infty$ is rate constant at the high-pressure limit, and $F_c$ is a broadening factor which is an empirical parameter for that specific reaction.

Another way, is the model of NASA/JPL Data Evaluation (Burkholder et al., 2015; Sander et al., 2011), with the equation:

$$k_i = \left( \frac{k_0}{1 + \frac{k_0}{k_\infty}} \right) 0.6^{\left\{ 1 + \left[ \frac{k_0}{k_\infty} \right]^2 \right\}^{-1}} \tag{3.18c}$$

It is worth mentioning that for the chemical reactions in this study, it has been appropriately presumed that all reaction rates are first-order in each component (second-order or maximum third-order in total) and besides, each component participates in the reaction in accordance with its stoichiometry number, unless it was specified otherwise by any reference.

- ***Photochemical Reactions***

A photochemical reaction is a reaction caused by absorption of a photon. The rate of a photochemical reaction, $r_i$, (molecules/cm$^3$ s) can be described as:

$$-r_i = \varphi_i \cdot C_i \cdot \sigma_i \cdot E_p \tag{3.19}$$

Where $\varphi_i$ is the quantum yield of molecule $i$ (molecule/photon), $C_i$ is the concentration of the component $i$ (molecule/cm$^3$), $\sigma_i$ is the absorption cross-section of molecule $i$ (cm$^2$/molecule) and $E_p$ is the photon fluence rate (i.e., the actinic flux), (photons/cm$^2$·s).

The detailed definition of variables, and formulations for the derivation of Equation (3.19) is given in Appendix B.

### *3.1.6 Model reactions*

This section covers all the reactions included in the model. The chemical and photochemical reactions with their corresponding values of reaction rates are given. The values for the chemical rate constant ($k_i$), quantum yield ($\varphi_i$) and absorption cross-section ($\sigma_i$) at the two given wavelengths of 185 nm and 254 nm, the two lines in the mercury (Hg) UV lamp spectrum in this study, were extracted from literature in the area of atmospheric chemistry (which is known as a mature field) and incorporated in the model. In case of lack of information, such as quantum yields and some reaction products, those values were assumed appropriately based on inter/extrapolation, similarities with other reactions, as required.

For each of the following models, the reactions and corresponding values are classified in two bases: one is the reaction name and number (which will be explained for each model, in this section), and one is the formatting – bold/italic/roman – (which will be explained in the Chapter 4, Section 4.1).

#### *3.1.6.1 Background air*

As it was assumed that all pollutant gases are diluted with ambient air, all reactions and corresponding chemical species of air should be included in the model as a first step. The dilution of hydrocarbons with air necessitates to always include the background common

reactions and species, regardless of any hydrocarbon introduced to the reactor. These reactions include oxygen, nitrogen, water content, which produce radicals photochemically, and/or react with the radicals chemically. The background model contains 21 chemical species in the most comprehensive version of the model. These components are reported in Appendix A, Table A-1.

Table 3-1 shows chemical reactions in the background air with their rate constants. All the reactions are assigned with a number and two letters: "B" stands for "Background" reactions and "C" stands for "Chemical" reactions, respectively.

**Table 3-1:Chemical reactions and rate constants in the background air model (bold: the primary kinetics; italic: reactions added for the primary + $NO_x$ kinetics; roman: reactions added for the comprehensive kinetics.)**

| Reaction Number | Reaction | Rate Constant ($cm^3$/molecules·s) | Reference |
|---|---|---|---|
| **BC1** | **$O(^3P) + OH\cdot \rightarrow H\cdot + O_2$** | $1.8 \times 10^{-11} \exp(180/T)$ | (Sander et al., 2011) |
| **BC2** | **$O(^3P) + HO_2\cdot \rightarrow OH\cdot + O_2$** | $3.0 \times 10^{-11} \exp(200/T)$ | (Sander et al., 2011) |
| **BC3** | **$O(^3P) + O_2 + M \rightarrow O_3 + M$** | $k_0 = 6 \times 10^{-34} (T/300)^{-2.8} [O_2]$ + $5.6 \times 10^{-34} (T/300)^{-2.8} [N_2]$ | (Atkinson et al., 2004) |
| **BC4** | **$O(^3P) + O_3 \rightarrow 2\ O_2$** | $8.0 \times 10^{-12} \exp(-2060/T)$ | (Sander et al., 2011) |
| **BC5** | **$O(^1D) + H_2O \rightarrow 2\ OH\cdot$** | $1.63 \times 10^{-10} \exp(60/T)$ | (Sander et al., 2011) |
| **BC6** | **$O(^1D) + O_2 \rightarrow O(^3P) + O_2$** | $3.3 \times 10^{-11} \exp(55/T)$ | (Sander et al., 2011) |
| **BC7** | **$O(^1D) + N_2 \rightarrow O(^3P) + N_2$** | $2.15 \times 10^{-11} \exp(110/T)$ | (Sander et al., 2011) |
| **BC8** | **$OH\cdot + H_2O_2 \rightarrow HO_2\cdot + H_2O$** | $2.9 \times 10^{-12} \exp(-160/T)$ | (Atkinson et al., 2004) |
| **BC9** | **$OH\cdot + O_3 \rightarrow HO_2\cdot + O_2$** | $1.7 \times 10^{-12} \exp(-940/T)$ | (Sander et al., 2011) |
| **BC10** | **$OH\cdot + HO_2\cdot \rightarrow H_2O + O_2$** | $4.8 \times 10^{-11} \exp(250/T)$ | (Sander et al., 2011) |
| **BC11** | **$2\ OH\cdot + M \rightarrow H_2O_2 + M$** | $k_0 = 6.9 \times 10^{-31} (T/300)^{-0.8} [N_2]$ $k_\infty = 2.6 \times 10^{-11}$ $F_c = 0.5$ | (Atkinson et al., 2004) |
| **BC12** | **$HO_2\cdot + O_3 \rightarrow OH\cdot + 2\ O_2$** | $1.0 \times 10^{-14} \exp(-490/T)$ | (Sander et al., 2011) |
| **BC13** | **$2\ HO_2\cdot + M \rightarrow H_2O_2 + O_2 + M$** | $\{2.2 \times 10^{-13} \exp(600/T) + 1.9 \times 10^{-33} \exp(980/T) [N_2] + 1.6 \times 10^{-33} \exp(980/T) [O_2]\} \times (1 + 1.4\times10^{-21} \exp(2200/T) [H_2O])$ | (De Visscher et al., 2008) |
| **BC14** | **$\cdot H + O_3 + M \rightarrow OH\cdot + O_2 + M$** | $1.4 \times 10^{-10} \exp(-470/T)$ | (Sander et al., 2011) |

| | | | |
|---|---|---|---|
| **BC15** | **·H + $O_2$ + M → $HO_2$· + M** | $k_0 = 4.4 \times 10^{-32} (T/300)^{-1.3}$ [$N_2$]<br>$k_\infty = 7.5 \times 10^{-11} (T/300)^{0.2}$ | (Sander et al., 2011) |
| *BC16* | *$O(^3P)$ + $NO_2$ → NO + $O_2$* | $5.15 \times 10^{-12} \exp(210/T)$ | (Sander et al., 2011) |
| *BC17* | *·H + $NO_2$ → ·OH + NO* | $4 \times 10^{-10} \exp(-340/T)$ | (Sander et al., 2011) |
| *BC18* | *OH· + NO + M→ $HNO_2$ + M* | $k_0 = 7.4 \times 10^{-31} (T/300)^{-2.4}$ [$N_2$]<br>$k_\infty = 3.3 \times 10^{-11} (T/300)^{-0.3}$<br>$F_c = \exp(-T/1420)$ | (Atkinson et al., 2004) |
| *BC19* | *OH· + $NO_2$ + M→ $HNO_3$ + M* | $k_0 = 3.3 \times 10^{-30} (T/300)^{-3}$ [$N_2$]<br>$k_\infty = 4.1 \times 10^{-11}$<br>$F_c = 0.4$ | (Atkinson et al., 2004) |
| *BC20* | *OH· + $NO_3$ → ·$HO_2$ + $NO_2$* | $2.0 \times 10^{-11}$ § | (Atkinson et al., 2004) |
| *BC21* | *OH· + $HNO_2$ → $H_2O$ + $NO_2$* | $1.8 \times 10^{-11} \exp(-390/T)$ | (Atkinson et al., 2004) |
| *BC22* | *OH· + $HNO_3$ → $H_2O$ + $NO_3$* | $8.3 \times 10^{-15} \exp(850/T)$ | (Sander et al., 2011) |
| *BC23* | *OH· + $HO_2NO_2$ → $H_2O$ + $O_2$ + $NO_2$* | $1.3 \times 10^{-12} \exp(380/T)$ | (Atkinson et al., 2004) |
| *BC24* | *·$HO_2$ + NO → $NO_2$ + OH·* | $3.3 \times 10^{-12} \exp(270/T)$ | (Atkinson et al., 2004) |
| *BC25* | *·$HO_2$ + $NO_2$+M → $HO_2NO_2$ + M* | $k_0 = 1.8 \times 10^{-31} (T/300)^{-3.2}$ [$N_2$]<br>$k_\infty = 4.7 \times 10^{-12}$<br>$F_c = 0.6$ | (Atkinson et al., 2004) |
| *BC26* | *$HO_2NO_2$ + M →·$HO_2$+ $NO_2$+ M* | $k_0 = 4.1 \times 10^{-5} \exp(-10650/T)$ [$N_2$]<br>$k_\infty = 4.8 \times 10^{15} \exp(-11170/T)$<br>$F_c = 0.6$ | (Atkinson et al., 2004) |
| *BC27* | *·$HO_2$ + $NO_3$ → ·HO + $NO_2$ + $O_2$* | $2.3 \times 10^{-12} \exp(170/T)$ | (Atkinson et al., 2004) |
| *BC28* | *NO + $O_3$ → $NO_2$ + $O_2$* | $3.0 \times 10^{-12} \exp(-1500/T)$ | (Sander et al., 2011) |
| *BC29* | *NO + $NO_3$ → 2$NO_2$* | $1.5 \times 10^{-11} \exp(170/T)$ | (Sander et al., 2011) |
| *BC30* | *$NO_2$ + $NO_3$ + M→ $N_2O_5$ + M* | $k_0 = 3.6 \times 10^{-30} (T/300)^{-4.1}$ [$N_2$]<br>$k_\infty = 1.9 \times 10^{-12} (T/300)^{0.2}$<br>$F_c = 0.35$ | (Atkinson et al., 2004) |
| *BC31* | *$N_2O_5$ + M → $NO_2$ + $NO_3$ + M* | $k_0 = 1.3 \times 10^{-3} (T/300)^{-3.5} \exp(-11000/T)$[$N_2$]<br>$k_\infty = 9.7 \times 10^{14} (T/300)^{0.1} \exp(-11080/T)$<br>$F_c = 0.35$ | (Atkinson et al., 2004) |
| BC32 | $O(^3P) + H_2O_2 \rightarrow OH\cdot + HO_2\cdot$ | $1.4 \times 10^{-12} \exp(-2000/T)$ | (Sander et al., 2011) |
| BC33 | $2\ O(^3P) + M \rightarrow O_2 + M$ | $2.7 \times 10^{-34}\ T^{-0.41}$ ([$N_2$ + $O_2$]) | (Atkinson et al., 2004) |
| BC34 | $O(^1D) + O_3 \rightarrow 2\ O_2 + O(^3P)$ | $1.2 \times 10^{-10} \exp(0/T)$ | (Sander et al., 2011) |
| BC35 | $O(^1D) + H_2 \rightarrow OH\cdot + H\cdot$ | $1.1 \times 10^{-10} \exp(0/T)$ | (Sander et al., 2011) |

| | | | |
|---|---|---|---|
| BC36 | $OH\cdot + H_2 \rightarrow H_2O + H\cdot$ | $2.8 \times 10^{-12} \exp(-1800/T)$ | (Sander et al., 2011) |
| BC37 | $2\ OH\cdot \rightarrow O(^3P) + H_2O$ | $7.9 \times 10^{-14} (T/298)^{2.6} \exp(945/T)$ | (De Visscher et al., 2008) |
| BC38 | $\cdot H + HO_2\cdot \rightarrow OH\cdot + OH\cdot$ | $7.2 \times 10^{-11} \exp(0/T)$ | (Sander et al., 2011) |
| BC39 | $\cdot H + HO_2\cdot \rightarrow O(^3P) + H_2O$ | $1.6 \times 10^{-12} \exp(0/T)$ | (Sander et al., 2011) |
| BC40 | $\cdot H + HO_2\cdot \rightarrow H_2 + O_2$ | $6.9 \times 10^{-12} \exp(0/T)$ | (Sander et al., 2011) |
| BC41 | $O(^1D) + N_2 + M \rightarrow N_2O + M$ | $k_0 = 2.8 \times 10^{-36} (T/300)^{-0.9} [N_2]$ | (Sander et al., 2011) |
| BC42 | $O(^1D) + N_2O \rightarrow O(^3P) + N_2O$ | $5.0 \times 10^{-13}$ | (Atkinson et al., 2004) |
| BC43 | $O(^1D) + N_2O \rightarrow N_2 + O_2$ | $4.64 \times 10^{-11} \exp(20/T)$ | (Sander et al., 2011) |
| BC44 | $O(^1D) + N_2O \rightarrow NO + NO$ | $7.25 \times 10^{-11} \exp(20/T)$ | (Sander et al., 2011) |
| BC45 | $O(^3P) + NO + M \rightarrow NO_2 + M$ | $k_0 = 9.0 \times 10^{-32} (T/300)^{-1.5} [N_2]$<br>$k_\infty = 3 \times 10^{-11}$ | (Sander et al., 2011) |
| BC46 | $O(^3P) + NO_2 + M \rightarrow NO_3 + M$ | $k_0 = 1.3 \times 10^{-31} (T/300)^{-1.5} [N_2]$<br>$k_\infty = 2.3 \times 10^{-11} (T/300)^{0.24}$<br>$F_c = 0.6$ | (Atkinson et al., 2004) |
| BC47 | $O(^3P) + NO_3 \rightarrow O_2 + NO_2$ | $1.0 \times 10^{-11} \exp(0/T)$ | (Sander et al., 2011) |
| BC48 | $NO_2 + NO_2 + M \rightarrow N_2O_4 + M$ | $k_0 = 1.4 \times 10^{-33} (T/300)^{-3.8} [N_2]$<br>$k_\infty = 1.0 \times 10^{-12}$<br>$F_c = 0.4$ | (Atkinson et al., 2004) |
| BC49 | $N_2O_4 + M \rightarrow NO_2 + NO_2 + M$ | $k_0 = 1.3 \times 10^{-5} (T/300)^{-3.8} \exp(-6400/T)[N_2]$<br>$k_\infty = 1.15 \times 10^{16} \exp(-6460/T)$<br>$F_c = 0.4$ | (Atkinson et al., 2004) |
| BC50 | $2NO + O_2 \rightarrow 2\ NO_2$ | $3.3 \times 10^{-39} \exp(530/T)$ | (Atkinson et al., 2004) |
| BC51 | $NO + NO_2 + M \rightarrow N_2O_3 + M$ | $k_0 = 3.1 \times 10^{-34} (T/300)^{-7.7} [N_2]$<br>$k_\infty = 7.9 \times 10^{-12} (T/300)^{1.4}$<br>$F_c = 0.6$ | (Atkinson et al., 2004) |
| BC52 | $N_2O_3 + M \rightarrow NO + NO_2 + M$ | $k_0 = 1.9 \times 10^{-7} (T/300)^{-8.7} \exp(-4880/T)[N_2]$<br>$k_\infty = 4.7 \times 10^{15} (T/300)^{0.4} \exp(-4880/T)$<br>$F_c = 0.6$ | (Atkinson et al., 2004) |
| BC53 | $N_2O_5 + H_2O \rightarrow 2\ HNO_3$ | $2.5 \times 10^{-22}$ § | (Atkinson et al., 2004) |
| BC54 | $NO_2 + O_3 \rightarrow NO_3 + O_2$ | $1.2 \times 10^{-13} \exp(-2450/T)$ | (Sander et al., 2011) |
| BC55 | $O_3 + HNO_2 \rightarrow O_2 + HNO_3$ | $2.5 \times 10^{-19}$ § | (Sander et al., 2011) |

*Notes*:

§ For rate constants which have a certain value at 298 K, the exact values are used; for those that are reported as an upper limit, half of the upper values are assumed. These reactions are not significant in the whole kinetic model, and choosing half of upper limit bisects the uncontrite range.

Table 3-2 shows the photochemical reactions in the background air with the value of adsorption cross-section ($\sigma$), and quantum yield ($\varphi$) at two wavelengths of 185 nm and 254 nm. All the reactions are assigned with a number and two letters: "B" stands for "Background" reactions and "P" stands for "Photochemical" reactions, respectively.

**Table 3-2: Photochemical reactions and their adsorption cross-section ($\sigma$) and quantum yield ($\varphi$) values in the background air model**
**(bold: the primary kinetics; italic: reactions added for the primary + $NO_x$ kinetics; roman: reactions added for the comprehensive kinetics.)**

| Reaction number | Reaction | $\sigma$ at 185 nm ($cm^2$)<br>$\sigma$ at 254 nm ($cm^2$) | $\varphi$ at 185 nm<br>$\varphi$ at 254 nm |
|---|---|---|---|
| **BP1** | **$H_2O + h\nu \rightarrow \cdot H + \cdot OH$** | $5.50\times10^{-20}$ (Sander et al., 2011) | 1 (Sander et al., 2011) |
| | | ------[§] | 0 (Sander et al., 2011) |
| **BP2** | **$O_2 + h\nu \rightarrow 2O(^3P)$** | $2.04\times10^{-21}$ (Yoshino et al., 1992) | 1 (Sander et al., 2011) |
| | | Not absorbed | ------- |
| **BP3** | **$O_3 + h\nu \rightarrow O(^1D) + O_2$** | $6.61\times10^{-19}$ (Sander et al., 2011) | 0.9 (Sander et al., 2011) |
| | | $1.15\times10^{-17}$ (Sander et al., 2011) | 0.9 (Sander et al., 2011) |
| **BP4** | **$\cdot HO_2 + h\nu \rightarrow \cdot OH + O(^3P)$** | $3.25\times10^{-18}$ (Sander et al., 2011) | 1 (Sander et al., 2011) |
| | | $2.99\times10^{-19}$ (Sander et al., 2011) | 1 (Sander et al., 2011) |
| **BP5** | **$H_2O_2 + h\nu \rightarrow \cdot OH + \cdot OH$** | $8.01\times10^{-19}$ (Sander et al., 2011) | 0.75 (Sander et al., 2011) |
| | | $6.99\times10^{-20}$ (Sander et al., 2011) | 1 (Sander et al., 2011) |
| *BP6* | *$NO_2 + h\nu \rightarrow NO + O(^3P)$* | $6.88\times10^{-18}$ (Bass et al., 1976) | 1 (Sander et al., 2011) |
| | | $1.16\times10^{-20}$ (Atkinson et al., 2004) | 1 (Sander et al., 2011) |
| *BP7* | $N_2O_5 + h\nu \rightarrow NO_3 + NO + O(^3P)$ | $1.85\times10^{-17}$ (Osborne et al., 2000) | 1 (Atkinson et al., 2004) |
| | | $3.26\times10^{-19}$ (Sander et al., 2011) | 0.72 (Sander et al., 2011) |
| *BP8* | *$HNO_3 + h\nu \rightarrow \cdot OH + NO_2$* | $1.63\times10^{-17}$ (Burkholder et al., 1993) | 1 (Johnston & Graham, 1974) |
| | | $1.95\times10^{-20}$ (Sander et al., 2011) | 0.97 (Atkinson et al., 2004) |
| *BP9* | *$HO_2NO_2 + h\nu \rightarrow \cdot HO_2 + NO_2$* | $1.24\times10^{-17}$ (Sander et al., 2011) | 0.7 (Sander et al., 2011) |
| | | $3.63\times10^{-19}$ (Sander et al., 2011) | 0.8 (Sander et al., 2011) |
| *BP10* | *$HO_2NO_2 + h\nu \rightarrow \cdot OH + NO_3$* | $1.24\times10^{-17}$ (Sander et al., 2011) | 0.3 (Sander et al., 2011) |
| | | $3.63\times10^{-19}$ (Sander et al., 2011) | 0.2 (Sander et al., 2011) |
| BP11 | $O_3 + h\nu \rightarrow O(^3P) + O_2$ | $6.61\times10^{-19}$ (Sander et al., 2011) | 0.1 (Sander et al., 2011) |
| | | $1.15\times10^{-17}$ (Sander et al., 2011) | 0.1 (Sander et al., 2011) |
| BP12 | $H_2O_2 + h\nu \rightarrow H_2O + O(^3P)$ | $8.01\times10^{-19}$ (Sander et al., 2011) | 0.16 (Sander et al., 2011) |
| | | $6.99\times10^{-20}$ (Sander et al., 2011) | 0 (Sander et al., 2011) |
| BP13 | $N_2O + h\nu \rightarrow N_2 + O(^1D)$ | $1.43\times10^{-19}$ (Sander et al., 2011) | 1 (Atkinson et al., 2004) |
| | | Minimal (Sander et al., 2011) | ------[§] |
| BP14 | $N_2O_5 + h\nu \rightarrow NO_3 + NO_2$ | $1.85\times10^{-17}$ (Osborne et al., 2000) | 0 (Atkinson et al., 2004) |
| | | $3.26\times10^{-19}$ (Sander et al., 2011) | 0.08 (Atkinson et al., 2004) |
| BP15 | $HNO_2 + h\nu \rightarrow \cdot OH + NO$ | $9.0\times10^{-19}$ (Sander et al., 2011) | 1 (Atkinson et al., 2004) |
| | | $1.45\times10^{-19}$ (Sander et al., 2011) | 1 (Atkinson et al., 2004) |

*Notes*:

[§] Since the value is low, and its corresponding quantum yield is negligible, this value no longer matters.

*3.1.6.2 Methane model ($CH_4$)*

The first hydrocarbon modeled in this research is methane. Once methane is added to the reaction system, on top of the air model components, 19 more chemical species (in the most comprehensive case of the model) were added to the reactive components in the model. These components are presented in Appendix A, Table A-2. Reaction modeling of $CH_4$ involved adding 37 chemical and 8 photochemical reactions to the air model.

Table 3-3 shows chemical reactions in the $CH_4$ model with their rate constants. All the reactions are assigned with a number and two letters: "M" stands for "Methane" reactions and "C" stands for "Chemical" reactions, respectively.

**Table 3-3:Chemical reactions and rate constants in the $CH_4$ model (bold: the primary kinetics; italic: reactions added for the primary + $NO_x$ kinetics; roman: reactions added for the comprehensive kinetics.)**

| Reaction Number | Reaction | Rate Constant ($cm^3$/molecules·s) | Reference |
|---|---|---|---|
| **MC1** | **$CH_4 + O(^1D) \rightarrow \cdot CH_3 + OH\cdot$** | $1.31 \times 10^{-10} \exp(0/T)$ | (Sander et al., 2011) |
| **MC2** | **$CH_4 + O(^1D) \rightarrow CH_2OH + H\cdot$** | $0.35 \times 10^{-10} \exp(0/T)$ | (Sander et al., 2011) |
| **MC3** | **$CH_4 + OH\cdot \rightarrow \cdot CH_3 + H_2O$** | $2.45 \times 10^{-12} \exp(-1775/T)$ | (Sander et al., 2011) |
| **MC4** | **$\cdot CH_3 + O_2 + M \rightarrow \cdot CH_3O_2 + M$** | $k_0 = 4 \times 10^{-31} (T/300)^{-3.6} [N_2]$ $k_\infty = 1.2 \times 10^{-12} (T/300)^{1.1}$ | (Sander et al., 2011) |
| **MC5** | **$\cdot CH_3O_2 + \cdot HO_2 \rightarrow CH_3OOH + O_2$** | $4.1 \times 10^{-13} \exp(750/T)$ | (Sander et al., 2011) |
| **MC6** | **$\cdot CH_3O_2 + \cdot CH_3O_2 \rightarrow CH_3OH + H_2CO + O_2$** | $1.03 \times 10^{-13} \exp(365/T) - 7.4 \times 10^{-13} \exp(-520/T)$ | (Atkinson et al., 2006) |
| **MC7** | **$\cdot CH_3O_2 + \cdot CH_3O_2 \rightarrow 2CH_3O\cdot + O_2$** | $7.4 \times 10^{-13} \exp(-520/T)$ | (Atkinson et al., 2006) |
| **MC8** | **$CH_3O\cdot + O_2 \rightarrow CH_2O + \cdot HO_2$** | $3.9 \times 10^{-14} \exp(-900/T)$ | (Sander et al., 2011) |
| **MC9** | **$CH_3OOH + \cdot OH \rightarrow H_2O + \cdot CH_2OOH \rightarrow H_2O + CH_2O + \cdot OH$** | $(0.35) \times 2.9 \times 10^{-12} \exp(1900/T)$ | (Atkinson et al., 2006) |
| **MC10** | **$CH_3OOH + \cdot OH \rightarrow H_2O + \cdot CH_3O_2$** | $(0.65) \times 2.9 \times 10^{-12} \exp(1900/T)$ | (Atkinson et al., 2006) |
| **MC11** | **$CH_3OH + \cdot OH + \rightarrow H_2O + \cdot CH_2OH$** | $(0.85) \times 6.38 \times 10^{-18} T^2 \exp(144/T)$ | (Atkinson et al., 2006) §§ |
| **MC12** | **$CH_3OH + \cdot OH \rightarrow H_2O + CH_3O\cdot$** | $(0.15) \times 6.38 \times 10^{-18} T^2 \exp(144/T)$ | (Atkinson et al., 2006) §§ |
| **MC13** | **$\cdot CH_2OH + O_2 \rightarrow CH_2O + \cdot HO_2$** | $9.1 \times 10^{-12} \exp(0/T)$ | (Sander et al., 2011) |
| **MC14** | **$CH_2O + HO\cdot \rightarrow H_2O + \cdot CHO$** | $5.5 \times 10^{-12} \exp(125/T)$ | (Sander et al., 2011) |

| | | | |
|---|---|---|---|
| **MC15** | **$\cdot CHO + O_2 \rightarrow CO + \cdot HO_2$** | $5.2 \times 10^{-12} \exp(0/T)$ | (Sander et al., 2011) |
| **MC16** | **$CO + \cdot OH + M \rightarrow CO_2 + \cdot H + M$** | $k_0 = 1.5 \times 10^{-13} (T/300)^{0.6} [N_2]$<br>$k_\infty = 2.1 \times 10^{-9} (T/300)^{6.1}$ | (Sander et al., 2011) |
| *MC17* | $\cdot CH_3O_2 + NO \rightarrow CH_3O\cdot + NO_2$ | $2.8 \times 10^{-12} \exp(300/T)$ | (Sander et al., 2011) |
| *MC18* | $\cdot CH_3O_2 + NO_2 + M \rightarrow \cdot CH_3O_2NO_2 + M$ | $k_0 = 2.5 \times 10^{-30} (T/300)^{-5.5} [N_2]$<br>$k_\infty = 1.8 \times 10^{-11}$<br>$F_c = 0.36$ | (Atkinson et al., 2006) |
| *MC19* | $\cdot CH_3O_2NO_2 + M \rightarrow \cdot CH_3O_2 + NO_2 + M$ | $k_0 = 9 \times 10^{-5} \exp(-9690/T) [N_2]$<br>$k_\infty = 1.1 \times 10^{16} \exp(-10560/T)$<br>$F_c = 0.60$ | (Atkinson et al., 2006) |
| *MC20* | $\cdot CH_3O_2 + NO_3 \rightarrow CH_3O\cdot + NO_2 + O_2$ | $1.3 \times 10^{-12}$ § | (Atkinson et al., 2006) |
| MC21 | $O(^1D) + CH_4 \rightarrow CH_2O + H_2$ | $0.09 \times 10^{-10} \exp(0/T)$ | (Sander et al., 2011) |
| MC22 | $\cdot CH_3 + O_3 \rightarrow CH_2O + \cdot HO_2$ | $4.7 \times 10^{-12} \exp(-210/T)$ | (Atkinson et al., 2006) |
| MC23 | $\cdot CH_3 + O(^3P) \rightarrow CH_2O + H\cdot$ | $(0.83) \times 1.3 \times 10^{-10}$ | (Sander et al., 2011) |
| MC24 | $\cdot CH_3 + O(^3P) \rightarrow CO + H_2 + H\cdot$ | $(0.17) \times 1.3 \times 10^{-10}$ | (Atkinson et al., 2006) |
| MC25 | $CH_3O\cdot + NO + M \rightarrow CH_3ONO\cdot + M$ | $k_0 = 2.3 \times 10^{-29} (T/300)^{-2.8} [N_2]$<br>$k_\infty = 3.8 \times 10^{-11} (T/300)^{-0.6}$ | (Sander et al., 2011) |
| MC26 | $\cdot CH_3O + NO_2 \rightarrow CH_2O + HNO_2$ | $1.1 \times 10^{-11} \exp(-1200/T)$ | (Sander et al., 2011) |
| MC27 | $\cdot CH_3O + NO_2 + M \rightarrow CH_3ONO_2 + M$ | $k_0 = 5.3 \times 10^{-29} (T/300)^{-4.4} [N_2]$<br>$k_\infty = 1.9 \times 10^{-11} (T/300)^{-1.8}$ | (Sander et al., 2011) |
| MC28 | $CH_2O + \cdot HO_2 \rightarrow HOCH_2OO$ (adduct) | $9.7 \times 10^{-15} \exp(625/T)$ | (Atkinson et al., 2006) |
| MC29 | $HOCH_2OO$ (adduct) $\rightarrow CH_2O + \cdot HO_2$ | $2.4 \times 10^{12} \exp(-7000/T)$ | (Atkinson et al., 2006) |
| MC30 | $CH_2O + NO_3 \rightarrow HNO_3 + \cdot HCO$ | $5.8 \times 10^{-16}$ § | (Atkinson et al., 2006) |
| MC31 | $CH_2O + O(^3P) \rightarrow \cdot OH + \cdot CHO$ | $3.4 \times 10^{-11} \exp(-1600/T)$ | (Sander et al., 2011) |
| MC32 | $\cdot CH_3O_2 + O_3 \rightarrow CH_3O\cdot + 2\ O_2$ [a] | $2.9 \times 10^{-16} \exp(-1000/T)$ | (Sander et al., 2011) |
| MC33 | $CH_3ONO_2 + \cdot OH \rightarrow H_2O + \cdot CH_2ONO_2$ [b] | $8.0 \times 10^{-13} \exp(-1000/T)$ | (Sander et al., 2011) |
| MC34 | $CO + \cdot OH + M \rightarrow \cdot CHO_2 + M$ | $k_0 = 5.9 \times 10^{-33} (T/300)^{-1.4} [N_2]$<br>$k_\infty = 1.1 \times 10^{-12} (T/300)^{1.3}$ | (Sander et al., 2011) |
| MC35 | $CO_2 + O(^1D) \rightarrow O(^3P) + CO_2$ | $7.5 \times 10^{-11} \exp(115/T)$ | (Sander et al., 2011) |
| MC36 | $\cdot CHO_2 + O_2 \rightarrow CO_2 + \cdot HO_2$ | $2 \times 10^{-12}$ § | (Sander et al., 2011) |
| MC37 | $CH_3O\cdot + NO \rightarrow CH_2O + HNO$ | $2.3 \times 10^{-12} (T/300)^{-0.7}$ | (Atkinson et al., 2006) |

*Notes*:

§ For rate constants which have a certain value at 298 K, the exact values are used; for those that are reported as an upper limit, half of the upper values are assumed. These reactions are not significant in the whole kinetic model, and choosing half of upper limit bisects the uncontrite range.

§§ For reactions MC11, and MC12, the rate constants were obtained by modeling of (Atkinson et al., 2006), based on the experiment studies of (Dillon et al., 2005; Hess & Tully, 1989; Jiménez et al., 2003; Wallington & Kurylo, 1987)

*Notes*: *Table 3-3 cont'd*

[a] reaction products are based on the research study of (Tyndall et al., 2001)

[b] reaction products are taken from research work of (Shallcross et al., 1997)

Table 3-4 shows photochemical reactions in the methane model with the value of adsorption cross-section ($\sigma$), and quantum yield ($\varphi$) at two wavelengths of 185 nm and 254 nm. All the reactions are assigned with a number and two letters: "M" stands for "Methane" reactions and "P" stands for "Photochemical" reactions, respectively.

**Table 3-4: Photochemical reactions and their adsorption cross-section ($\sigma$) and quantum yield ($\varphi$) values in the $CH_4$ model**
**(bold: the primary kinetics; italic: reactions added for the primary + $NO_x$ kinetics; roman: reactions added for the comprehensive kinetics.)**

| Reaction number | Reaction | $\sigma$ at 185 nm ($cm^2$)<br>$\sigma$ at 254 nm ($cm^2$) | $\varphi$ at 185 nm<br>$\varphi$ at 254 nm |
|---|---|---|---|
| **MP1** | **$CH_3OOH + h\nu \rightarrow CH_3O\cdot + \cdot OH$** | $1.50\times10^{-18}$ (Sander et al., 2011)<br>$3.38\times10^{-20}$ (Sander et al., 2011) | 1 (Atkinson et al., 2006)<br>1 (Atkinson et al., 2006) |
| *MP2* | *$CH_3O_2NO_2 + h\nu \rightarrow \cdot CH_3O_2 + NO_2$* | $1.11\times10^{-17}$ (Sander et al., 2011)<br>$3.40\times10^{-19}$ (Sander et al., 2011) | 0.5 [a] (Sander et al., 2011)<br>0.5 [a] (Sander et al., 2011) |
| *MP3* | *$CH_3O_2NO_2 + h\nu \rightarrow CH_3O\cdot + NO_3$* | $1.11\times10^{-17}$ (Sander et al., 2011)<br>$3.40\times10^{-19}$ (Sander et al., 2011) | 0.5 [a] (Sander et al., 2011)<br>0.5 [a] (Sander et al., 2011) |
| MP4 | $CH_2O + h\nu \rightarrow HCO\cdot + H\cdot$ | Minimal (Sander et al., 2011)<br>$3.42\times10^{-21}$ (Sander et al., 2011) | -----[§]<br>0.305 (Sander et al., 2011) |
| MP5 | $CH_2O + h\nu \rightarrow CO + H_2$ | Minimal (Sander et al., 2011)<br>$3.42\times10^{-21}$ (Sander et al., 2011) | -----[§]<br>0.495 (Sander et al., 2011) |
| MP6 | $CH_3ONO + h\nu \rightarrow CH_3O\cdot + NO$ | $1.2\times10^{-18}$ (Sander et al., 2011)<br>$1.12\times10^{-18}$ (Sander et al., 2011) | 0.76 [b] (Sander et al., 2011)<br>0.76 [b] (Sander et al., 2011) |
| MP7 | $CH_3ONO_2 + h\nu \rightarrow CH_3O\cdot + NO_2$ | $2.10\times10^{-17}$ (Sander et al., 2011)<br>$3.34\times10^{-20}$ (Sander et al., 2011) | 0.7 [a] (Sander et al., 2011)<br>1 [a] (Sander et al., 2011) |
| MP8 | $CH_3ONO_2 + h\nu \rightarrow CH_3ONO + O(^1D)$ [c] | $2.10\times10^{-17}$ (Sander et al., 2011)<br>$3.34\times10^{-20}$ (Sander et al., 2011) | 0.3 [a] (Sander et al., 2011)<br>0 [a] (Sander et al., 2011) |

*Notes*:

[§] Since the value is low, and its corresponding quantum yield is negligible, this value no longer matters.

[a] Assumed, based on the recommended values of (Sander et al., 2011).

[b] The one and the only value reported was 0.76 at 366 nm.

[c] Reaction products are adapted based on the recommendation of (Keller-Rudek et al., 2013).

### *3.1.6.3 Ethane model ($C_2H_6$)*

For the ethane model, as some of the methane reaction species were already presented in some reaction pathways of the ethane model, all the methane reactions should be included in the model

reactions of $C_2H_6$; which resulted in adding 18 new components (at the most comprehensive case of the model) to the system, on top of the $CH_4$ model. These components are presented in Appendix A, Table A-3. For the reactions of ethane model, 37 chemical reactions and 7 photochemical reactions were added to the reactive system in the model.

Table 3-5 shows chemical reactions in the $C_2H_6$ model with their rate constants. All the reactions are assigned with a number and two letters: "E" stands for "Ethane" reactions and "C" stands for "Chemical" reactions, respectively.

**Table 3-5:Chemical reactions and rate constants in the $C_2H_6$ model (bold: the primary kinetics; italic: reactions added for the primary + $NO_x$ kinetics; roman: reactions added for the comprehensive kinetics.)**

| Reaction Number | Reaction | Rate Constant ($cm^3$/molecules·s) | Reference |
|---|---|---|---|
| **EC1** | **$C_2H_6$ + ·OH → ·$C_2H_5$ + $H_2O$** | $7.66 \times 10^{-12} \exp(-1020/T)$ | (Sander et al., 2011) |
| **EC2** | **·$C_2H_5$ + $O_2$ + M → ·$C_2H_5O_2$ + M** | $k_0 = 1.5 \times 10^{-28} (T/300)^{-3} [N_2]$<br>$k_\infty = 8.0 \times 10^{-12} (T/300)^{0}$ | (Sander et al., 2011) |
| **EC3** | **·$C_2H_5O_2$ + ·$C_2H_5O_2$ → 2 $C_2H_5O$· + $O_2$** | $(0.6) \times 6.8 \times 10^{-14} \exp(0/T)$ | (Sander et al., 2011) |
| **EC4** | **·$C_2H_5O_2$+·$C_2H_5O_2$→ $CH_3CHO$+$C_2H_5OH$+$O_2$** | $(0.4) \times 6.8 \times 10^{-14} \exp(0/T)$ | (Sander et al., 2011) |
| **EC5** | **·$C_2H_5O_2$ + ·$HO_2$ → $C_2H_5OOH$ + $O_2$** | $7.5 \times 10^{-13} \exp(700/T)$ | (Sander et al., 2011) |
| **EC6** | **·$C_2H_5O$ + $O_2$ → $CH_3CHO$ + ·$HO_2$** | $6.3 \times 10^{-14} \exp(-550/T)$ | (Sander et al., 2011) |
| **EC7** | **$CH_3CHO$ + O($^3$P) → $CH_3CO$· + ·OH** | $1.8 \times 10^{-11} \exp(-1100/T)$ | (Sander et al., 2011) |
| **EC8** | **$CH_3CHO$ + ·OH → $H_2O$ + $CH_3CO$·** | $4.4 \times 10^{-12} \exp(365/T)$ | (Atkinson et al., 2006) |
| **EC9** | **$CH_3CH_2OH$ ($C_2H_5OH$) + ·OH → $H_2O$ + ·$CH_3CHOH$** | $3.35 \times 10^{-12} \exp(0/T)$ | (Sander et al., 2011) |
| **EC10** | **·$CH_3CHOH$ + $O_2$ → $CH_3CHO$ + ·$HO_2$** | $1.9 \times 10^{-11}$ § | (Atkinson et al., 2006) |
| **EC11** | **$CH_3CO$· + $O_2$ + M → ·$CH_3C(O)O_2$ + M** | $k_\infty = 5.1 \times 10^{-12}$ | (Atkinson et al., 2006) |
| **EC12** | **·$CH_3C(O)O_2$ + ·$CH_3C(O)O_2$ → 2 ·$CH_3$ + 2 $CO_2$ + $O_2$** | $2.9 \times 10^{-12} \exp(500/T)$ | (Sander et al., 2011) |
| **EC13** | **·$CH_3C(O)O_2$ + ·$CH_3O_2$ → ·$CH_3O$ + ·$CH_3$+$CO_2$ + $O_2$** | $(0.9) \times 2.0 \times 10^{-12} \exp(500/T)$ | (Sander et al., 2011) |
| **EC14** | **·$CH_3C(O)O_2$ + ·$CH_3O_2$ → $CH_3C(O)OH$ + HCHO + $O_2$** | $(0.1) \times 2.0 \times 10^{-12} \exp(500/T)$ | (Sander et al., 2011) |
| **EC15** | **·$CH_3C(O)O_2$ + ·$HO_2$ → $CH_3C(O)OOH$ + $O_2$** | $(0.8) \times 4.3 \times 10^{-13} \exp(1040/T)$ | (Sander et al., 2011) |

| | | | |
|---|---|---|---|
| **EC16** | **$\cdot CH_3C(O)O_2 + \cdot HO_2 \rightarrow CH_3C(O)OH + O_3$** | $(0.2) \times 4.3\times10^{-13} \exp(1040/T)$ | (Sander et al., 2011) |
| **EC17** | **$\cdot CH_3C(O)O_2 + \cdot C_2H_5O_2 \rightarrow C_2H_5O\cdot + \cdot CH_3 + CO_2 + O_2$** | $(0.9) \times 4.4 \times 10^{-13} \exp(1070/T)$ [a] | (Atkinson et al., 2006) |
| **EC18** | **$\cdot CH_3C(O)O_2 + \cdot C_2H_5O_2 \rightarrow CH_3CHO + CH_3C(O)OH + O_2$** | $(0.1) \times 4.4 \times 10^{-13} \exp(1070/T)$ | (Atkinson et al., 2006) |
| **EC19** | **$CH_3C(O)OH + \cdot OH \rightarrow H_2O + \cdot CH_3 + CO_2$** | $(0.64) \times 3.15\times10^{-14} \exp(920/T)$ [b] | (Sander et al., 2011) |
| **EC20** | **$CH_3C(O)OOH + \cdot OH \rightarrow \cdot CH_3C(O)O_2 + H_2O$** | $3.6 \times 10^{-12} \exp(0/T)$ | (Sander et al., 2011) |
| **EC21** | **$C_2H_5OOH + \cdot OH \rightarrow H_2O + \cdot C_2H_5O_2$** | $(0.5) \times 3.11\times10^{-12} \exp(190/T)$ | §§ |
| **EC22** | **$C_2H_5OOH + \cdot OH \rightarrow H_2O + \cdot CH_3CHOOH$ ($CH_3CHO + \cdot OH$)** [c] | $(0.5) \times 3.11\times10^{-12} \exp(190/T)$ | §§ |
| *EC23* | *$\cdot C_2H_5O_2 + NO \rightarrow C_2H_5O\cdot + NO_2$* [d] | $2.6 \times 10^{-12} \exp(380/T)$ | (Atkinson et al., 2006) |
| *EC24* | *$\cdot C_2H_5O_2 + NO_3 \rightarrow C_2H_5O + NO_2 + O_2$* | $2.3 \times 10^{-12}$ § | (Atkinson et al., 2006) |
| *EC25* | *$\cdot CH_3C(O)O_2+NO_2+M \rightarrow CH_3C(O)O_2NO_2+M$* | $k_0 = 2.7 \times 10^{-28} (T/300)^{-7.1} [N_2]$<br>$k_\infty = 1.2 \times 10^{-11} (T/300)^{-0.9}$<br>$F_C = 0.3$ | (Atkinson et al., 2006) |
| *EC26* | *$CH_3C(O)O_2NO_2+M \rightarrow \cdot CH_3C(O)O_2+NO_2+M$* | $k_0 = 4.9 \times 10^{-3} \exp(-12100/T) [N_2]$<br>$k_\infty = 5.4 \times 10^{16} \exp(-13830/T)$<br>$F_c = 0.3$ | (Atkinson et al., 2006) |
| EC27 | $C_2H_6 + NO_3 \rightarrow \cdot C_2H_5 + HNO_3$ | $5 \times10^{-18}$ § | (Atkinson et al., 2006) |
| EC28 | $\cdot C_2H_5O_2 + NO_2 + M \rightarrow C_2H_5O_2NO_2 + M$ | $k_0 = 1.3 \times 10^{-29} (T/300)^{-6.2} [N_2]$<br>$k_\infty = 8.8 \times 10^{-12}$<br>$F_c = 0.31$ | (Atkinson et al., 2006) |
| EC29 | $\cdot C_2H_5O_2NO_2 + M \rightarrow \cdot C_2H_5O_2 + NO_2 + M$ | $k_0 = 4.8 \times 10^{-4} \exp(-9285/T) [N_2]$<br>$k_\infty = 8.8 \times 10^{15} \exp(-10440/T)$<br>$F_c = 0.31$ | (Atkinson et al., 2006) |
| EC30 | $C_2H_5O\cdot + NO + M \rightarrow C_2H_5ONO + M$ | $k_0 = 2.8 \times 10^{-27} (T/300)^{-4} [N_2]$<br>$k_\infty = 5.0 \times 10^{-11} (T/300)^{-0.2}$ | (Sander et al., 2011) |
| EC31 | $C_2H_5O\cdot + NO \rightarrow CH_3CHO + HNO$ | $1.1 \times 10^{-11}$ § | (Atkinson et al., 2006) |
| EC32 | $C_2H_5O\cdot + NO_2 + M \rightarrow C_2H_5ONO_2 + M$ | $k_0 = 2.0 \times 10^{-27} (T/300)^{-4} [N_2]$<br>$k_\infty = 2.8 \times 10^{-11} (T/300)^{-1.0}$ | (Sander et al., 2011) |
| EC33 | $CH_3CHO + NO_3 \rightarrow HNO_3 + CH_3CO\cdot$ | $1.4 \times 10^{-12} \exp(-1860/T)$ | (Atkinson et al., 2006) |
| EC34 | $C_2H_5ONO_2 + \cdot OH \rightarrow C_2H_5O\cdot + HNO_3$ [e] | $(0.5) \times 1.0 \times 10^{-12} \exp(-490/T)$ [f] | (Sander et al., 2011) |
| EC35 | $C_2H_5ONO_2 + \cdot OH \rightarrow C_2H_5OOH + NO_2$ | $(0.5) \times 1.0 \times 10^{-12} \exp(-490/T)$ [f] | (Sander et al., 2011) |
| EC36 | $\cdot CH_3C(O)O_2 + NO \rightarrow \cdot CH_3 + CO_2 + NO_2$ | $7.5\times10^{-12} \exp(290/T)$ | (Atkinson et al., 2006) |
| EC37 | $\cdot C_2H_5 + O_2 \rightarrow C_2H_4 + \cdot HO_2$ | $3.8 \times 10^{-15}$ §, [g] | (Atkinson et al., 2006) |

*Notes*:

[a] The value of $k_1/k$ is in the range 1.0-0.8, so 0.9 is assumed as an average value.

*Notes*: *Table 3-5 cont'd*

[b] 36% of the products is still unknown.

[c] reaction products are based on the study of (Hasson et al., 2005) and (Carr, 2007)

[d] this reaction has a "falloff type" as $C_2H_5O_2 + NO + M \rightarrow C_2H_5ONO_2 + M$, but since the branching ratio for this reaction is less than 2% (Atkinson et al., 2006), the falloff reaction is ignored.

[e] reaction products are based on the experimental work of (He et al., 2011)

[f] Assumed equal rate constant.

[g] Although the reaction rate is pressure sensitive, this value can be used directly as the pressure condition does not change in the model.

[§] For rate constants which have a certain value at 298 K, the exact values are used; for those that are reported as an upper limit, half of the upper values are assumed. These reactions are not significant in the whole kinetic model, and choosing half of upper limit bisects the uncontrite range.

[§§] the rate constant is calculated based on the model of (Baulch et al., 2005), and experimental studies of (Wang & Chen, 2008).

Table 3-6 shows photochemical reactions in the ethane model with the value of adsorption cross-section ($\sigma$), and quantum yield ($\varphi$) at two wavelengths of 185 nm and 254 nm. All the reactions are assigned with a number and two letters: "E" stands for "Ethane" reactions and "P" stands for "Photochemical" reactions, respectively.

**Table 3-6: Photochemical reactions and their adsorption cross-section ($\sigma$) and quantum yield ($\varphi$) values in the $C_2H_6$ model**
**(bold: the primary kinetics; italic: reactions added for the primary + $NO_x$ kinetics; roman: reactions added for the comprehensive kinetics.)**

| Reaction number | Reaction | $\sigma$ at 185 nm ($cm^2$)<br>$\sigma$ at 254 nm ($cm^2$) | $\varphi$ at 185 nm<br>$\varphi$ at 254 nm |
|---|---|---|---|
| *EP1* | *$CH_3C(O)O_2NO_2 + h\nu \rightarrow CH_3C(O)O_2 + NO_2$* | -----[§] | Minimal |
| | | $1.0\times10^{-19}$ (Atkinson et al., 2006) | 0.76 (Atkinson et al., 2006) |
| *EP2* | *$CH_3C(O)O_2NO_2 + h\nu \rightarrow \cdot CH_3 + CO_2 + NO_3$* | -----[§] | Minimal |
| | | $1.0\times10^{-19}$ (Atkinson et al., 2006) | 0.24 (Atkinson et al., 2006) |
| EP3 | $CH_3CHO + h\nu \rightarrow \cdot CH_3 + HCO$ | $1.28\times10^{-17}$ (Lucazeau & Sandorfy, 1970) | 0 [a] (Sander et al., 2011) |
| | | $1.57\times10^{-20}$ (Sander et al., 2011) | 0.28 [b] (Horowitz & Calvert, 1982) |
| EP4 | $CH_3CHO + h\nu \rightarrow CH_4 + CO$ | $1.28\times10^{-17}$ (Lucazeau & Sandorfy, 1970) | 0 [a] (Sander et al., 2011) |
| | | $1.57\times10^{-20}$ (Sander et al., 2011) | 0.63 (Parmenter & Albert Noyes, 1963) |
| EP5 | $C_2H_5ONO_2 + h\nu \rightarrow C_2H_5O\cdot + NO_2$ | $1.71\times10^{-17}$ (Atkinson et al., 2006) | 1 (Atkinson et al., 2006) |
| | | $4.18\times10^{-20}$ (Atkinson et al., 2006) | 1 (Atkinson et al., 2006) |
| EP6 | $CH_3C(O)OH + h\nu \rightarrow \cdot CH_3 + \cdot COOH$ | $3.95\times10^{-19}$ (Limao-Vieira et al., 2006) | 0.5 [c] (Sander et al., 2011) |
| | | $5.07\times10^{-21}$ (Limao-Vieira et al., 2006) | 0.5 [c] (Sander et al., 2011) |
| EP7 | $CH_3C(O)OH + h\nu \rightarrow CH_3CO + \cdot OH$ | $3.95\times10^{-19}$ (Limao-Vieira et al., 2006) | 0.5 [c] (Sander et al., 2011) |
| | | $5.07\times10^{-21}$ (Limao-Vieira et al., 2006) | 0.5 [c] (Sander et al., 2011) |

*Notes Table 3-6*:

§ Since the value is low, and its corresponding quantum yield is negligible, this value no longer matters.

[a] These values are assumed based on the values reported by (Horowitz & Calvert, 1982; Parmenter & Albert Noyes, 1963; Sander et al., 2011).

[b] Extrapolated value.

[c] Assumed, based on the recommended values of (Sander et al., 2011).

### *3.1.6.4 Ethylene model ($C_2H_4$)*

When an ethylene reaction model was introduced to the reactive system in the model, some of its components and reaction products were previously in the reaction model of ethane. Consequently, all the new reactions of the ethylene model should be added to the model of $C_2H_6$. Hence, for the most comprehensive version of the model, 11 new components (Appendix A, Table A-4), 31 chemical reactions and 4 photochemical reactions were added to the reaction section in the model.

Table 3-7 shows chemical reactions in $C_2H_4$ model with their rate constants. All the reactions are assigned with a number and two letters: "Ey" stands for "Ethylene" reactions and "C" is standing for "Chemical" reactions, respectively.

**Table 3-7:Chemical reactions and rate constants in the $C_2H_4$ model (bold: the primary kinetics; italic: reactions added for the primary + $NO_x$ kinetics; roman: reactions added for the comprehensive kinetics.)**

| Reaction Number | Reaction | Rate Constant ($cm^3$/molecules·s) or ($s^{-1}$) | Reference |
|---|---|---|---|
| **EyC1** | **$C_2H_4$ + ·OH + M → ·$HOCH_2CH_2$ + M** | $k_0$=1.1 × $10^{-28}$ ($T$/300)$^{-3.5}$ [$N_2$]<br>$k_\infty$=8.4 × $10^{-12}$ ($T$/300)$^{-1.75}$ | (Burkholder et al., 2015) |
| **EyC2** | **$C_2H_4$ + O($^3$P) → ·$CH_2CHO$ + H·** | (0.35) 2.25 × $10^{-17}$ $T^{1.88}$ exp(-92/$T$) | (Baulch et al., 2005) |
| **EyC3** | **$C_2H_4$ + O($^3$P) → ·HCO + ·$CH_3$** | (0.60) 2.25 × $10^{-17}$ $T^{1.88}$ exp(-92/$T$) | (Baulch et al., 2005) |
| **EyC4** | **$C_2H_4$ + O($^3$P) → $CH_2CO$ + $H_2$** | (0.05) 2.25 × $10^{-17}$ $T^{1.88}$ exp(-92/$T$) | (Baulch et al., 2005) |
| **EyC5** | **$C_2H_4$ + $O_3$ → 2 $CH_2O$ + ½ $O_2$** [a] | 1.2×$10^{-14}$ exp(-2630/$T$) | (Burkholder et al., 2015) |
| **EyC6** | **·$C_2H_4OH$ + $O_2$ → ·$O_2C_2H_4OH$** | 4.7 × $10^{-13}$ exp(553/$T$) | (Filimonova et al., 2002) |

| | | | |
|---|---|---|---|
| **EyC7** | **$\cdot OC_2H_4OH \rightarrow CH_2O + \cdot CH_2OH$** | $1.56 \times 10^{14} \exp(-7225/T)$ | (Filimonova et al., 2002) based on calculation of (Atkinson, 1997) and (Orlando et al., 1998) |
| **EyC8** | **$CH_2CO + \cdot OH \rightarrow \cdot CH_3 + CO_2$** | (0.4) $2.8 \times 10^{-12} \exp(510/T)$ | (Baulch et al., 2005) |
| **EyC9** | **$CH_2CO + \cdot OH \rightarrow \cdot CH_2OH + CO$** | (0.6) $2.8 \times 10^{-12} \exp(510/T)$ | (Baulch et al., 2005) |
| **EyC10** | **$\cdot CH_2CHO + O_2 \rightarrow HCHO + CO + \cdot OH$** | $k_{298} = 3.0 \times 10^{-14}$ § | (Baulch et al., 2005) |
| **EyC11** | **$\cdot CH_2CHO + O_2 \rightarrow CH_2CO + \cdot HO_2$** | $2.7 \times 10^{-14} \exp(668/T)$ † | (Lorenz et al., 1985) |
| **EyC12** | **$2\ \cdot O_2C_2H_4OH \rightarrow 2\ \cdot OC_2H_4OH + O_2$** | $3.9 \times 10^{-14} \exp(1000/T)$ | (Atkinson et al., 2006) |
| **EyC13** | **$\cdot O_2C_2H_4OH + \cdot HO_2 \rightarrow \cdot OH + O_2 + \cdot OC_2H_4OH$** [b] | $k_{298} = 1.2 \times 10^{-11}$ § | (Atkinson et al., 2006) |
| *EyC14* | *$C_2H_4 + NO_3 \rightarrow 2\ CH_2O + NO$* [c] | $3.3 \times 10^{-12} \exp(-2880/T)$ | (Atkinson et al., 2006) |
| *EyC15* | *$\cdot O_2C_2H_4OH + NO \rightarrow \cdot OC_2H_4OH + NO_2$* | $9 \times 10^{-12}$ | (Orlandini & Riedel, 2000) |
| EyC16 | $C_2H_4 + \cdot H \rightarrow H_2 + \cdot C_2H_3$ | $9.0 \times 10^{-10} \exp(-7500/T)$ | (Baulch et al., 2005) |
| EyC17 | $C_2H_4 + \cdot H + M \rightarrow \cdot C_2H_5 + M$ | $k_0 = 7.7 \times 10^{-30} \exp(-380/T)\ [N_2]$<br>$k_\infty = 6.6 \times 10^{-15} \exp(-650/T)$<br>$F_c = 0.24 \exp(-T/40) + 0.76 \exp(-T/1025)$ | (Baulch et al., 2005) |
| EyC18 | $\cdot O_2C_2H_4OH \rightarrow \cdot C_2H_4OH + O_2$ | $5.4 \times 10^{-7}\ T^{-1} \exp(-15097/T)$ | (Orlandini & Riedel, 2000) |
| EyC19 | $\cdot C_2H_4OH \rightarrow \cdot CH_3 + CH_2O$ | $1.66 \times 10^{-15} \exp(-8660/T)$ | (Orlandini & Riedel, 2000) |
| EyC20 | $\cdot O_2C_2H_4OH \rightarrow CH_2O + CH_2O + \cdot OH$ | $1.66 \times 10^{-8} \exp(-12580/T)$ | (Orlandini & Riedel, 2000) |
| EyC21 | $CH_2CO + \cdot H \rightarrow \cdot CH_3 + CO$ | $5.4 \times 10^{-14}\ T^{0.85} \exp(-1430/T)$ | (Baulch et al., 2005) |
| EyC22 | $\cdot C_2H_3 + O_2 \rightarrow CH_2O + HCO\cdot$ | $6.4 \times 10^{-12} \exp(120/T)$ | (Baulch et al., 2005) |
| EyC23 | $\cdot C_2H_3 + \cdot C_2H_3 \rightarrow C_2H_2 + C_2H_4$ | $k_{298} = 1.5 \times 10^{-11}$ § | (Ismail et al., 2009) |
| EyC24 | $C_2H_2 + \cdot OH + M \rightarrow \cdot C_2H_2OH(\cdot HOCHCH) + M$ | $k_0 = 5.5 \times 10^{-30}\ (T/300)^0\ [N_2]$<br>$k_\infty = 8.3 \times 10^{-13}\ (T/300)^2$ | (Burkholder et al., 2015) |
| EyC25 | $C_2H_2 + O(^3P) \rightarrow \cdot HCCO + \cdot H$ [c] | (0.7) $3.0 \times 10^{-11} \exp(-1600/T)$ | (Baulch et al., 2005; Burkholder et al., 2015) |
| EyC26 | $\cdot HCCO + O(^3P) \rightarrow 2\ CO + \cdot H$ | $1.65 \times 10^{-10}$ | (Frank et al., 1988) |
| EyC27 | $\cdot HCCO + O_2 \rightarrow CO_2 + \cdot H + CO$ [e] | $2.7 \times 10^{-12} \exp(-430/T)$ | (Baulch et al., 2005) |
| EyC28 | $\cdot C_2H_2OH + O_2 \rightarrow CHOCHO\ ((HCO)_2) + \cdot OH$ | $1.66 \times 10^{-12} \exp(-2517/T)$ | (Battin-Leclerc et al., 2007) |
| EyC29 | $\cdot C_2H_2OH + O_2 \rightarrow CHO + CO_2 + H_2$ [f] | $5.1 \times 10^{-12}$ | (Warnek & Williams, 2012) |
| EyC30 | $\cdot C_2H_2OH + \cdot OH \rightarrow CH_2CO + H_2O$ | $1.66 \times 10^{-11} \exp(-1007/T)$ | (Battin-Leclerc et al., 2007) |
| EyC31 | $(HCO)_2 + \cdot OH \rightarrow H_2O + HC(O)CO\cdot$ | $k_{298} = 1.1 \times 10^{-11}$ § | (Atkinson et al., 2006) |
| EyC32 | $HC(O)CO\cdot \rightarrow HCO\cdot + CO$ | $1.4 \times 10^{-12} \exp(-3160/T)$ | (Orlando & Tyndall, 2001) |
| EyC33 | $C_2H\cdot + H_2 \rightarrow C_2H_2 + H\cdot$ | $1.2 \times 10^{-11} \exp(-998/T)$ | (Opansky & Leone, 1996) |
| EyC34 | $C_2H_4OH\cdot + C_2H_4OH\cdot \rightarrow CH_3CHO + C_2H_5OH$ | $k_{298} = (0.12)\ 5.6 \times 10^{-11}$ § | (Anastasi et al., 1990) |

*Notes Table 3-7*:

§ For rate constants which have a certain value at 298 K, the exact values are used; for those that are reported as an upper limit, half of the upper values are assumed.

† There is another reaction with $O_2$ for this radical, but the dissociation reaction has a significant higher rate constant with a factor of $1.8\times10^{18}$ at room temperature (Orlando et al., 1998), so that reaction neglected.

[a] Assumed products based on (Atkinson et al., 2006).

[b] The product is assumed based on the study of (Dillon & Crowley, 2008).

[c] The product is assumed based on the modeling study of (Nguyen et al., 2011).

[d] Reaction products reported by (Peeters et al., 1994).

[e] Reaction products reported by (Peeters et al., 1994).

[f] Reaction products reported by (Dagaut et al., 2000).

Table 3-8 shows photochemical reactions in the ethylene model with the value of adsorption cross-section ($\sigma$), and quantum yield ($\varphi$) at two wavelengths of 185 nm and 254 nm. All the reactions are assigned with a number and two letters: "Ey" stands for "Ethylene" reactions and "C" is standing for "Chemical" reactions, respectively.

**Table 3-8: Photochemical reactions and their adsorption cross-section ($\sigma$) and quantum yield ($\varphi$) values in the $C_2H_4$ model**
**(roman: reactions added for the comprehensive kinetics.)**

| Reaction number | Reaction | $\sigma$ at 185 nm ($cm^2$)<br>$\sigma$ at 254 nm ($cm^2$) | $\varphi$ at 185 nm<br>$\varphi$ at 254 nm |
|---|---|---|---|
| EyP1 | $C_2H_2 + h\nu \rightarrow C_2H\cdot + H\cdot$ | $3.3\times10^{-19}$ (Wu et al., 1989)<br>-----§ | 0.14 (Atreya, 2013)<br>0 (Atkinson et al., 2006) |
| EyP2 | $(CHO)_2 + h\nu \rightarrow HCO\cdot + HCO\cdot$ [a] | Minimal<br>$1.34\times10^{-20}$ (Horowitz et al., 2001) | -----§<br>0.156 (Burkholder et al., 2015) |
| EyP3 | $(CHO)_2 + h\nu \rightarrow H_2 + 2\ CO$ [a] | Minimal<br>$1.34\times10^{-20}$ (Horowitz et al., 2001) | -----§<br>0.514 (Zhu et al., 1996) |
| EyP4 | $(CHO)_2 + h\nu \rightarrow HCHO + CO$ [a] | Minimal<br>$1.34\times10^{-20}$ (Horowitz et al., 2001) | -----§<br>0.330 (Zhu et al., 1996) |

*Notes*:

§ Since the value is low, and its corresponding quantum yield is negligible, this value no longer matters.

[a] Reaction products reported by (Atkinson et al., 2006; Burkholder et al., 2015)

### *3.1.7 Removal efficiency*

The removal efficiency ($\eta_i$), which is the main purpose of the model simulation, can be defined as:

$$\eta_i = 1 - \frac{\overline{C_i}}{C_{i,\text{initial}}} \tag{3.20}$$

Where $\overline{C_i}$ is the average concentration of species *i* at the reactor outlet, and $C_{i,\text{initial}}$ is the initial concentration of component *i*.

Because of the tubular shape of the reactor, the average concentration in the outlet should be calculated by dividing the integration of the molecular flow rate for a specific component across the reactor radius by the integration of its volumetric flow rate:

$$\overline{C_i} = \frac{\int_{R_0}^{R_1} C_i \cdot V \cdot 2\pi r \cdot \mathrm{d}r}{\int_{R_0}^{R_1} V \cdot 2\pi r \cdot \mathrm{d}r} \tag{3.21}$$

where $C_i$ is the local concentration of component *i* at the reactor outlet (molecules/cm$^3$), $V$ is the local gas velocity at any radius of reactor (cm/s), and $R_0$ and $R_1$ are the lamp radius (cm) and inner reactor radius (cm), respectively. The physical meaning of Equation (3.21) can be interpreted as the average concentration is equal to mass flow rate divided by volumetric flow rate.

Table 3-9 summarizes the main equations in the model that had to be solved to find out the concentration value, $C_i$, for each component at each location of the reactor.

**Table 3-9: Summary of model equations**

| Equation Number | Equation | Description |
|---|---|---|
| (3.5) | $V = \dfrac{\dfrac{2U(R_1^2 - R_0^2)}{\ln\dfrac{R_1}{R_0}} \ln\dfrac{r}{R_0} - 2U(r^2 - R_0^2)}{R_1^2 + R_0^2 - \dfrac{R_1^2 - R_0^2}{\ln\dfrac{R_1}{R_0}}}$ | Velocity profile;<br>local gas velocity for any *r* for an annular space |
| (3.10) | $V \cdot \dfrac{\partial C_i}{\partial z} = D_i \cdot \dfrac{\partial^2 C_i}{\partial r^2} + \dfrac{D_i}{r} \cdot \dfrac{\partial C_i}{\partial r} + r_i$ | Material balance;<br>one partial differential equation for each compound |
| (3.15) | $\dfrac{\mathrm{d}E_p}{\mathrm{d}r} = -\dfrac{E_p}{r} - \sum_i C_i \sigma_i E_p$ | Radiation field;<br>one differential equation for each wavelength, at each location in the reactor |
| (3.16c) | $-r_i = A\exp(-\dfrac{E}{RT})\, C_A^{n_{i,A}} C_B^{n_{i,B}}$ | General chemical reaction rate for a binary reaction |
| (3.19) | $-r_i = \varphi_i \cdot C_i \cdot \sigma_i \cdot E_p$ | Photochemical reaction rate for each component participating in a photochemical reaction |
| (3.21) | $\overline{C_i} = \dfrac{\int_{R_0}^{R_1} C_i \cdot V \cdot 2\pi r \cdot \mathrm{d}r}{\int_{R_0}^{R_1} V \cdot 2\pi r \cdot \mathrm{d}r}$ | Concentration of each species in the outlet of the reactor |
| (3.20) | $\eta_i = 1 - \dfrac{\overline{C_i}}{C_{i,\,\mathrm{initial}}}$ | Removal efficiency, for each reactive component in the reactor |

### *3.1.8 Numerical procedure and implementation*

The material balance is a set of partial differential equations (PDEs), one for the concentration $C_i$ of each species *i*. The independent variables are the length coordinate (*z*) and the radial coordinate (*r*). The PDEs arising from the material balance equation (Equation (3.10)) are converted to sets of ordinary differential equations (ODEs) by finite differences in the radial

direction. Cylindrical symmetry is assumed. Hence, the radial cross-section of the reactor is defined by a grid with 16 internal node points (i.e., $\Delta r$ = 0.5 mm). Concentrations at the wall and the lamp are calculated with the zero-flux boundary condition. In the length direction, numerical integration of the ordinary differential equations was carried out with Gear's algorithm, as implemented in MATLAB© (Function ode15s). The method is an implicit algorithm which is a backward difference of order ($k$ + 1) when working in order $k$ (Finlayson, 2012). Gear's algorithm is an auto-adaptive algorithm which can select step size automatically and change orders from one to five (e.g., $k$ = 1 – 5). In comparison with other numerical methods, Gear's method has higher calculation precision and efficiency (Wang & Wen, 2006). This algorithm is a solver for stiff sets of ODEs. It is a practically appropriate choice for the proposed model, as the order of the numerical system which is characterized by the reaction rate constants (i.e., eigenvalues of the linearized set of differential equations are dependent on the rate constants) are different by several orders of magnitude.

The light field equation (Equation (3.15)) is solved numerically using finite difference method in the radial direction. Since the concentration values ($C_i$) are also unknown in this equation, the light field equation should be solved simultaneously with material balance equations (Equation (3.10)). As Equation (3.15) only contains $r$ as independent variable, the algorithm was invoked at every length increment as part of the numerical integration of the material balance.

Furthermore, the simulation results were not affected significantly by decreasing the grid resolution to 84 internal grid points (i.e., $\Delta r$ = 0.1 mm), or by changing the relative and absolute tolerance by an order of magnitude (e.g., the absolute difference between removal efficiencies

using 16 and 84 grid points was less than 0.00003). Hence, the accuracy of the numerical solver was established.

## 3.2 Temperature Profile

One of the disadvantages of using a UV lamp in the gas phase is that most of the input electrical power is not absorbed by the gas. This causes a substantial heat loss in the reactor that may create a temperature profile through the reactive area.

### *3.2.1 Thermal model development*

To investigate this effect, a cylindrical annulus element has been assumed consistent with the assumed reactor. Figure 3-5 shows this element.

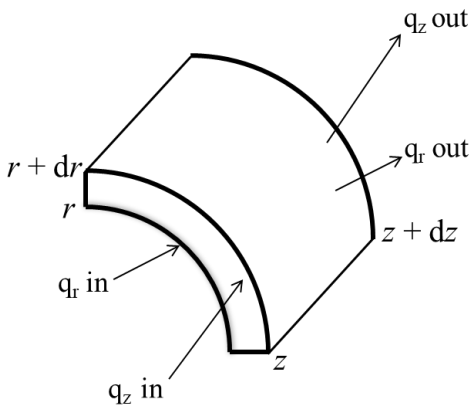


**Figure 3-5: Energy balance on an annular element**

For consistency, steady state laminar flow in the reactor was assumed, and therefore conduction is the dominant mechanism in the radial direction ($r$), whereas convection can be assumed in the flow direction ($z$); which means:

$$q_r = -k\frac{\partial T}{\partial r} \tag{3.22}$$

$$q_z = \sum H_i w_i = C_p \cdot T \cdot \dot{w} = V \cdot \overset{*}{\rho} \cdot C_p \cdot T \tag{3.23}$$

where $k$ is the thermal conductivity (W/m·K), $T$ is the temperature (K), $V$ is the local velocity (m/s), $\overset{*}{\rho}$ is the specific density (mol/m$^3$), and $C_p$ is the heat capacity (J/mol·K). Also, $q_r$ and $q_L$ are the energy fluxes (W/m$^2$) in the radial and lateral direction, respectively. $A_r$ and $A_z$ are the cross-sectional area for the effective heat flux in the radial and lateral direction, respectively.

So, the steady-state energy balance equation for the assumed reactor is:

$$A_r\,(q_{r,\,in} - q_{r,\,out}) + A_z\,(q_{L,\,in} - q_{L,out}) = 0 \tag{3.24}$$

Substituting the terms leads to:

$$q_r\big|_r \cdot 2\pi r \cdot \mathrm{d}z - q_r\big|_{r+\mathrm{d}r} \cdot 2\pi(r+\mathrm{d}r) \cdot \mathrm{d}z + q_z\big|_z \cdot 2\pi r \cdot \mathrm{d}r - q_z\big|_{z+\mathrm{d}z} \cdot 2\pi r \cdot \mathrm{d}r = 0 \tag{3.25a}$$

Replacing the flux terms, and dividing all terms by $2\pi r \cdot \mathrm{d}r \cdot \mathrm{d}z$ results in:

$$\left( \frac{k\left.\frac{\partial T}{\partial r}\right|_{r+\mathrm{d}r} - k\left.\frac{\partial T}{\partial r}\right|_{r}}{\mathrm{d}r} \right) + k\left.\frac{\partial T}{\partial r}\right|_{r+\mathrm{d}r} = V \cdot \overset{*}{\rho} \cdot C_p \cdot \left( \frac{T\big|_{z+\mathrm{d}z} - T\big|_z}{\mathrm{d}z} \right) \tag{3.25b}$$

Taking the limits and approaching $\mathrm{d}r \rightarrow 0$ and $\mathrm{d}z \rightarrow 0$:

$$V \cdot \frac{\partial T}{\partial z} = \frac{k}{\overset{*}{\rho} \cdot C_p} \left( \frac{1}{r}\frac{\partial T}{\partial r} + \frac{\partial^2 T}{\partial r^2} \right) \tag{3.26}$$

Equation (3.26) is one partial differential equation for temperature of the gas inside the reactor. Defining $\alpha = \dfrac{k}{\overset{*}{\rho} \cdot C_p}$ as thermal diffusivity (m$^2$/s), this equation can be written in closed form as:

(Holman, 2010)

$$\frac{1}{\alpha} \cdot \frac{\partial T}{\partial z} = \frac{1}{V \cdot r}\frac{\partial}{\partial r}\left( r\frac{\partial T}{\partial r} \right) \tag{3.27}$$

The boundary conditions for Equation (3.26) should be written in both radial and lateral directions. At the reactor entrance, the temperature can be assumed as a constant inlet value. At the UV lamp wall, there is a constant heat flux originating from the lamp heat loss. At the reactor wall, the constant ambient temperature is sensible assumption. These boundary conditions can be summarized as:

$$\begin{cases} -k\left.\dfrac{\partial T}{\partial r}\right|_r = Q_{Lamp} & @\ r = R_0 \\ T = T_{ambient} & @\ r = R_1 \\ T = T_{inlet} & @\ z = 0 \end{cases} \tag{3.28}$$

In Equation (3.26), the value of the local velocity is already calculated in Section 3.1.2 using Equation (3.5). For thermal conductivity ($k$), specific density ($\overset{*}{\rho}$), and heat capacity ($C_p$), as all values are dependent on temperature (kelvin), they should be adjusted with the local temperate value; so, for each quantity a temperature-dependent function is required. With the proper assumption of pure air (if an ideal gas is assumed) in the reactor in this part, the following functions can be conducted to the model.

- For the heat capacity (J/mol·K), the functionality can be described as: (Kyle, 1984)

$$C_p(T) = 28.11 + 0.1967\times10^{-2}\,T + 0.4802\times10^{-5}T^{\,2} - 1.966\times10^{-9}T^{\,3} \tag{3.29a}$$

- For thermal conductivity, after curve fitting of the individual data from (Bergman & Incropera, 2011) the functionality can be derived as:

$$k(T) = 1.5207\times10^{-11}T^{\,3} - 4.8574\times10^{-8}\,T^{\,2} + 1.0184\times10^{-4}\,T - 3.9333\times10^{-4} \tag{3.29b}$$

- For the specific density (mol/m$^3$) of air, using the ideal gas law ($R$ = 8.314 J/mol·K), and constant pressure (Pa), the function can be written as:

$$\overset{*}{\rho} = \frac{P}{RT} \tag{3.29c}$$

In the general form of Equation (3.24), a general form of heat loss/generation from reactions in terms of enthalpy of reaction should be included (i.e., $\Delta H_r$). This term is neglected in this section of modeling for a few reasons. First, there are 165 chemical reactions in the model, and considering this value for each reaction would require an excessive computational time. Second, most of the reactions contained a radical species which have lower heat of reactions in comparison with a fully molecular reaction. Third, black-box simulation of the reactor by considering the enthalpy of formation for the reactant, and for the products showed that the total temperature increase due to reactions is negligible in comparison with the heat transfer from the UV lamp (Chapter 4, Section 4.7.3). And finally, with the solution of the thermal model, some of the reaction rates that contained temperature values (i.e., $k_i = A\exp(-\frac{E_a}{RT})$), the rate constant was updated in accordance with the local temperature value. However, as will be discussed in Chapter 4, the whole model results are not sensitive to this temperature variation. All things considered, neglecting the enthalpy of reaction is a justifiable assumption.

It is useful to show Equation (3.26) in a non-dimensional form. The following dimensionless variables can be defined:

$$T^* = T/T_0 \tag{3.30a}$$

$$z^* = z/L_0 \tag{3.30b}$$

$$r^* = r/R_0 \tag{3.30c}$$

So, Equation (3.26) can be re-arranged in the form of a dimensionless equation, in which each term between parentheses is non-dimensional:

$$(\frac{V}{\alpha}\cdot\frac{R_0^2}{L_0})\cdot(\frac{\partial T^*}{\partial z^*}) = (\frac{1}{r^*}\cdot\frac{\partial T^*}{\partial r^*}) + (\frac{\partial^2 T^*}{\partial r^{*2}}) \tag{3.31}$$

### *3.2.2 Numerical procedure*

To solve the main equation (Equation (3.26)), using the boundary conditions of Equation (3.28), the equation was converted to a set of algebraic equations using the finite difference method, with a fine-resolution discretization on the reactor domain (e.g., $\Delta r$ = 0.5 mm, and $\Delta z$ = 1 mm). Then, with the inverse matrix calculation with Newton's iterative approach (inverse matrix method), and setting a relative tolerance of $10^{-5}$, the numerical solver converged. Changing the domain parameters (i.e., $\Delta r$ and $\Delta z$) as well as relative tolerance order, does not change the results. For instance, the absolute difference between average temperature found to be 0.002 K, when $\Delta r$ was changed from 0.5 mm to 0.1 mm, and 0.006 when $\Delta z$ was changed from 1 mm to 0.5 mm. Hence, it can be concluded that the accuracy of the numerical solver is established.

The solution of this equation returned as a temperature value for each location in the reactor, as $T(r, z)$. So, the temperature values were conducted in the general reactor model (Section 3.1), and all variables of the model that have the functionality of temperature (such as gas diffusivities, rate constants, and absorption cross-section, if applicable) were updated in each run of the thermal model. Henceforth, the model representing the results with the adjusted temperature value is called "model-thermal", and the model runs with constant temperature is called "model-nonthermal".

### 3.3 COMSOL Assessment

In order to verify the MATLAB model results and confirm the justifications of the base model, the whole modeled reactor was simulated with COMSOL. COMSOL Multiphysics is a powerful software to simulate and provide the most accurate results by minimizing the assumptions, by coupling related physical applications together to include all the necessary factors for a complete model. In the context of chemical engineering, COMSOL solves numerically the governing equations of energy, momentum, and continuity simultaneously using finite element method.

The photoreactor was completely modeled with the following steps in the Multiphysics software. After defining the reactor parameters (consistent with the Table 4-1); and assuming Air as the leading stream in the reactor, the geometry of the reactor was set as a 2D domain, due to rotational symmetry. The model was also run with a full 3D simulation, and because the results were exactly the same as 2D version (except the fact that the 3D version was very time expensive), all the upcoming assessments and future results are consistent with 2D version, unless specified otherwise. The 3D simulation was necessary to verify that the heat produced by the UV lamp did not cause convective cycling in the photoreactor.

Since the gas flowing in the photoreactor is affected by the transfer from the UV lamp, non-isothermal flow (NITF) was selected as the principal physics of the model. In this section, the type of the flow model should be selected. The model type can be either laminar, or turbulent. Both cases were studied, and the results will be discussed in Chapter 4. When turbulent flow is selected, the turbulent model should be selected in accordance with the nature of the reactor. COMSOL uses RANS (Reynolds Averaged Navier Stokes) as the main turbulence model. Among the turbulent models suggested by COMSOL, Low Reynolds $k$-$\varepsilon$ (LRKE hereafter) was

applied to the model. This is a practical choice, as discussed before the Reynolds number in the photoreactor is noticeably small. This model solves the turbulent model for two variables, *k*, the turbulence kinetic energy ($m^2/s^2$); and $\varepsilon$ (epsilon), the rate of dissipation of turbulence kinetic energy ($m^2/s^3$). The beauty of LRKE model compared to the other models is that the model can solve the flow everywhere in the reactor (i.e., inside the flow and near the walls). This model also often gives a very accurate description of the boundary layer; however, it requires very high mesh resolutions and that, in turn, means that the high accuracy comes at a high computational cost.

The next required step was setting the mesh in the model. Meshing the model could be critical sometimes as the model required very refined mesh near the walls makes the model computationally intensive. To overcome this, different mesh types were employed in the model, and after each run, the values for velocity were compared. Figure 3-6 shows the normal meshing type that was built in COMSOL to run the simulation.

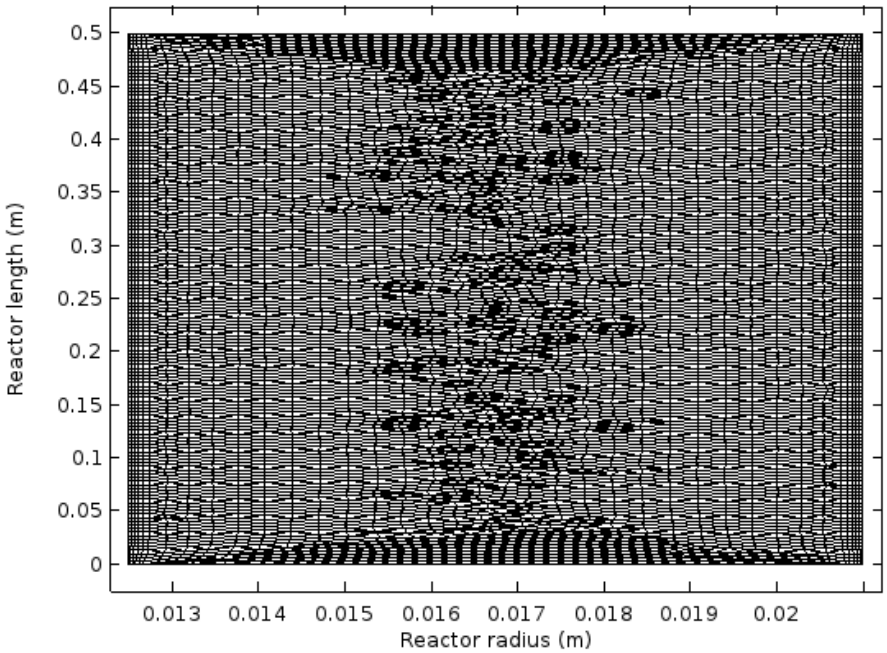


**Figure 3-6: Normal meshing used in the simulation**

Table 3-10 shows the accuracy and relative computation time for various meshings. In this table, the mean velocity values are compared between the theoretical profile assuming laminar flow and the profile simulated by COMSOL, then the relative deviation of simulated mean velocity from theoretical mean velocity are presented. The absolute value of the relative error for the normal meshing gives the smallest deviation. Although for the fine or extra fine meshing, the absolute differences of mean velocities from theoretical values are less than 1%, the time factor significantly increases by refining the mesh type. This justifies the use of normal mesh in subsequent calculations. It is also worth-mentioning that calculation of mean velocity deviation from the extra fine meshing values returns the second order of measure of accuracy, when the errors were plotted as a function of cell size; this means differences between velocity values get smaller when the numerical simulation is converging to the final solution.

**Table 3-10: Different mesh types employed in the COMSOL model**

| Mesh type | Number of elements | Average mesh size ($m^2$) | Deviation of simulated mean velocity from theoretical mean velocity (%) | Time factor [a] |
|---|---|---|---|---|
| Extra fine | 70579 | $6.02 \times 10^{-8}$ | -0.46 | 7.4 |
| Fine | 11065 | $3.84 \times 10^{-7}$ | -0.29 | 2.6 |
| Normal | 7040 | $6.04 \times 10^{-7}$ | -0.17 | 1 |
| Coarse | 3513 | $1.21 \times 10^{-6}$ | 0.26 | 0.6 |
| Extra coarse | 1263 | $3.37 \times 10^{-6}$ | 1.91 | 0.4 |

*Note:* the time factor was calculated as convergence time in the specified mesh type divided by convergence time in the normal mesh type, which is about 16 seconds in the simulation of laminar flow model.

Once the mesh was built, the type of study should be specified. Stationary study (steady state) and time dependent study (non-steady state) both were selected for this simulation. Although the simulation predicted that the steady states condition happened quickly (e.g., in the order of a

minute), to be consistent with the main model results, the COMSOL simulation values will be reported in Chapter 4 at steady states condition; unless specified otherwise.

COMSOL uses very sophisticated numerical methods to evaluate the parameters, based on the defined physics, material and meshing defined in the software. The accuracy of solver was established, since the results did not change by changing the solver parameters (such as relative tolerance) by two orders of magnitude.

# Chapter 4: Simulation Results and Discussion

The simulation model geometry is based on the actual photoreactor that has been used experimentally in previous research for benzene (Mahmoudkhani et al., 2016), toluene (De Visscher et al., 2010) and m-xylene (Atyabi, 2013) degradation. This photoreactor is made of stainless steel with around 3 cm of outside radius. Table 4-1 shows the simulated operating conditions for the proposed modeled reactor. The reactor properties are directly provided by the reactor manufacturer (NeoTech® Aqua Solutions) and other variables are chosen to be consistent with previous studies of the model of $H_2S$+$NO_x$ (Asili & De Visscher, 2014), and experimental condition of benzene (Mahmoudkhani et al., 2016). All the simulation results were obtained according to these conditions unless they are specified otherwise. Model assumptions and justifications are previously presented in Chapter 3, Section 3.1.1.

**Table 4-1: Simulation operation conditions**

| | |
|---|---|
| UV lamp electrical power | 40 W |
| Irradiation power | 3.2 W @ 185 nm<br>12 W @ 254 nm |
| Reactor length ($L$) | 50 cm |
| Reactor radius ($R_1$) | 2.10 cm |
| Lamp radius ($R_0$) | 1.25 cm |
| Pressure (barometric) | 89 kPa |
| Inlet temperature | 300 K |
| Relative humidity (RH) | 28 % |
| Inlet concentration ($CH_4$; $C_2H_6$; $C_2H_4$) | 0.5 – 5 g/m$^3$ |
| Volumetric flow rate | 0.5 – 5 L/min |

Some of the simulation results presented in this chapter are already presented in a recently published journal paper, which presents only the methane and ethane models (Asili & De Visscher, 2018). This chapter includes some of those published data, with addition of ethylene model, detailed calculations and discussion, justifying assumptions, and a clear path of contribution of a photolysis model to a bigger scale.

## 4.1 Developments of Reaction Networks

### *4.1.1 Effective reaction network*

The baseline calculation is the complete reaction network consisting of all reactions in Tables 3-1 to 3-8 in Chapter 3. This version of the model is called "the comprehensive kinetics" henceforth. The model was run with a constant volumetric flow rate of 1 L/min, a methane concentration of 1 g/m$^3$, an ethane concentration of 1.5 g/m$^3$, and an ethylene concentration of 2.5 g/m$^3$. In these conditions, the degradation efficiency of a compound (conversion), is 11.81% for methane, 34.16% for ethane, and 63.57% for ethylene. Different initial concentrations for each of $CH_4$, $C_2H_6$, and $C_2H_4$ were chosen because of different chemical reactivity of each hydrocarbon leading to a transparent result for the sensitivity of the model to a specific reaction. Otherwise, near-complete degradation would be obtained in all simulations, and no meaningful sensitivity data would be found.

Next, the model was re-run with the rate of each reaction (chemical and photochemical) in the model set to zero, one at a time; and the degradation efficiency of each calculation was compared with the baseline degradation efficiency. With this process, all the reactions that affect the degradation efficiency by less than ±0.1%, were removed from the model and the rest were kept. In other words, in the procedure for removing reactions from the baseline kinetics is such that the removal efficiency (e.g., $\eta_{base}$) for each methane, ethane, and ethylene model at constant flow rate and constant inlet concentration, is compared with the new efficiency (or conversion; e.g., $\eta_{new}$) obtained when the reaction rates are set to zero one at a time. If the difference between $\eta_{base}$ and $\eta_{new}$ was less than ±0.1%, the reaction was removed. The resulting version of the model is called the "primary kinetics" model.

Another way to prioritize the reactions is to calculate the Damköhler number, which is a dimensionless number and defined as flow time scale divided by chemical time scale. As mentioned previously, the main degradation chemical reactions are initiated with hydroxyl radical (e.g., reactions MC3 for methane in Table 3-3, EC1 for ethane in Table 3-5, and EyC1 for ethylene in Table 3-7). Taking each of methane, ethane, and ethylene at above-discussed initial conditions (i.e., constant flow rate of 1 L/min, and a methane concentration of 1 $g/m^3$, an ethane concentration of 1.5 $g/m^3$, and an ethylene concentration of 2.5 $g/m^3$), and calculating the average OH radical concentration and rate constant for each of these three reactions, leads to obtain the Damköhler number of 0.11, 0.41, and 0.69 for $CH_4$, $C_2H_6$, and $C_2H_4$, respectively. So, if the Damköhler number for other reactions is far below the above values, those reactions can be eliminated from the network. In addition, comparing these Damköhler numbers with the above-mentioned values of conversion of each of methane, ethane, and ethylene (i.e., conversion of 11.81% for methane, 34.16% for ethane, and 63.57% for ethylene) indicates that the reaction of these hydrocarbons with hydroxyl radical is the primary reaction for degradation.

In addition, as a priori criterion, calculating first-order rate constant of a reaction times the space time returns a dimensionless number and if this number is far less than one, that reaction can be removed without running the whole model. This assessment is not useful in this study, as most reactions are not first-order; and to obtain the Damköhler number with pseudo-first-order rate constants times the space time, the radical concentrations are required, and those radical concentration can be obtained by running the whole model. Hence, for instance, calculating the average hydroxyl radical concentration, and the rate constants of Reactions MC3, EC1, and EyC1 gives the pseudo-first order rate (i.e., $k\cdot[OH]$) of these reactions evaluated under above-discussed conditions. These values were found to be $3.93\times10^{-3}$ $s^{-1}$, $1.54\times10^{-2}$ $s^{-1}$,and $2.57\times10^{-2}$ $s^{-1}$

for MC3, EC1, and EyC1, respectively. Although this indicates that the reason of more reactivity of ethylene in compare with ethane, and methane (due to smaller pseudo-first order rate constant), but the method cannot be used as a judgment of keeping and/or leaving reactions in the system as it requires all the intermediate concentrations after running the model. Hence, pre-screening of the reactions with this method, and removing it before running the whole model is not practical, and reaction sensitivity by setting the reactions them to zero is the best approach.

By removing all those reactions at the same time and keeping only the effective reactions, the model results were affected by less than ±1%. By this modification, the most effective reactions were specified, and these reactions are shown in the Tables 3-1 to 3-8 in Chapter 3 with bold font. Hence, the "primary kinetics" model includes only the bold reactions in Tables 3-1 to 3-8 in Chapter 3.

In the next stage, a reaction network in the presence of $NO_x$ was established. To find this, the target gas stream (e.g. $CH_4$ or $C_2H_6$ or $C_2H_4$ in air) was presumed to be mixed with a NO concentration of 0.1 $g/m^3$ (96 ppm) and introduced to the photoreactor. Using the same above-discussed process for the sensitivity of the model to the reaction rates yields a few more reactions added to the "primary kinetic" model. These reactions are specified with italic font in the Tables 3-1 to 3-8 in Chapter 3; and the model after this will be called "the primary+$NO_x$ kinetics".

Comparing the model results with the "comprehensive kinetics" with the "primary kinetics" and the "primary+$NO_x$" kinetics, the accuracy of the reaction network is established, as there is only less than 1% difference between the model results for both $CH_4$, $C_2H_6$ and $C_2H_4$ models. Table 4-2 shows the number of reactions included in the three models. For instance, the "comprehensive

kinetic" model of ethylene contains 199 reactions in total, including 165 chemical reactions and 34 photochemical reactions.

**Table 4-2: Detailed number of effective reactions in the different models (A: Air; M: Methane; E: Ethane; Ey: Ethylene)**

| **Model type** | **the primary kinetics** | | | | **the primary+$NO_x$ kinetics** | | | | **the comprehensive kinetics** | | | |
|---|---|---|---|---|---|---|---|---|---|---|---|---|
| Group compound | A | A+M | A+M+E | A+M+E+Ey | A | A+M | A+M+E | A+M+E+Ey | A | A+M | A+M+E | A+M+E+Ey |
| # Chemical reactions | 15 | 31 | 54 | 67 | 31 | 51 | 77 | 92 | 55 | 92 | 131 | 165 |
| # Photochemical reactions | 5 | 6 | 6 | 6 | 10 | 13 | 15 | 15 | 15 | 23 | 30 | 34 |
| **# Total reactions** | **20** | **37** | **60** | **73** | **41** | **64** | **92** | **107** | **70** | **115** | **161** | **199** |

### *4.1.2 Effective reaction pathway*

To find out which reactions are fast (i.e., non-rate limiting), the chemical rate constant of each reaction in the "primary kinetics" was multiplied by factors of 10 and 100 one at a time; the model was run again, and the results were compared with the "comprehensive kinetic" model results. If increasing the rate constant does not affect the outcome, it means that the reaction is not a rate-limiting step for any reaction network, and the reaction can be treated as instantaneous. This assessment leads to a general view of degradation reaction pathways which are shown in the following figures, for each model.

#### *4.1.2.1 Methane model*

Figure 4-1 shows a schematic pathway of methane degradation, covering the chemical reactions of the "primary kinetics" for $CH_4$, excluding $NO_x$ reactions as there was not a huge impact found on the product concentration of the process. Moreover, the background and radical species are omitted from the graph to have a clear scheme of the methane degradation pathway.

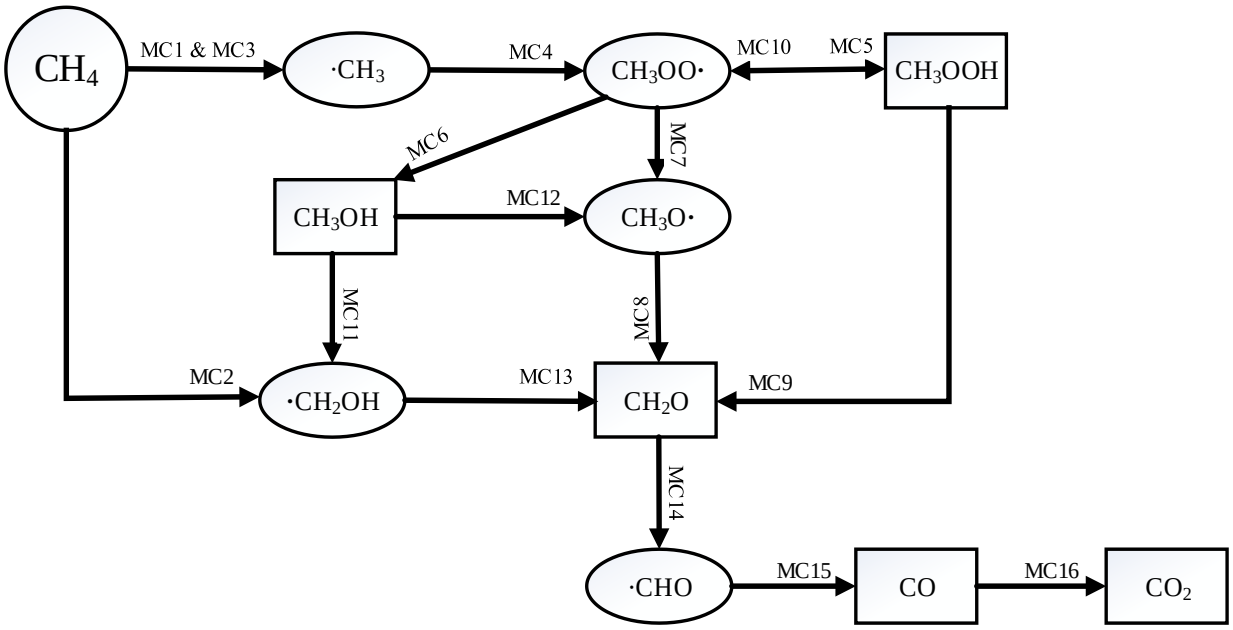


**Figure 4-1: Schematic diagram for $CH_4$ reaction network, based on the primary kinetics**

For the methane model, the reactions MC4, MC8, MC13, MC15, and MC16 were found to be near-instantaneous. For example, the model specifies that the reaction between $\cdot CH_3$ and $O_2$ (MC4) is fast. This seems obvious to some extent, since all other reactions involving methyl radical ($\cdot CH_3$) were found to be insignificant in the previous section. Hence, it would be possible to replace the reaction product $\cdot CH_3$ by $\cdot CH_3O_2$ in reactions MC1 and MC3 (adding $O_2$ as a reactant to maintain atom conservation), and to leave $\cdot CH_3$ out of the species list altogether, without changing the reactor outlet composition significantly.

*4.1.2.2 Ethane model*

Figure 4-2 shows a schematic pathway of the ethane degradation reaction network. Some intermediate species and reaction products are converted to the methane model species (i.e., lower C-alkane). Hence, their pathway continues as in Figure 4-1. Here again, the background and radical species are omitted from the graph to have a clear scheme of the ethane degradation pathway, based on the "primary kinetics".

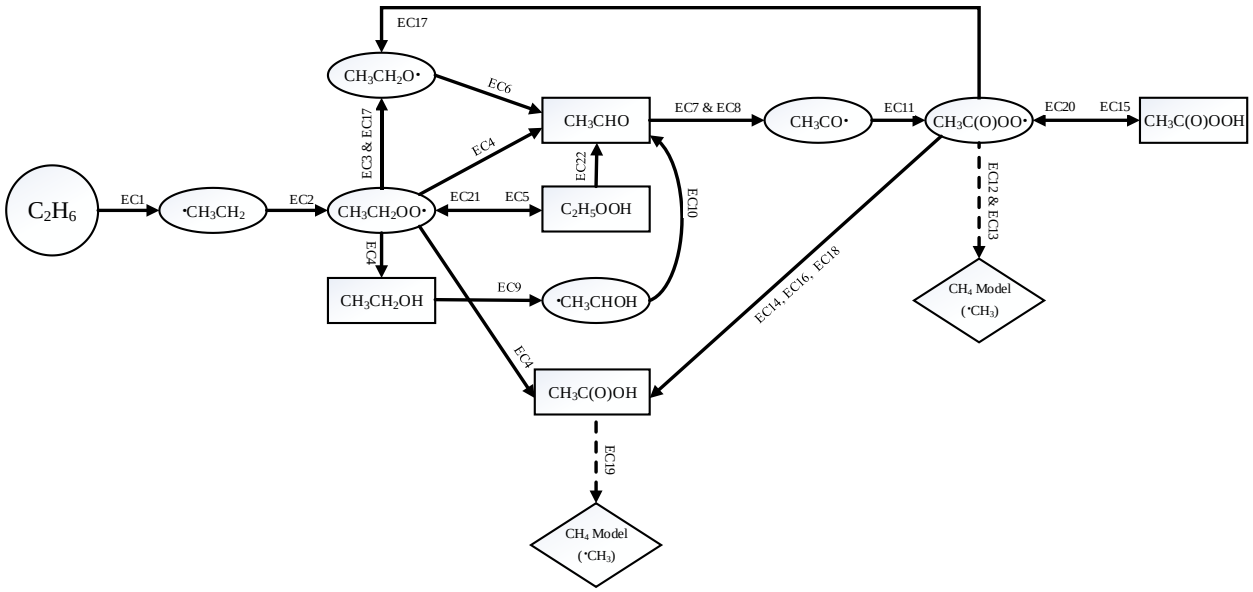


**Figure 4-2: Schematic diagram for $C_2H_6$ reaction network, based on the primary kinetics**

For the ethane model, the reactions EC2, EC6, EC10, and EC11 were found to be near-instantaneous.

### *4.1.2.3 Proposing alkane degradation*

Based on the above reaction networks for methane and ethane, a general reaction pathway can be projected for the degradation of alkanes, including higher alkanes. Figure 4-3 shows the proposed reaction network based on the model described in this research.

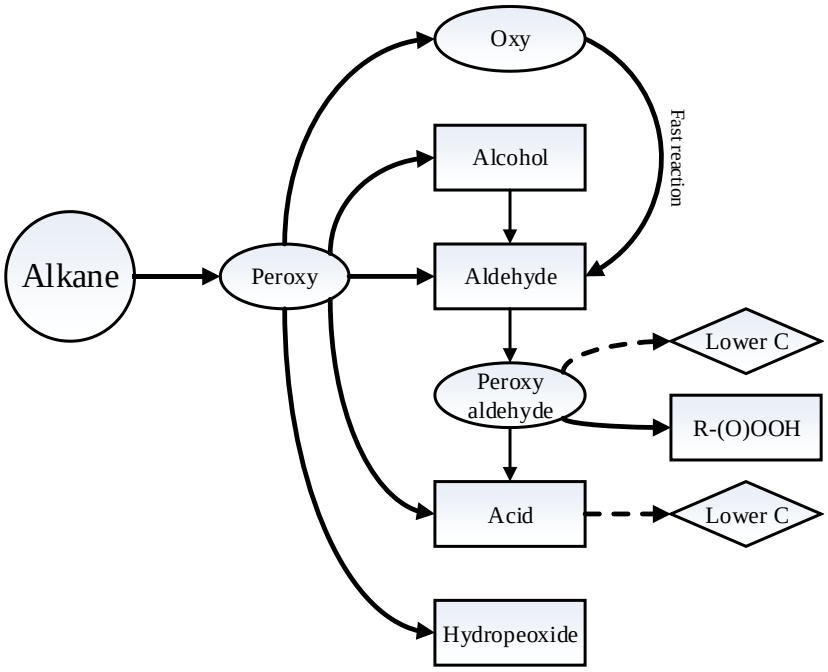


**Figure 4-3: Proposed reaction network for a general alkane degradation pathway. The lower C species are alkyl/alkoxy (from peroxy aldehyde) and alkyl (from acid), in addition to $CO_2$.**

In Figure 4-3, the compounds shown in the rectangles form the major reaction products. $CO_2$ is potentially one of the predominant reaction products, but its concentration nevertheless is significantly lower than a complete oxidation process of alkanes. This may present issues when photolysis is used for pollution remediation, but the organic reaction products tend to be highly water-soluble (e.g., alcohol/acid), therefore they can be eliminated by absorption.

*4.1.2.4 Ethylene model*

Figure 4-4 shows a schematic pathway of ethylene degradation, covering the chemical reactions of the "primary kinetics" for $C_2H_4$, excluding $NO_x$ reactions. Similar to the other pathways, the background and radical species are omitted from the graph to have a clear scheme of the ethylene degradation pathway. For the ethylene model, the reactions EyC6, EyC10, and EyC11 were

found to be near-instantaneous, where the ratio of rate constants for EyC10 and EyC11 can be defined as $\frac{k_{EyC10}}{k_{EyC11}} = 1.11\ \exp(-668/T)$.

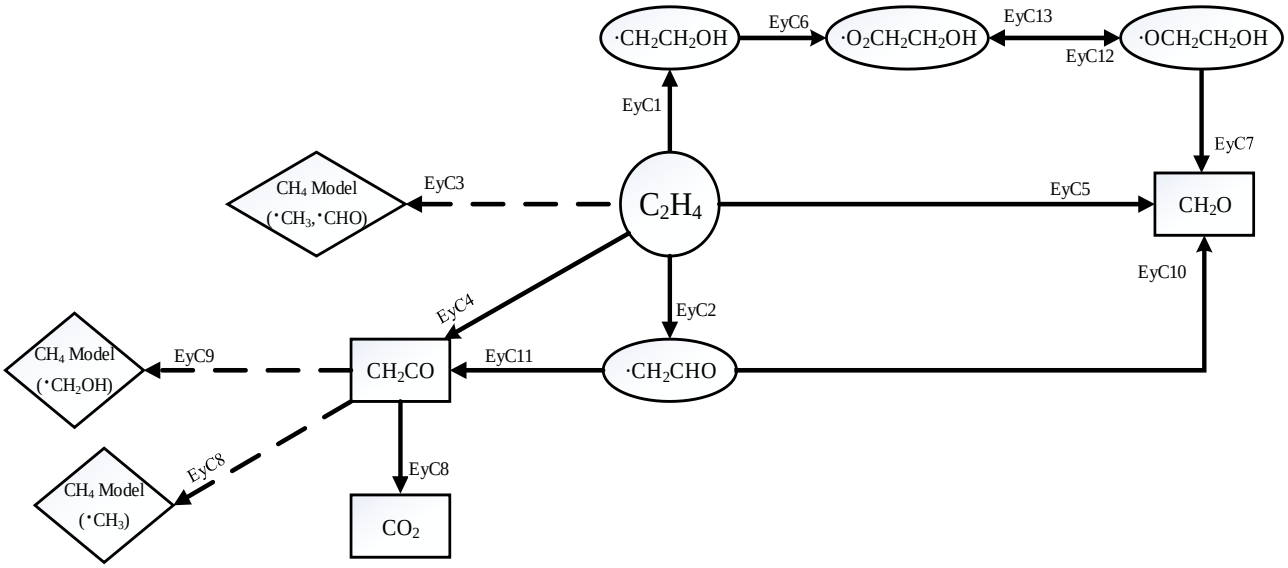


**Figure 4-4: Schematic diagram for $C_2H_4$ reaction network, based on the primary kinetics**

As the product analysis, besides $CO_2$ as one of the main products (which has a lower concentration than in the complete combustion), formaldehyde ($CH_2O$) and ketene ($CH_2CO$) are the predominant reaction products for the photolysis of the ethylene in the gas phase, according to the model results.

### 4.2 Model Run-Time

One of the factors of each modeling and simulation project is to achieve accurate results in a reasonable amount of time. Figure 4-5 shows different run times of all versions of the reaction model discussed in the Section 4.1 ("the primary kinetics", "the primary+$NO_x$ kinetics", and "the comprehensive kinetics"). All of these results are obtained at the same operational conditions

and with an identical computer (Processor: Intel® Core™ i7-870 @ 2.93 GHz) and the same MATLAB® code. In Figure 4-5, each point in the graph is marked with three values: the number of active chemical components (i.e., reactive species) in that specific model, total number of chemical and photochemical reactions in that particular model, and the average model run time (in seconds) for every single run of that model.

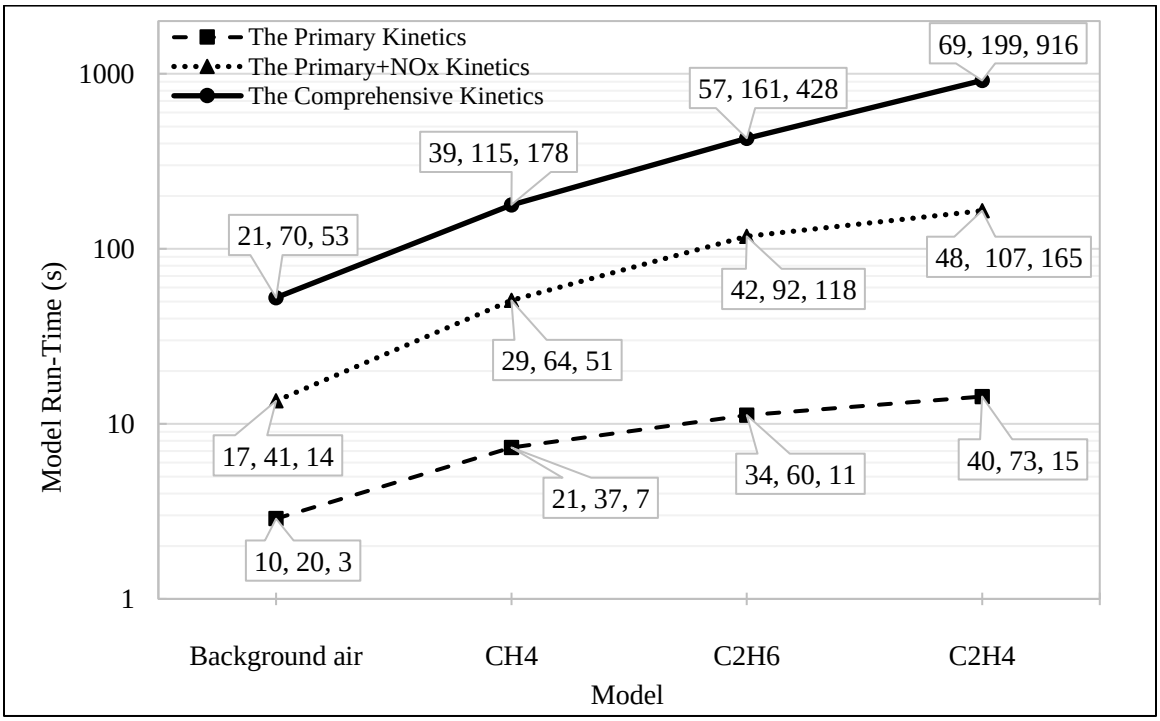


**Figure 4-5: Average model run time for each different model kinetic type (the numbers for each point are: number of chemical components, number of chemical and photochemical reactions, and average model run time (in seconds), consecutively.)**

According to Figure 4-5, it is expected that by increasing the carbon number (i.e., heavier hydrocarbons), the most comprehensive reaction network will have rapidly increasing run times with increasing carbon number. The results show how careful consideration of the relevance of each reaction shaves off considerable amounts of simulation time. With minimum loss of accuracy and defining the most effective reactions (e.g., the "primary kinetics"), it is feasible to have a model with run times that increase more slowly with carbon number, yet provide the same

results to within 1%. Hence, it is expected that this methodology will save computation time by several orders of magnitude in the case of higher hydrocarbons; if some of the reaction products in these future models already exist in the methane, ethane, or ethylene model.

The run time reductions shown in Figure 4-5 were obtained without removing any reactions that were found to be near-instantaneous mentioned in Section 4.1 for each model. If near-instantaneous reactions are removed from the reaction network, it is anticipated that further run time reductions are possible. However, those reactions are kept in the model to have a clear view of reaction pathways. Moreover, the run time is currently reasonable for these pathways, so there is no need to remove near-instantaneous reactions for now.

One of the benefits of using different models based on the effective reactions is that these types of classification can be used in some of the air dispersion models that contain atmospheric reactions. Generally, air quality modeling with Eulerian models including detailed photochemical chemistry and are known to have long run times and require significant computational resources. 50-90 % of the run time of these models is spent on resolving the complicated kinetics (Byun & Ching, 1999). It is expected that the methodology developed in this work can lead to significant run time reductions in these models as well. The run-time presented in this section might not be significant (order of 20 minutes for each run of the comprehensive kinetic of ethylene model), but in the context of environmental engineering study, these run-time reductions are considered substantial. Running larger and more complex reactors would take more simulation time. Eulerian dispersion models can take hours, even days to run.

## 4.3 Degradation of Individual Hydrocarbons (Parameter Study)

### *4.3.1 Effect of hydrocarbon inlet concentration*

Figure 4-6 shows the simulation results of the photolysis removal efficiency for a fixed volumetric gas flow rate of 1 L/min, as a function of hydrocarbon inlet concentration. Each curve represents the degradation of hydrocarbon in the absence of other hydrocarbons. The conversion of ethylene is significantly higher than ethane on the identical conditions; and removal efficiency of ethane is higher than methane, due to its higher reactivity, as expected.

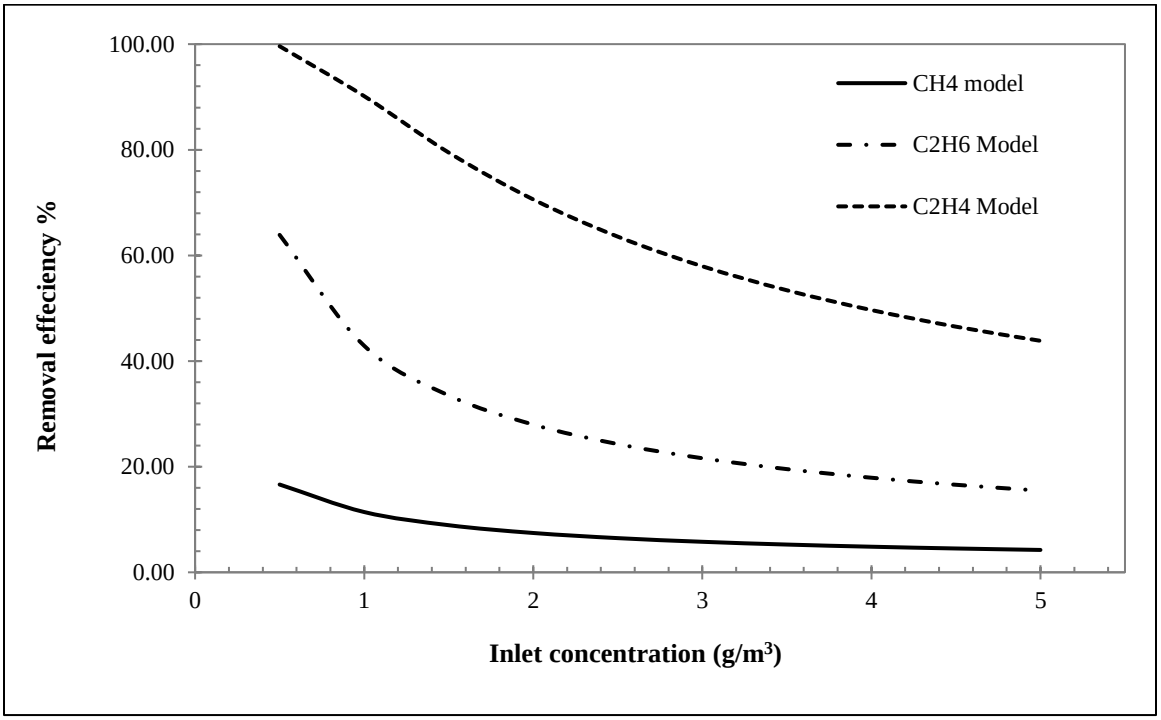


**Figure 4-6: Model results for degradation efficiency as a function of initial pollutant concentration at fixed gas flow rate (1 L/min)**

At a fixed UV lamp power, the energy and number of photons and active radicals in the reaction area do not change; hence, with constant gas flow rate, by increasing inlet pollutant concentration, their molecules obtain less energy, which results in a lower removal efficiency. This effect was experimentally observed in a few studies that worked on some hydrocarbon

pollutants such as benzene (De Visscher et al., 2010; Mahmoudkhani et al., 2016), and m-xylene (Atyabi, 2013) in a photolysis process, using the same photoreactor as modeled. Also, near-complete conversion is expected for ethylene at low initial concentration and lower flow rates.

- ***Comparison of the Kinetic Models***

As discussed, the selection of different reaction network pathways was based on the sensitivity of removal efficiency to the reaction rate constants; and the three types of kinetics (i.e., "primary", "primary+$NO_x$", and "comprehensive" kinetics) were split when the removal efficiency values differed within ±0.1% of the comprehensive kinetics. Since these values are not recognizable in a graph, Table 4-3 shows the comparison of the removal efficiency for the two cases of "primary" and "comprehensive" kinetics, as a function of variable inlet hydrocarbon concentration, at constant flow rate of 1 L/min.

**Table 4-3: Comparison of model results for different kinetic approach, as a function of inlet concentration**

| **Inlet concentration ($g/m^3$)** | **$CH_4$ Model** | | **$C_2H_6$ Model** | | **$C_2H_4$ model** | |
|---|---|---|---|---|---|---|
| | Removal efficiency (%) | | Removal efficiency (%) | | Removal efficiency (%) | |
| | *Primary* | *Comprehensive* | *Primary* | *Comprehensive* | *Primary* | *Comprehensive* |
| 1 | 11.42 | 11.48 | 42.90 | 43.02 | 90.16 | 90.50 |
| 2 | 7.45 | 7.51 | 27.97 | 28.05 | 70.60 | 70.59 |
| 3 | 5.78 | 5.84 | 21.60 | 21.66 | 57.94 | 57.98 |
| 4 | 4.85 | 4.90 | 17.91 | 17.96 | 49.66 | 49.73 |
| 5 | 4.24 | 4.29 | 15.46 | 15.51 | 43.83 | 43.91 |

### *4.3.2 Effect of gas flow rate*

Figure 4-7 shows the removal efficiency of $CH_4$, $C_2H_6$, and $C_2H_4$ as a function of gas flow rate at fixed inlet concentration of pollutant of 1 $g/m^3$. Again, only one hydrocarbon at the inlet was included in the model at a time. As before, the removal efficiency of ethylene is predicted to be

considerably higher than that of ethane, followed by methane. The smaller gas flow rate which leads to longer gas residence time provides both longer collision time and higher collision probability with photons and OH radicals, which increases the conversion of the hydrocarbon. Also, near-complete conversion is expected for ethylene at low initial concentration and lower flow rates.

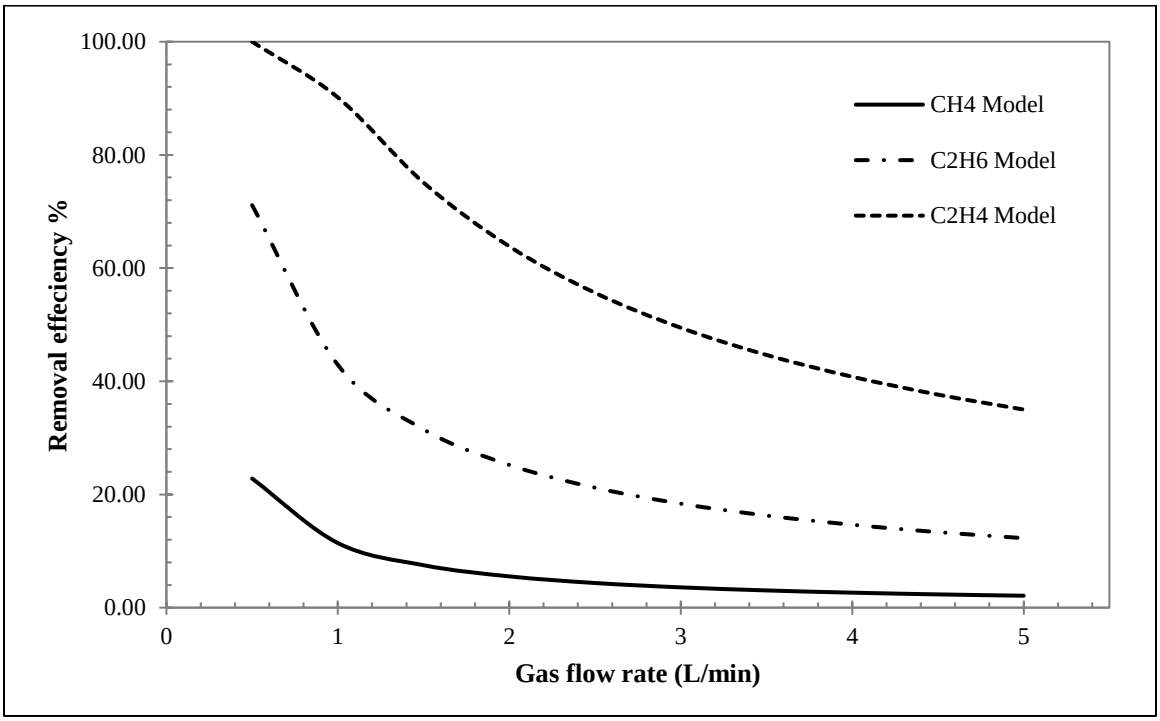


**Figure 4-7: Model results for degradation efficiency as a function of gas flow rate at fixed initial hydrocarbon concentration (1 g/m$^3$)**

## 4.4 Product Analysis of the Models

One of the important factors of any photolysis process is the study of the degradation and transformation of a concerned compound to other product compounds. The mechanism of this transformation for hydrocarbons is usually called hydroxylation or slow oxidation of hydrocarbons. It was previously found that apart from the end products of hydrocarbon oxidation (CO, $CO_2$, and $H_2O$), formaldehyde and formic acid were found during the oxidation of methane;

and formaldehyde, acetaldehyde and formic acid were found during the oxidation of ethane and oxidation of ethylene (Shtern, 1964). Among investigation of methane, ethane, ethylene, and acetylene, it was found that the methane appeared to be the most difficult to oxidize (Shtern, 1964). This fact is also confirmed in the study of atmospheric oxidation of alkanes (Calvert et al., 2008).

The proposed model in this study is able to predict the reaction products of the photolysis process in the gas phase, for each individual model of methane, ethene, and ethylene, as will be argued below.

### *4.4.1 Methane model*

In the absence of $NO_x$, primary products for the oxidation of methane were found to be $CH_2O$, $CH_3OH$, and $CH_3OOH$ (Hanst & Gay, 1983; Horie et al., 1990; Qi et al., 1999; Tyndall et al., 1998). The secondary products, which are worth mentioning, with the subsequent oxidation of formaldehyde, were found to be CO, $CO_2$, and HCOOH, were also reported in some studies (Hanst & Gay, 1983; Qi et al., 1999). This agrees with the proposed model. The main reactions of the atmospheric oxidation of methane, in the absence of $NO_x$, (which are all included in the "primary kinetics" of the $CH_4$ model) can be summarized as: (Calvert et al., 2008)

$$CH_4 + OH\cdot \rightarrow \cdot CH_3 + H_2O \quad (4.1)$$

$$\cdot CH_3 + O_2 \rightarrow \cdot CH_3O_2 \quad (4.2)$$

$$\cdot CH_3O_2 + \cdot CH_3O_2 \rightarrow 2\ CH_3O\cdot + O_2 \quad (4.3a)$$

$$\rightarrow CH_3OH + CH_2O + O_2 \quad (4.3b)$$

$$CH_3O\cdot + O_2 \rightarrow CH_2O + \cdot HO_2 \quad (4.4)$$

$$CH_3O_2 + \cdot HO_2 \rightarrow CH_3OOH + O_2 \quad (4.5)$$

In the presence of $NO_x$, it was found that formaldehyde is primary product of the oxidation of methane in air, while the formation of methyl nitrite ($CH_3ONO$) and methyl nitrate ($CH_3ONO_2$) were formed minimally (Cox et al., 1976). The main reactions of the atmospheric oxidation of methane, in the presence of $NO_x$, can be summarized as follows (Calvert et al., 2008). Among the reactions below, reactions (4.1), (4.2), (4.4), and (4.6) are categorized in the "primary+$NO_x$ kinetics" in the model; and reactions (4.7) and (4.8) are not important in the model, as reported.

$$CH_4 + OH\cdot \rightarrow \cdot CH_3 + H_2O \quad (4.1)$$

$$\cdot CH_3 + O_2 \rightarrow \cdot CH_3O_2 \quad (4.2)$$

$$CH_3O\cdot + O_2 \rightarrow CH_2O + \cdot HO_2 \quad (4.4)$$

$$\cdot CH_3O_2 + NO \rightarrow CH_3O\cdot + NO_2 \quad (4.6)$$

$$\cdot CH_3O + NO \rightarrow CH_3ONO\cdot \quad (4.7)$$

$$\cdot CH_3O + NO_2 \rightarrow CH_3ONO_2 \quad (4.8)$$

Figure 4-8 shows results of the predicted methane product yields at different initial concentrations of $CH_4$, in the methane-air mixture, in accordance with the comprehensive kinetic model in the absence of $NO_x$.

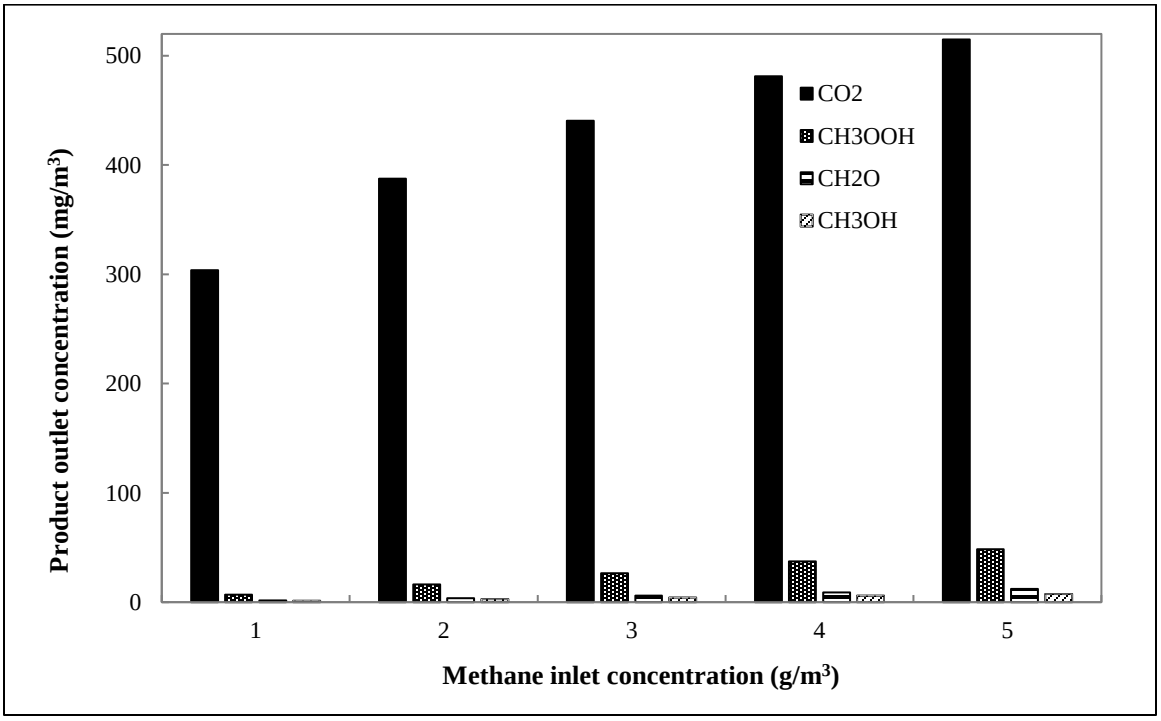


**Figure 4-8: Model product yields for methane model, (based on the comprehensive kinetics at 1 L/min of flow rate)**

Based on the simulation results, $CO_2$ is one of the main products of the model photolysis, but the concentration values are lower than would be obtained with complete combustion. Also, other than the unreacted $CH_4$ and $CO_2$ as the major compounds at the outlet of the reactor, formaldehyde, peroxide and/or alcoholic compounds are significant reaction products in the reactor efflux. On a carbon basis, $CO_2$ represents 91% of the reacted methane for an inlet concentration of 3 g/m$^3$.

### *4.4.2 Ethane model*

In the absence of $NO_x$, primary products for the oxidation of ethane were found to be $CH_3CHO$, $CH_3CH_2OH$, and $C_2H_5OOH$ (Anastasi et al., 1983). Also, CO, $CO_2$, ethyl hydroperoxide, and peracetic acid are other products of atmospheric oxidation of ethane (Hanst & Gay, 1983; Qi et al., 1999; Wallington et al., 1989). The main reactions of the atmospheric oxidation of ethane, in

the absence of $NO_x$, (which are all included in the "primary kinetics" of $C_2H_6$ model) can be summarized as: (Calvert et al., 2008)

$$C_2H_6 + \cdot OH \rightarrow \cdot C_2H_5 + H_2O \quad (4.9)$$

$$\cdot C_2H_5 + O_2 \rightarrow \cdot C_2H_5O_2 \quad (4.10)$$

$$\cdot C_2H_5O_2 + \cdot HO_2 \rightarrow C_2H_5OOH + O_2 \quad (4.11)$$

$$\cdot C_2H_5O_2 + \cdot C_2H_5O_2 \rightarrow CH_3CHO + C_2H_5OH + O_2 \quad (4.12a)$$

$$\rightarrow 2\ C_2H_5O\cdot + O_2 \quad (4.12b)$$

$$\cdot C_2H_5O + O_2 \rightarrow CH_3CHO + \cdot HO_2 \quad (4.13)$$

Subsequent oxidation of acetaldehyde would lead to form formaldehyde, methanol, CO, and $CO_2$ (Hanst & Gay, 1983; Qi et al., 1999); which shows that the oxidation process can be moved to the pathway of methane oxidation mechanism, as expected in this study.

In the presence of $NO_x$, once the ethylperoxy radical ($\cdot C_2H_5O_2$) is formed, it is converted to acetaldehyde through the following reactions (Calvert et al., 2008). All the following reactions are appropriately categized in the "primary+$NO_x$ kinetics" in the model of ethane.

$$C_2H_6 + \cdot OH \rightarrow \cdot C_2H_5 + H_2O \quad (4.9)$$

$$\cdot C_2H_5 + O_2 \rightarrow \cdot C_2H_5O_2 \quad (4.10)$$

$$\cdot C_2H_5O_2 + NO \rightarrow \cdot C_2H_5O + NO_2 \quad (4.14)$$

$$\cdot C_2H_5O + O_2 \rightarrow CH_3CHO + \cdot HO_2 \quad (4.13)$$

Figure 4-9 shows results of the predicted methane reaction products at different initial concentration of $C_2H_6$, in the ethane-air mixture, in accordance with the comprehensive kinetic model in the absence of $NO_x$.

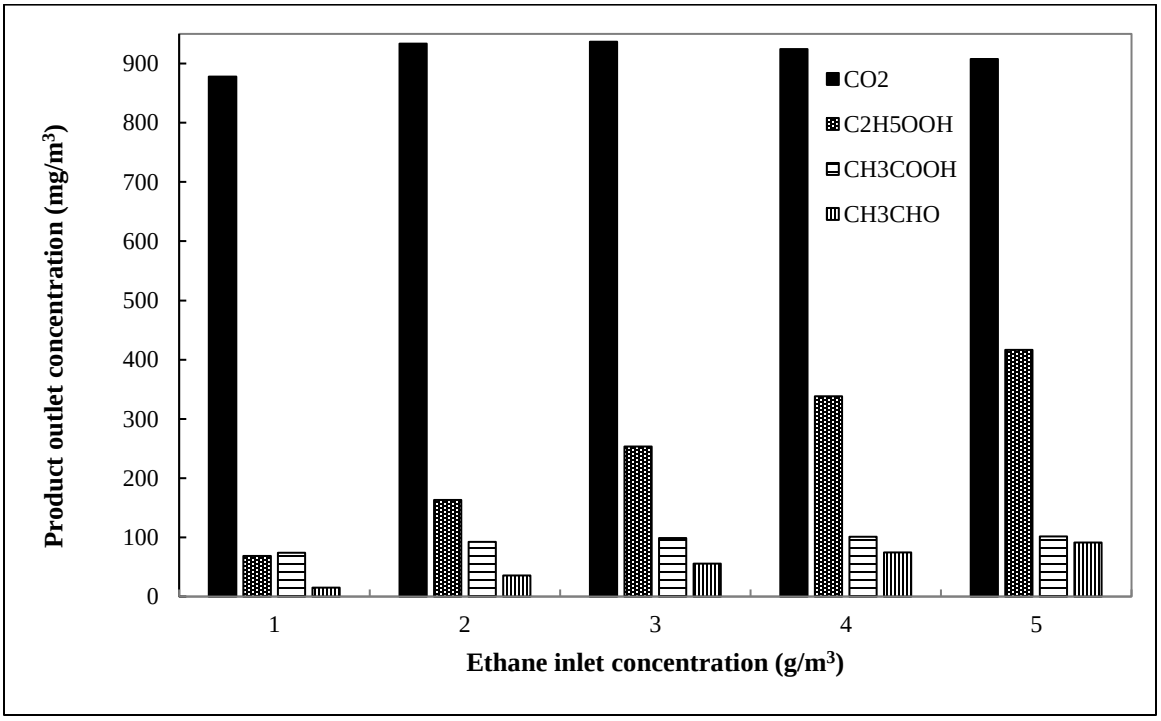


**Figure 4-9: Model product yields for ethane model, (based on the comprehensive kinetics at 1 L/min of flow rate)**

Based on the simulation results, $CO_2$ is one of the main products of this photolysis, but the concentration values are noticeably lower than would be obtained with complete combustion. Also, other than the unreacted $C_2H_6$ and $CO_2$ as the major compounds at the outlet of the reactor, acidic and/or alcoholic compounds are significant reaction products in the reactor efflux. On a carbon basis, $CO_2$ represents 57% of the reacted ethane for an inlet concentration of 3 g/m$^3$.

### *4.4.3 Ethylene model*

The primary products for the oxidation of ethylene were found to be formaldehyde, ketene, CO, and $CO_2$ (Orlandini & Riedel, 2000; Stockwell et al., 1997). The main end-products of the atmospheric oxidation of ethylene, in the absence of $NO_x$, (which are all included in the "primary kinetics" of $C_2H_4$ model) can be summarized as follows:

$$C_2H_4 + \cdot OH \rightarrow \cdot C_2H_4OH \quad (4.14a)$$

$$\cdot C_2H_4OH + O_2 \rightarrow \cdot O_2C_2H_4OH \leftrightarrow \cdot OC_2H_4OH \quad (4.14b)$$

$$\cdot OC_2H_4OH \rightarrow \cdot CH_2OH + CH_2O \quad (4.14c)$$

$$C_2H_4 + \cdot O \rightarrow \cdot CH_2CHO + H\cdot \quad (4.15a)$$

$$\cdot CH_2CHO + O_2 \rightarrow CO + \cdot OH + HCHO \quad (4.15b)$$

$$\rightarrow \cdot HO_2 + CH_2CO \quad (4.15c)$$

Further oxidation of formaldehyde would lead to production of more $CO_2$, while subsequent oxidation of ketene would result in formation of more formaldehyde, as described in Chapter 3, Table 3-7.

In the presence of $NO_x$, the formed hydroxyalkyl radical ($\cdot O_2C_2H_4OH$) can promote converting NO to $NO_2$, and then by formation of ethanediol radical ($\cdot OC_2H_4OH$) would lead to continue in the reaction (4.14) for other reactions to yield formaldehyde (Orlandini & Riedel, 2000). Yet, considerable uncertainty of ethylene oxidation at low temperature (e.g., room temperature) is a challenge (Curran et al., 2000; Ju et al., 2015).

Figure 4-10 shows results of the predicted ethylene reaction products at different initial concentration of $C_2H_4$, in the ethylene-air mixture, predicted by the comprehensive kinetic model in the absence of $NO_x$.

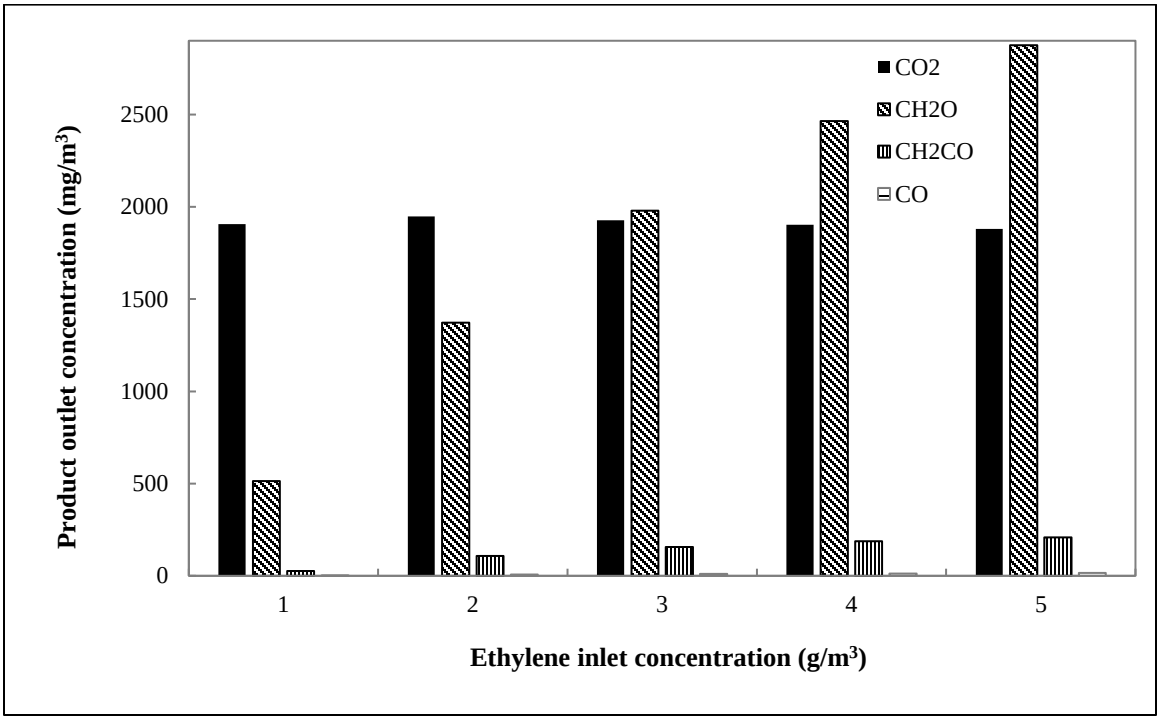


**Figure 4-10: Model product yields for ethylene model, (based on the comprehensive kinetics at 1 L/min of flow rate)**

Based on the simulation results, $CO_2$ is one of the main products of this photolysis at lower ethylene concentration, while formaldehyde is the predominant product at higher inlet ethylene concentration. Also, with increasing inlet concentration of ethylene in the system, the concentration of produced ketene will increase, as well. Moreover, consistent with the methane and ethane model, on a carbon basis, $CO_2$ represents 35% of the reacted ethylene for an inlet concentration of 3 $g/m^3$.

- ***Polymerization of Ethylene***

A concern in the study of the reactions of ethylene is the polymerization of the ethylene. Classically, polymerization reactions of the ethylene to a long-chained molecule (polymer) happens at two different sets of conditions; one is the high temperature polymerization (which also requires a high pressure of around 2000 atm) at a temperature above 200°C (Peacock, 2000);

and the other is low temperature (around 60°C) and atmospheric pressure which essentially requires a catalyst to form a polymer (Spalding & Chatterjee, 2017). However, there are a few polymerization reactions that have a reported rate constant at room temperature, so it is interesting to study the potential effect of polymerization from those reactions. In order to study those reactions, the rate constants for those reactions should be compared with the main degradation reaction rate constants of ethylene. It is worth mentioning that the main degradation reactions of ethylene have a value of the rate constant on the order of $10^{-10}$ to $10^{-12}$ $cm^3$/molecule·s at room temperature, according to the rate constants in Table 3-7, Chapter 3.

One reaction that may lead to polymerization from ethylene at low temperature is:

$$C_2H_4 + \cdot CH_3 + M \rightarrow n\text{-}\cdot C_3H_7 + M \quad (4.16)$$

Reaction (4.16) has a rate constant of $k = 5.5\times10^{-13} \exp(-3880/T)$ in the rage of 300-500 K (Kerr & Parsonage, 1972). Calculation of the rate constant at room temperature leads to a value of $1.2\times10^{-18}$ $cm^3$/molecules·s, which is at least 6 orders of magnitude smaller than the main reaction rate constants; hence, this polymerization to propane from this reaction is negligible.

Another reaction that might be important for chain growth is:

$$C_2H_4 + \cdot C_2H_5 + M \rightarrow n\text{-}\cdot C_4H_9 + M \quad (4.17)$$

Reaction (4.17) has a rate constant of $k = 2.62\times10^{-13} \exp(-3670/T)$ in the range of 300-600 K (Baulch et al., 2005; Heuts et al., 1995). The rate constant at room temperature is found to be $1.1\times10^{-18}$ $cm^3$/molecule·s, which is at least 6 orders of magnitude smaller than the main reaction rate constants. Moreover, since the ethyl radical concentration at the worst case is in the order of $10^4$ molecules per $cm^3$, the apparent first-order rate constant of $10^{-10}$ 1/s in ethylene is expected,

thus unless the oxygen concertation is very low to have a significantly high $\cdot C_2H_5$ concentration, the polymerization to butane from this reaction is also insignificant.

There is also one more reaction that could potentially lead to a chain growth reaction, which is:

$$C_2H_4 + \cdot H + M \rightarrow \cdot C_2H_5 + M \quad (4.18)$$

For Reaction (4.18), the low-pressure limit and high-pressure limit rate constant are reported $k_0 = 1.3\times10^{-29}\ \exp(-380/T)$, $k_\infty = 6.6\times10^{-15}\ T^{1.28}\ \exp(-650/T)$, respectively, in the range of 300-800 K, with the broadening factor of $F_c = 0.24\ \exp(-T/40) + 0.76\ \exp(-T/1025)$ (Baulch et al., 2005). Subsequently, calculation of the falloff rate constants will be in the order of $10^{-12}$ to $10^{-13}$ $cm^3$/molecule·s, at room temperature. So, there might be competition between this reaction and the main reactions of ethylene degradation when the oxygen concentration is low and ethylene concentration is tremendously high. However, since the gas stream is assumed to be diluted with air, the Reaction (4.18) also does not play a significant role in the whole model, which means that the effect of this reaction is also insignificant. In addition, the calculation of some radical concentrations ($\cdot C_2H_5$, $\cdot H$, $\cdot CH_3$) in the middle and the outlet of reactor, applied to the kinetics of the above reactions, showed that the formation of these radicals is not significant enough to make a polymerization and/or propagation process.

Overall, based on the above discussed justification, it can be concluded that the production of the polymeric molecules in the proposed model is negligible, and under conditions evaluated (i.e., dilution of the hydrocarbon with air) the model is valid.

### 4.5 Degradation Efficiency Sensitivity Analysis

To conduct a degradation efficiency sensitivity analysis, some important process conditions have

to be changed, and then the simulation results are compared at those different cases. Concerning this, the effect of changing process conditions on degradation efficiency was studied for different types of processes.

The results of reactor optimization of the methane, ethane, and ethylene models are summarized in Table 4-4. In each step, all the base case conditions have been kept fixed as stated in Table 4-1 except the variable for which the sensitivity is evaluated. For the most accurate results, all of these removal efficiencies in Table 4-4 are obtained in accordance with the "comprehensive kinetics" for each individual model. The gas flow rate for each of the models were kept constant at 1 L/min. In order to see the resulting differences more clearly, the base case for methane was selected as initial concentration of 1 $g/m^3$ (1 mg/min of $CH_4$ mass flow rate), for ethane was selected as initial concentration of 1 $g/m^3$ (1 mg/min of $C_2H_6$ mass flow rate), and for ethylene was selected as initial concentration of 2.5 $g/m^3$ (2.5 mg/min of $C_2H_6$ mass flow rate). A different initial concentration for ethylene was chosen because of its higher reactivity. Otherwise, near-complete degradation would be obtained in all simulations, and no meaningful sensitivity data would be found.

**Table 4-4: Sensitivity analysis for the photolysis removal efficiency of each of $CH_4$, $C_2H_6$, and $C_2H_4$ models**

| Changing Condition | Removal degradation efficiency % | | |
|---|---|---|---|
| | $CH_4$ Model | $C_2H_6$ Model | $C_2H_4$ Model |
| Base case | 11.48 | 43.02 | 63.56 |
| Halving $O_2$ content (compared with regular air) | 8.16 | 35.76 | 56.96 |
| Doubling reactor length ($L \times 2$) | 11.82 | 43.31 | 63.51 |
| Doubling relative humidity ($y_{H2O} \times 2$) | 12.97 | 50.84 | 74.24 |
| Doubling temperature ($T \times 2$) | 17.28 | 50.76 | 44.31 |
| Premixing with ozone ($y_{O3} = 2\%$) | 19.41 | 78.66 | 90.88 |
| Doubling reaction area | 18.15 | 59.39 | 81.77 |
| Doubling reaction area at constant space time | 17.62 | 58.90 | 81.72 |
| Plug flow velocity ($V$=$U$) | 11.67 | 43.57 | 64.26 |

In the above table, “doubling reaction area” refers to the cross-sectional area, and was obtained when the reactor radius ($R_1$) was increased to 2.694 cm from 2.1 cm. Also, to have a better judgment, with another run, the doubling of the reaction area was combined with a halving of the length of the reactor to maintain a constant residence time in the reactor; both results are separately shown in the above table.

According to the simulation results presented in Table 4-4, one of the main influencing factors is changing the reactor diameter. Increasing the reactor diameter is predicted to increase the removal efficiency markedly since it provides better utilization of the light. With increasing reactor diameter even at constant residence time, with more utilization of the light, the absorption of the reflected light by the UV lamp decreases and the gas inside the reactor receives more energy required for reaction.

Increasing the reactor diameter may have a side impact of mass transfer limitation. One way to investigate that is the calculation of non-st.st diffusion time, which is approximately the ratio of mass transfer thickness squared divided by the gas diffusivity (i.e., time = $(\Delta r)^2/D_i$). If the initial values in Table 4-1 is used, the non-st.st diffusion time returns a value of 3.4 s. With increasing the reactor diameter to 2.694 cm from 2.1 cm, this value was found to be 9.9 s. Both non-st.st diffusion times are much shorter than the gas residence time (26.84 s). Further expansion of the reaction gap (e.g., $R_1$>3.6 cm) is required to exceed the reactor residence time, and mass transfer limitation may be dominated after that point. Hence, under conditions evaluated, mass transfer limitation due to the radius expansion, if any, is largely compensated by absorption effect, as radial expansion the absorption of the reflected light by lamp decreases significantly which causes better utilization of light path and eventually more conversion.

Additionally, premixing ozone (which is known to be an effective technique in wastewater treatment) with the gas stream can be another option to significantly improve the photolysis efficiency. As mentioned before, the UV light at the 253.7 nm line directly breaks reaction products and also breaks ozone into reactive species leading to an increase of the reaction rate and resulting in higher efficiency; which dramatically increases the removal efficiency as shown in the above table.

One of the other noteworthy factors of efficiency enhancement, is the presence of water molecules (relative humidity) in the inlet gas stream. The water content is decomposed to produce hydroxyl (·OH) radicals; the produced OH radicals react with the hydrocarbon and their reaction products which yields a faster and more efficient degradation of the hydrocarbons. The effects of the hydroxyl radical (·OH) and its importance in the oxidation of hydrocarbons in the previous studies are presented in Chapter 2, Section 2.2. Moreover, increasing oxygen content increases the removal efficiency which is probably due to reaction of oxygen radicals to produce OH radicals.

As shown, among the variables in this analysis, changing the absolute temperature changes the removal efficiency to some extent. However, the results are not comparable with other factors such as effect of water vapor, ozone premixing, or diameter expansion, since these efficiencies are obtained when the model was run at constant 300 K, and then was run again at constant 600 K. Although most of the reaction kinetics are temperature dependent, the overall process removal efficiency is not sensitive to the temperature variation, because the process is mainly photon-limited.

Increasing temperature shows also the removal efficiency for methane and ethane increases, while for ethylene the conversion decreases with increasing temperature. The reason can be investigated by comparing the rate constants for the main degradation reaction for each of these hydrocarbons. As discussed, the degradation pathways of these hydrocarbons are initiated by the chemical reactions of each of $CH_4$, $C_2H_6$, and $C_2H_4$ with hydroxyl radicals (·OH), these reactions are MC3 for methane in Table 3-3, EC1 for ethane in Table 3-5, and EyC1 for ethylene in Table 3-7. Calculation of rate constant of these reactions at 300 K leads to have a value of $6.60\times10^{-15}$, $2.56\times10^{-13}$, and $7.73\times10^{-12}$ $cm^3$/molecules·s for MC3, EC1, and EyC1, respectively. Same calculations at 600 K yields the values of $1.27\times10^{-13}$, $1.40\times10^{-12}$, $2.18\times10^{-12}$ $cm^3$/molecules·s for MC3, EC1, and EyC1, respectively. As calculations show, by increasing the absolute temperature, the rate constant for MC3 and EC1 increases, and for EyC1 decreases. This clearly justifies that the increasing removal efficiency by increasing temperature for methane and ethane and decreasing removal efficiency for ethylene.

In addition, minimum effects on removal degradation efficiency of the whole process was observed with changing the velocity profile from laminar to plug flow, indicating that the model results have a minimal dependency on flow regime selection. Moreover, increasing the length of the reactor has the lowest impact on the removal efficiency.

### 4.6 Degradation of Mixed Hydrocarbons

The proposed model is capable of handling more than one hydrocarbon at a time at the reactor inlet. The objective of using this capability is to test the possibility of removing impurities of natural gas without degrading the main component, methane. To test this effect distinguishably,

the model was run at two different cases: one is the mixture of methane, ethane, and ethylene all together; and the other is the degradation of each hydrocarbon in the presence of elevated $NO_x$.

### *4.6.1 Mixture model*

It is assumed that the gas stream is a mixture of methane, ethane, and ethylene diluted with moist air. This gas mixture is introduced to the photoreactor, in the absence of elevated $NO_x$. Four cases were modeled: first, with variable concentration of methane in the absence of ethane and ethylene; second, with a variable concentration of ethane and zero methane and zero ethylene at the reactor entrance; third, with a variable concentration of ethylene and zero methane and zero ethane, and last, with equal inlet concentrations of each of methane, ethane and ethylene (i.e., $C_{CH_4} = C_{C_2H_6} = C_{C_2H_4}$). The last case is called "Mixture model" in Figure 4-11. The results are obtained in accordance with the "comprehensive kinetics", at a constant flow rate of 1 L/min, for all four cases.

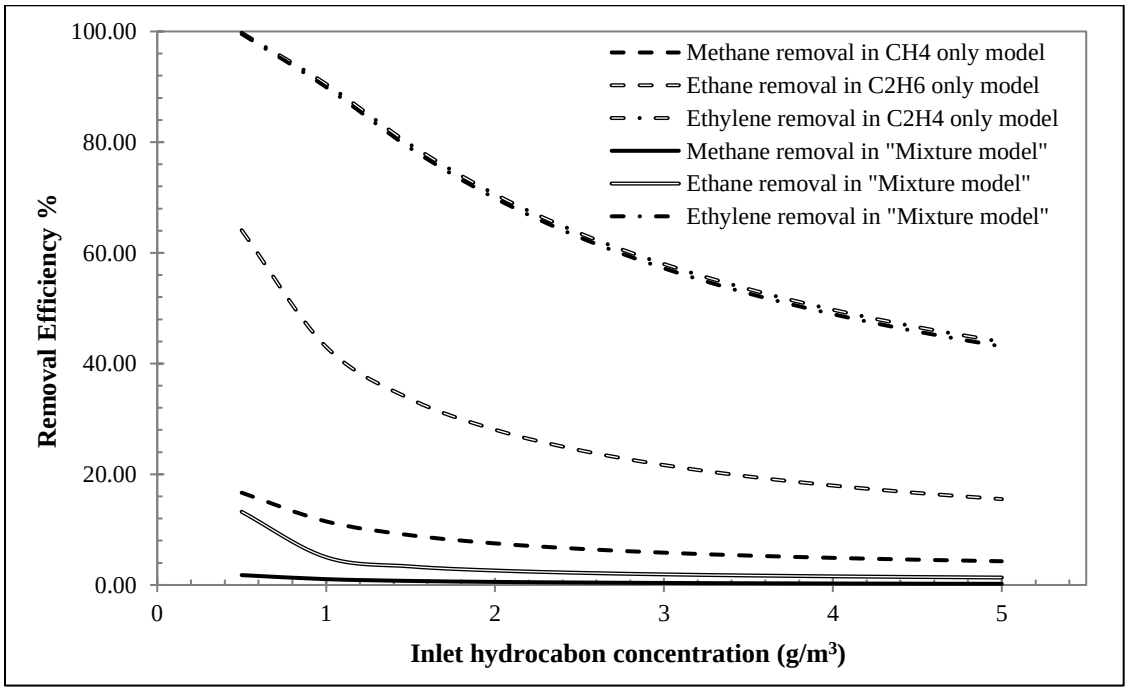


**Figure 4-11: Removal efficiency of methane, ethane, and ethylene as sole pollutants and as a mixture (based on the comprehensive kinetics) (Flow rate 1 L/min)**

Based on the simulation results, as shown in Figure 4-11, the removal efficiency of ethylene in the "Mixture model" is almost the same as sole ethylene model, while the conversion of ethane and methane drastically decreased in case of a mixture of hydrocarbons. It is not surprising that the removal efficiency of ethylene is higher than all other cases due to higher reactivity of ethylene in comparison with methane and ethane. As a promising result, amazingly, when higher hydrocarbon such as ethylene is diluted in the air stream containing methane, the predicted removal efficiency for that hydrocarbon does not change significantly, while methane will be left intact.

In the model of $CH_4$, $C_2H_6$ and $CH_4$+$C_2H_6$ (Asili & De Visscher, 2018), it was shown that methane would meaningfully react less in case of mixture of methane-ethane in air, in comparison with methane-air degradation. Hence, if it is assumed that there is natural gas stream contaminated with the impurities of ethane and ethylene, first ethylene can be removed from the stream, without significant changes in the concentration of methane and ethane, and then the outlet stream of that process can be sent through another photo-dissociation for removing ethane, and inhibiting methane degradation at the end.

### *4.6.2 Degradation of hydrocarbon combined with $NO_x$*

The simulation results are compared for each individual hydrocarbon model, in the absence and in the presence of high concentration of $NO_x$. The cases are defined such that each hydrocarbon is present alone (i.e., zero concentration for the other two), one in the absence of nitrogen monoxide (NO) in the background air, and the other in a rich concentration of NO. The inlet concentration of NO is maintained constant at 0.1 $g/m^3$ (or 96 ppm under the conditions

evaluated), at a constant gas flow rate of 1 L/min. Figure 4-12 shows the comparison of individual models, in the absence and in the presence of $NO_x$.

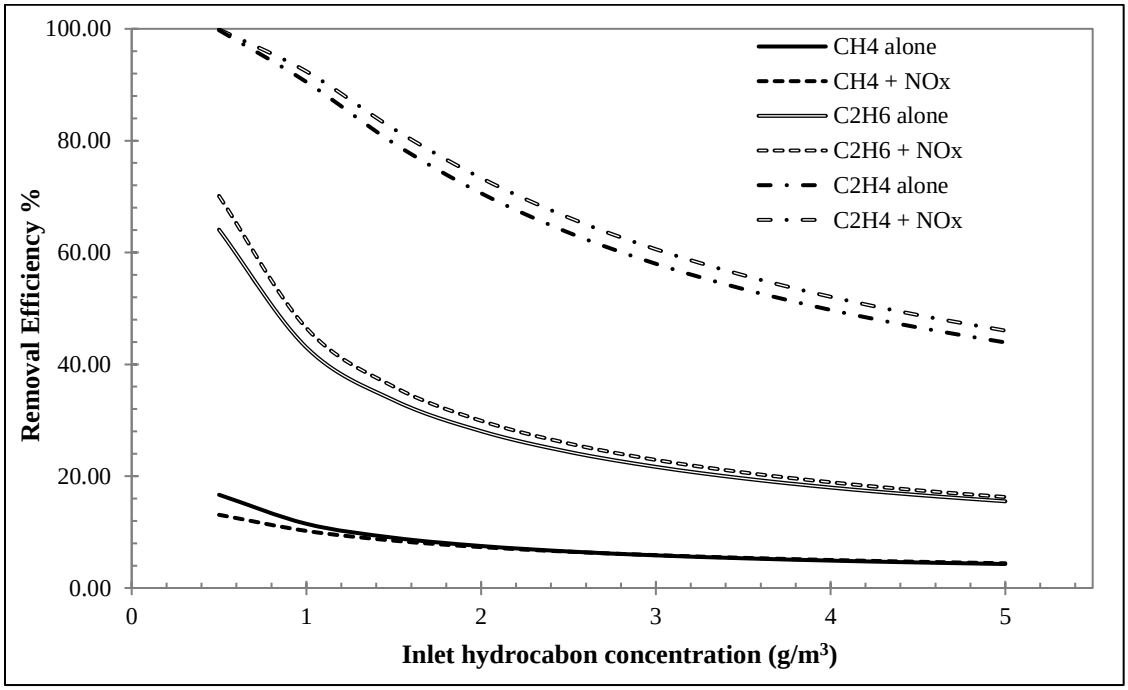


**Figure 4-12: Removal efficiency of individual methane, ethane, and ethylene, in absence and in the presence of $NO_x$ (based on the comprehensive kinetics) (Flow rate 1 L/min)**

The simulation results show a complete conversion (more than 99%) of NO for all cases during the photolysis process of these hydrocarbons. The main conversion products are $NO_2$, $N_2O_5$, and ozone. According to Figure 4-12, the predicted removal efficiencies show a synergism for ethane and ethylene mixed with $NO_x$ to some extent, while addition of elevated NO in the system does not have a noteworthy influence on the predicted removal efficiency for methane. So, it can be concluded that removal of ethylene combined with $NO_x$ is slightly more effective than ethane, and then methane.

### 4.7 Temperature Variation in the Model

As discussed, the UV lamp may have a significant heat loss in the photolysis process, which could cause a temperature variation in the photoreactor. As the research on photolysis in the gas

phase originates from the mature field of aqueous photolysis, where thermal effects are usually negligible, normally the variation of temperature is ignored in gas photolysis. This section addresses some concerns about the effect of temperature variation in the proposed photoreactor. Simulation conditions are consistent with Table 4-1, except that the temperature in the model is not constant any more.

### *4.7.1 Temperature profile*

Figure 4-13 shows the temperature profile of the photoreactor, which has been obtained based on the governing equations showed in Chapter 3, Section 3.2. The temperature profile is shown at the upper and lower limits of the assumed flow rate ranges (e.g., 0.5 and 5.0 L/min, in Table 4-1). As anticipated, the heat dissipation is faster at higher flow rates. Also, once the gas passed through the entrance region, the temperature profile established a radial distribution in the photoreactor.

*flow rate = 0.5 L/min*

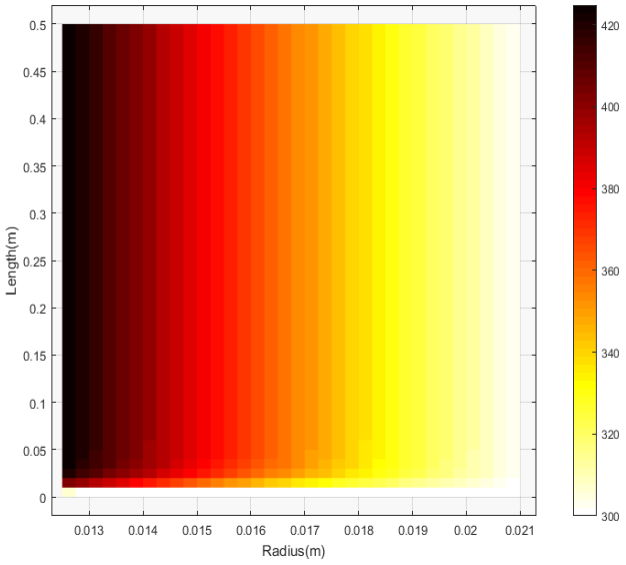


*flow rate = 5.0 L/min*

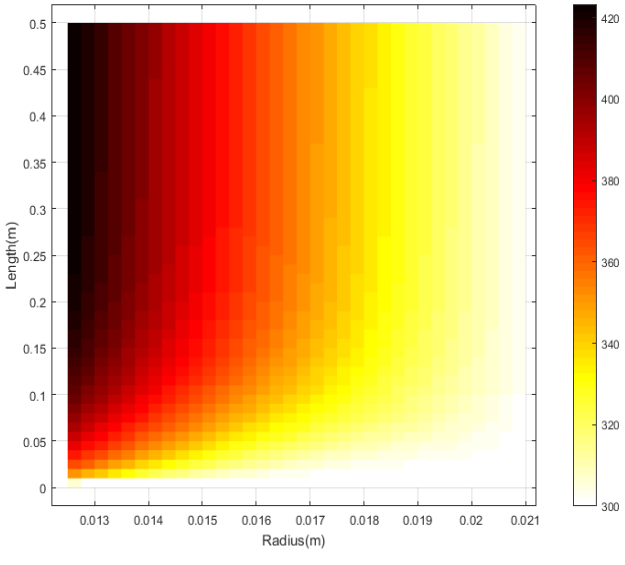


**Figure 4-13: Temperature profile in the reactor (K)**

### *4.7.2 Parameters of degradation – thermal models*

One of the main concerns of variable temperature in the photoreactor is the removal efficiency when non-constant temperature simulation has been carried out. To investigate this effect, the individual models of methane, ethane, and ethylene with the "primary kinetics" models, have been updated to have a variable temperature in each code. As shown before, temperature functionality could affect the reaction rate constants, and diffusivity values when developing the reaction models. The new models, "model-thermal", are the updated version of the previous models (in which all the rate constants and gas diffusivities were calculated at the constant inlet temperature). In the "model-thermal" version of the codes, the temperature values, $T(r,z)$, have been adjusted based on the numerical solution of the new model at each location of the reactor.

Simulation results were compared for each individual model, at the constant temperature and the new models of variable temperature; all in accordance with the "primary kinetics".

#### *4.7.2.1 Methane model*

Figure 4-14 shows the comparison of the removal efficiency of methane, for the two parameters of inlet concentration or gas flow rate. In this figure, the X-axis represents either the variable gas flow rate (while the inlet concentration of methane is constant at 1 $g/m^3$), or the variable inlet concentration of methane (while the gas flow rate is constant at 1 L/min). The model with the constant temperature was covered in the previous section at the constant temperature of 300 K, at any location in the reactor.

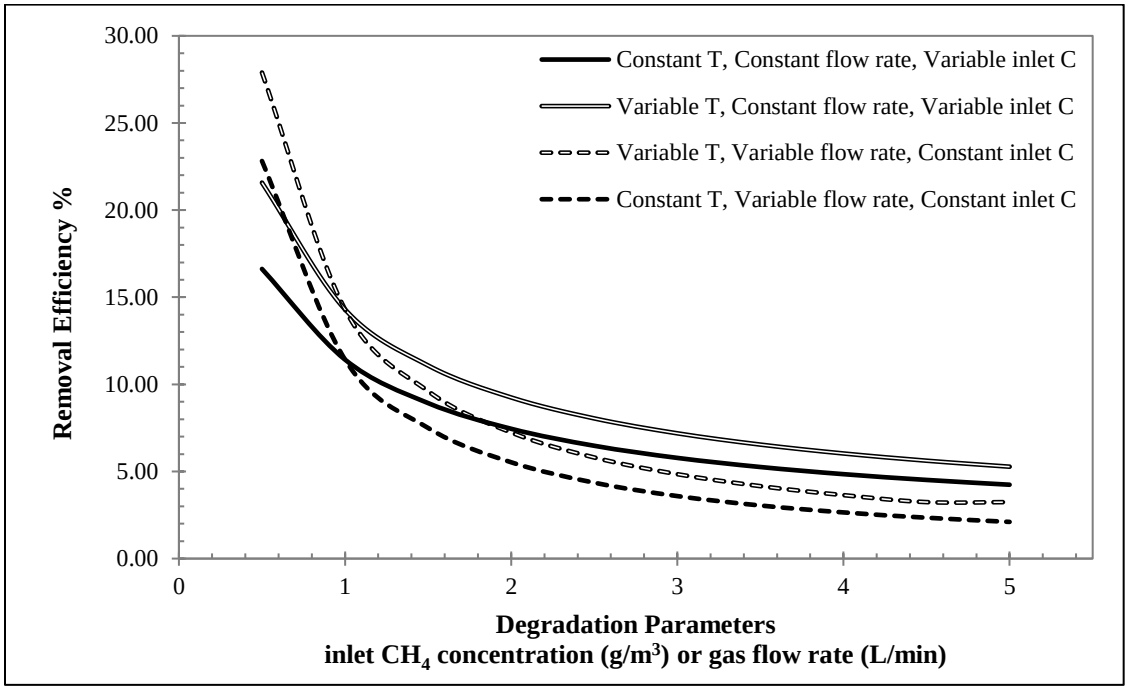


**Figure 4-14: Comparison of the removal efficiency of methane with constant and variable temperature**

As shown, the removal efficiency values for the models with the variable temperature are slightly higher than the model results assuming constant temperature in the photoreactor. However, the differences between the two models, at the same X-axis variable, are noteworthy. In terms of the methane entering the reactor, the methane degradation is 3% less at constant temperature, but the difference between both models is up to 20% in terms of converted $CH_4$. So, it can be concluded that using the variable temperature profile has a small but significant effect on the removal efficiency predictions of methane. In relative terms, the difference between removal efficiency values of constant temperature and variable temperature decreases as the conversion increases.

*4.7.2.2 Ethane model*

Figure 4-15 shows the comparison of the removal efficiency of ethane, for the two parameters of inlet concentration or gas flow rate. In this figure, the X-axis represents either the variable gas

flow rate (while the inlet concentration of ethane is constant at 1 g/m$^3$), or the variable inlet concentration of ethane (while the gas flow rate is constant at 1 L/min). The model with the constant temperature represents the model that is covered in the previous section at the constant temperature of 300 K, at any location in the reactor.

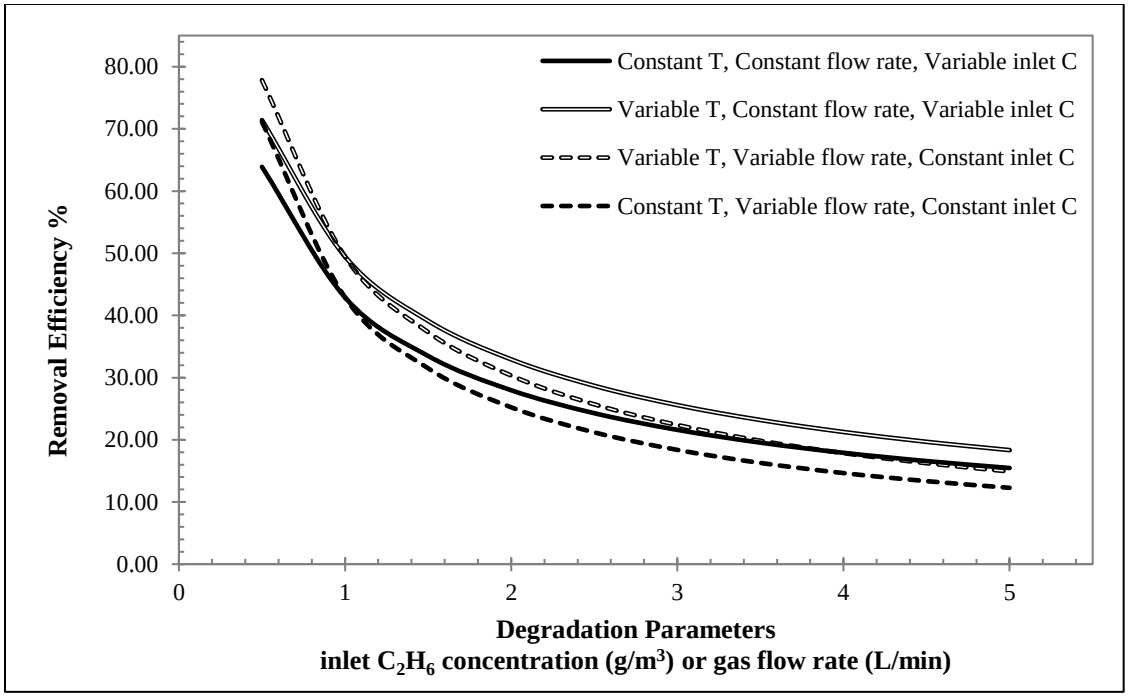


**Figure 4-15: Comparison of the removal efficiency of ethane with constant and variable temperature**

Based on the model results, the removal efficiency values for the models with the variable temperature are slightly higher than the model results assuming constant temperature in the photoreactor. However, the differences between the two models, at the same X-axis variable, are not significant. In terms of the ethane entering the reactor, the ethane degradation is 3% less at constant temperature when the overall efficiency is 15%, but the difference between both models is up to 20% in terms of converted $C_2H_6$; and when the overall degradation efficiency is 70%, the ethane degradation is 6% less at constant temperature, but then again the difference between both models is up to 10% in terms of converted $C_2H_6$.

Hence, it can be concluded that using the variable temperature profile has a small but significant effect on the removal efficiency predictions of ethane. In relative terms, the difference between removal efficiency values of constant temperature and variable temperature decreases as the conversion increases.

*4.7.2.3 Ethylene model*

Figure 4-16 shows the comparison of the removal efficiency of ethylene, for the two parameters of inlet concentration or gas flow rate. In this figure, the X-axis represents either the variable gas flow rate (while the inlet concentration of ethylene is constant at 1 $g/m^3$), or the variable inlet concentration of ethylene (while the gas flow rate is constant at 1 L/min). The model with the constant temperature represents the model that is covered in the previous section at the constant temperature of 300 K, at any location in the reactor.

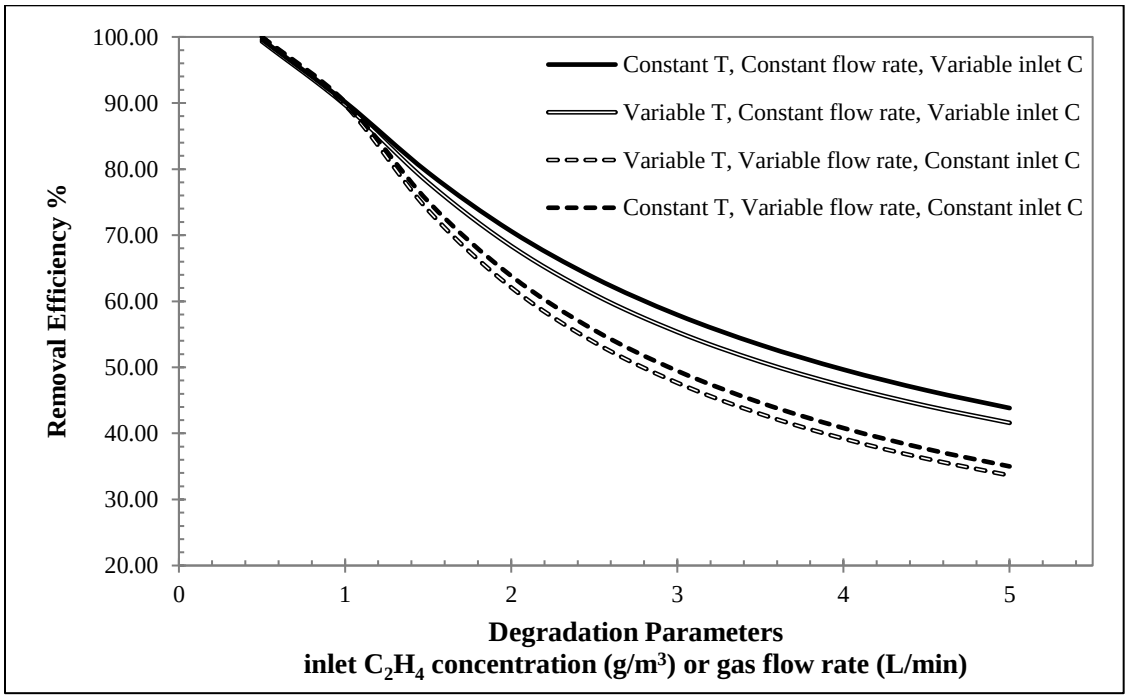


**Figure 4-16: Comparison of the removal efficiency of ethylene with constant and variable temperature**

According to simulation results, at lower inlet concentration of ethylene (e.g., less than 1 $g/m^3$) or at lower flow rate (e.g., less than 1 L/min), the model predicts the same removal efficiency regardless of constant or variable temperature; this might be reflected due to uncertainty of reaction kinetic of ethylene oxidation at lower temperature, as discussed in Section 4.4.3.

As shown, the removal efficiency values for the models with the variable temperature are lower slightly, than the model results assuming constant temperature in the photoreactor. However, the differences between the two models, at the same X-axis variable, are insignificant. In fact, around 2% of ethylene are getting in the reactor are more degraded at constant temperature, but the difference between both models can be around 8% in terms of converted $C_2H_4$. Thus, it can be concluded that using the variable temperature profile does not markedly affect the removal efficiency of ethylene. In relative terms, the difference between removal efficiency values of constant temperature and variable temperature decreases as the conversion increases.

### *4.7.3 Heat of reaction*

Due to the numerous reactions in the proposed model, there might be concern about the production or consumption of the energy in the photoreactor that may cause temperature fluctuation in the system due to heat of reactions. One simple and noncomplex way to look at this effect is to study the system as a black-box heat simulation. In this way, it can be assumed that the photoreactor is black-box, with defined molecules – with known concentration and enthalpy of formation at entrance – as the reactants, and defined molecules – with known concentration and enthalpy of formation at reactor outlet – as the products, for each individual model of methane, ethane, or ethylene. Figure 4-17 shows a schematic diagram of each model for the black-box simulation of heat of reaction.

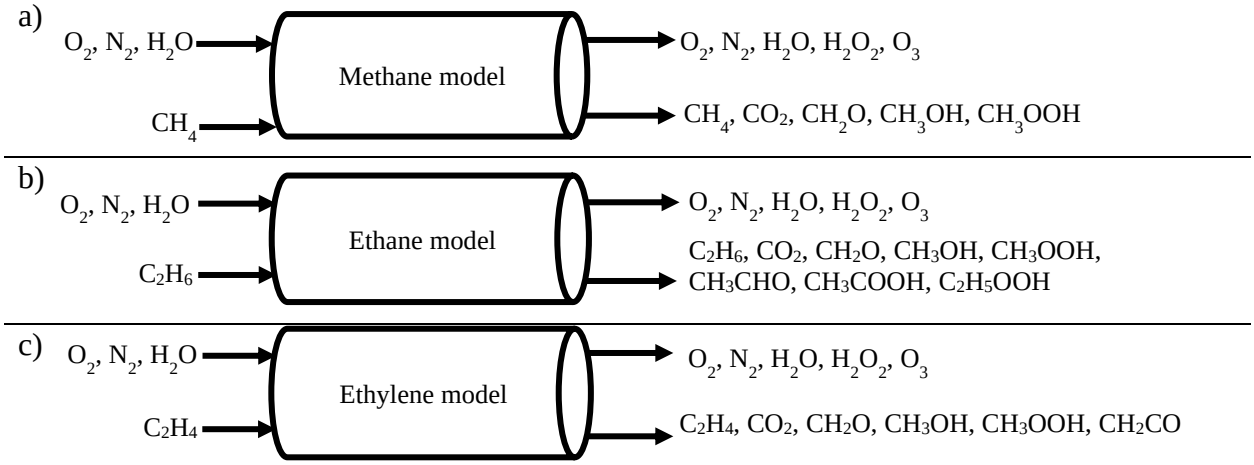


**Figure 4-17: Schematic diagram of black-box heat of reaction, a) $CH_4$ model, b) $C_2H_6$ model, c) $C_2H_4$ model**

The estimated overall heat produced or consumed in that black-box can be calculated as:

$$Q_{\text{overall}} = \dot{v}\left( \sum_{\text{products}} \Delta_f H_j \cdot C_j - \sum_{\text{reactants}} \Delta_f H_i \cdot C_i \right) \tag{4.19}$$

Where $Q_{\text{overall}}$ is the produced or consumed heat in the system (kJ/s), $\dot{v}$ is the overall constant flow rate ($cm^3/s$), $\Delta_f H$ is the standard enthalpy of formation (kJ/molecules, when the original value with unit of kJ/mol divided by Avogadro's number $6.022\times10^{23}$ molecules/mol), and $C$ is the concentration of the reactants or products (molecules/$cm^3$). By assuming a constant flow rate of 1 L/min (equivalent to 16.667 $cm^3/s$), and 1 $g/m^3$ of inlet for methane, ethane, and ethylene in each individual model, and then running the models, with the comprehensive kinetics of non-thermal models, the concentration values for products can be obtained in each model. Conducting the enthalpy of formations at standard conditions for each component leads to a rough estimation of heat of reaction for each model. Table 4-5 shows the summary of calculation for each model using Equation (4.19).

**Table 4-5: Heat of reaction for each model with black-box simulation**

| Model | $Q_{overall}$ (W) | $\rho_{avg}$ (kg/m$^3$) | $C_{p,avg}$ (kJ/kg·K) | $\Delta T$ (K) |
|---|---|---|---|---|
| Methane | -0.084 | 1.137 | 1.081 | 4.12 |
| Ethane | -0.106 | 1.142 | 1.076 | 5.18 |
| Ethylene | -0.188 | 1.141 | 1.074 | 9.22 |

The released energy by heat of reaction calculation for each model shows that the heat production in the system is meaningfully lower than the original heat source of UV lamp heat loss (28.2 W). Moreover, the expected increased temperature in the reactor caused by the heat of reaction, based on an estimation of the average values of gas density ($\rho_{avg}$) and heat capacity ($C_{p,avg}$) , is less than 10 K, which is a strong indication of a low-impact of the heat of reaction. In addition, as shown before, increasing temperature, even by a factor 2, does not play a significant role in the whole process of degradation for each model. Overall, it can be concluded that the heat generation caused by the enthalpy of reaction, does not contribute to the photolysis process. Besides, these calculations evidently justify why the term of heat of reaction can be neglected in the governing heat balance equation (Equation (3.26)) for the temperature variation in the reactor.

### *4.7.4 Conduction dominant regime*

One of the key factors to see the behavior of heat transfer in an annulus space is to calculate Rayleigh number, which is defined as: (Holman, 2010)

$$Ra = \frac{g \cdot \beta \cdot \Delta T \cdot L_c^3}{\nu \cdot \alpha} \tag{4.20}$$

Where $g$ is gravitational force (9.81 m/s$^2$), $\beta$ is the thermal expansion coefficient (=1/$T_{avg}$ for ideal gas, 1/K), $\Delta T$ is the temperature gradient in the system (K), $L_c$ is the characteristic length (m), which is equal to ($D_o$ – $D_i$)/2 for annulus gap distance, $\nu$ is the kinematic viscosity (m$^2$/s),

and $\alpha$ is the thermal diffusivity ($m^2/s$), when all the thermal properties are obtained at the average temperature ($T_{avg}$).

For a horizontal annulus space (like the modeled photoreactor), it was previously shown experimentally and with a fully developed CFD model that if the *Ra* number is small ($Ra < 10^6$), the heat transfer boundary layer is completely laminar, and the chance for forming a convective cycle is fairly small (Desai & Vafai, 1994). As a worst-case scenario, it was assumed that heat transfer is only in the radial direction, and there is no flow in the photoreactor, as the flow in the lateral direction dissipates energy in the reactor and decreases the natural convection effect. If there is no convective cycle under these conditions, there will be no convective cycle in the actual reactor.

To find out the dominant mechanism in annulus space, a parameter called "overall equivalent conductivity", $k_{eq}$, should be calculated. As long as this value is one or close to one, the mechanism of the heat transfer is dominantly by conduction, without formation of convective cycles due to natural convection (Teertstra & Yovanovich, 1998). The calculation of $k_{eq}$ is as follows: (Kuehn & Goldstein, 1976)

$$k_{eq} = \frac{\overline{Nu_i}}{Nu_{i,cond}} \tag{4.21}$$

Where $Nu_{i,cond}$ is the conductive Nusselt number, and $\overline{Nu_i}$ is the overall Nusselt number, which is defined as:

$$\overline{Nu_i} = [(Nu_{i,cond})^{15} + (Nu_{i,conv})^{15}]^{1/15} \tag{4.22}$$

With the following definition of $Nu_{i,cond}$ and $Nu_{i,conv}$ for the conductive and convective Nusselt number, respectively:

$$Nu_{i,cond} = \frac{2}{\ln(\frac{D_{out}}{D_{in}})} \tag{4.23a}$$

$$Nu_{i,conv} = \frac{2}{\ln(\frac{1+2/Nu_i}{1-2/Nu_o})} \tag{4.23b}$$

Derivation of $Nu_i$ and $Nu_o$ for inner and outer surface inside the annulus is often very complex. However, for the particular case of an air-filled annulus, with $Pr$ = 0.7 (Prandtl number, $Pr = \nu/\alpha$), (Teertstra & Yovanovich, 1998) proposed a simplified model based on extensive literature review:

$$\begin{cases} Nu_i = 0.3987\,Ra^{1/4} \\ Nu_o = (39.24 + (\frac{D_{out}}{D_{in}})^{5/4} \cdot Ra^{5/12})^{3/5} \end{cases} \tag{4.24}$$

To calculate the above-discussed variables, first the temperature change in the reactor should be obtained. As properly assumed, the major heat temperature variation in the model is caused by the UV lamp heat loss, which has a value of 28.2 W. Since the calculations are now desired with no flow (worst-case scenario assumption), assuming complete heat conduction in the hollow cylinder, temperature variation can be obtained with the following classical formulation of heat transfer:

$$\frac{q}{L} = \frac{2\pi \cdot k \cdot \Delta T}{\ln(\frac{D_{out}}{D_{in}})} \tag{4.25}$$

Substituting the terms consistent with the values reported in Table 4-1 results in $\Delta T$ = 156 K. Hence, the thermal properties can be obtained at the average temperate ($T_{avg}$ = 378 K). Using the

obtained properties, in Equation (4.20) gives a Rayleigh number of $Ra = 3.08\times10^3$, much less than the minimum value for convective cycling (~$10^6$ as given above). Combining these values, to evaluate the Equations (4.21) – (4.24) yields the overall equivalent conductivity of $k_{eq}$= 1.0045. This calculation adequately indicates that under conditions evaluated, even at the worst-case scenario, the heat transfer in the proposed photoreactor is dominated by absolute conduction without a natural convection. In addition, the evaluated $k_{eq}$ value is in the agreement with the experimental and modeling studies of (Liu et al., 1961), who showed that for a long horizonal cylindrical annulus, if $Ra < 9\times10^3$, the $k_{eq}$ will be one and which means the hollow cylinder is not affected by natural convection effect.

## 4.8 COMSOL Multiphysics® Simulation

In order to visualize the behaviour of the flow inside the reactor, the modeled photoreactor has been simulated with the powerful software COMSOL. The modeling was done on the entire reactive volume of the reactor as the main domain, using a non-isothermal flow scheme, to simulate the flow and thermal effects.

### *4.8.1 Flow simulation*

The flow has been modeled in the photoreactor in two different cases; laminar and turbulent conditions. Assuming laminar conditions amounts to a direct numerical simulation (DNS). It assumes that all turbulence, if any, is captured by the Navier-Stokes equations. When turbulent conditions are assumed, a turbulence model is used to predict the velocity fluctuations, while Reynolds-averaged Navier-Stokes equations simulate the average flow.

*4.8.1.1 Laminar flow*

The laminar flow simulation in the steady state conditions is done on the domain, based on the minimum and maximum assumed gas flow rate of the reactor. Figure 4-18 shows the laminar simulation of the reaction domain at constant gas flow rate of 0.5 L/min. It shows the flow quickly form the fully developed profile, as the Reynolds number and consequently the entrance region is small.

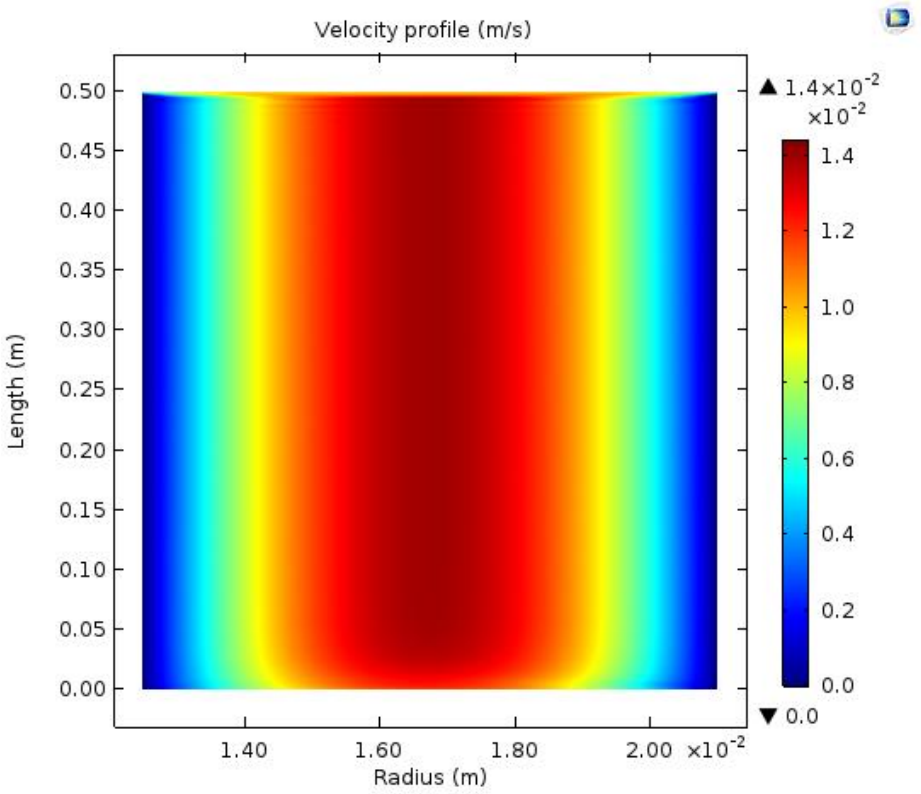


**Figure 4-18: Laminar flow at constant flow rate (0.5 L/min)**

Figure 4-19 shows the laminar simulation of the reactive domain at constant gas flow rate of 5.0 L/min. For both cases, the shape of velocity profile, and maximum velocity, and the entrance lengths are consistent with the analytical calculations. A small entrance effect is observed at the low flow rate (~2 cm). The entrance region is more pronounced (<15 cm) at the high flow rate.

In both cases the deviation from fully developed flow in the entrance region is small (see below for details).

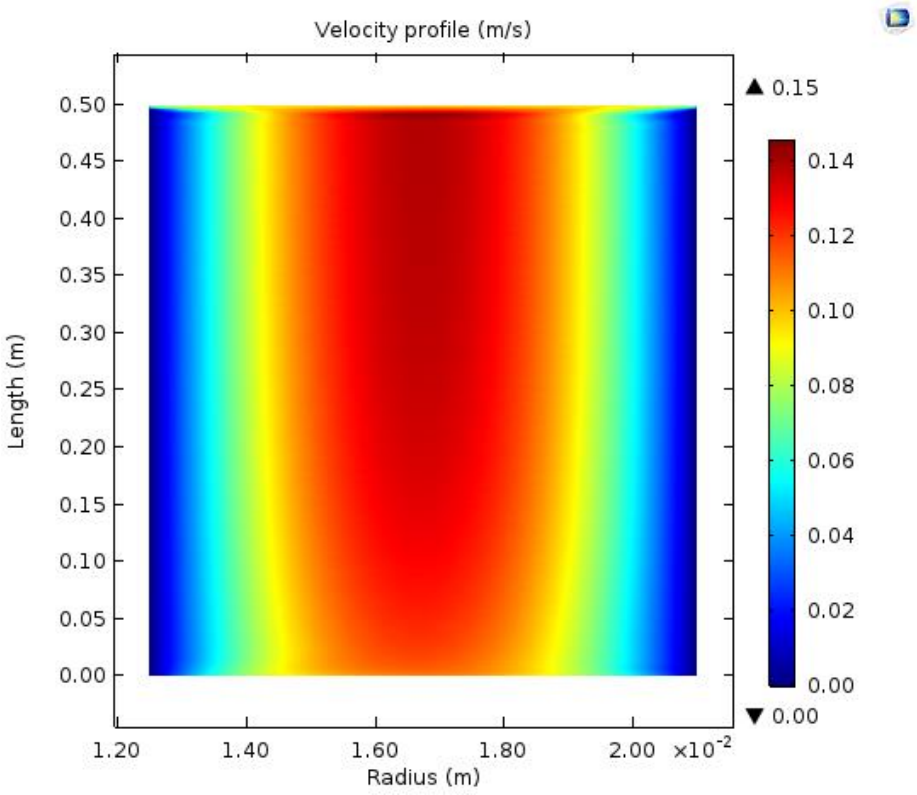


**Figure 4-19: Laminar flow at constant flow rate (5.0 L/min)**

*4.8.1.2 Turbulent flow*

For turbulent flow simulations, as discussed before, based on the geometry and the values of the model, Low-Reynolds *k-ε* (LRKE) was assumed properly as the main scheme of the simulation in the RANS turbulent model. Figure 4-20 shows the turbulent simulation of the reactive domain at constant gas flow rate of 0.5 L/min. It shows that the flow quickly forms the fully developed profile, as it passes through the small entrance region due to lower flow rate and consequently lower Reynolds number.

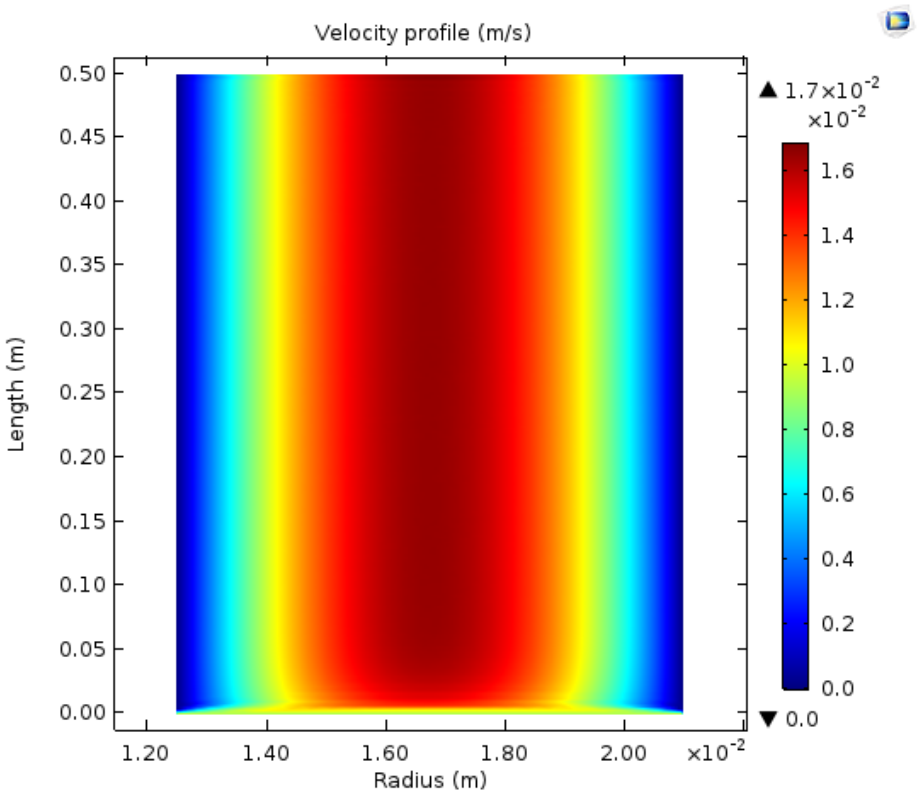


**Figure 4-20: Turbulent (LRKE) flow simulation at constant flow rate (0.5 L/min)**

Figure 4-21 shows the LRKE simulation of the reactive domain at constant gas flow rate of 5.0 L/min. The velocity profile in these cases are very similar to the laminar simulation. The flow will form a uniform parabolic flow, except the fact that in the LRKE model, the predicted velocity values are slightly different (<1% of the maximum velocity) from the laminar model. For the entrance lengths, the values are smaller than the laminar and analytical model.

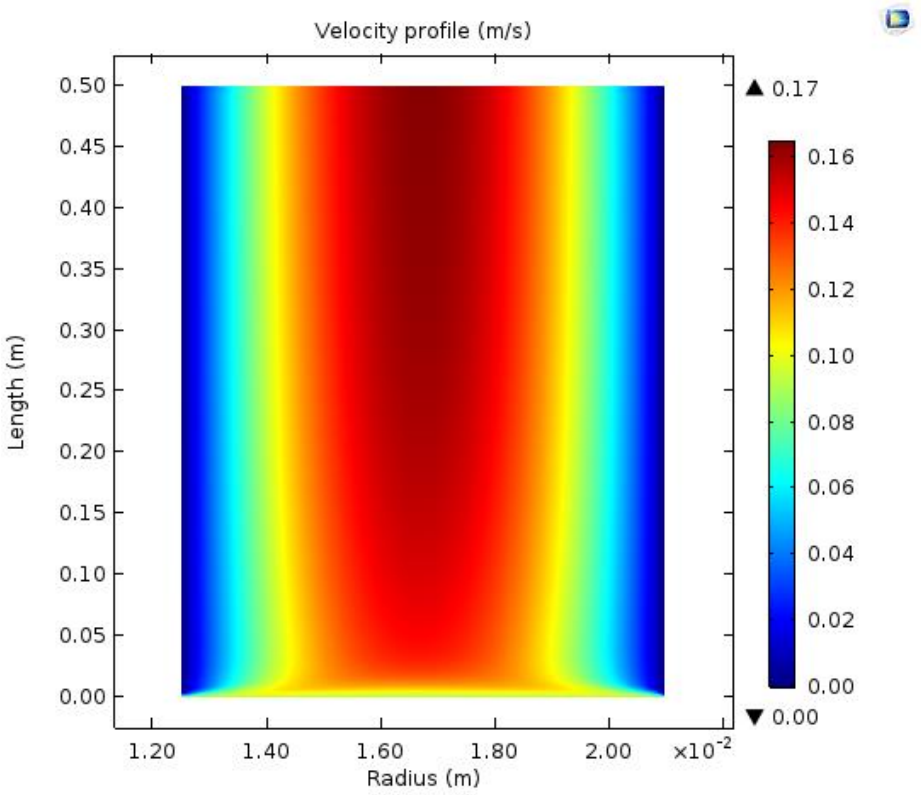


**Figure 4-21: Turbulent (LRKE) flow simulation at constant flow rate (5.0 L/min)**

- ***Comparison of Turbulent and Molecular Diffusivity***

One of the ways to measure the amount of turbulence in a turbulent flow is to calculate the turbulent diffusivity, $K_t$, with the following equations at the low Reynolds numbers: (Jones & Launder, 1972)

$$K_t = C_\mu \cdot f_\mu \cdot \frac{k^2}{\varepsilon} \tag{4.26}$$

Where $K_t$ is the turbulent diffusivity ($m^2/s$), $k$ is the turbulent kinetic energy ($m^2/s^2$), $\varepsilon$ is the turbulent dissipation rate of kinetic energy ($m^2/s^3$), and $C_\mu$ is the empirical dimensionless constant (0.09), and $f_\mu$ is the empirical function for the turbulence Reynolds number, which can be calculated as: (Jones & Launder, 1972)

$$f_\mu = \exp\left(-\frac{2.5}{1+\frac{Re}{50}}\right) \tag{4.27}$$

Considering the worst-case scenario (i.e., the maximum of turbulent kinetic dissipation rate) will happen at the highest flow rate in the model (e.g., Q = 5 L/min), the values for $k$ and $\varepsilon$ are obtained $3.25\times10^{-5}$ $m^2/s^2$, and $7.76\times10^{-3}$ $m^2/s^3$, respectively, according to the flow simulation in COMSOL. Also, considering the same situation, calculation of $f_\mu$ will result in the value of 0.446. The whole calculation of turbulent diffusivity results in the value of $K_t = 5.48\times10^{-9}$ $m^2/s$.

On the other hand, the average value of the molecular diffusivity in the model has the value of $D_{Air\text{-}Species} = 1.91\times10^{-5}$ $m^2/s$. Comparison of these two values, ($D_{AB}$ and $K_t$) shows that the turbulent diffusivity in the model is at least 4 orders of magnitude smaller than the molecular diffusivity in the model, hence it can be concluded that the model is effectively diffusion-controlled rather than turbulent-controlled. This evidently justifies the assumption of the models that the mechanical dispersion is negligible in the model.

- ***Calculation of Length Microscale***

Another way to show the accuracy of the simulation in turbulent regime is to calculate the Kolmogorov length microscale. It is a measure of the size of the smallest turbulent structures in a flow field. This value is calculated by: (De Visscher, 2013)

$$\eta = \left(\frac{\nu^3}{\varepsilon}\right)^{1/4} \tag{4.28}$$

Where $\eta$ is the Kolmogorov length microscale (m), $\nu$ is the kinematic viscosity ($m^2/s$), and $\varepsilon$ is the turbulent dissipation rate of kinetic energy ($m^2/s^3$). Considering the worst-case scenario (i.e.,

the same as the previous section at highest flow rate, e.g., Q = 5 L/min), the $\varepsilon$ was found to be $7.76\times10^{-3}$ $m^2/s^3$, and average value of $\nu$ was obtained $1.07\times10^{-5}$ $m^2/s$, according to the flow simulation in COMSOL. Using these numbers, the calculation of Kolmogorov length microscale ($\eta$) gives a value of $6.32\times10^{-4}$ m, which is greater than the largest element size ($3.82\times10^{-4}$ m) in the simulation. This indicates that any turbulence has been covered in the defined grid spacing in the domain.

- ***Comparison of The Velocity Profiles***

The velocity profile of air in the model has been compared at two different regions: the fully developed flow region and the entrance length region, with three different modeling approaches: one with the theoretical laminar flow assumption and using the Equation (3.5) for the gas velocity, one with the laminar flow assumption and simulation with COMSOL, and other one with the turbulent flow assumption and simulation with COMSOL. Figure 4-22 shows the comparison of the velocity profiles in the fully developed region in the reactor, at the same flow rate of 1L/min for all cases.

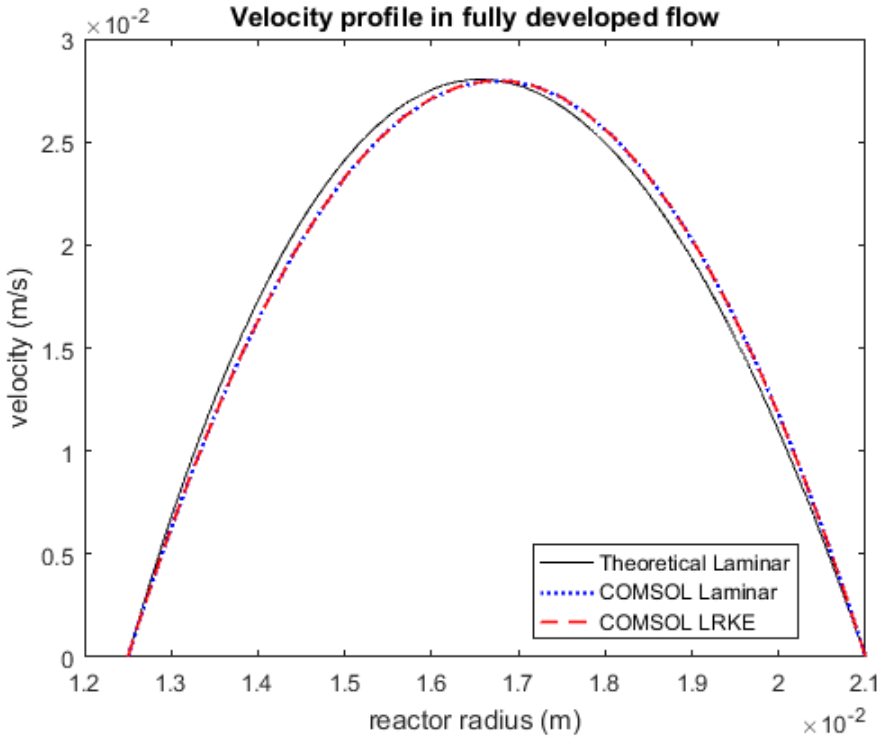


**Figure 4-22: Velocity profiles of the model in the fully developed region with three different calculations**

The comparison clearly shows that the velocity profile is nearly the same in all three approaches. The slight difference in the laminar cases arise from the variation of the temperature in the reaction area on the case of COMSOL simulation (dotted line), which can affect the viscosity of the fluid in the model which leads to a deviation of velocity from the theoretical values (solid line). The velocity values in the turbulent simulation deviate to some extent in comparison with the laminar calculations (possibly due to variation of kinematic viscosity), but nevertheless these differences are negligible, and specially the shape of the profile will evidently prove that using a laminar velocity calculation in the model is a sensible assumption.

Likewise, Figure 4-23 shows the comparison of the velocity profiles in the entrance length region in the reactor (at 1 cm from the inlet, where the entrance length is 2 cm), at the same flow rate of 1 L/min for all cases.

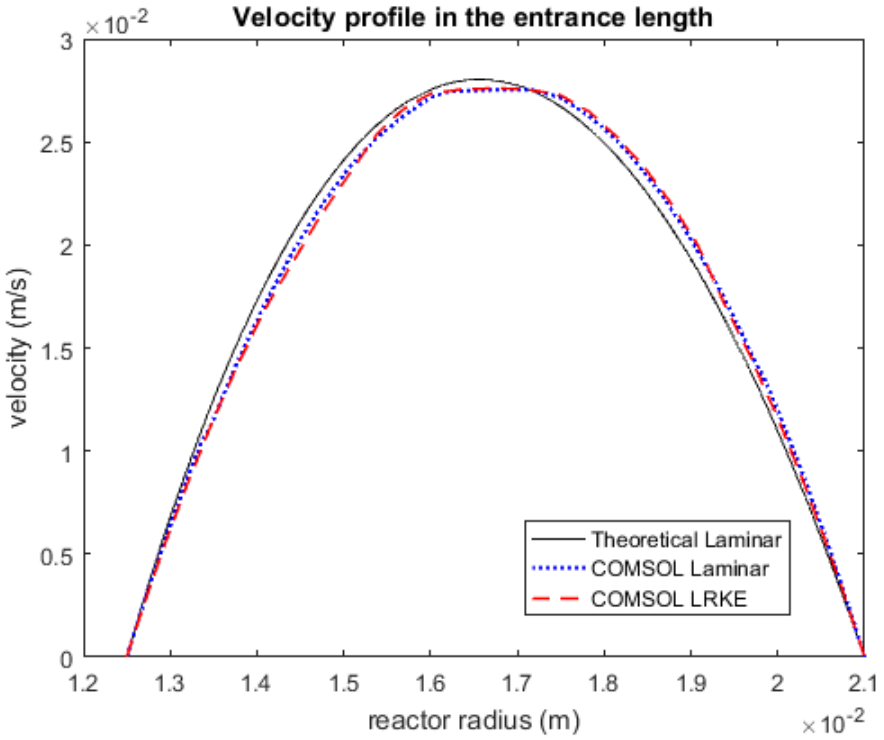


**Figure 4-23: Velocity profiles of the model in the entrance length region with three different calculations**

Comparison of velocity profiles shows that the flow is forming a laminar-type velocity profile even in the entrance region. Although the values of velocity for the turbulent simulation are somewhat higher than the laminar simulation, both simulated velocities are in close agreement with the theoretical velocity calculations. Hence, it can be concluded that the hypothesis of establishing a fully developed flow once after entering the reactor is a practical assumption.

### *4.8.2 Temperature simulation*

As discussed, a considerable amount of energy is lost from the UV lamp which can affect the gas passing through the reaction area. The software solves simultaneously the heat transfer in the annulus space, in accordance with the type of flow. Whereas, the temperature simulation in Section 4.7.1 was based on the governing equations shown in Chapter 3, Section 3.2, the results presented in this section were obtained with the CFD simulation in COMSOL.

*4.8.2.1 Temperature profile in laminar flow simulation*

Figure 4-24 shows the temperature profile of the reactor, when the flow simulated with the laminar assumption. The temperature profile was obtained in the limits of assumed flow rates (e.g., 0.5 and 5.0 L/min, in accordance with Table 4-1).

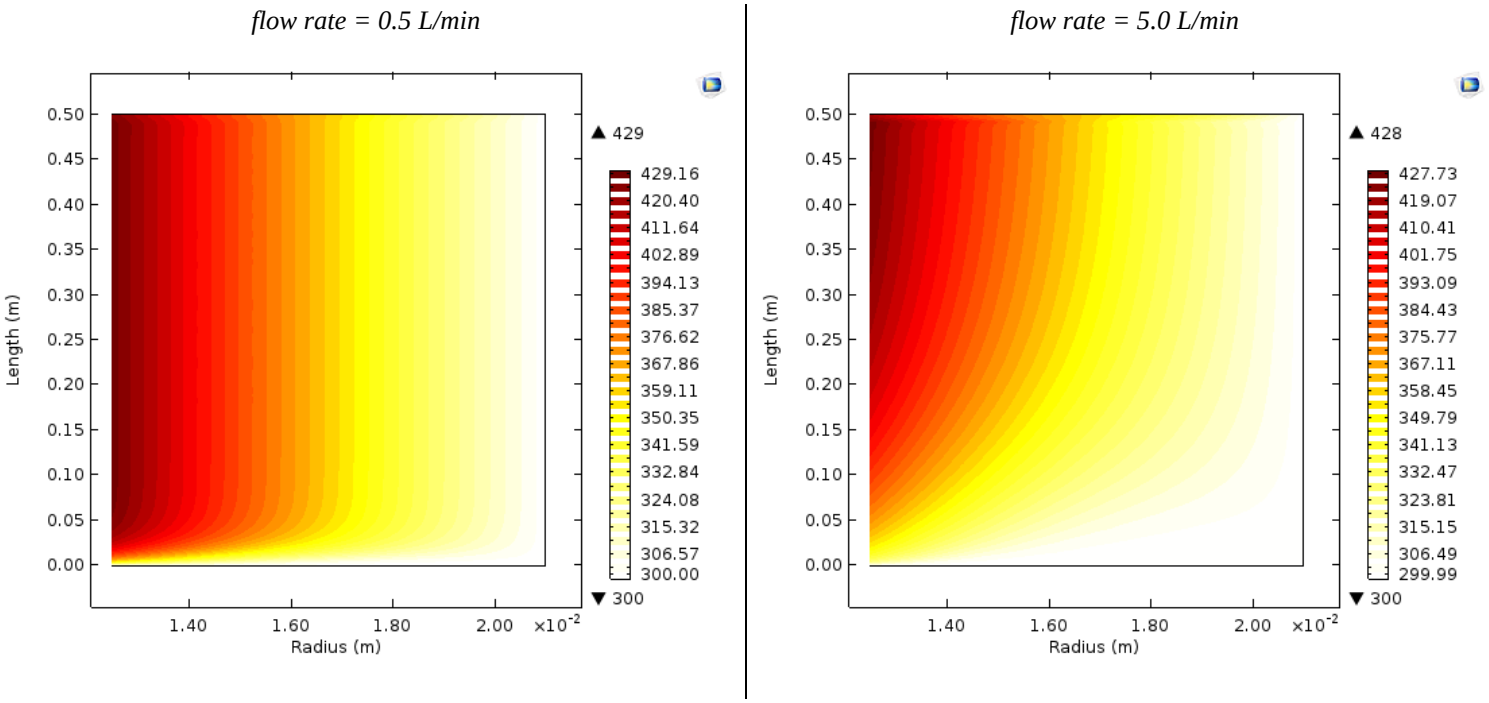


**Figure 4-24: Temperature profile in the reactor with laminar simulation (K)**

The temperature profile for the laminar simulation with software is in a good agreement with the temperature profile for laminar model showed in Figure 4-13 (Section 4.7.1); expect the fact that the predicted temperate values near the UV lamps are slightly higher in the COMSOL simulation, which is probably due to the selection of higher resolution and more accurate solver. Slight differences in the calculation of the heat capacity and thermal conductivity of air as a function of temperature may also be responsible for a slight difference in temperature profile. As shown, the temperature profile develops a more pronounced radial distribution as the heat transfer mechanism shifts from predominantly axial convection (high flow rate or near inlet) to predominantly radial conduction (low flow rate or far from inlet). Moreover, it is clear from the

simulation results that the temperature variations in the reactor is independent of the flow rate, once the temperature profile is fully developed (no axial convection). The flow rate mainly determines how quickly the full temperature profile is developed.

#### *4.8.2.2 Temperature profile in turbulent flow simulation*

Figure 4-25 shows the temperature profile of the reactor, when the flow is simulated with the turbulent assumption. The temperature profile was obtained in the limits of assumed flow rates (e.g., 0.5 and 5.0 L/min, in accordance with Table 4-1).

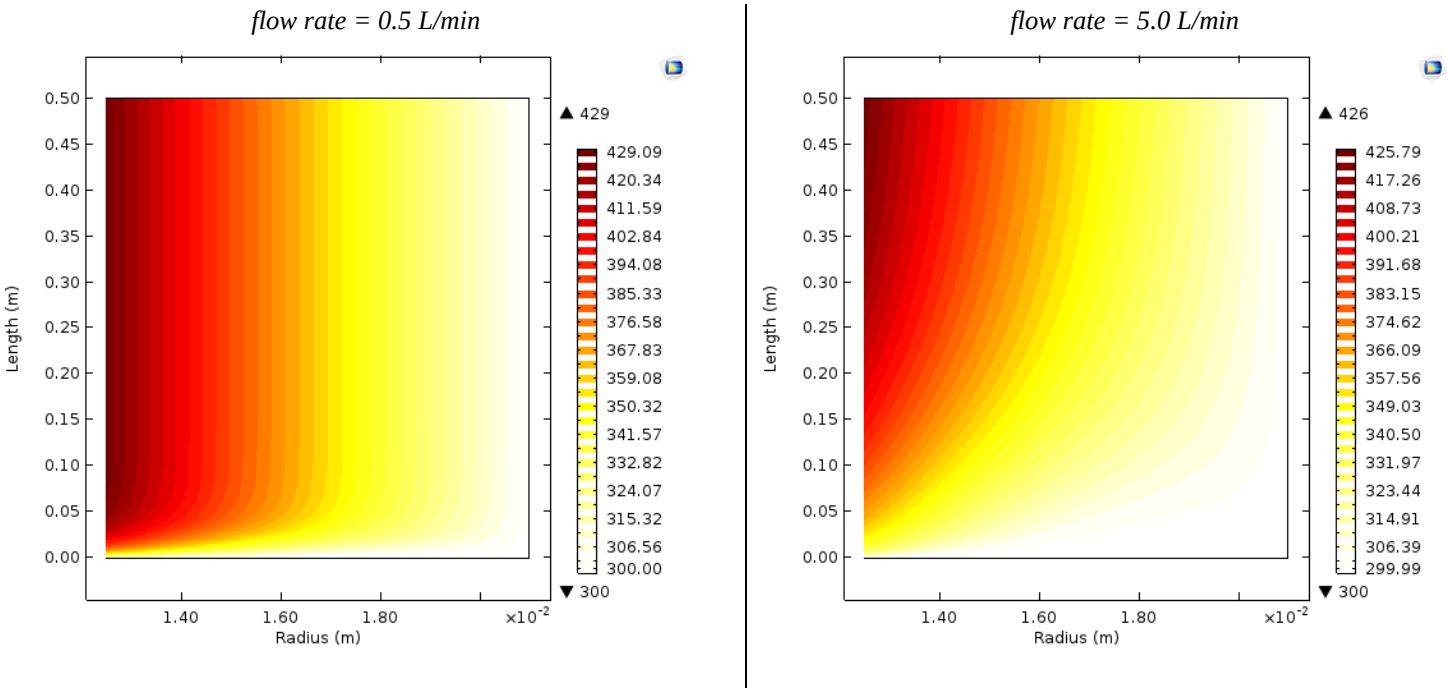


**Figure 4-25: Temperature profile in the reactor with turbulent simulation (K)**

Similar to the laminar cases, for turbulent simulation as well, the temperature profile is developing a pronounced radial distribution as the heat transfer mechanism shifts from predominantly axial convection to predominantly radial conduction. However, for the higher flowrate, the heat loss in the reactor will be dissipated faster which causes slightly lower temperature in comparison with the same case in laminar simulation.

All over, with comparison of the temperature values in the reactor for all cases, it can be concluded that the type of flow model (laminar or turbulent) does not have a significant influence on the temperature variation, and hence the model results are independent of selection of flow type.

### *4.8.3 Three-Dimensional model simulation*

The simulation of the reactor has been carried out in a full three-dimensional model in COMSOL. The purpose of the 3D simulation is to verify the conclusion made earlier that there is no convective cycling occurring in the reactor. For this particular purpose, the normal meshing was selected with 358,008 3D elements (comparing with 7,040 normal meshing elements in 2D simulation). The element sizes are varied between $2.77\times10^{-9}$ $m^3$ and $3.08\times10^{-8}$ $m^3$ based on the location of elements in the mesh. Figure 4-26 Shows the meshing of the reactor in the 3D simulation. It will be shown that the velocity and temperature values are exactly the same as for the 2D simulation; except the fact that the 3D simulation is highly expensive in time.

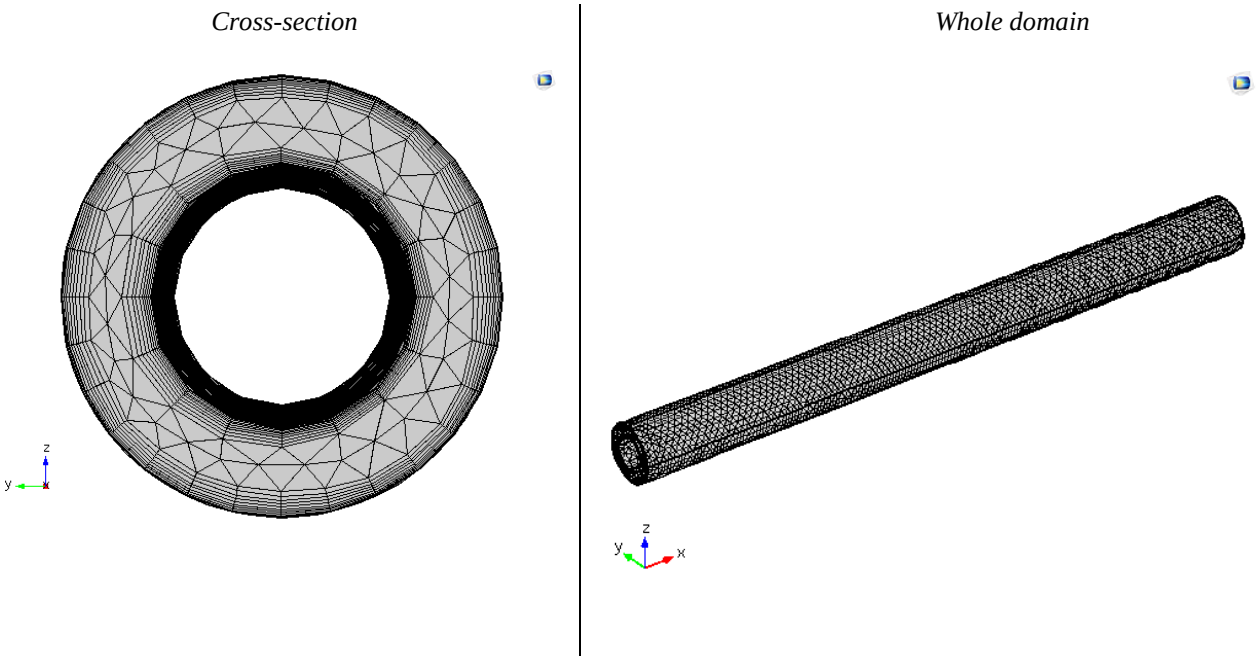


**Figure 4-26: Meshing pattern in 3D simulation**

The model was run in the two different cases of laminar and turbulent regime, to be consistent with the previous results.

*4.8.3.1 Flow simulation*

Figure 4-27 shows the comparison of the flow simulation for the two cases of laminar and turbulent (LRKE) at constant flow rate of 1 L/min. The results are shown both in the cross-sectional area and lateral direction (horizontal annulus reactor).

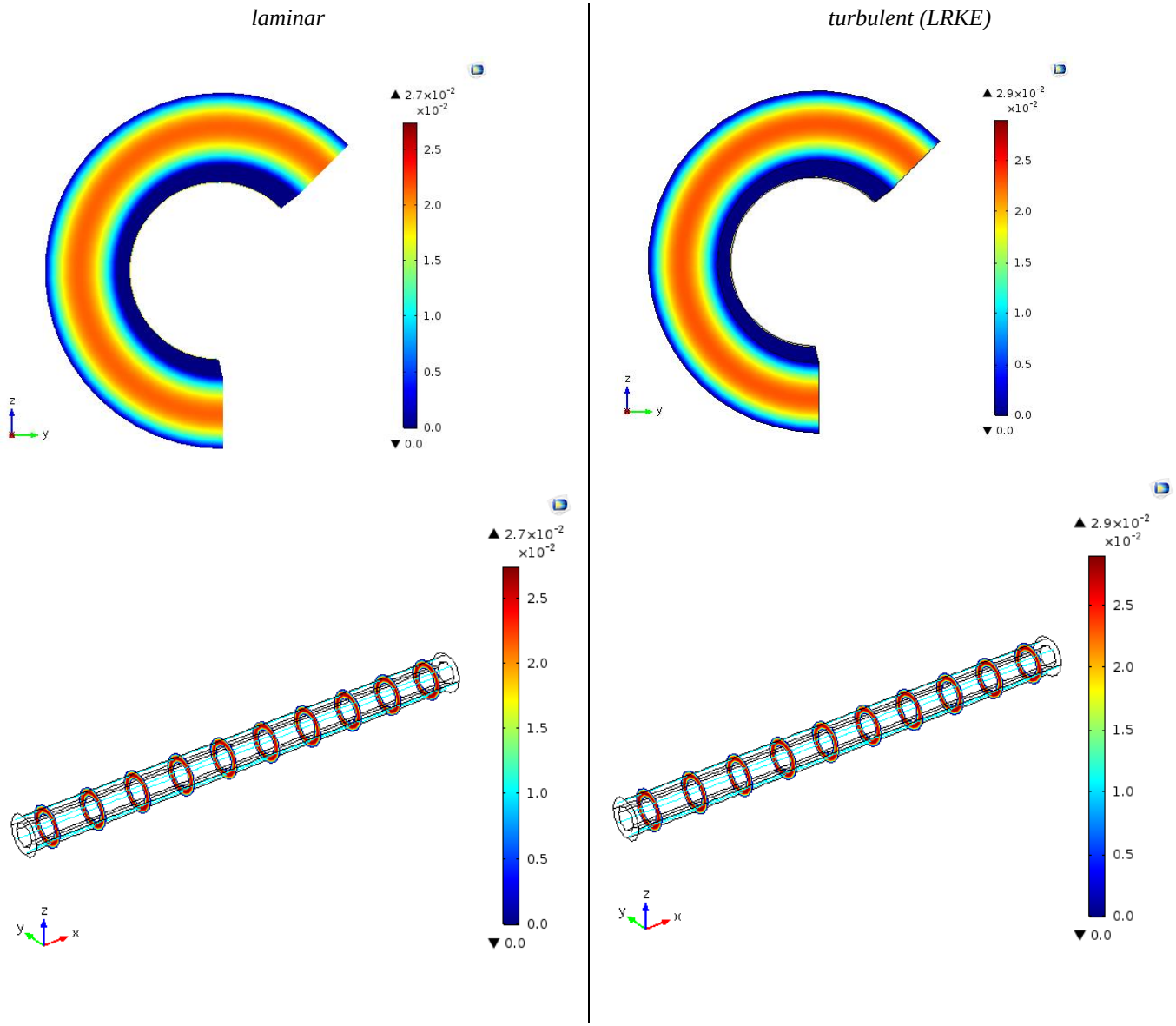


**Figure 4-27: 3D flow simulation for laminar and turbulent model**

The velocity values are calculated in the whole domain, and presented in the cross-sectional slices. Also, velocity streamlines are plotted (green lines) confirming that the velocity profile is completely forming in the horizontal direction (i.e., X direction in the above figure). Here again, similar to the 2D simulation, the velocity values for turbulent (LRKE) model are slightly different from the laminar model.

- ***Evaluating the Results of the Turbulent Model***

After solving the flow simulation in 3D, the wall resolution should be checked in order to verify the accuracy of the solution, and of course the meshing pattern. This plot is generated by COMSOL when a turbulent model is simulated. According to the COMSOL user guide (Multiphysics, 2016), for low Reynolds numbers, and with the two-equation turbulent model (e.g., $k$-$\varepsilon$), the value of dimensionless distance to cell center (which has a similar definition to $y^+$ in algebraic CFD equations, where $y^+=y\cdot u^*/\nu$, with $u^*$ is friction velocity and $\nu$ is kinematic viscosity) should be less than 0.5. Figure 4-28 shows this value in the modeled domain. As shown, this parameter has a value of less than 0.5 in the entire domain, which indicates that the meshing pattern is correct, and the simulation results are accurate. With this confirmation, the accuracy of the solution is now established, and it can be concluded that the results in 2D simulations are now verified.

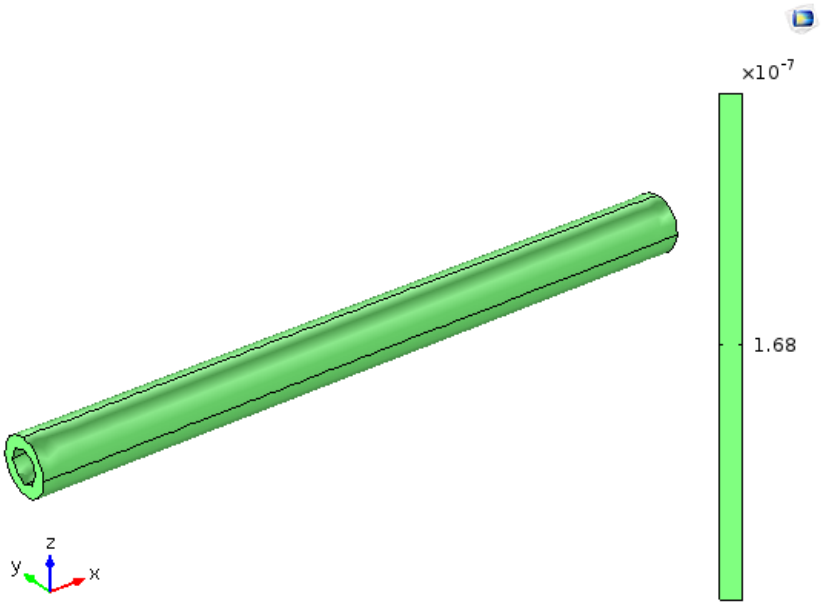


**Figure 4-28: Dimensionless distance to cell center**

*4.8.3.2 Temperature profile*

Figure 4-29 shows the comparison of the temperature profile for the two cases of laminar and turbulent (LRKE) at constant flow rate of 1 L/min. The results are shown both in the cross-sectional area and lateral direction (horizontal annulus reactor).

*laminar*

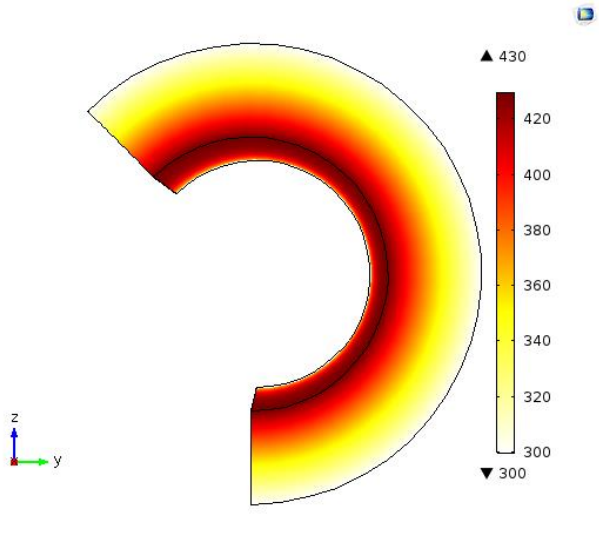


*turbulent (LRKE)*

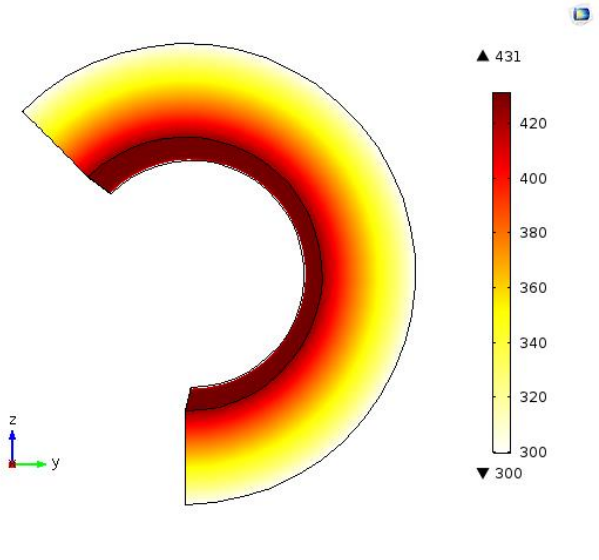

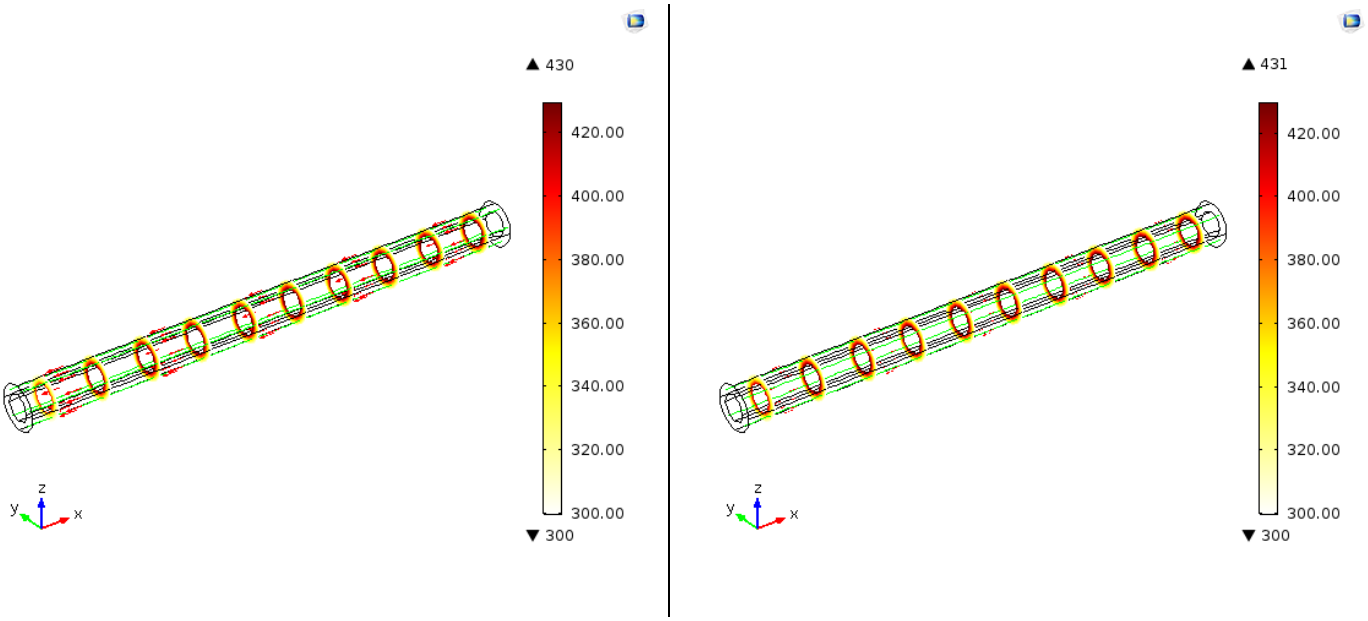


**Figure 4-29: 3D temperature profile simulation for laminar and turbulent model**

The temperature values are calculated in the whole domain, and presented in the cross-sectional slices. Also, the convective heat flux (red arrows) confirming that the convective heat flux is transferring completely in the flow direction and there is no cycle or dissipation in other directions happening. Yet again, similar to 2D simulation, the temperature values for turbulent (LRKE) model are negligibly higher than the laminar model.

### *4.8.4 Non-Steady State 2D simulation*

The modeled reactor has been simulated with a non-stationary solver to see the behaviour of the flow and temperature inside the reactor in a 2D domain. According to the simulation results, it takes about 2 minutes to establish a steady-state condition. However, in the previous experimental set up with the same modeled reactor (Atyabi, 2013; De Visscher et al., 2010; Mahmoudkhani et al., 2016), there was always about 2-hour wait to make sure that the steady-state had been established.

The conservative wait time of two hours was assumed for some important reasons. First, the UV lamp should be heated up completely to create a steady-state temperature at the surface of the lamp. Second, when there was a VOC introduced to the reactor working with complete air stream with a high concentration value, there was some condensation on the lamp surface occurring due to polymerization of the VOCs, which covered the effective UV surface and caused lower removal efficiency. So, in order to use the maximum benefit of the lamp irradiation, the wait should be long enough to make sure that those condensation and/or polymerizations on the lamp surface were evaporated as the lamp heats up. However, for low concentration values of VOCs, it was confirmed that the steady state was established very quickly, which is confirmed in this simulation as well. Overall, if there is a low concentration of the pollutant mixed with air reacting in the photoreactor, fast formation of steady-state temperature and velocity is predicable, while for high concentration of pollutants steady state conditions require significant wait time.

- ***Flow Simulation***

Figure 4-30 shows the velocity profiles for the two cases of laminar and turbulent model (LRKE) at constant flow rate of 1 L/min. The results are shown at two different times of two seconds ($t$ = 2 s) and two minutes ($t$ = 120 s) when the steady-state conditions are completely established.

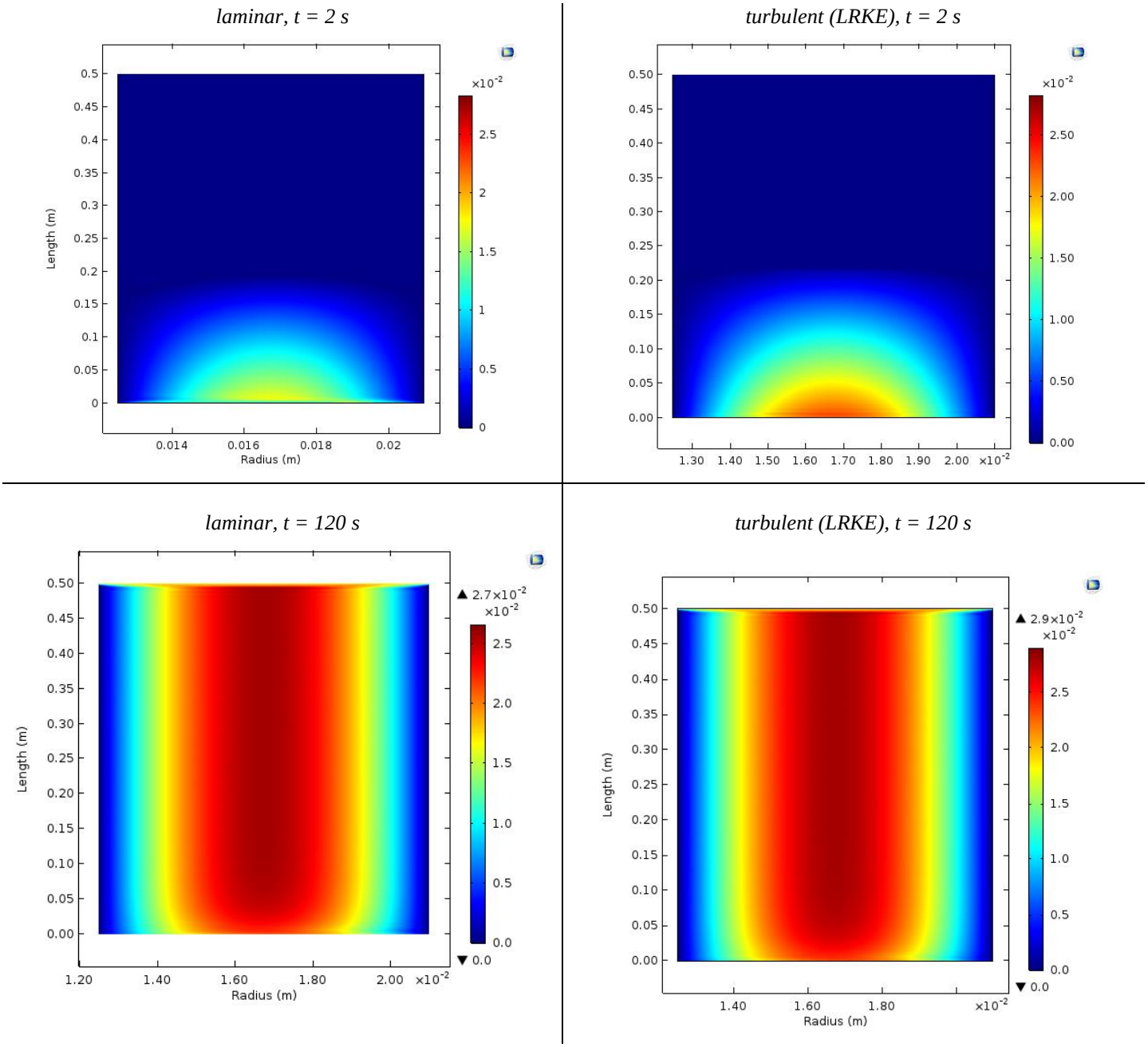


**Figure 4-30: Velocity profile of non-steady state flow simulation after 2 and 120 seconds**

- ***Temperature Profile***

Figure 4-31 shows the of the temperature profile for the two cases of laminar and turbulent (LRKE) at constant flow rate of 1 L/min. The results are shown at two different times of two seconds ($t$ = 2 s) and two minutes ($t$ = 120 s) when the steady-state conditions are completely established.

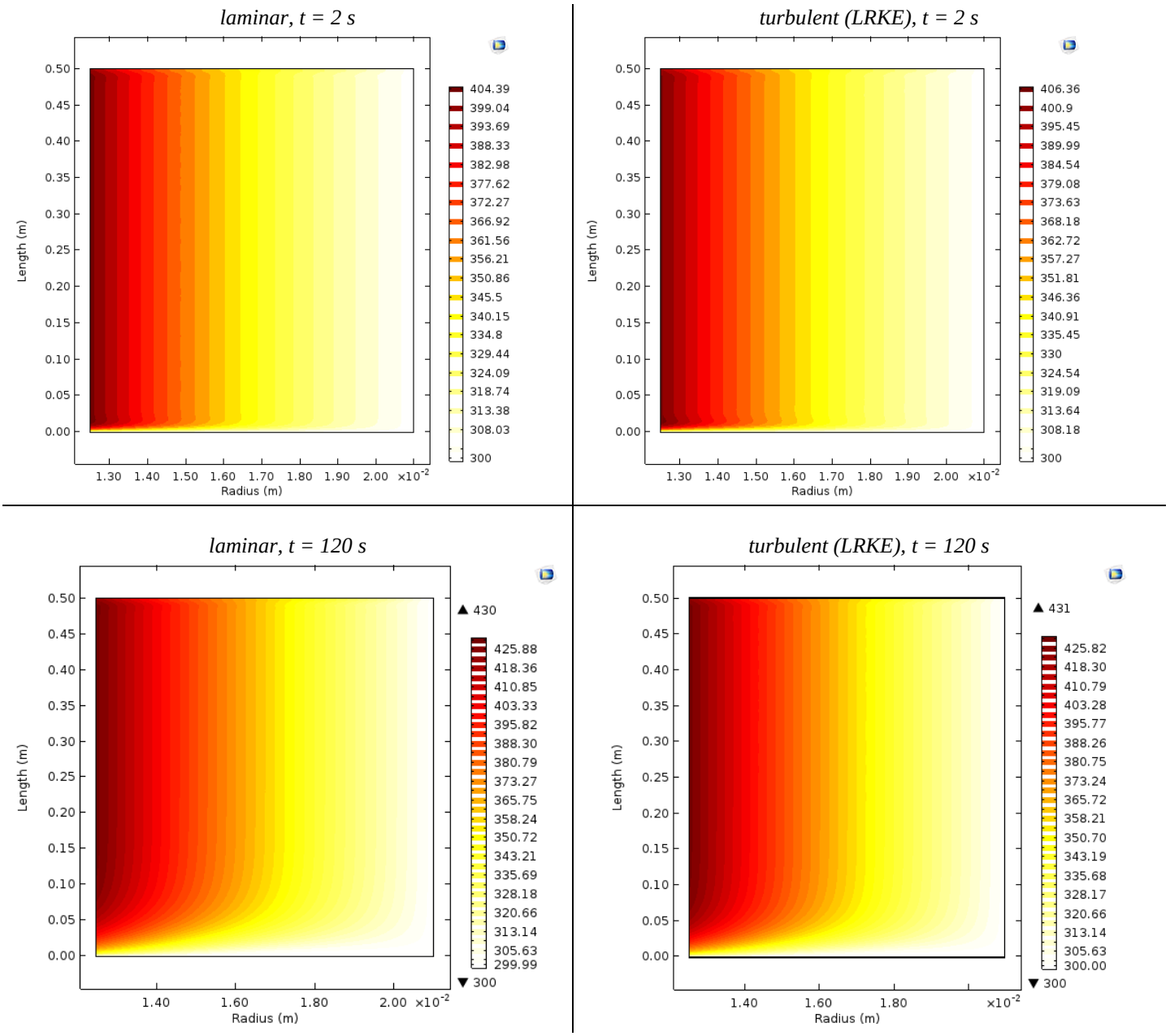


**Figure 4-31: Non-steady state temperature profile after 2 and 120 seconds**

## 4.9 Software Development

One of the importance of any model can be transferability of that model to an interface so that everyone may get the benefit of using that model. The codes of the different models discussed in this research, for a gas phase photoreactor, were compiled to a software package to enable the use by any user that has some interest in this research area.

The software is now called "*PhotoSim*" and the version is 1.4, which includes methane, ethane, and ethylene reactions. *PhotoSim* was prepared with the "primary kinetic" reactions to maintain both fast run-time and the results with minimum deviation of the "comprehensive kinetics". The program is written in the MATLAB® deployment tools and can be run on any platform of Windows or iOS, as an executable file (e.g., PhotoSim.exe). Once the user installs *PhotoSim* on the computer, by running it, a new window will appear such as the following figure.

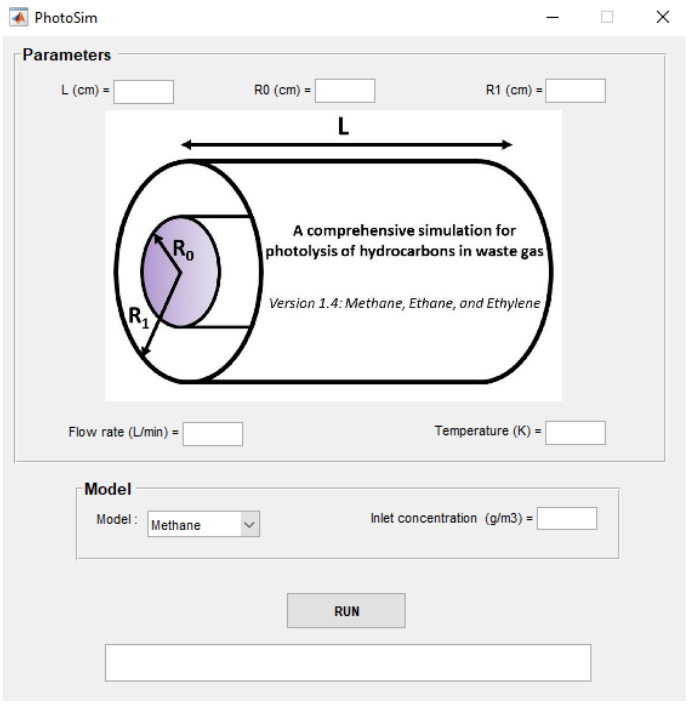


**Figure 4-32: *PhotoSim* appearance after execution on windows**

In the upper box, "Parameters", the user should enter the values for the reactor parameters, such as reactor length ($L$(cm)), UV lamp radius ($R_0$(cm)), photoreactor radius ($R_1$(cm)), the gas flow rate (L/min), and the inlet temperature (K). As shown in the previous chapter, the effects of the temperature variations do not have a significant impact on the model results, so the current version of *PhotoSim* assumes constant temperature in the simulation.

In the lower box, “Model”, the user should select which hydrocarbon is the leading pollutant in the gas stream. The model can be selected from a drop-down menu between: Methane, Ethane, and Ethylene. The current version of *PhotoSim* is only able to handle individual hydrocarbons in the waste gas stream, but not a mixture of them. When the model type is selected, the user should enter the initial concentration value ($g/m^3$) of that particular hydrocarbon in the waste gas stream.

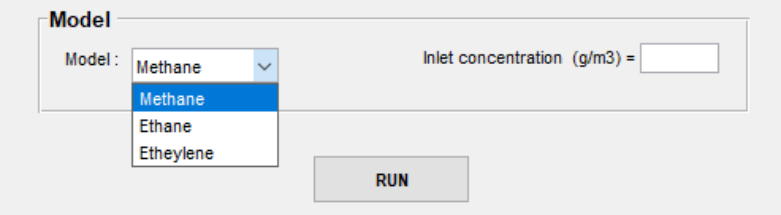


**Figure 4-33: Model selection and entering the inlet concentration of the hydrocarbon in *PhotoSim***

Once all the required fields are filled properly, by clicking the “RUN” button, *PhotoSim* will run the simulation, and in a reasonable run time (current version run time is about 15 seconds.), the removal efficiency (conversion) will appear on the *PhotoSim* result panel. Figure 5-34 shows the *PhotoSim* during the runtime and after the convergence.

a)

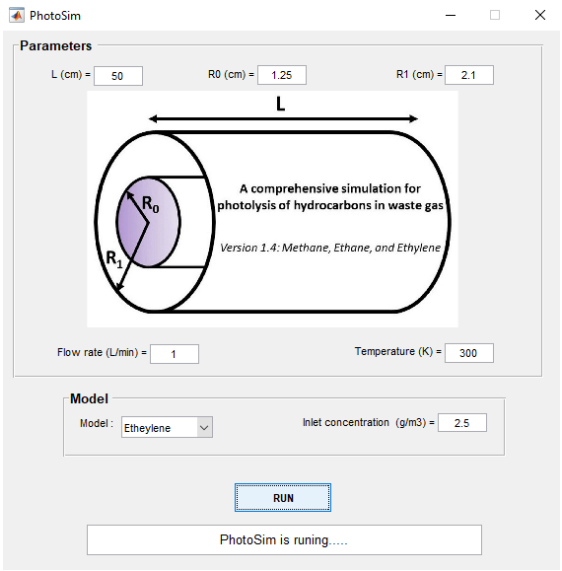


b)

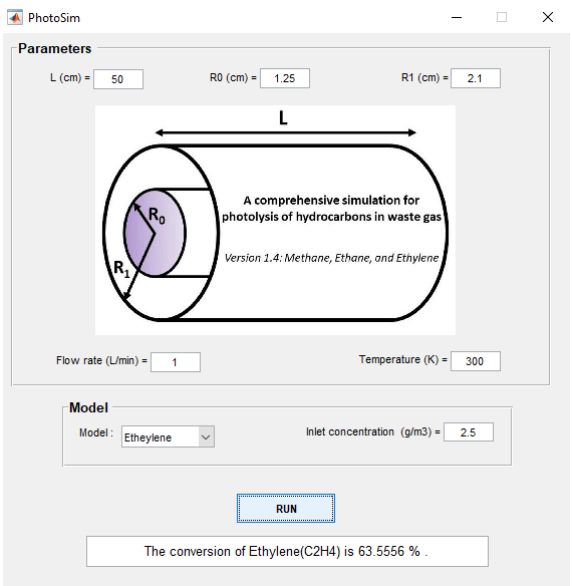


**Figure 4-34: *PhotoSim* interface: a) during runtime, b) after convergence**

# Chapter 5: Conclusions and Recommendations

## 5.1 Concluding Remarks

A mechanistic simulation model was developed to describe ultraviolet waste gas treatment of hydrocarbons, with the focus on methane, ethane, and ethylene. The photochemical reactor has been modeled to include chemical and photochemical reactions, light field, material balance and flow pattern have been completely considered for each species in the model.

Numerous efforts were made to include all the possible chemical and photochemical reactions arising from the interactions between air components with each of methane, ethane, and ethylene. This led to an inclusive reaction list for each model component, $CH_4$, $C_2H_6$, and $C_2H_4$. The latest comprehensive model of ethylene, for instance, consists of 199 reactions (165 chemical reactions, and 34 photochemical reactions) with 69 reactive species in the modeled photoreactor.

Extensive simulation trials indicated that most of the computation time is spent on calculation of reaction rates that have insignificant effects on the effluent concentration. Therefore, three different kinetic models were obtained for each of $CH_4$, $C_2H_6$, and $C_2H_4$. The kinetic models are named “the primary kinetics”, including only the essential reactions; “the primary+$NO_x$ kinetics”, including the essential reactions and $NO_x$ reactions, and “the comprehensive kinetics”, including all reactions. Based on these kinetic models, the most effective reaction pathway for each of methane, ethane, and ethylene was established.

Simulation results indicate that every time new hydrocarbons are introduced, the model run-time for each single run increases disproportionally with the number of reactions involved, for the case of comprehensive kinetic models. It can be included that when the model is further extended

by adding more components, particularly higher hydrocarbons, the expected run-time may increase to several days. Nevertheless, when the primary kinetic models were introduced (the models include only the main important chemical and photochemical reactions), the run time can be maintained as low as possible, without loss of accuracy. This can be beneficial in the field of air quality modelling with Eulerian models, where around 50-90% of the computation time is usually spent resolving the complicated chemistry (Byun & Ching, 1999).

The simulation results confirmed that the removal efficiency (i.e., conversion) of ethylene is significantly higher than ethane, followed by methane, as expected due to higher chemical reactivity. However, the removal efficiency for all three main components ($CH_4$, $C_2H_6$, and $C_2H_4$) decreases with increasing initial concentration of those compounds or increasing gas flow rate in the system. In addition, sensitivity analysis of the models indicated that the water content, ozone premixing, and reactor radius are the strongest contributing factors to increase the removal of modeled hydrocarbons in waste gas, while changing temperature has a smaller but still significant effect on the conversions, and changing flow pattern and the reactor length do not influence the conversions, significantly.

The proposed model in this study can predict the reaction products of the photolysis process in the gas phase, for each individual model of methane, ethene, and ethylene. Findings show that the main process products are $CO_2$, formaldehyde, and methyl peroxide for the methane model; $CO_2$, acetic acid, ethyl hydroperoxide, and acetaldehyde for the ethane model; and $CO_2$, formaldehyde and ketene for the ethylene model. These predicted products are consistent with the experimental findings of oxidation reactions for each of methane, ethane, and ethylene, confirming that the model is sound to predict the photoreactor effluxes. Also, for the ethylene

photolysis exclusively, calculations proved that the formation of higher hydrocarbons due to polymerization and/or propagation processes is not a concern, if the ethylene gas is diluted with air. Moreover, although $CO_2$ is potentially one of the predominant reaction products, its concentration nevertheless is significantly less than a complete oxidation process. This may present some concerns when photolysis is used for pollution remediation, but the organic reaction products tend to be highly water-soluble, thus they can be removed by other chemical process techniques such as absorption.

The projected model is also able to deal with a mixture of pollutants in the waste gas stream. This mixture can be either a combination of methane, ethane, and ethylene, or a mixture of each of those hydrocarbons with concentrated $NO_x$. Simulation results showed that, if there is a mixture of $CH_4$, $C_2H_6$, and $C_2H_4$ present in the waste gas, the predicted removal efficiency of ethylene did not change to the case of a mixture or ethylene as a sole pollutant, while the removal efficiency of ethane and methane drastically decreased for the case of a mixture. The same trend was observed when only $CH_4$ and $C_2H_6$ mixed in the air stream, and the removal efficiency of methane decreased significantly in comparison with the model containing methane only. This indicates that it is possible to photochemically degrade higher hydrocarbons in a mixture with methane, leaving the methane largely intact. Similarly, results for the models with a mixture of each of $CH_4$, $C_2H_6$, and $C_2H_4$ and NO indicated that including $NO_x$ in the model can cause complete degradation of nitrogen monoxide and have a slightly synergistic effect for removal efficiency of hydrocarbons in comparison with hydrocarbons in the absence of $NO_x$.

The proposed model is also extended to include the temperature gradient in the photoreactor, which is formed in the reactor due to the main heat source, the UV lamp. The UV lamp heat loss

may cause significant temperature variations in the reactor, which is normally neglected in the photolysis process. In the extended thermal model, the temperature is no longer assumed to be constant, and the values of the temperature were updated at each location in the reactor. Evaluation of the model results for both constant and non-constant temperature values indicates that although there might be a noteworthy temperature gradient in the gas phase photoreactor, the impact of this temperature adjustment is nevertheless less significant on the model removal efficiencies (less than 5% maximum of the inlet hydrocarbon, up to 20% of the degraded hydrocarbon). Furthermore, black-box simulation for the heat of reactions in all three models indicated that the heat production in the photoreactor due to reaction is markedly lower than the original heat source of UV lamp heat loss, and hence heat of reactions can be simply ignored for the waste gas photolysis process. Additionally, detailed calculation of heat transfer factors indicated that the proposed modeled photoreactor, under conditions evaluated, is not affected by any convective cycle and consequently conduction is the predominant heat transfer mechanism in the radial direction.

The proposed photoreactor was simulated with COMSOL software to verify the major assumptions made in the original model development. Non-isothermal flow simulation has been selected to study the flow behavior and temperature variation in the reactor. Flow simulations for both laminar and Low-Reynolds $k$-$\varepsilon$ (LRKE) indicated that the velocity profile is not meaningfully different, consistent with the fully-developed laminar assumption in the base model. Also, according to the calculation of turbulent diffusivity in the worst-case scenario, clearly the assumed photoreactor is not affected by any mechanical dispersion, since the whole system is a diffusion-controlled process. In a similar way, software simulation for temperature variation in the reactor indicated that the predicted temperature profile for both laminar and

turbulent cases are consistent with the numerical model developed for temperature profile. The software simulation results were validated by a 3D simulation for both flow and heat transfer.

To sum up, the developed model is in turn a unique model in the area of gas phase photolysis of methane, ethane, and ethylene. The capability of the presented model can be extended to both environmental engineering aspects (for remediation and conversion of natural gas condensate emissions), and to chemical engineering applications (for conversion of condensate to more valuable products). With the adequate justification of assumptions, the importance of various transport phenomena in a gas-phase photoreactor was tested, indicating that in the development of any gas phase photoreactor, some effects can be ignored (such as flow development in inlet, turbulence, and convection), and some effects that should not be ignored but nevertheless tend to be small (such as velocity profile, diffusion, conduction, UV lamp heat loss, and effect of temperature on transport properties). Detailed calculations and the results of previous models for other pollutants (i.e., models of benzene and $H_2S$ that have been both validated with experimental results) lend confidence that the development of the reaction models for the proposed photoreactor is sound, and hence it can be used to establish the feasibility of the gas phase photolysis process.

## 5.2 Research Limitations

One of the limitations of this research study is the lack of some values such as rate constants or quantum yields for some reactions; as well as the reaction products for some reactions. This may pose a challenge when it comes to compiling a comprehensive reaction network. In this regard, for such reactions, the assumptions, justifications and calculations based on analogues of the previous works are explained accordingly as required.

Another limitation of the presented research can be the simplicity of the light field model formulation. In the previously validated models (Asili & De Visscher, 2014; Mahmoudkhani et al., 2016) it was shown that the simplified light field model equation (presented in this research) overestimates the degradation efficiency to some extent, while a more detailed equation, described by (Mahmoudkhani, 2012; Mahmoudkhani et al., 2016), slightly underestimates the experimental values of degradation efficiency, with increasing the computational time by a factor 20. In fact, it is doable to include a refined mathematical equation for light field model; however, it may cause the computational time to increase excessively and lead to increasing complexity, as it will create at minimum a 4D matrix only for the light field equation that should be solved simultaneously with other governing equations for concentration. This is in contrast with one of objectives of this research study, which is having the most comprehensive model that runs in the shortest possible time.

### 5.3 Future Work and Recommendations

One of the main areas of future research can be experimental work with the same modeled apparatus to ensure that the reactor configuration conforms to the model assumptions. It is acknowledged that the lack of experimental data for all three models with the same reactor could limit the scope of the research, but it is not a significant obstacle in finding meaningful trends and data relationship. Since the previous model results were validated experimentally with the presented reactor (Mahmoudkhani et al., 2016), and with a totally different type of reactor (Asili & De Visscher, 2014), it can be confidently concluded that the modeling approach is sound, and it is expected the same trend of results will be obtained in the future experimental studies.

One of the other areas of future research might be to test the effect of adding more pollutant species to see the predicted effects of interactions between molecules for each pollutant. As shown, the proposed modeling scheme is able to handle combination of reactants, and analyze the possible products and conversion of reactants. One of the applications of this work could be for the removal of natural gas impurities. The presented model methane contains all of the possible UV/oxidation reactions, model of Asili and De Visscher (Asili & De Visscher, 2014) contains all of possible UV/oxidation reactions of $H_2S$ and $NO_x$; thus, in the case of interest, if the reactions between methane and $H_2S$ gathered, it is possible to extend the model for natural gas impurities removal.

In the current model, all reaction terms are manually entered into the chemical kinetics model; even for the simplified kinetics models. Now, since it is established that the model is capable of handling more than one pollutant, it is proposed for the future to have all the reaction information, both chemical and photochemical, in a data bank, to be recalled automatically by the model when they are present as pollutants. In other words, it may be planned to have a comprehensive and sophisticated general model for any kind of pollutant and any type of photoreactor which can be used either for any specific pollutant or combining more than one and then see the efficiency and product predictions; which means a general modular comprehensive model. This can be interpreted as a more sophisticated version of *PhotoSim 1.4* presented in this research which has shown that the model can be applied to a software package for industrial usage.

As mentioned, some rate constants are not available, and have been estimated based on analogous. Calculating these rate constants with computational methods (e.g., ab initio or DFT)

would help establish possible values of these rate constants.

Obviously, in all cases discussed above, pilot scale studies would be useful to examine the practical process feasibility. Further prospected research areas are also mentioned in Chapter 1.

# References


Alberta Environment. (2008). *Alberta Air Emissions Trends and Projections*. Retrieved from http://www.environment.alberta.ca/625.html

Alpert, S. M., Knappe, D. R., & Ducoste, J. J. (2010). Modeling the UV/hydrogen peroxide advanced oxidation process using computational fluid dynamics. *Water Research, 44*(6), 1797-1808.

Anastasi, C., Simpson, V., Munk, J., & Pagsberg, P. (1990). UV spectrum and the kinetics and reaction pathways of the self-reaction of hydroxyethyl radicals. *Journal of Physical Chemistry, 94*(16), 6327-6331.

Anastasi, C., Waddington, D. J., & Woolley, A. (1983). Reactions of oxygenated radicals in the gas phase. Part 10.—Self-reactions of ethylperoxy radicals. *Journal of the Chemical Society, Faraday Transactions 1: Physical Chemistry in Condensed Phases, 79*(2), 505-516.

APEI. (2017). *Air Pollutant Emission Inventory of Canada*. Retrieved from http://ec.gc.ca/pollution/default.asp?lang=En&n=E96450C

Asili, V. & De Visscher, A. (2018), Modelling methane and ethane photolysis in waste gas: Optimization of reaction networks. *The Canadian Journal of Chemical Engineering, 96*, 1674-1683. doi:10.1002/cjce.23124

Asili, V., & De Visscher, A. (2014). Mechanistic model for ultraviolet degradation of $H_2S$ and $NO_x$ in waste gas. *Chemical Engineering Journal, 244*, 597-603.

Atkinson, B., Brocklebank, M. P., Card, C. C. H., & Smith, J. M. (1969). Low Reynolds Number Developing Flows. *AIChE Journal, 15*(4), 548-553.

Atkinson, R. (1994). Gas-phase tropopheric chemistry of organic compounds. *Journal of Physical and Chemical Reference Data Monograph, 2*, 1-216.

Atkinson, R. (1997). Gas-phase tropospheric chemistry of volatile organic compounds: 1. Alkanes and alkenes. *Journal of Physical and Chemical Reference Data, 26*(2), 215-290.

Atkinson, R., Baulch, D., Cox, R., Crowley, J., Hampson, R., Hynes, R., & Troe, J. (2004). Evaluated kinetic and photochemical data for atmospheric chemistry: Volume I-gas phase reactions of $O_x$, $HO_x$, $NO_x$ and $SO_x$ species. *Atmospheric Chemistry and Physics, 4*(6), 1461-1738.

Atkinson, R., Baulch, D., Cox, R., Crowley, J., Hampson, R., & Hynes, R., Subcommittee I. (2006). Evaluated kinetic and photochemical data for atmospheric chemistry: Volume II–gas phase reactions of organic species. *Atmospheric Chemistry and Physics, 6*(11), 3625-4055.

Atreya, S. K. (2013). *Atmospheres and Ionospheres of the Outer Planets and their Satellites* (Vol. 15): Springer Science & Business Media.

Atyabi, M. (2013). *Ultraviolet Degradation of BTX in Waste Gas: Effects of Photocatalysis and Ozone Premixing.* M.Sc. Thesis. University of Calgary.

Bansal, R. (2010). *A Textbook of Fluid Mechanics and Hydraulic Machines*, (9th Ed.), Laxmi Publications (p) Ltd.

Barrera, M. (2011). *Photochemical treatment of organic constituents and bacterial pathogens from synthetic slaughterhouse wastewater by combining Vacuum-UV and UV-C*. M.A.Sc. Thesis. Ryerson University.

Bass, A., Ledford Jr, A., & Laufer, A. (1976). Extinction coefficients of $NO_2$ and $N_2O_4$. *Journal of Research of the National Bureau of Standards, 80A*(2), 143-166.

Battin-Leclerc, F., Konnov, A. A., Jaffrezo, J.-L., & Legrand, M. (2007). To better understand the formation of short-chain acids in combustion systems. *Combustion Science and Technology, 180*(2), 343-370.

Baulch, D., Bowman, C., Cobos, C., Cox, R., Just, T., Kerr, J., & Tsang, W. (2005). Evaluated kinetic data for combustion modeling: supplement II. *Journal of Physical and Chemical Reference Data, 34*(3), 757-1397.

Bergman, T. L., Lavine, A. S., Incropera, F. P., & DeWitt, D. P. (2011). *Fundamentals of Heat and Mass Transfer*, (7th Ed.), John Wiley & Sons.

Berry, W. O., & Brammer, J. (1977). Toxicity of water-soluble gasoline fractions to fourth-instar larvae of the mosquito Aedes aegypti L. *Environmental Pollution (1970), 13*(3), 229-234.

Bird, R. B., Stewart, W. E., & Lightfoot, E. N. (2002). *Transport Phenomena*, (2nd Ed.), JohnWiley & Sons.

Blacet, F. (1952). Photochemistry in the lower atmosphere. *Industrial & Engineering Chemistry, 44*(6), 1339-1342.

Blanksby, S. J., & Ellison, G. B. (2003). Bond dissociation energies of organic molecules. *Accounts of Chemical Research, 36*(4), 255-263.

Burkholder, J. B., Talukdar, R. K., Ravishankara, A., & Solomon, S. (1993). Temperature dependence of the $HNO_3$ UV absorption cross sections. *Journal of Geophysical Research: Atmospheres (1984–2012), 98*(D12), 22937-22948.

Burkholder, J., Sander, S., Abbatt, J., Barker, J., Huie, R., Kolb, C., & Wine, P. (2015). *Chemical Kinetics and Photochemical Data for Use in Atmospheric Studies*. NASA/JPL Data Evaluation, JPL Publication 15-10 Evaluation No. 18, NASA, Pasadena, CA, October, 2015. https://jpldataeval.jpl.nasa.gov/

Byun, D. W., & Ching, J. K. S. (1999). *Science Algorithms of the EPA Models-3 Community Multiscale Air Quality (CMAQ) Modeling System*. Report EPA/600R-99/030, *US-EPA.*

Calvert, J. G., Derwent, R. G., Orlando, J. J., Tyndal, G. S., & Wallington, T. J. (2008). *Mechanisms of atmospheric oxidation of the alkanes*, Oxford University Press.

Canada GHG Emissions. (2017). *Canada's Greenhouse Gas Emissions*. Retrieved from https://www.ec.gc.ca/ges-ghg/

CAPP. (1999). $CH_4$ and VOC Emissions from the Canadian Upstream Oil and Gas Industry. *Canadian Association of Petroleum Producers, Vol. 1*.

CAPP. (2005). Technical report of a National Inventory of Greenhouse Gas (GHG), Criteria Air Contaminant (CAC) and Hydrogen Sulphide ($H_2S$) Emissions by the Upstream Oil and Gas Industry. *Canadian Association of Petroleum Producers, Vol. 2*.

Carr, R. W. (2007). *Modeling of Chemical Reactions* (Vol. 42), Elsevier.

Chen, F., Yang, Q., Pehkonen, S., & Ray, M. B. (2004). Modeling of gas-phase photodegradation of chloroform and carbon tetrachloride. *Journal of the Air & Waste Management Association, 54*(10), 1281-1292.

Cockerham, L. G., & Shane, B. S. (1993). *Basic Environmental Toxicology*, CRC Press.

Collins, W., Derwent, R., Johnson, C., & Stevenson, D. (2002). The oxidation of organic compounds in the troposphere and their global warming potentials. *Climatic Change, 52*(4), 453-479.

Cox, R. A., Derwent, R. G., Holt, P. M., & Kerr, J. A. (1976). Photo-oxidation of methane in the presence of NO and $NO_2$. *Journal of the Chemical Society, Faraday Transactions 1: Physical Chemistry in Condensed Phases, 72*, 2044-2060.

Curran, H., Fischer, S., & Dryer, F. (2000). The reaction kinetics of dimethyl ether. II: Low-temperature oxidation in flow reactors. *International Journal of Chemical Kinetics, 32*(12), 741-759.

Cussler, E. L. (2009). *Diffusion: Mass Transfer in Fluid Systems,* (3rd Ed.), Cambridge University Press.

Dagaut, P., Luche, J., & Cathonnet, M. (2000). Experimental and kinetic modeling of the reduction of NO by propene at 1 atm. *Combustion and Flame, 121*(4), 651-661.

De Visscher, A. (2013). *Air Dispersion Modeling: Foundations and Applications,* John Wiley & Sons.

De Visscher, A., Dewulf, J., Van Durme, J., Leys, C., Morent, R., & Van Langenhove, H. (2008). Non-thermal plasma destruction of allyl alcohol in waste gas: kinetics and modelling. *Plasma Sources Science and Technology, 17*(1), 015004.

De Visscher, A., Rezaei, M., Mahmoudkhani, F., Langford, C. H., & Vaisman, E. (2010). *Photochemical Degradation of BTEX in Waste Gas: Experiments and Modeling.* Paper presented at the Proceedings of The Air & Waste Management Association 103rd Annual Conference and Exhibition. Calgary, Canada.

Demeestere, K., Dewulf, J., & Van Langenhove, H. (2007). Heterogeneous photocatalysis as an advanced oxidation process for the abatement of chlorinated, monocyclic aromatic and sulfurous volatile organic compounds in air: state of the art. *Critical Reviews in Environmental Science and Technology, 37*(6), 489-538.

Desai, C., & Vafai, K. (1994). An investigation and comparative analysis of two-and three-dimensional turbulent natural convection in a horizontal annulus. *International Journal of Heat and Mass Transfer, 37*(16), 2475-2504.

Dillon, T. J., & Crowley, J. N. (2008). Direct detection of OH formation in the reactions of $HO_2$ with $CH_3C(O)O_2$ and other substituted peroxy radicals. *Atmospheric Chemistry and Physics, 8*(16), 4877-4889.

Dillon, T., Hölscher, D., Sivakumaran, V., Horowitz, A., & Crowley, J. (2005). Kinetics of the reactions of HO with methanol (210–351 K) and with ethanol (216–368 K). *Physical Chemistry Chemical Physics, 7*(2), 349-355.

Duran, J. E., Taghipour, F., & Mohseni, M. (2009). CFD modeling of mass transfer in annular reactors. *International Journal of Heat and Mass Transfer, 52*(23), 5390-5401.

Environment Canada. (2016). *Environment and Climate Change Canada - Screening Assessment.* Retrieved from https://www.ec.gc.ca/ese-ees/

Feiyan, C., Pehkonen, S., & Ray, M. B. (2002). Kinetics and mechanisms of UV-photodegradation of chlorinated organics in the gas phase. *Water Research, 36*(17), 4203-4214.

Filimonova, E., Kim, Y., Hong, S. H., & Song, Y.-H. (2002). Multiparametric investigation on $NO_x$ removal from simulated diesel exhaust with hydrocarbons by pulsed corona discharge. *Journal of Physics D: Applied Physics, 35*(21), 2795.

Finlayson, B. A. (2012). *Introduction to Chemical Engineering Computing*, John Wiley & Sons.

Fogler, H. S. (2016). *Elements of Chemical Reaction Engineering*, (5th Ed.), Pearson Education.

Frank, P., Bhaskaran, K., & Just, T. (1988). *Acetylene oxidation: The reaction $C_2H_2$+O at high temperatures.* Paper presented at the Symposium (International) on Combustion.

Froment, G. F., Bischoff, K. B., & De Wilde, J. (1990). *Chemical Reactor Analysis and Design* (Vol. 2), John Wiley & Sons.

Fuller, E. N., Ensley, K., & Giddings, J. C. (1969). Diffusion of halogenated hydrocarbons in helium. The effect of structure on collision cross sections. *The Journal of Physical Chemistry, 73*(11), 3679-3685.

Gutierrez, R. L., Bourgeous, K. N., Salveson, A., Meir, J., & Slater, A. (2006). Microwave UV: A New Wave of Tertiary Disinfection. *Proceedings of the Water Environment Federation, 2006*(10), 2853-2864.

Hanst, P. L., & Gay, B. W. (1983). Atmospheric oxidation of hydrocarbons: formation of hydroperoxides and peroxyacids. *Atmospheric Environment (1967), 17*(11), 2259-2265.

Hasson, A. S., Kuwata, K. T., Arroyo, M. C., & Petersen, E. B. (2005). Theoretical studies of the reaction of hydroperoxy radicals ($HO_2$) with ethyl peroxy ($CH_3CH_2O_2$), acetyl peroxy ($CH_3C(O)O_2$), and acetonyl peroxy ($CH_3C(O)CH_2O_2$) radicals. *Journal of Photochemistry and Photobiology A: Chemistry, 176*(1), 218-230.

He, S., Chen, Z., & Zhang, X. (2011). Photochemical reactions of methyl and ethyl nitrate: a dual role for alkyl nitrates in the nitrogen cycle. *Environmental Chemistry, 8*(6), 529-542.

Hess, W. P., & Tully, F. P. (1989). Hydrogen-atom abstraction from methanol by hydroxyl radical. *The Journal of Physical Chemistry*, *93*(5), 1944-1947.

Heuts, J. P., Gilbert, R. G., & Radom, L. (1995). A priori prediction of propagation rate coefficients in free-radical polymerizations: Propagation of ethylene. *Macromolecules, 28*(26), 8771-8781.

Holman, J. (2010). *Heat Transfer*. (10th Ed.), Boston, Massachusetts. McGraw-Hill.

Horie, O., Crowley, J., & Moortgat, G. (1990). Methylperoxy self-reaction: products and branching ratio between 223 and 333 K. *Journal of Physical Chemistry, 94*(21), 8198-8203.

Horowitz, A., & Calvert, J. G. (1982). Wavelength dependence of the primary processes in acetaldehyde photolysis. *The Journal of Physical Chemistry, 86*(16), 3105-3114.

Horowitz, A., Meller, R., & Moortgat, G. K. (2001). The UV–VIS absorption cross sections of the α-dicarbonyl compounds: pyruvic acid, biacetyl and glyoxal. *Journal of Photochemistry and Photobiology A: Chemistry, 146*(1), 19-27.

Ichimura, T., & Mori, Y. (1973). Photolysis of monochlorobenzene in gas phase. *The Journal of Chemical Physics, 58*(1), 288-292.

IPCC. (2005). *Special Report on Safeguarding the Ozone Layer and the Global Climate System.* The Intergovernmental Panel on Climate Change, Cambridge University Press.

Irwin, J., Van Mouwerik, M., Stevens, L., Seese, M. D., & Basham, W. (1997). Environmental contaminants encyclopedia: alkanes entry. *National Park Service, Water Resources Division, Colorado*.

Ismail, H., Abel, P. R., Green, W. H., Fahr, A., Jusinski, L. E., Knepp, A. M., & Osborn, D. L. (2009). Temperature-Dependent kinetics of the vinyl radical ($C_2H_3$) self-reaction. *The Journal of Physical Chemistry A, 113*(7), 1278-1286.

Jiménez, E., Gilles, M., & Ravishankara, A. (2003). Kinetics of the reactions of the hydroxyl radical with $CH_3OH$ and $C_2H_5OH$ between 235 and 360 K. *Journal of Photochemistry and Photobiology A: Chemistry, 157*(2), 237-245.

Johnston, H. S., & Graham, R. (1974). Photochemistry of $NO_x$ and $HNO_x$ compounds. *Canadian Journal of Chemistry, 52*(8), 1415-1423.

Jones, W., & Launder, B. (1972). The prediction of laminarization with a two-equation model of turbulence. *International Journal of Heat and Mass Transfer, 15*(2), 301-314.

Ju, Y., Lefkowitz, J., Wada, T., & Won, S. (2015). *Plasma Assisted Combustion: Flame Regimes and Kinetic Studies*. 53rd AIAA Aerospace Sciences Meeting and Exhibit. Kissimmee, Florida.

Keller-Rudek, H., Moortgat, G., Sander, R., & Sörensen, R. (2013). The MPI-Mainz UV/VIS spectral atlas of gaseous molecules of atmospheric interest. *Earth System Science Data, 5*(2), 365-373.

Kerr, J. A., & Parsonage, M. J. (1972). *Evaluated kinetic data on gas phase addition reactions: reactions of atoms and radicals with alkenes, alkynes and aromatic compounds*: Butterworths, London.

Kralik, P., Kusic, H., Koprivanac, N., & Bozic, A. L. (2010). Degradation of chlorinated hydrocarbons by UV/$H_2O_2$: the application of experimental design and kinetic modeling approach. *Chemical Engineering Journal, 158*(2), 154-166.

Kuehn, T., & Goldstein, R. (1976). Correlating equations for natural convection heat transfer between horizontal circular cylinders. *International Journal of Heat and Mass Transfer, 19*(10), 1127-1134.

Kyle, B. G. (1984). *Chemical and Process Thermodynamics*, (2nd Ed.), Pearson Education.

Leighton, P. (2012). *Photochemistry of Air Pollution*, Elsevier.

Limao-Vieira, P., Giuliani, A., Delwiche, J., Parafita, R., Mota, R., Duflot, D., & Mason, N. (2006). Acetic acid electronic state spectroscopy by high-resolution vacuum ultraviolet photo-absorption, electron impact, He (I) photoelectron spectroscopy and ab initio calculations. *Chemical Physics, 324*(2), 339-349.

Liu, C.-Y., Mueller, W., & Landis, F. (1961). *Natural convection heat transfer in long horizontal cylindrical annuli.* Paper presented at the International Developments in Heat Transfer, Part V, New York.

Lorenz, K., Rhasa, D., Zellner, R., & Fritz, B. (1985). Laser Photolysis-LIF Kinetic Studies of the Reactions of $CH_3O$ and $CH_2CHO$ with $O_2$ between 300 and 500 K. *Berichte der Bunsengesellschaft für Physikalische Chemie, 89*(3), 341-342.

Lucazeau, G., & Sandorfy, C. (1970). On the far-ultraviolet spectra of some simple aldehydes. *Journal of Molecular Spectroscopy, 35*(2), 214-231.

Luo, Y.-R. (2007). *Comprehensive Handbook of Chemical Bond Energies*: CRC press.

Mahmoudkhani, F. (2012). *Simulation of a Photochemical Reactor for Benzene Elimination from Waste Gas.* M.Sc. Thesis, University of Calgary Canada.

Mahmoudkhani, F., Rezaei, M., Asili, V., Atyabi, M., Vaisman, E., Langford, C. H., & De Visscher, A. (2016). Benzene degradation in waste gas by photolysis and photolysis-ozonation: experiments and modeling. *Frontiers of Environmental Science & Engineering*, *10*(6), 10.

Mallery, M. R., & Heinsohn, R. J. (1996). *Numerical model of a photolytic reactor for VOC destruction*. Proceedings of the Air & Waste Management Association Conference on Emerging Solutions to VOC and Air Toxics Control, Clearwater, Florida.

Manahan, S. E. (2002). *Toxicological Chemistry and Biochemistry*, (3rd Ed.), CRC Press.

McMurry, J. (2006). *Organic Chemistry*, (8th Ed.). Belmont, CA. Brooks Cole, Cengage Learning.

Meller, R., & Moortgat, G. K. (2000). Temperature dependence of the absorption cross sections of formaldehyde between 223 and 323 K in the wavelength range 225–375 nm. *Journal of Geophysical Research: Atmospheres*, *105*(D6), 7089-7101.

Multiphysics, (2016). *Comsol Multiphysics® User's Guide.* (Version: 5.2a).

Nguyen, T. L., Park, J., Lee, K., Song, K., & Barker, J. R. (2011). Mechanism and Kinetics of the Reaction $NO_3$+ $C_2H_4$. *The Journal of Physical Chemistry A*, *115*(19), 4894-4901.

NPRI. (2017). *National Pollutant Release Inventory of Canada*. Retrieved from http://www.ec.gc.ca/inrp-npri/

Opansky, B. J., & Leone, S. R. (1996). Rate coefficients of $C_2H$ with $C_2H_4$, $C_2H_6$, and $H_2$ from 150 to 359 K. *The Journal of Physical Chemistry*, *100*(51), 19904-19910.

Oppenländer, T. (2003). *Photochemical Purification of Water and Air: Advanced Oxidation Processes (AOPs)-Principles, Reaction Mechanisms, Reactor Concepts*, John Wiley & Sons.

Orlandini, I., & Riedel, U. (2000). Chemical kinetics of NO removal by pulsed corona discharges. *Journal of Physics D: Applied Physics*, *33*(19), 2467.

Orlando, J. J., & Tyndall, G. S. (2001). The atmospheric chemistry of the HC(O)CO radical. *International Journal of Chemical Kinetics*, *33*(3), 149-156.

Orlando, J. J., Tyndall, G. S., Bilde, M., Ferronato, C., Wallington, T. J., Vereecken, L., & Peeters, J. (1998). Laboratory and theoretical study of the oxy radicals in the OH-and Cl-initiated oxidation of ethene. *The Journal of Physical Chemistry A, 102*(42), 8116-8123.

Osborne, B. A., Marston, G., Kaminski, L., Jones, N., Gingell, J., Mason, N., & Hubin-Franskin, M.-J. (2000). Vacuum ultraviolet spectrum of dinitrogen pentoxide. *Journal of Quantitative Spectroscopy and Radiative Transfer, 64*(1), 67-74.

Parmenter, C., & Albert Noyes, W. (1963). Energy dissipation from excited acetaldehyde molecules. *Journal of the American Chemical Society, 85*(4), 416-421.

Patnaik, P. (2007). *A Comprehensive Guide to the Hazardous Properties of Chemical Substances*, (3rd Ed.), John Wiley & Sons.

Peacock, A. (2000). *Handbook of Polyethylene: Structures, Properties, and Applications*, Taylor & Francis.

Peeters, J., Boullart, W., & Langhans, I. (1994). Branching ratio of the $C_2H_2$+ O reaction at 290 K from kinetic modelling of relative methylene concentration versus time profiles in $C_2H_2$/O/H systems. *International Journal of Chemical Kinetics, 26*(9), 869-886.

Pereira, V. J., Weinberg, H. S., Linden, K. G., & Singer, P. C. (2007). UV degradation kinetics and modeling of pharmaceutical compounds in laboratory grade and surface water via direct and indirect photolysis at 254 nm. *Environmental Science & Technology*, *41*(5), 1682-1688.

Perry, R. H., Green, D. W., Maloney, J. O., Abbott, M. M., Ambler, C. M., & Amero, R. C. (1997). *Perry's Chemical Engineers' Handbook* (Vol. 7): McGraw-hill New York.

Qi, B., Zhang, Y., Chen, Z., Shao, K., Tang, X., & Hu, M. (1999). Identification of organic peroxides in the oxidation of C1-C3 alkanes. *Chemosphere, 38*(6), 1213-1221.

Ray, M. B. (2000). Photodegradation of the volatile organic compounds in the gas phase: a review. *Asia-Pacific Journal of Chemical Engineering, 8*(5-6), 405-439.

Sanches, S., Leitão, C., Penetra, A., Cardoso, V., Ferreira, E., Benoliel, M., & Pereira, V. (2011). Direct photolysis of polycyclic aromatic hydrocarbons in drinking water sources. *Journal of Hazardous Materials, 192*(3), 1458-1465.

Sander, S., Friedl, R., Barker, J., Golden, D., Kurylo, M., Wine, P., & Moortgat, G. (2011). *Chemical Kinetics and Photochemical Data for Use in Atmospheric Studies*, NASA/JPL Data Evaluation, JPL Publication 06-2 Evaluation No. 17, NASA, Pasadena, CA, June, 2011. https://jpldataeval.jpl.nasa.gov/

Seader, J., Henley, E. J., & Roper, D. K. (2011). *Separation Process Principles*, (3rd Ed.), Hoboken, NJ, John Wiley & Sons.

Sellami, M. H., Hassen, A., & Sifaoui, M. S. (2003). Modelling of UV radiation field inside a photoreactor designed for wastewater disinfection Experimental validation. *Journal of Quantitative Spectroscopy and Radiative Transfer, 78*(3), 269-287.

Shallcross, D. E., Biggs, P., Canosa-Mas, C. E., Clemitshaw, K. C., Harrison, M. G., Alañón, M. R. L., .& Wayne, R. P. (1997). Rate constants for the reaction between OH and $CH_3ONO_2$ and $C_2H_5ONO_2$ over a range of pressure and temperature. *Journal of the Chemical Society, Faraday Transactions, 93*(16), 2807-2811.

Shtern, V. Y. (1964). *The Gas-Phase Oxidation of Hydrocarbons* (M. F. Mullins, Translated by B. P. Mullins), Pergamon Press Ltd.

Singh, H. B., & Zimmerman, P. B. (1992). Atmospheric distribution and sources of nonmethane hydrocarbons. Presented in the proceeding of *Gaseous pollutants: Characterization and Cycling*, 177-235.

Sneep, M., & Ubachs, W. (2005). Direct measurement of the Rayleigh scattering cross section in various gases. *Journal of Quantitative Spectroscopy & Radiative Transfer,* 92, 293-310.

Sozzi, D. A., & Taghipour, F. (2006). Computational and experimental study of annular photo-reactor hydrodynamics. *International Journal of Heat and Fluid Flow, 27*(6), 1043-1053.

Spalding, M. A., & Chatterjee, A. (2017). *Handbook of Industrial Polyethylene and Technology: Definitive Guide to Manufacturing, Properties, Processing, Applications and Markets*: John Wiley & Sons.

Stockwell, W. R., Kirchner, F., Kuhn, M., & Seefeld, S. (1997). A new mechanism for regional atmospheric chemistry modeling. *Journal of Geophysical Research: Atmospheres, 102*(D22), 25847-25879.

Taghipour, F., & Mohseni, M. (2005). CFD simulation of UV photocatalytic reactors for air treatment. *AIChE Journal, 51*(11), 3039-3047.

Teertstra, P., & Yovanovich, M. (1998). Comprehensive review of natural convection in horizontal circular annuli. *ASME Publications HTD, 357*(4), 141-152.

Topudurtir, K., Tay, S., & Monschein, E. (1998). *Advanced Photochemical Oxidation Processes Handbook,* EPA.

Treybal, R. E. (1980). *Mass Transfer Operations*, (3rd Ed.), McGraw-Hill.

Troe, J. (1979). Predictive possibilities of unimolecular rate theory. *Journal of Physical Chemistry, 83*(1), 114-126.

Tyndall, G., Cox, R., Granier, C., Lesclaux, R., Moortgat, G., Pilling, M., & Wallington, T. (2001). Atmospheric chemistry of small organic peroxy radicals. *Journal of Geophysical Research: Atmospheres (1984–2012), 106*(D11), 12157-12182.

Tyndall, G., Wallington, T., & Ball, J. (1998). FTIR product study of the reactions $CH_3O_2$+$CH_3O_2$ and $CH_3O_2$+$O_3$. *The Journal of Physical Chemistry A, 102*(15), 2547-2554.

Vincent, G., Schaer, E., Marquaire, P.-M., & Zahraa, O. (2011). CFD modelling of an annular reactor, application to the photocatalytic degradation of acetone. *Process Safety and Environmental Protection, 89*(1), 35-40.

Wade Jr, L. (2006). *Organic Chemistry*, (6th Ed.), Pearson Prentice Hall.

Wallington, T. J., & Kurylo, M. J. (1987). The gas phase reactions of hydroxyl radicals with a series of aliphatic alcohols over the temperature range 240–440 K. *International Journal of Chemical Kinetics, 19*(11), 1015-1023.

Wallington, T., Gierczak, C., Ball, J., & Japar, S. (1989). Fourier transform infrared study of the self reaction of $C_2H_5O_2$ radicals in air at 295 K. *International Journal of Chemical Kinetics, 21*(11), 1077-1089.

Wang, C., & Chen, Z. (2008). An experimental study for rate constants of the gas phase reactions of $CH_3CH_2OOH$ with OH radicals, $O_3$, $NO_2$ and NO. *Atmospheric Environment, 42*(27), 6614-6619.

Wang, J. H., & Ray, M. B. (2000). Application of ultraviolet photooxidation to remove organic pollutants in the gas phase. *Separation and Purification Technology, 19*(1), 11-20.

Wang, Y., & Wen, J. (2006). Gear method for solving differential equations of gear systems. *Journal of Physics: Conference Series 48*, 143-148.

Warnek, P., & Williams, J. (2012). *The Atmospheric Chemist's Companion: Numerical Data for Use in the Atmospheric Science*, Springer, Dordrecht, The Netherlands.

White, F. M. (2003). *Fluid Mechanics*, (7th Ed.), McGraw-Hill.

Wu, C. R., Chien, T., Liu, G., Judge, D., & Caldwell, J. (1989). Photoabsorption and direct dissociation cross sections of $C_2H_2$ in the 1530–1930 Å region: A temperature dependent study. *The Journal of Chemical Physics, 91*(1), 272-280.

Xia, L.-Y., Gu, D.-H., Tan, J., Dong, W.-B., & Hou, H.-Q. (2008). Photolysis of low concentration $H_2S$ under UV/VUV irradiation emitted from microwave discharge electrodeless lamps. *Chemosphere, 71*(9), 1774-1780.

Yoshino, K., Esmond, J., Cheung, A.-C., Freeman, D., & Parkinson, W. (1992). High resolution absorption cross sections in the transmission window region of the Schumann-Runge bands and Herzberg continuum of $O_2$. *Planetary And Space Science, 40*(2), 185-192.

Yu, M. (2001). *Environmental Toxicology: Impacts of Environmental Toxicants on Living Systems*, Lewis Publishers.

Yue, P. (1993). Modelling of kinetics and reactor for water purification by photo-oxidation. *Chemical Engineering Science, 48*(1), 1-11.

Zhang, L., & Anderson, W. A. (2013). Kinetic analysis of the photochemical decomposition of gas-phase chlorobenzene in a UV reactor: Quantum yield and photonic efficiency. *Chemical Engineering Journal, 218*, 247-252.

Zhu, L., Kellis, D., & Ding, C.-F. (1996). Photolysis of glyoxal at 193, 248, 308 and 351 nm. *Chemical Physics Letters*, *257*(5-6), 487-491.

# Appendix A: List of components used in the reactive system of the model

## A.1. Air Model

**Table A-1: List of the components in the background air model (bold: the primary kinetics; italic: reactions added for the primary + $NO_x$ kinetics; roman: reactions added for the comprehensive kinetics.)**

| Components |
|---|
| **H Radical** |
| **$O(^3P)$ Radical** |
| **$O(^1D)$ Radical** |
| **OH Radical** |
| **$HO_2$ Radical** |
| **$O_2$** |
| **$N_2$ + Ar** |
| **$H_2O$** |
| **$O_3$** |
| **$H_2O_2$** |
| *NO* |
| *$NO_2$* |
| *$NO_3$* |
| *$N_2O_5$* |
| *$HNO_2$* |
| *$HNO_3$* |
| *$HO_2NO_2$* |
| $H_2$ |
| $N_2O$ |
| $N_2O_4$ |
| $N_2O_3$ |

## A.2. $CH_4$ Model

**Table A-2: List of the components in the $CH_4$ model**
**(bold: the primary kinetics; italic: reactions added for the primary + $NO_x$ kinetics; roman: reactions added for the comprehensive kinetics.)**

| Component |
|---|
| **$CH_4$** |
| **$CH_3$ Radical** |
| **CO** |
| **$CO_2$** |
| **$CH_2OH$ Radical** |
| **$CH_2O$** |
| **$CH_3O_2$ Radical** |
| **$CH_3O$ Radical** |
| **$CH_3OH$** |
| **HCO Radical** |
| **$CH_3OOH$** |
| *$CH_3O_2NO_2$ Radical* |
| $CHO_2$ Radical |
| $CH_2OOH$ Radical |
| $HOCH_2OO$ Radical |
| $CH_3ONO$ Radical |
| $CH_3ONO_2$ |
| $CH_2ONO_2$ Radical |
| HNO |

## A.3. $C_2H_6$ Model

**Table A-3: List of the components in the $C_2H_6$ model (bold: the primary kinetics; italic: reactions added for the primary + $NO_x$ kinetics; roman: reactions added for the comprehensive kinetics.)**

| Component |
|---|
| **$C_2H_6$** |
| **$C_2H_5$ Radical** |
| **$C_2H_5O_2$ Radical** |
| **$C_2H_5O$ Radical** |
| **$C_2H_5OOH$** |
| **$CH_3CHO$** |
| **$C_2H_5OH$ ($CH_3CH_2OH$)** |
| **$CH_3CO$ Radical** |
| **$CH_3C(O)O_2$ Radical** |
| **$CH_3C(O)OH$** |
| **$CH_3C(O)OOH$** |
| **$CH_3CHOH$ Radical** |
| *$C_2H_5O_2NO_2$ Radical* |
| $C_2H_4$ |
| $C_2H_4OH$ ($CH_2CH_2OH$) Radical |
| $C_2H_5ONO$ |
| $C_2H_5ONO_2$ |
| $CH_3C(O)OONO_2$ |

## A.4. $C_2H_4$ Model

**Table A-4: List of the components in the $C_2H_4$ model (bold: the primary kinetics; italic: reactions added for the primary + $NO_x$ kinetics; roman: reactions added for the comprehensive kinetics.)**

| Component |
|---|
| **$C_2H_4$** |
| **$C_2H_4OH$ ($CH_2CH_2OH$) Radical** |
| **$O_2C_2H_4OH$ Radical** |
| **$CH_2CO$** |
| **$CH_2CHO$ Radical** |
| **$OC_2H_4OH$ Radical** |
| $C_2H_3$ Radical |
| $C_2H_2$ |
| $C_2H_2OH$ (HOCHCH) Radical |
| HCCO Radical |
| CHOCHO ($(HCO)_2$) |
| HC(O)CO Radical |
| $C_2H$ Radical |

## Appendix B: Definition of photolysis terms

*Photochemistry*, a chemistry subfield, is the study of chemical reactions that conduct with the absorption of light (ultraviolet, visible or infrared) by atoms or molecules (Braslavsky, 2007).

*Absorbance*, *A* ($\lambda$), is logarithm to the base 10 (linear absorbance) of the incident spectral radiant power, $P_\lambda^0$, divided by the transmitted spectral radiant power, $P_\lambda$:

$$A(\lambda) = \log(\frac{P_\lambda^0}{P_\lambda}) = -\log T(\lambda) \tag{B.1}$$

$T$ ($\lambda$) is the transmittance at the particular wavelength ($\lambda$).

*Absorption coefficient*, *a* ($\lambda$), for a molecule is absorbance divided by the optical path-length:

$$a(\lambda) = \frac{A(\lambda)}{l} = \frac{1}{l}\log(\frac{P_\lambda^0}{P_\lambda}) \tag{B.2a}$$

If the natural logarithm (logarithm to the base e) is used, the absorption coefficient is defined as:

$$\alpha(\lambda) = a(\lambda)\ln(10) = \frac{1}{l}\ln(\frac{P_\lambda^0}{P_\lambda}) \tag{B.2b}$$

*Absorption cross-section*, $\sigma$ ($\lambda$), has been defined as linear napierian absorption coefficient, $\alpha$ ($\lambda$), divided by the number of existing molecules in a volume of the absorbing medium along the light radiation path typically with the unit of $cm^2$: (Braslavsky, 2007)

$$\sigma(\lambda) = \frac{\alpha(\lambda)}{C} \tag{B.3}$$

Where $C$ is the number concentration of molecular entities (number of molecules per volume); which is usually expressed as molecule/$cm^3$ specifically in photochemistry.

*Quantum yield*, $\varphi(\lambda)$, is the number of certain events occurring per photon absorbed by the system. The integral quantum yield is:

$$\varphi(\lambda) = \frac{\text{number of events}}{\text{number of photons absorbed}} \tag{B.4a}$$

For a photochemical reaction, the quantum yield is defined as:

$$\varphi(\lambda) = \frac{\text{amount of reactant consumed or product formed}}{\text{amount of photons absorbed}} \tag{B.4b}$$

*Irradiance*, *E*, (at a point of a surface) has been defined as radiant power, *P*, of all wavelengths coming toward the surface from all directions on a small element of surface (d*S*) divided by the area of the element:

$$E = \mathrm{d}P \big/ \mathrm{d}S \tag{B.5a}$$

If the radiant power is constant over the surface area considered:

$$E = P \big/ S \tag{B.5b}$$

There is an alternative definition which is integrating over the hemisphere observable from the certain point, of the expression $L \cdot \cos\theta \cdot \mathrm{d}\Omega$, where $L$ is the radiance at the certain point in the several directions of the incident elementary rays of solid angle $\Omega$, and $\theta$ is the angle between any of the rays and the normal to the surface at the certain point:

$$E = \int_{2\pi} L \cdot \cos\theta \cdot \mathrm{d}\Omega \tag{B.5c}$$

*Fluence rate*, $E_0$, (radiant energy fluence rate) has been defined as total radiant power, *P*, occurrence from all directions onto a small sphere divided by the cross-sectional area of that sphere which has unit of $W/m^2$ in SI:

$$E_0 = \mathrm{d}P \big/ \mathrm{d}S \tag{B.6a}$$

If the radiant power is constant over the area $S$:

$$E_0 = P \big/ S \tag{B.6b}$$

Also, there is an alternative definition for $E_0$:

$$E_0 = \int_{4\pi} L \cdot \mathrm{d}\Omega \tag{B.6c}$$

With $\Omega$ the solid angle of each light ray passing through the specific point on the surface and $L$ the radiance of the beam at that point.

According to the above defined terms, an equivalent for photochemical reaction rate can be derived as follows.

Based on equation (B.2b),

$$l \cdot \alpha(\lambda) = \ln(\frac{P_\lambda^0}{P_\lambda}) \tag{B.7}$$

Consequently:

$$\exp(l \cdot \alpha(\lambda)) = \frac{P_\lambda^0}{P_\lambda} \tag{B.8a}$$

So:

$$P_\lambda = P_\lambda^0 \cdot \exp(-l \cdot \alpha(\lambda)) \tag{B.8b}$$

Differentiating of both sides of equation (B.8b) results in:

$$\frac{\mathrm{d}P_\lambda}{\mathrm{d}l} = P_\lambda^0 \cdot (-\alpha(\lambda)) \cdot \exp(-l \cdot \alpha(\lambda)) \tag{B.9}$$

Replacing equation (B.8b) to equation (B.9) yields:

$$\frac{dP_\lambda}{dl} = -\alpha(\lambda) \cdot P_\lambda \tag{B.10}$$

Now, taking a cylindrical element in the reactor and applying energy balance over that:


**Figure B-1: Energy balance on a cylindrical element**

Energy rate consumed = Incoming energy rate – Outgoing energy rate (B.11)

Energy consumed = $A \cdot P_\lambda - A \cdot (P_\lambda + dP_\lambda)$ (B.12)

In both equations (B.11) and (B.12) it is assumed that all light energy is dissipated as heat, or consumed in energy of reaction.

Dividing equation (B.12) by the volume of the element and substituting equation (B.10) results in:

$$\frac{\text{Energy consumed}}{\text{Volume}} = \frac{-A \cdot dP_\lambda}{A \cdot dl} = -\frac{dP_\lambda}{dl} = \alpha(\lambda) \cdot P_\lambda \tag{B.13}$$

Photon irradiance for each wavelength is defined as:

$$E_{P_\lambda} = \frac{P_\lambda}{E_{photon,\lambda}} \tag{B.14}$$

Where $P_\lambda$ is spectral radiant power, (J/s cm$^2$ nm) and $E_{photon,\lambda}$ is energy per photon in the wavelength of $\lambda$, (J/photon). So $E_{P\lambda}$ has a unit of (photon/s cm$^2$ nm) and integrating over wavelength $\lambda$ removes nm from units.

Taking equation (B.13) divided by the energy per photon, and merging with (B.14) yields to:

$$\frac{\text{Photons consumed}}{\text{Volume}} = \alpha(\lambda) \cdot \frac{P_\lambda}{E_{\text{photon}}} = \alpha(\lambda) \cdot E_P \tag{B.15}$$

Substituting absorption coefficient, $\alpha$ ($\lambda$), from equation (B.3) gives:

$$\frac{\text{Photons consumed}}{\text{Volume}} = C \cdot \sigma \cdot E_P \tag{B.16}$$

Based on the definition of quantum yield in equation (B.4b),

$$\varphi = \frac{\text{Reactanat consumed}}{\text{Photon absorbed}} \tag{B.4b}$$

If both numerator and denominator are divided by (time × volume),

$$\phi = \frac{\text{Reactant consumed / time} \cdot \text{volume}}{\text{Photon absorbed / time} \cdot \text{volume}} \tag{B.17}$$

The numerator is then the definition of the reaction rate ($r$), hence the equation (B.17) can be written as:

$$r = \varphi \cdot \frac{\text{Photons consumed}}{\text{Volume}} \tag{B.18}$$

Therefore:

$$r = \varphi \cdot C \cdot \sigma \cdot E_P \tag{B.19}$$

This can be written for each component $i$ as:

$$-r_i = \varphi_i \cdot C_i \cdot \sigma_i \cdot E_P \tag{B.20}$$

If the value of quantum yields, the concentration of component $i$, the absorption cross section and the fluence rate are determined, the photochemical reaction rate of component $i$ can be calculated.

# Appendix C: The source code in MATLAB

The source code of the Ethylene Non-Thermal Comprehensive Model

### C.1. Data File

```
%%
length = 50;            % Reactor length in cm
dz = 1;
zspan = 0:dz:length;
Nnodes = 16;            % Number of internal nodes in the grid
Ncomp = 69;             % Number of compounds considered
P = 89000;              % Pressure in Pa
T = 300;                % Temperature in K
Ctot = P/1.38e-23/T;    % Concentration in molecules per m3
Ctot = Ctot/1e6;        % Concentration in molecules per cm3
%% CH4
MWCH4=16.04;
CmCH4=0;                %Concentration in grams per m3
CCH4=CmCH4/MWCH4;       %Concentration in moles per m3
CCH4=CCH4*6.022e23;     %Concentration in molecules per m3
yCH4 = CCH4/Ctot/1e6;   %CH4 mole fraction
%% C2H6
MWC2H6 = 30.07;
CmC2H6 = 0;               %Concentration in grams per m3
CC2H6=CmC2H6/MWC2H6;      %Concentration in moles per m3
CC2H6=CC2H6*6.022e23;     %Concentration in molecules per m3
yC2H6 = CC2H6/Ctot/1e6;   %C2H6 mole fraction
%% C2H4
MWC2H4=28.054;
CmC2H4=1;                   %Concentration in grams per m3
CC2H4=CmC2H4/MWC2H4;        %Concentration in moles per m3
CC2H4=CC2H4*6.022e23;       %Concentration in molecules per m3
yC2H4 = CC2H4/Ctot/1e6;     %C2H4 mole fraction
%%
yH2O = 0.02;            % Water mole fraction
yO3 = 0.00;
yO2 = 0.21*(1-yH2O-yCH4-yC2H6-yC2H4-yO3); % O2 mole fraction
yN2 = 0.79*(1-yH2O-yCH4-yC2H6-yC2H4-yO3); % N2 mole fraction
CCH4 = Ctot*yCH4;         % CH4 concentration (molecules/cm3)
CC2H6 = Ctot*yC2H6;       % C2H6 concentration (molecules/cm3)
CC2H4 = Ctot*yC2H4;       % C2H4 concentration (molecules/cm3)
CH2O = Ctot*yH2O;
CO2 = Ctot*yO2;
CN2 = Ctot*yN2;
CO3 = Ctot*yO3;

% Initial concentrations:
% y0(i+(j-1)*Ncomp) is initial concentration
% of compound j in node point i from the center

%% j  Compound
% -- --------
% 1     H radical
```

```
% 2     O2
% 3     N2 + Ar
% 4     H2O
% 5     O(3P) Radical
% 6     OH Radical
% 7     HO2 Radical
% 8     O(1D) Radical
% 9     O3
% 10    H2O2
% 11    H2
% 12    N2O
% 13    NO
% 14    NO2
% 15    NO3
% 16    N2O4
% 17    N2O3
% 18    N2O5
% 19    HNO2
% 20    HNO3
% 21    HO2NO2

% 22    CH4
% 23    CH3
% 24    CO
% 25    CO2
% 26    CH2OH
% 27    CH2O
% 28    CH3O2
% 29    CH3O
% 30    CH3OH
% 31    HCO
% 32    CH3OOH
% 33    CHO2
% 34    CH2OOH
% 35    HOCH2OO
% 36    CH3ONO
% 37    CH3ONO2
% 38    CH3O2NO2
% 39    CH2ONO2
% 40    HNO

% 41    C2H6
% 42    C2H5
% 43    C2H5O2
% 44    C2H5O
% 45    C2H4
% 46    C2H5OOH
% 47    CH3CHO
% 48    C2H5OH (CH3CH2OH)
% 49    CH3CO
% 50    C2H5ONO
% 51    C2H5ONO2
% 52    C2H5O2NO2
% 53    CH3C(O)O2
% 54    CH3C(O)OONO2
```

```
% 55    CH3C(O)OH
% 56    CH3C(O)OOH
% 57    CH3CHOH

% 45    C2H4*
% 58    C2H4OH (CH2CH2OH)
% 59    OC2H4OH
% 60    O2C2H4OH
% 61    CH2CO
% 62    CH2CHO
% 63    C2H3
% 64    C2H2
% 65    C2H2OH (HOCHCH)
% 66    HCCO
% 67    CHOCHO ((HCO)2)
% 68    HC(O)CO
% 69    C2H

%% Concertation Profile Forms

for i = 1:Nnodes
    y0(i) = 0;
    y0(i+Nnodes) = CO2;
    y0(i+2*Nnodes) = CN2;
    y0(i+3*Nnodes) = CH2O;
    for j = 4:Ncomp-1
        y0(i+j*Nnodes) = 0;
    end
    y0(i+8*Nnodes) = CO3;
    y0(i+21*Nnodes) = CCH4;
    y0(i+40*Nnodes) = CC2H6;
    y0(i+44*Nnodes) = CC2H4;
end

r0 = 1.25;                % Internal diameter, cm
r1 = 2.1;                 % External diameter, cm

for j = 1:Ncomp
    for k = 1:2      % k is spectral line (1 = 185 nm, 2 = 254 nm)
        sig(j,k) = 0;
    end
end

%% Adsorption Cross-Section (Sigma)
sig(2,1) = 2.04e-21;
sig(4,1) = 5.5e-20;
sig(7,1) = 3.25e-18;
sig(7,2) = 2.99e-19;
sig(9,1) = 6.61e-19;
sig(9,2) = 1.148e-17;
sig(10,1) = 8.01e-19;
sig(10,2) = 6.99e-20;
sig(12,1) = 1.43e-19;
sig(14,1) = 6.88e-18;
sig(14,2) = 1.16e-20;
```

```
sig(18,1) = 1.85e-17;
sig(18,2) = 3.26e-19;
sig(19,1) = 9.0e-19;
sig(19,2) = 1.456e-19;
sig(20,1) = 1.63e-17;
sig(20,2) = 1.95e-20;
sig(21,1) = 1.24e-17;
sig(21,2) = 3.63e-19;
sig(27,2) = 3.42e-21;
sig(28,2) = 3.47e-18;
sig(32,1) = 1.5e-18;
sig(32,2) = 3.38e-20;
sig(36,1) = 1.2e-18;
sig(36,2) = 1.12e-18;
sig(37,1) = 2.1e-17;
sig(37,2) = 3.34e-20;
sig(38,1) = 1.11e-17;
sig(38,2) = 3.4e-19;
sig(47,1) = 1.28e-17;
sig(47,2) = 1.57e-20;
sig(51,1) = 1.71e-17;
sig(51,2) = 4.18e-20;
sig(54,2) = 1e-19;
sig(55,1) = 3.95e-19;
sig(55,2) = 5.07e-21;

sig(64,1) = 3.3e-19;
sig(67,2) = 1.34e-20;

%% Quantum yield (Phi)
phi(2,1) = 1;
phi(4,1) = 1;
phi(7,1) = 1;
phi(7,2) = 1;
phi_a(9,1) = 0.9;
phi_a(9,2) = 0.9;
phi_b(9,1) = 0.1;
phi_b(9,2) = 0.1;
phi_a(10,1) = 0.75;
phi_a(10,2) = 1;
phi_b(10,1) = 0.16;
phi(12,1) = 1;
phi(14,1) = 1;
phi(14,2) = 1;
phi_a(18,1) = 0;
phi_a(18,2) = 0.08;
phi_b(18,1) = 1;
phi_b(18,2) = 0.72;
phi(19,1) = 1;
phi(19,2) = 1;
phi(20,1) = 1;
phi(20,2) = 0.97;
phi_a(21,1) = 0.7;
phi_a(21,2) = 0.8;
phi_b(21,1) = 0.3;
phi_b(21,2) = 0.2;
```

```
phi_a(27,2) = 0.305;
phi_b(27,2) = 0.495;
phi(32,1) = 1;
phi(32,2) = 1;
phi(36,1) = 0.76;
phi(36,2) = 0.76;
phi_a(37,1) = 0.7;
phi_a(37,2) = 1;
phi_b(37,1) = 0.3;
phi_b(37,2) = 0;
phi_a(38,1) = 0.5;
phi_a(38,2) = 0.5;
phi_b(38,1) = 0.5;
phi_b(38,2) = 0.5;
phi_a(47,1) = 0;
phi_a(47,2) = 0.28;
phi_b(47,1) = 0;
phi_b(47,2) = 0.63;
phi(51,1) = 1;
phi(51,2) = 1;
phi_a(54,2) = 0.76;
phi_b(54,2) = 0.24;
phi_a(55,1) = 0.5;
phi_a(55,2) = 0.5;
phi_b(55,1) = 0.5;
phi_b(55,2) = 0.5;

phi(64,1) = 0.14;
phi_a(67,2) = 0.156;
phi_b(67,2) = 0.514;
phi_c(67,2) = 0.330;

%% Light Property
power1 = 40*0.08;              % Emitted light at 185nm (W)
power2 = 40*0.30;              % Emitted light at 254nm (W)
nu1 = 299792458/185e-9;
nu2 = 299792458/254e-9;
photon1 = 6.626e-34*nu1; % Photon energy at 185 nm
photon2 = 6.626e-34*nu2; % Photon energy at 254 nm
E0(1) = power1/photon1/length/2/pi/r0; % Photons per cm2 per s leaving lamp
E0(2) = power2/photon2/length/2/pi/r0; % 1 = 185 nm, 2 = 254 nm
%% diffusivity
D_coeff = xlsread('diffusivity.xlsx','C2H4','J5:J73');
D = D_coeff * T^1.75/P;
%% Reactor
Q = 1000/60;             % Flow rate (cm3/s)
U = Q/pi/(r1*r1-r0*r0); % Mean gas velocity (cm/s)
reflamp = 0.7;           % Reflection at the lamp
```

## C.2. Function File

```
function dydz = f(z,y,dz,Nnodes,Ncomp,r0,r1,sig,E0,D,U,P,T,reflamp,phi,
phi_a, phi_b,phi_c)

dydz = zeros(Nnodes*Ncomp,1);

dr = (r1-r0)/(Nnodes+1);   % Node distance

% User-friendly notation of concentrations: i = node number
%                                           j = compound number

for j = 1:Ncomp
    for i = 1:Nnodes
        C(j,i+1) = y(i+Nnodes*(j-1));          % concentration of j in node i,
molecules/cm3
    end
    C(j,1) = C(j,2) - (C(j,3) - C(j,2))/3;     % boundary condition: zero
radial flux
    C(j,Nnodes+2) = C(j,Nnodes+1) - (C(j,Nnodes) - C(j,Nnodes+1))/3;
end

% Calculate radiation fields

Eref(1,1)=E0(1)/reflamp;    %Considering original radiation from the lamp
Eref(1,2)=E0(2)/reflamp;    %Considering original radiation from the lamp
for k = 1:2
    for i=1:Nnodes+1
        Etot(i+1,k)=0;
    end
    while (Eref(1,k)>0.01*E0(k))
    E(1,k) = reflamp*Eref(1,k);
    for i = 1:Nnodes+1
        Ei = E(i,k);
        r = r0 + dr*(i-0.5);
        alpha = 0;
        for j = 1:Ncomp
            Ci(j) = (C(j,i) + C(j,i+1))/2;
            alpha = alpha + Ci(j)*sig(j,k);
        end
        E(i+1,k) = (Ei/dr - alpha*Ei/2 - Ei/2/r)/(1/dr + alpha/2 + 1/2/r);
        if E(i+1,k) < 0
            E(i+1,k) = 0;
        end
    end
    Eref(Nnodes+2,k)=0.99*E(Nnodes+2,k);
    for i=Nnodes+1:-1:1
        Erefi=Eref(i+1,k);
        r=r0+dr*(i-0.5);
        alpha=0;
        for j=1:Ncomp
            Ci(j)=(C(j,i)+C(j,i+1))/2;
            alpha=alpha+Ci(j)*sig(j,k);
        end
```

```
        Eref(i,k)=(Erefi/dr+Erefi/2/r-alpha*Erefi/2)/(1/dr-1/2/r+alpha/2);
        if Eref(i,k)<0
            Eref(i,k)=0;
        end
    end
    for i=1:Nnodes+2
        Etot(i,k)=Etot(i,k)+E(i,k)+Eref(i,k);
    end
    end
end

for i = 2:Nnodes+1


    % Calculate reaction rates per reaction

%% Photochemical reactions - Background (bp = background photochemical)
    rbp1(i) = C(4,i)*sig(4,1)*Etot(i,1)*phi(4,1);
    rbp2(i) = C(2,i)*sig(2,1)*Etot(i,1)*phi(2,1);
    rbp3a(i) = C(9,i)*((sig(9,1)*Etot(i,1)*phi_a(9,1)) +
(sig(9,2)*Etot(i,2)*phi_a(9,2)));
    rbp3b(i) = C(9,i)*((sig(9,1)*Etot(i,1)*phi_b(9,1)) +
(sig(9,2)*Etot(i,2)*phi_b(9,2)));
    rbp4(i) = C(7,i)*(sig(7,1)*Etot(i,1)*phi(7,1) +
sig(7,2)*Etot(i,2)*phi(7,2));
    rbp5a(i) = C(10,i)*(sig(10,1)*Etot(i,1)*phi_a(10,1) +
sig(10,2)*Etot(i,2)*phi_a(10,2));
    rbp5b(i) = C(10,i)*sig(10,1)*Etot(i,1)*phi_b(10,1);
    rbp6(i) = C(14,i)*(sig(14,1)*Etot(i,1)*phi(14,1) +
sig(14,2)*Etot(i,2)*phi(14,2));
    rbp7(i) = C(12,i)*(sig(12,1)*Etot(i,1)*phi(12,1));
    rbp8a(i) = C(18,i)*(sig(18,1)*Etot(i,1)*phi_a(18,1) +
sig(18,2)*Etot(i,2)*phi_a(18,2));
    rbp8b(i) = C(18,i)*(sig(18,1)*Etot(i,1)*phi_b(18,1) +
sig(18,2)*Etot(i,2)*phi_b(18,2));
    rbp9(i) = C(19,i)*(sig(19,1)*Etot(i,1)*phi(19,1) +
sig(19,2)*Etot(i,2)*phi(19,2));
    rbp10(i) = C(20,i)*(sig(20,1)*Etot(i,1)*phi(20,1) +
sig(20,2)*Etot(i,2)*phi(20,2));
    rbp11a(i) = C(21,i)*(sig(21,1)*Etot(i,1)*phi_a(21,1) +
sig(21,2)*Etot(i,2)*phi_a(21,2));
    rbp11b(i) = C(21,i)*(sig(21,1)*Etot(i,1)*phi_b(21,1) +
sig(21,2)*Etot(i,2)*phi_b(21,2));

%% Photochemical reactions - Pollutant degradation (pdp = pollutant
degradation photochemical)
    rpdp2a(i) = C(27,i)*(sig(27,2)*Etot(i,2)*phi_a(27,2));
    rpdp2b(i) = C(27,i)*(sig(27,2)*Etot(i,2)*phi_b(27,2));
    rpdp4(i) = C(36,i)*(sig(36,1)*Etot(i,1)*phi(36,1) +
sig(36,2)*Etot(i,2)*phi(36,2));
```

```
    rpdp5a(i) = C(37,i)*(sig(37,1)*Etot(i,1)*phi_a(37,1) +
sig(37,2)*Etot(i,2)*phi_a(37,2));
    rpdp5b(i) = C(37,i)*(sig(37,1)*Etot(i,1)*phi_b(37,1) +
sig(37,2)*Etot(i,2)*phi_b(37,2));
    rpdp6(i) = C(32,i)*(sig(32,1)*Etot(i,1)*phi(32,1) +
sig(32,2)*Etot(i,2)*phi(32,2));
    rpdp7a(i) = C(38,i)*(sig(38,1)*Etot(i,1)*phi_a(38,1) +
sig(38,2)*Etot(i,2)*phi_a(38,2));
    rpdp7b(i) = C(38,i)*(sig(38,1)*Etot(i,1)*phi_b(38,1) +
sig(38,2)*Etot(i,2)*phi_b(38,2));

%% Photochemical reactions - Pollutant degradation (rethp = R of Ehanol -
Photochemical)
    rethp3a(i) = C(47,i)*(sig(47,1)*Etot(i,1)*phi_a(47,1) +
sig(47,2)*Etot(i,2)*phi_a(47,2));
    rethp3b(i) = C(47,i)*(sig(47,1)*Etot(i,1)*phi_b(47,1) +
sig(47,2)*Etot(i,2)*phi_b(47,2));
    rethp4(i) = C(51,i)*(sig(51,1)*Etot(i,1)*phi(51,1) +
sig(51,2)*Etot(i,2)*phi(51,2));
    rethp6a(i) = C(54,i)*(sig(54,2)*Etot(i,2)*phi_a(54,2));
    rethp6b(i) = C(54,i)*(sig(54,2)*Etot(i,2)*phi_b(54,2));
    rethp7a(i) = C(55,i)*(sig(55,1)*Etot(i,1)*phi_a(55,1) +
sig(55,2)*Etot(i,2)*phi_a(55,2));
    rethp7b(i) = C(55,i)*(sig(55,1)*Etot(i,1)*phi_b(55,1) +
sig(55,2)*Etot(i,2)*phi_b(55,2));

%% Photochemical reactions - Pollutant degradation (rethylp = R of Ethylene -
Photochemical)
     rethylp1(i) = C(64,i)*sig(64,1)*Etot(i,1)*phi(64,1);
     rethylp2a(i) = C(67,i)*sig(67,2)*Etot(i,2)*phi_a(67,2);
     rethylp2b(i) =C(67,i)*sig(67,2)*Etot(i,2)*phi_b(67,2);
     rethylp2c(i) = C(67,i)*sig(67,2)*Etot(i,2)*phi_c(67,2);

%% Chemical Reactions - Background (rate constant)
    kb1 = 1.8e-11*exp(180/T);
    kb2 = 3e-11*exp(200/T);
    kb3 = 1.4e-12*exp(-2000/T);
    kb4 = 6e-34*(T/300)^(-2.8)*C(2,i) + 5.6e-34*(T/300)^(-2.8)*C(3,i);
    kb5 = 2.7e-34*T^(-0.41)*(C(2,i)+C(3,i));
    kb6 = 8e-12*exp(-2060/T);
    kb7 = 1.63e-10*exp(60/T);
    kb8 = 3.3e-11*exp(55/T);
    kb9 = 2.15e-11*exp(110/T);
    kb10 = 1.2e-10*exp(0/T);
    kb11 = 1.1e-10*exp(0/T);
    kb12 = 2.9e-12*exp(-160/T);
    kb13 = 1.7e-12*exp(-940/T);
    kb14 = 2.8e-12*exp(-1800/T);
    kb15 = 7.9e-14*(T/298)^(2.6)*exp(945/T);
    kb16 = 4.8e-11*exp(250/T);
```

```
    kb17zero = 6.9e-31*(T/300)^(-0.8)*C(3,i);
    kb17inf = 2.6e-11;
    kb17Fc = 0.5;
    Nkb17 = 0.75 - 1.27*log10(kb17Fc);
    kb17F = 10^((log10(kb17Fc))/(1+((log10(kb17zero/kb17inf))/Nkb17)^2));
    kb17 = kb17zero*kb17inf*kb17F/(kb17zero + kb17inf);

    kb18 = 1e-14*exp(-490/T);
    kb19 = 2.2e-13*exp(600/T) + 1.9e-33*exp(980/T)*C(3,i) + 1.6e-
33*exp(980/T)*C(2,i);
    kb19 = kb19*(1 + 1.4e-21*exp(2200/T)*C(4,i));
    kb20 = 1.4e-10*exp(-470/T);
    kb21a = 7.2e-11;
    kb21b = 1.6e-12;
    kb21c = 6.9e-12;
    kb22 = 2.8e-36*(T/300)^(-0.9)*C(3,i);
    kb23a = 5.0e-13;
    kb23b = 4.64e-11*exp(20/T);
    kb23c = 7.25e-11*exp(20/T);

    kb24zero = 9e-32*(T/300)^(-1.5)*C(3,i);
    kb24inf = 3e-11;
    kb24 =
(kb24zero/(1+(kb24zero/kb24inf)))*0.6^((1+(log10(kb24zero/kb24inf))^2)^(-1));

    kb25 = 5.15e-12*exp(210/T);

    kb26zero = 1.3e-31*(T/300)^(-1.5)*C(3,i);
    kb26inf = 2.3e-11*(T/300)^(0.24);
    kb26Fc = 0.6;
    Nkb26 = 0.75 - 1.27*log10(kb26Fc);
    kb26F = 10^((log10(kb26Fc))/(1+((log10(kb26zero/kb26inf))/Nkb26)^2));
    kb26 = kb26zero*kb26inf*kb26F/(kb26zero + kb26inf);

    kb27 = 1e-11;

    kb28zero = 1.4e-33*(T/300)^(-3.8)*C(3,i);
    kb28inf = 1e-12;
    kb28Fc = 0.4;
    Nkb28 = 0.75 - 1.27*log10(kb28Fc);
    kb28F = 10^((log10(kb28Fc))/(1+((log10(kb28zero/kb28inf))/Nkb28)^2));
    kb28 = kb28zero*kb28inf*kb28F/(kb28zero + kb28inf);

    kb29zero = 1.3e-5*(T/300)^(-3.8)*exp(-6400/T)*C(3,i);
    kb29inf = 1.15e16*exp(-6400/T);
    kb29Fc = 0.4;
    Nkb29 = 0.75 - 1.27*log10(kb29Fc);
    kb29F = 10^((log10(kb29Fc))/(1+((log10(kb29zero/kb29inf))/Nkb29)^2));
    kb29 = kb29zero*kb29inf*kb29F/(kb29zero + kb29inf);

    kb30 = 4e-10*exp(-340/T);

    kb31zero = 7.4e-31*(T/300)^(-2.4)*C(3,i);
    kb31inf = 3.3e-11*(T/300)^(-0.3);
```

```
kb31Fc = exp(-T/1420);
Nkb31 = 0.75 - 1.27*log10(kb31Fc);
kb31F = 10^((log10(kb31Fc))/(1+((log10(kb31zero/kb31inf))/Nkb31)^2));
kb31 = kb31zero*kb31inf*kb31F/(kb31zero + kb31inf);

kb32zero = 3.3e-30*(T/300)^(-3)*C(3,i);
kb32inf = 4.1e-11;
kb32Fc = 0.4;
Nkb32 = 0.75 - 1.27*log10(kb32Fc);
kb32F = 10^((log10(kb32Fc))/(1+((log10(kb32zero/kb32inf))/Nkb32)^2));
kb32 = kb32zero*kb32inf*kb32F/(kb32zero + kb32inf);

kb33 = 2e-11;
kb34 = 1.8e-11*exp(-390/T);
kb35 = 8.3e-15*exp(850/T);
kb36 = 1.3e-12*exp(380/T);
kb37 = 3.3e-12*exp(270/T);

kb38zero = 1.8e-31*(T/300)^(-3.2)*C(3,i);
kb38inf = 4.7e-12;
kb38Fc = 0.6;
Nkb38 = 0.75 - 1.27*log10(kb38Fc);
kb38F = 10^((log10(kb38Fc))/(1+((log10(kb38zero/kb38inf))/Nkb38)^2));
kb38 = kb38zero*kb38inf*kb38F/(kb38zero + kb38inf);

kb39zero = 4.1e-5*exp(-10650/T)*C(3,i);
kb39inf = 4.8e15*exp(-11170/T);
kb39Fc = 0.6;
Nkb39 = 0.75 - 1.27*log10(kb39Fc);
kb39F = 10^((log10(kb39Fc))/(1+((log10(kb39zero/kb39inf))/Nkb39)^2));
kb39 = kb39zero*kb39inf*kb39F/(kb39zero + kb39inf);

kb40 = 2.3e-12*exp(170/T);
kb41 = 3.0e-12*exp(-1500/T);
kb42 = 3.3e-39*exp(530/T);
kb43 = 1.5e-11*exp(170/T);

kb44zero = 3.1e-34*(T/300)^(-7.7)*C(3,i);
kb44inf = 7.9e-12*(T/300)^(1.4);
kb44Fc = 0.6;
Nkb44 = 0.75 - 1.27*log10(kb44Fc);
kb44F = 10^((log10(kb44Fc))/(1+((log10(kb44zero/kb44inf))/Nkb44)^2));
kb44 = kb44zero*kb44inf*kb44F/(kb44zero + kb44inf);

kb45zero = 1.9e-7*(T/300)^(-8.7)*exp(-4880/T)*C(3,i);
kb45inf = 4.7e15*(T/300)^(0.4)*exp(-4880/T);
kb45Fc = 0.6;
Nkb45 = 0.75 - 1.27*log10(kb45Fc);
kb45F = 10^((log10(kb45Fc))/(1+((log10(kb45zero/kb45inf))/Nkb45)^2));
kb45 = kb45zero*kb45inf*kb45F/(kb45zero + kb45inf);

kb46zero = 3.6e-30*(T/300)^(-4.1)*C(3,i);
kb46inf = 1.9e-12*(T/300)^(0.2);
kb46Fc = 0.35;
```

```
    Nkb46 = 0.75 - 1.27*log10(kb46Fc);
    kb46F = 10^((log10(kb46Fc))/(1+((log10(kb46zero/kb46inf))/Nkb46)^2));
    kb46 = kb46zero*kb46inf*kb46F/(kb46zero + kb46inf);

    kb47zero = 1.3e-3*(T/300)^(-3.5)*exp(-11000/T)*C(3,i);
    kb47inf = 9.7e14*(T/300)^(0.1)*exp(-11080/T);
    kb47Fc = 0.35;
    Nkb47 = 0.75 - 1.27*log10(kb47Fc);
    kb47F = 10^((log10(kb47Fc))/(1+((log10(kb47zero/kb47inf))/Nkb47)^2));
    kb47 = kb47zero*kb47inf*kb47F/(kb47zero + kb47inf);

    kb48 = 2.5e-22;
    kb49 = 1.2e-13*exp(-2450/T);
    kb50 = 2.5e-19;

    kb51zero = 4.4e-32*(T/300)^(-1.3)*C(3,i);
    kb51inf = 7.5e-11*(T/300)^(0.2);
    kb51 =
(kb51zero/(1+(kb51zero/kb51inf)))*0.6^((1+(log10(kb51zero/kb51inf))^2)^(-1));

%% Chemical Reactions - Background (reaction rate)
    rb1(i) = kb1*C(5,i)*C(6,i);
    rb2(i) = kb2*C(5,i)*C(7,i);
    rb3(i) = kb3*C(5,i)*C(10,i);
    rb4(i) = kb4*C(5,i)*C(2,i);
    rb5(i) = kb5*C(5,i)*C(5,i);
    rb6(i) = kb6*C(5,i)*C(9,i);
    rb7(i) = kb7*C(8,i)*C(4,i);
    rb8(i) = kb8*C(8,i)*C(2,i);
    rb9(i) = kb9*C(8,i)*C(3,i);
    rb10(i) = kb10*C(8,i)*C(9,i);
    rb11(i) = kb11*C(8,i)*C(11,i);
    rb12(i) = kb12*C(6,i)*C(10,i);
    rb13(i) = kb13*C(6,i)*C(9,i);
    rb14(i) = kb14*C(6,i)*C(11,i);
    rb15(i) = kb15*C(6,i)*C(6,i);
    rb16(i) = kb16*C(6,i)*C(7,i);
    rb17(i) = kb17*C(6,i)*C(6,i);
    rb18(i) = kb18*C(7,i)*C(9,i);
    rb19(i) = kb19*C(7,i)*C(7,i);
    rb20(i) = kb20*C(1,i)*C(9,i);
    rb21a(i) = kb21a*C(1,i)*C(7,i);
    rb21b(i) = kb21b*C(1,i)*C(7,i);
    rb21c(i) = kb21c*C(1,i)*C(7,i);
    rb22(i) = kb22*C(8,i)*C(3,i);
    rb23a(i) = kb23a*C(8,i)*C(12,i);
    rb23b(i) = kb23b*C(8,i)*C(12,i);
    rb23c(i) = kb23c*C(8,i)*C(12,i);
    rb24(i) = kb24*C(5,i)*C(13,i);
    rb25(i) = kb25*C(5,i)*C(14,i);
    rb26(i) = kb26*C(5,i)*C(14,i);
    rb27(i) = kb27*C(5,i)*C(15,i);
    rb28(i) = kb28*C(14,i)*C(14,i);
    rb29(i) = kb29*C(16,i);
    rb30(i) = kb30*C(1,i)*C(14,i);
```

```
    rb31(i) = kb31*C(6,i)*C(13,i);
    rb32(i) = kb32*C(6,i)*C(14,i);
    rb33(i) = kb33*C(6,i)*C(15,i);
    rb34(i) = kb34*C(6,i)*C(19,i);
    rb35(i) = kb35*C(6,i)*C(20,i);
    rb36(i) = kb36*C(6,i)*C(21,i);
    rb37(i) = kb37*C(7,i)*C(13,i);
    rb38(i) = kb38*C(7,i)*C(14,i);
    rb39(i) = kb39*C(21,i);
    rb40(i) = kb40*C(7,i)*C(15,i);
    rb41(i) = kb41*C(13,i)*C(9,i);
    rb42(i) = kb42*C(13,i)*C(13,i)*C(2,i);
    rb43(i) = kb43*C(13,i)*C(15,i);
    rb44(i) = kb44*C(13,i)*C(14,i);
    rb45(i) = kb45*C(17,i);
    rb46(i) = kb46*C(14,i)*C(15,i);
    rb47(i) = kb47*C(18,i);
    rb48(i) = kb48*C(18,i)*C(4,i);
    rb49(i) = kb49*C(14,i)*C(9,i);
    rb50(i) = kb50*C(9,i)*C(19,i);
    rb51(i) = kb51*C(1,i)*C(2,i);

%% Chemical Reactions - Pollutant (pd = pollutant degradation)
    kpd1a = 1.31e-10;
    kpd1b = 0.35e-10;
    kpd1c = 0.09e-10;
    kpd2 = 2.45e-12*exp(-1775/T);

    kpd3zero = 4e-31*(T/300)^(-3.6)*C(3,i);
    kpd3inf = 1.2e-12*(T/300)^(1.1);
    kpd3 =
(kpd3zero/(1+(kpd3zero/kpd3inf)))*0.6^((1+(log10(kpd3zero/kpd3inf))^2)^(-1));

    kpd4 = 4.7e-12*exp(-210/T);
    kpd5a = 0.83*1.3e-10;
    kpd5b = 0.17*1.3e-10;
    kpd6 = 9.1e-12;
    kpd7 = 3.9e-14*exp(-900/T);

    kpd8zero = 2.3e-29*(T/300)^(-2.8)*C(3,i);
    kpd8inf = 3.8e-11*(T/300)^(-0.6);
    kpd8 =
(kpd8zero/(1+(kpd8zero/kpd8inf)))*0.6^((1+(log10(kpd8zero/kpd8inf))^2)^(-1));

    kpd9 = 1.1e-11*exp(-1200/T);

    kpd10zero = 5.3e-29*(T/300)^(-4.4)*C(3,i);
    kpd10inf = 1.9e-11*(T/300)^(-1.8);
    kpd10 =
(kpd10zero/(1+(kpd10zero/kpd10inf)))*0.6^((1+(log10(kpd10zero/kpd10inf))^2)^(
-1));

    kpd11 = 9.7e-15*exp(625/T);
    kpd12 = 2.4e12*exp(-7000/T);
```

```
    kpd13 = 5.8e-16;
    kpd14 = 3.4e-11*exp(-1600/T);
    kpd15 = 5.5e-12*exp(125/T);
    kpd16 = 4.1e-13*exp(750/T);
    kpd17 = 2.9e-16*exp(-1000/T);
    kpd18a = 1.03e-13*exp(365/T) - (7.4e-13*exp(-520/T));
    kpd18b = 7.4e-13*exp(-520/T);
    kpd19 = 2.8e-12*exp(300/T);

    kpd20zero = 2.5e-30*(T/300)^(-5.5)*C(3,i);
    kpd20inf = 1.8e-11;
    kpd20Fc = 0.36;
    Nkpd20 = 0.75 - 1.27*log10(kpd20Fc);
    kpd20F =
10^((log10(kpd20Fc))/(1+((log10(kpd20zero/kpd20inf))/Nkpd20)^2));
    kpd20 = kpd20zero*kpd20inf*kpd20F/(kpd20zero + kpd20inf);

    kpd21zero = 9e-5*exp(-9690/T)*C(3,i);
    kpd21inf = 1.1e16*exp(-10560/T);
    kpd21Fc = 0.6;
    Nkpd21 = 0.75 - 1.27*log10(kpd21Fc);
    kpd21F =
10^((log10(kpd21Fc))/(1+((log10(kpd21zero/kpd21inf))/Nkpd21)^2));
    kpd21 = kpd21zero*kpd21inf*kpd21F/(kpd21zero + kpd21inf);

    kpd22 = 1.3e-12;
    kpd23 = 8e-13*exp(-1000/T);
    kpd24 = 5.2e-12;
    kpd25a = 0.35*2.9e-12*exp(190/T);
    kpd25b = 0.65*2.9e-12*exp(190/T);

    kpd26azero = 5.9e-33*(T/300)^(-1.4)*C(3,i);
    kpd26ainf = 1.1e-12*(T/300)^(1.3);
    kpd26a =
(kpd26azero/(1+(kpd26azero/kpd26ainf)))*0.6^((1+(log10(kpd26azero/kpd26ainf))
^2)^(-1));

    kpd26bzero = 1.5e-13*(T/300)^(0.6)*C(3,i);
    kpd26binf = 2.1e-9*(T/300)^(6.1);
    kpd26b =
(kpd26bzero/(1+(kpd26bzero/kpd26binf)))*0.6^((1+(log10(kpd26bzero/kpd26binf))
^2)^(-1));

    kpd27 = 7.5e-11*exp(115/T);
    kpd28 = 2e-12;
    kpd29 = 2.3e-12*(T/300)^(-0.7);
    kpd30a = (0.85)*6.38e-18*(T^2)*exp(144/T);
    kpd30b = (0.15)*6.38e-18*(T^2)*exp(144/T);

%% Chemical Reactions - pollutant (CH4) (reaction rate)
    rpd1a(i) = kpd1a*C(22,i)*C(8,i);
    rpd1b(i) = kpd1b*C(22,i)*C(8,i);
    rpd1c(i) = kpd1c*C(22,i)*C(8,i);
    rpd2(i) = kpd2*C(22,i)*C(6,i);
```

```
    rpd3(i) = kpd3*C(23,i)*C(2,i);
    rpd4(i) = kpd4*C(23,i)*C(9,i);
    rpd5a(i) = kpd5a*C(23,i)*C(5,i);
    rpd5b(i) = kpd5b*C(23,i)*C(5,i);
    rpd6(i) = kpd6*C(26,i)*C(2,i);
    rpd7(i) = kpd7*C(29,i)*C(2,i);
    rpd8(i) = kpd8*C(29,i)*C(13,i);
    rpd9(i) = kpd9*C(29,i)*C(14,i);
    rpd10(i) = kpd10*C(29,i)*C(14,i);
    rpd11(i) = kpd11*C(27,i)*C(7,i);
    rpd12(i) = kpd12*C(35,i);
    rpd13(i) = kpd13*C(27,i)*C(15,i);
    rpd14(i) = kpd14*C(27,i)*C(5,i);
    rpd15(i) = kpd15*C(27,i)*C(6,i);
    rpd16(i) = kpd16*C(28,i)*C(7,i);
    rpd17(i) = kpd17*C(28,i)*C(9,i);
    rpd18a(i) = kpd18a*C(28,i)*C(28,i);
    rpd18b(i) = kpd18b*C(28,i)*C(28,i);
    rpd19(i) = kpd19*C(28,i)*C(13,i);
    rpd20(i) = kpd20*C(28,i)*C(14,i);
    rpd21(i) = kpd21*C(38,i);
    rpd22(i) = kpd22*C(28,i)*C(15,i);
    rpd23(i) = kpd23*C(37,i)*C(6,i);
    rpd24(i) = kpd24*C(31,i)*C(2,i);
    rpd25a(i) = kpd25a*C(32,i)*C(6,i);
    rpd25b(i) = kpd25b*C(32,i)*C(6,i);
    rpd26a(i) = kpd26a*C(24,i)*C(6,i);
    rpd26b(i) = kpd26b*C(24,i)*C(6,i);
    rpd27(i) = kpd27*C(25,i)*C(8,i);
    rpd28(i) = kpd28*C(33,i)*C(2,i);
    rpd29(i) = kpd29*C(29,i)*C(13,i);
    rpd30a(i) = kpd30a*C(6,i)*C(30,i);
    rpd30b(i) = kpd30b*C(6,i)*C(30,i);

%% Ethane Reactions (keth = K of Ethane rxn's)
    keth1 = 7.66e-12*exp(-1020/T);
    keth2 = 0.5e-17;

    keth3zero = 1.5e-28*(T/300)^(-3)*C(3,i);
    keth3inf = 8e-12*(T/300)^(0);
    keth3 =
(keth3zero/(1+(keth3zero/keth3inf)))*0.6^((1+(log10(keth3zero/keth3inf))^2)^(
-1));

    keth4a = 0.6*6.8e-14;
    keth4b = 0.4*6.8e-14;
    keth5 = 2.6e-12*exp(380/T);
    keth6 = 7.5e-13*exp(700/T);

    keth7zero = 1.3e-29*(T/300)^(-6.2)*C(3,i);
    keth7inf = 8.8e-12;
    keth7Fc = 0.31;
    Nketh7 = 0.75 - 1.27*log10(keth7Fc);
    keth7F =
10^((log10(keth7Fc))/(1+((log10(keth7zero/keth7inf))/Nketh7)^2));
```

```
    keth7 = keth7zero*keth7inf*keth7F/(keth7zero + keth7inf);

    keth8zero = 4.8e-4*exp(-9285/T)*C(3,i);
    keth8inf = 8.8e15*exp(-10440/T);
    keth8Fc = 0.31;
    Nketh8 = 0.75 - 1.27*log10(keth8Fc);
    keth8F =
10^((log10(keth8Fc))/(1+((log10(keth8zero/keth8inf))/Nketh8)^2));
    keth8 = keth8zero*keth8inf*keth8F/(keth8zero + keth8inf);

    keth9 = 2.3e-12;
    keth10 = 6.3e-14*exp(-550/T);

    keth11zero = 2.8e-27*(T/300)^(-4)*C(3,i);
    keth11inf = 5e-11*(T/300)^(-0.2);
    keth11 =
(keth11zero/(1+(keth11zero/keth11inf)))*0.6^((1+(log10(keth11zero/keth11inf))
^2)^(-1));

    keth12 = 1.1e-11;

    keth13zero = 2.0e-27*(T/300)^(-4)*C(3,i);
    keth13inf = 2.8e-11*(T/300)^(-1);
    keth13 =
(keth13zero/(1+(keth13zero/keth13inf)))*0.6^((1+(log10(keth13zero/keth13inf))
^2)^(-1));

    keth14 = 1.8e-11*exp(-1100/T);
    keth15 = 4.4e-12*exp(365/T);
    keth16 = 1.4e-12*exp(-1860/T);
    keth17a = 0.5*1e-12*exp(-490/T);
    keth17b = 0.5*1e-12*exp(-490/T);
    keth18a = 1.0*3.35e-12;
    keth18b = 0.0*3.35e-12;
    keth18c = 0.0*3.35e-12;
    keth19 = 1.9e-11;
    keth20 = 5.1e-12;
    keth21a = 0.8*4.3e-13*exp(1040/T);
    keth21b = 0.2*4.3e-13*exp(1040/T);
    keth22a = 0.9*2e-12*exp(500/T);
    keth22b = 0.1*2e-12*exp(500/T);
    keth23a = 0.9*4.4e-13*exp(1070/T);
    keth23b = 0.1*4.4e-13*exp(1070/T);
    keth24 = 2.9e-12*exp(500/T);
    keth25 = 7.5e-12*exp(290/T);

    keth26zero = 2.7e-28*(T/300)^(-7.1)*C(3,i);
    keth26inf = 1.2e-11*(T/300)^(-0.9);
    keth26Fc = 0.3;
    Nketh26 = 0.75 - 1.27*log10(keth26Fc);
    keth26F =
10^((log10(keth26Fc))/(1+((log10(keth26zero/keth26inf))/Nketh26)^2));
    keth26 = keth26zero*keth26inf*keth26F/(keth26zero + keth26inf);
```

```
    keth27zero = 4.9e-3*exp(-12100/T)*C(3,i);
    keth27inf = 5.4e16*exp(-13830/T);
    keth27Fc = 0.3;
    Nketh27 = 0.75 - 1.27*log10(keth27Fc);
    keth27F =
10^((log10(keth27Fc))/(1+((log10(keth27zero/keth27inf))/Nketh27)^2));
    keth27 = keth27zero*keth27inf*keth27F/(keth27zero + keth27inf);

    keth28 = 0.64*3.15e-14*exp(920/T);
    keth29 = 3.8e-15;

    keth33 = 3.6e-12;
    keth34a = 0.5*3.11e-12*exp(190/T);
    keth34b = 0.5*3.11e-12*exp(190/T);

%% Chemical Reactions - pollutant (C2H6) (reth = reaction rate of Ethane)
    reth1(i) = keth1*C(41,i)*C(6,i);
    reth2(i) = keth2*C(41,i)*C(15,i);
    reth3(i) = keth3*C(42,i)*C(2,i);
    reth4a(i) = keth4a*C(43,i)*C(43,i);
    reth4b(i) = keth4b*C(43,i)*C(43,i);
    reth5(i) = keth5*C(43,i)*C(13,i);
    reth6(i) = keth6*C(43,i)*C(7,i);
    reth7(i) = keth7*C(43,i)*C(14,i);
    reth8(i) = keth8*C(52,i);
    reth9(i) = keth9*C(43,i)*C(15,i);
    reth10(i) = keth10*C(44,i)*C(2,i);
    reth11(i) = keth11*C(44,i)*C(13,i);
    reth12(i) = keth12*C(44,i)*C(13,i);
    reth13(i) = keth13*C(44,i)*C(14,i);
    reth14(i) = keth14*C(47,i)*C(5,i);
    reth15(i) = keth15*C(47,i)*C(6,i);
    reth16(i) = keth16*C(47,i)*C(15,i);
    reth17a(i) = keth17a*C(51,i)*C(6,i);
    reth17b(i) = keth17b*C(51,i)*C(6,i);
    reth18a(i) = keth18a*C(48,i)*C(6,i);
    reth18b(i) = keth18b*C(48,i)*C(6,i);
    reth18c(i) = keth18c*C(48,i)*C(6,i);
    reth19(i) = keth19*C(57,i)*C(2,i);
    reth20(i) = keth20*C(49,i)*C(2,i);
    reth21a(i) = keth21a*C(53,i)*C(7,i);
    reth21b(i) = keth21b*C(53,i)*C(7,i);
    reth22a(i) = keth22a*C(53,i)*C(28,i);
    reth22b(i) = keth22b*C(53,i)*C(28,i);
    reth23a(i) = keth23a*C(53,i)*C(43,i);
    reth23b(i) = keth23b*C(53,i)*C(43,i);
    reth24(i) = keth24*C(53,i)*C(53,i);
    reth25(i) = keth25*C(53,i)*C(13,i);
    reth26(i) = keth26*C(53,i)*C(14,i);
    reth27(i) = keth27*C(54,i);
    reth28(i) = keth28*C(55,i)*C(6,i);
    reth29(i) = keth29*C(42,i)*C(2,i);
    reth33(i) = keth33*C(56,i)*C(6,i);
    reth34a(i) = keth34a*C(46,i)*C(6,i);
    reth34b(i) = keth34b*C(46,i)*C(6,i);
```

```
%% Ethylene Reactions (kethyl = K of Ethylene rxn's)
    kethyl_1zero = 1.1e-28*(T/300)^(-3.5)*C(3,i);
    kethyl_1inf = 8.4e-12*(T/300)^(-1.75);
    kethyl_1 =
(kethyl_1zero/(1+(kethyl_1zero/kethyl_1inf)))*0.6^((1+(log10(kethyl_1zero/ket
hyl_1inf))^2)^(-1));

    kethyl_2a = (0.35)* 2.25e-17* T^1.88* exp(-92/T);
    kethyl_2b = (0.60)* 2.25e-17* T^1.88* exp(-92/T);
    kethyl_2c = (0.05)* 2.25e-17* T^1.88* exp(-92/T);
    kethyl_3 = 1.2e-14*exp(-2630/T);
    kethyl_4 = 3.3e-12*exp(-2880/T);
    kethyl_5a = 9.0e-10*exp(-7500/T);

    kethyl_5b_zero = 7.7e-30*exp(-380/T)*C(3,i);
    kethyl_5b_inf = 6.6e-15*exp(-650/T);
    kethyl_5b_Fc = (0.24*exp(-T/40)) + (0.76*exp(-T/1025));
    Nkethyl_5b = 0.75 - 1.27*log10(kethyl_5b_Fc);
    kethyl_5b_F =
10^((log10(kethyl_5b_Fc))/(1+((log10(kethyl_5b_zero/kethyl_5b_inf))/Nkethyl_5
b)^2));
    kethyl_5b = kethyl_5b_zero*kethyl_5b_inf*kethyl_5b_F/(kethyl_5b_zero +
kethyl_5b_inf);

    kethyl_6 = 4.7e-13*exp(553/T);
    kethyl_7 = 5.4e-7*(T^-1)*exp(-15097/T);
    kethyl_8 = 1.66e-15*exp(-8660/T);
    kethyl_9 = 9e-12;
    kethyl_10 = 1.66e-8*exp(-12580/T);
    kethyl_11 = 1.56e14*exp(-7225/T);
    kethyl_12 = 5.4e-14*(T^0.85)*exp(-1430/T);
    kethyl_13a = (0.4)*2.8e-12*exp(510/T);
    kethyl_13b = (0.6)*2.8e-12*exp(510/T);
    kethyl_14 = 6.4e-12*exp(120/T);
    kethyl_15 = 1.5e-11;

    kethyl_16zero = 5.5e-30*(T/300)^0*C(3,i);
    kethyl_16inf = 8.3e-13*(T/300)^2;
    kethyl_16 =
(kethyl_16zero/(1+(kethyl_16zero/kethyl_16inf)))*0.6^((1+(log10(kethyl_16zero
/kethyl_16inf))^2)^(-1));

    kethyl_17 = (0.7)*3.0e-11*exp(-1600/T);
    kethyl_18 = 1.65e-10;
    kethyl_19 = 2.7e-12*exp(-430/T);
    kethyl_20a = 3.0e-14;
    kethyl_20b = 2.7e-14*exp(668/T);
    kethyl_21a = 1.66e-12*exp(-2517/T);
    kethyl_21b = 5.1e-12;
    kethyl_22 = 1.66e-11*exp(-1007/T);
    kethyl_23 = 1.1e-11;
    kethyl_24 = 1.4e-12*exp(-3160/T);
    kethyl_25 = 1.2e-11*exp(-998/T);
    kethyl_26 = (0.5)*7.8e-14*exp(1000/T);
```

```
    kethyl_27 = 1.2e-11;
    kethyl_28 = (0.12)*5.6e-11;

%% Chemical Reactions - pollutant (C2H4) (rethyl = reaction rate of Ethylene)
    rethyl_1(i) = kethyl_1 * C(45,i) * C(6,i);
    rethyl_2a(i) = kethyl_2a * C(45,i) * C(5,i);
    rethyl_2b(i) = kethyl_2b * C(45,i) * C(5,i);
    rethyl_2c(i) = kethyl_2c * C(45,i) * C(5,i);
    rethyl_3(i) = kethyl_3 * C(45,i) * C(9,i);
    rethyl_4(i) = kethyl_4 * C(45,i) * C(15,i);
    rethyl_5a(i) = kethyl_5a * C(45,i) * C(1,i);
    rethyl_5b(i) = kethyl_5b * C(45,i) * C(1,i);
    rethyl_6(i) = kethyl_6 * C(58,i) * C(2,i);
    rethyl_7(i) = kethyl_7 * C(60,i);
    rethyl_8(i) = kethyl_8 * C(58,i);
    rethyl_9(i) = kethyl_9 * C(60,i) * C(13,i);
    rethyl_10(i) = kethyl_10 * C(60,i);
    rethyl_11(i) = kethyl_11 * C(59,i);
    rethyl_12(i) = kethyl_12 * C(61,i) * C(1,i);
    rethyl_13a(i) = kethyl_13a * C(61,i) * C(6,i);
    rethyl_13b(i) = kethyl_13b * C(61,i) * C(6,i);
    rethyl_14(i) = kethyl_14 * C(63,i) * C(2,i);
    rethyl_15(i) = kethyl_15 * C(63,i) * C(63,i);
    rethyl_16(i) = kethyl_16 * C(64,i) * C(6,i);
    rethyl_17(i) = kethyl_17 * C(64,i) * C(5,i);
    rethyl_18(i) = kethyl_18 * C(66,i) * C(5,i);
    rethyl_19(i) = kethyl_19 * C(66,i) * C(2,i);
    rethyl_20a(i) = kethyl_20a * C(62,i) * C(2,i);
    rethyl_20b(i) = kethyl_20b * C(62,i) * C(2,i);
    rethyl_21a(i) = kethyl_21a * C(65,i) * C(2,i);
    rethyl_21b(i) = kethyl_21b * C(65,i) * C(2,i);
    rethyl_22(i) = kethyl_22 * C(65,i) * C(6,i);
    rethyl_23(i) = kethyl_23 * C(67,i) * C(6,i);
    rethyl_24(i) = kethyl_24 * C(68,i);
    rethyl_25(i) = kethyl_25 * C(69,i) * C(11,i);
    rethyl_26(i) = kethyl_26 * C(60,i) * C(60,i);
    rethyl_27(i) = kethyl_27 * C(60,i) * C(7,i);
    rethyl_28(i) = kethyl_28 * C(58,i) * C(58,i);

%% Calculate reaction rates per species using stoichiometry
react(1,i) = rb1(i) + rb11(i) + rb14(i) - rb20(i) - rb21a(i)- rb21b(i)-
rb21c(i) - rb30(i) - rb51(i) + rbp1(i) + rpd1b(i) + rpd5a(i) + rpd5b(i) +
rpd26b(i) + rpdp2a(i) + rethyl_2a(i) - rethyl_5a(i) - rethyl_5b(i) -
rethyl_12(i) + rethyl_17(i) + rethyl_18(i) + rethyl_19(i) + rethyl_25(i) +
rethylp1(i);


react(2,i) = rb1(i) + rb2(i) - rb4(i) + rb5(i) + 2*rb6(i) - rb8(i) + rb8(i) +
rb10(i) + rb13(i) + rb16(i) + 2*rb18(i) + rb19(i) + rb20(i) + rb21c(i) +
rb23b(i) + rb25(i) + rb27(i) + rb36(i) + rb40(i) + rb41(i) - rb42(i) +
rb49(i) + rb50(i) - rb51(i) - rbp2(i) + rbp3a(i) + rbp3b(i) - rpd3(i) -
rpd6(i) - rpd7(i) + rpd16(i) + 2*rpd17(i) + rpd18a(i) + rpd18b(i) + rpd22(i)
- rpd24(i) - rpd28(i) - reth3(i) + reth4a(i) + reth4b(i) + reth6(i) +
reth9(i) - reth10(i) - reth19(i) - reth20(i) + reth21a(i) + reth22a(i) +
reth22b(i) + reth23a(i) + reth23b(i) + reth24(i) - reth29(i) +
(0.5*rethyl_3(i)) - rethyl_6(i) + rethyl_7(i) - rethyl_14(i) - rethyl_19(i) -
```

```
rethyl_20a(i) - rethyl_20b(i) - rethyl_21a(i) - rethyl_21b(i) + rethyl_26(i)
+ rethyl_27(i);

react(3,i) = -rb9(i) + rb9(i) - rb22(i) + rb23b(i) + rbp7(i);

react(4,i) = -rb7(i) + rb12(i) + rb14(i) + rb15(i) + rb16(i) + rb21b(i) +
rb34(i) + rb35(i) + rb36(i) - rb48(i) - rbp1(i) + rbp5b(i) + rpd2(i) +
rpd15(i) + rpd23(i) + rpd25a(i) + rpd25b(i) + reth1(i) + reth15(i) +
reth18a(i) + reth18b(i) + reth18c(i) + reth28(i) + rpd30a(i) + rpd30b(i) +
reth33(i) + reth34a(i) + reth34b(i) + rethyl_22(i) + rethyl_23(i);

react(5,i) = -rb1(i) - rb2(i) - rb3(i) - rb4(i) - 2*rb5(i) - rb6(i) + rb8(i)
+ rb9(i) + 2*rb10(i) + rb15(i) + rb21b(i) + rb23a(i) - rb24(i) - rb25(i) -
rb26(i) - rb27(i) + 2*rbp2(i) + rbp3b(i) + rbp4(i) + rbp5b(i) + rbp6(i) +
rbp8b(i) - rpd5a(i) - rpd5b(i) - rpd14(i) + rpd27(i) - reth14(i) -
rethyl_2a(i) - rethyl_2b(i) - rethyl_2c(i) - rethyl_17(i) - rethyl_18(i) ;

react(6,i) = -rb1(i) + rb2(i) + rb3(i) + 2*rb7(i) + rb11(i) - rb12(i) -
rb13(i) - rb14(i) - 2*rb15(i) - rb16(i) - 2*rb17(i) + rb18(i) + rb20(i) +
2*rb21a(i) + rb30(i) - rb31(i) - rb32(i) - rb33(i) - rb34(i) - rb35(i) -
rb36(i) + rb37(i) + rb40(i) + rbp1(i) + rbp4(i) + 2*rbp5a(i) + rbp9(i) +
rbp10(i) + rbp11b(i) + rpd1a(i) - rpd2(i) + rpd14(i) - rpd15(i) - rpd23(i) -
rpd25a(i) - rpd25b(i) - rpd26a(i) - rpd26b(i) + rpdp6(i) - reth1(i) +
reth14(i) - reth15(i) - reth17a(i) - reth17b(i) - reth18a(i) - reth18b(i) -
reth18c(i) - reth28(i) + rethp7b(i) + rpd25a(i) - rpd30a(i) - rpd30b(i) -
reth33(i) - reth34a(i) - reth34b(i) + reth34b(i) - rethyl_1(i) + rethyl_10(i)
- rethyl_13a(i) - rethyl_13b(i) - rethyl_16(i) + rethyl_20a(i) +
rethyl_21a(i) - rethyl_22(i) - rethyl_23(i) + rethyl_27(i);

react(7,i) = -rb2(i) + rb3(i) + rb12(i) + rb13(i) - rb16(i) - rb18(i) -
2*rb19(i) - rb21a(i) - rb21b(i) - rb21c(i) + rb33(i) - rb37(i) - rb38(i) +
rb39(i) - rb40(i) + rb51(i) - rbp4(i) + rbp11a(i) + rpd4(i) + rpd6(i) +
rpd7(i) - rpd11(i) + rpd12(i) - rpd16(i) + rpd24(i) + rpd28(i) - reth6(i) +
reth10(i) + reth19(i) - reth21a(i) - reth21b(i) + reth29(i) + rethyl_20b(i) -
rethyl_27(i);

react(8,i) = -rb7(i) - rb8(i) - rb9(i) - rb10(i) -rb11(i) - rb22(i) -
rb23a(i) - rb23b(i) - rb23c(i) + rbp3a(i) + rbp7(i) - rpd1a(i) - rpd1b(i) -
rpd1c(i) - rpd27(i) + rpdp5b(i);

react(9,i) = rb4(i) - rb6(i) - rb10(i) - rb13(i) - rb18(i) - rb20(i) -
rb41(i) - rb49(i) - rb50(i) - rbp3a(i) - rbp3b(i) - rpd4(i) - rpd17(i) +
reth21b(i)  - rethyl_3(i);

react(10,i) = -rb3(i) - rb12(i) + rb17(i) + rb19(i) - rbp5a(i) - rbp5b(i);

react(11,i) = -rb11(i) - rb14(i) + rb21c(i) + rpd1c(i) + rpd5b(i) + rpdp2b(i)
+ rethyl_2c(i) + rethyl_5a(i) + rethyl_21b(i) - rethyl_25(i) + rethylp2b(i);

react(12,i) = rb22(i) - rb23a(i) + rb23a(i) - rb23b(i) - rb23c(i) - rbp7(i);

react(13,i) = 2*rb23c(i) - rb24(i) + rb25(i) + rb30(i) - rb31(i) - rb37(i) -
rb41(i) - 2*rb42(i) - rb43(i) - rb44(i) + rb45(i) + rbp6(i) + rbp8b(i) +
rbp9(i) - rpd8(i) - rpd19(i) - rpd29(i) + rpdp4(i) - reth5(i) - reth11(i) -
reth12(i) - reth25(i) + rethyl_4(i) - rethyl_9(i) ;

react(14,i) = rb24(i) - rb25(i) - rb26(i) + rb27(i) - 2*rb28(i) + 2*rb29(i) -
rb30(i) - rb32(i) + rb33(i) + rb34(i) + rb36(i) + rb37(i) - rb38(i) + rb39(i)
+ rb40(i) + rb41(i) + 2*rb42(i) + 2*rb43(i) - rb44(i) + rb45(i) - rb46(i) +
rb47(i) - rb49(i) - rbp6(i) + rbp8a(i) + rbp10(i) + rbp11a(i) - rpd9(i) -
```

```
rpd10(i) + rpd19(i) - rpd20(i) + rpd21(i) + rpd22(i) + rpdp5a(i) + rpdp7a(i)
+ reth5(i) - reth7(i) + reth8(i) + reth9(i) - reth13(i) + reth17b(i) +
reth25(i) - reth26(i) + reth27(i) + rethp4(i) + rethp6a(i) + rethyl_9(i) ;

react(15,i) = rb26(i) - rb27(i) - rb33(i) + rb35(i) - rb40(i) - rb43(i) -
rb46(i) + rb47(i) + rb49(i) + rbp8a(i) + rbp8b(i) + rbp11b(i) - rpd13(i) -
rpd22(i) + rpdp7b(i) - reth2(i) - reth9(i) - reth16(i) + rethp6b(i) -
rethyl_4(i);

react(16,i) = rb28(i) - rb29(i);

react(17,i) = rb44(i) - rb45(i);

react(18,i) = rb46(i) - rb47(i) - rb48(i) - rbp8a(i) - rbp8b(i);

react(19,i) = rb31(i) - rb34(i) - rb50(i) - rbp9(i) + rpd9(i);

react(20,i) = rb32(i) - rb35(i) + 2*rb48(i) + rb50(i) - rbp10(i) + rpd13(i) +
reth2(i) + reth16(i) + reth17a(i);

react(21,i) = -rb36(i) + rb38(i) - rb39(i) - rbp11a(i) - rbp11b(i);

react(22,i) = -rpd1a(i)- rpd1b(i) - rpd1c(i) - rpd2(i) + rethp3b(i);

react(23,i) = rpd1a(i) + rpd2(i) - rpd3(i) - rpd4(i) - rpd5a(i) - rpd5b(i) +
reth22a(i) + reth23a(i) + (2*reth24(i)) + reth25(i) + reth28(i) + rethp3a(i)
+ rethp6b(i) + rethp7a(i) + rethyl_2b(i) + rethyl_8(i) + rethyl_12(i) +
rethyl_13a(i);

react(24,i) = rpd5b(i) + rpd24(i) - rpd26a(i) - rpd26b(i) + rpdp2b(i) +
rethp3b(i) + rethyl_12(i) + rethyl_13b(i) + (2*rethyl_18(i)) + rethyl_19(i) +
rethyl_20a(i) + rethyl_24(i) + (2*rethylp2b(i)) + rethylp2c(i);

react(25,i) = rpd26b(i) - rpd27(i) + rpd27(i) + rpd28(i) + reth22a(i) +
reth23a(i) + (2*reth24(i)) + reth25(i) + reth28(i) + rethp6b(i) +
rethyl_13a(i) + rethyl_19(i) + rethyl_21b(i);

react(26,i) = rpd1b(i) - rpd6(i) + rpd30a(i) + rethyl_11(i) + rethyl_13b(i) ;

react(27,i) = rpd1c(i) + rpd4(i) + rpd5a(i) + rpd6(i) + rpd7(i) + rpd9(i) -
rpd11(i) + rpd12(i) - rpd13(i) - rpd14(i) - rpd15(i) + rpd18a(i) + rpd29(i) -
rpdp2a(i) - rpdp2b(i) + reth22b(i) + rpd25a(i) + (2*rethyl_3(i)) +
(2*rethyl_4(i)) + rethyl_8(i) + (2*rethyl_10(i)) + rethyl_11(i) +
rethyl_14(i) + rethyl_20a(i) + rethylp2c(i);

react(28,i) = rpd3(i) - rpd16(i) - rpd17(i) - 2*rpd18a(i) - 2*rpd18b(i) -
rpd19(i) - rpd20(i) + rpd21(i) - rpd22(i) + rpd25b(i) + rpdp7a(i) -
reth22a(i) - reth22b(i);

react(29,i) = -rpd7(i) - rpd8(i) - rpd9(i) - rpd10(i) + rpd17(i) +
2*rpd18b(i) + rpd19(i) + rpd22(i) - rpd29(i) + rpdp4(i) + rpdp5a(i) +
rpdp6(i) + rpdp7b(i) + reth22a(i) + rpd30b(i);

react(30,i) = rpd18a(i) - rpd30a(i) - rpd30b(i);

react(31,i) = rpd13(i) + rpd14(i) + rpd15(i) - rpd24(i) + rpdp2a(i) +
rethp3a(i) + rethyl_2b(i) + rethyl_14(i) + rethyl_21b(i) + rethyl_24(i) +
(2*rethylp2a(i));

react(32,i) = rpd16(i) - rpd25a(i) - rpd25b(i) - rpdp6(i);

react(33,i) = rpd26a(i) - rpd28(i) + rethp7a(i) ;
```

```
react(34,i) = 0;

react(35,i) = rpd11(i) - rpd12(i);

react(36,i) = rpd8(i) - rpdp4(i) + rpdp5b(i);

react(37,i) = rpd10(i) - rpd23(i) - rpdp5a(i) - rpdp5b(i);

react(38,i) = rpd20(i) - rpd21(i) - rpdp7a(i) - rpdp7b(i);

react(39,i) = rpd23(i);

react(40,i) = rpd29(i) + reth12(i);

react(41,i) = - reth1(i) - reth2(i);

react(42,i) = reth1(i) + reth2(i) - reth3(i) - reth29(i) + rethyl_5b(i);

react(43,i) = reth3(i) - (2*reth4a(i)) - (2*reth4b(i)) - reth5(i) - reth6(i)
- reth7(i) + reth8(i) - reth9(i) - reth23a(i) - reth23b(i) + reth34a(i);

react(44,i) = 2*reth4a(i) + reth5(i) + reth9(i) - reth10(i) - reth11(i) -
reth12(i) - reth13(i) + reth17a(i) + reth18c(i) + reth23a(i) + rethp4(i);

react(45,i) = reth29(i) - rethyl_1(i) - rethyl_2a(i) - rethyl_2b(i) -
rethyl_2c(i) - rethyl_3(i) - rethyl_4(i) - rethyl_5a(i) - rethyl_5b(i) +
rethyl_15(i);

react(46,i) = reth6(i) + reth17b(i) - reth34a(i) - reth34b(i);

react(47,i) = reth4b(i) + reth10(i) + reth12(i) - reth14(i) - reth15(i) -
reth16(i) + reth19(i) + reth23b(i) - rethp3a(i) - rethp3b(i) + reth34b(i) +
rethyl_28(i);

react(48,i) = reth4b(i) - reth18a(i) - reth18b(i) - reth18c(i) +
rethyl_28(i);

react(49,i) = reth14(i) + reth15(i) + reth16(i) - reth20(i) + rethp7b(i);

react(50,i) = reth11(i);

react(51,i) = reth13(i) - reth17a(i) - reth17b(i) - rethp4(i);

react(52,i) = reth7(i) - reth8(i);

react(53,i) = reth20(i) - reth21a(i) - reth21b(i) - reth22a(i) - reth22b(i) -
reth23a(i) - reth23b(i) - (2*reth24(i)) - reth25(i) - reth26(i) + reth27(i) +
rethp6a(i) + reth33(i) ;

react(54,i) = reth26(i) - reth27(i) - rethp6a(i) - rethp6b(i);

react(55,i) = reth21b(i) + reth22b(i) + reth23b(i) - reth28(i) - rethp7a(i) -
rethp7b(i);

react(56,i) = reth21a(i) - reth33(i);

react(57,i) = reth18a(i) - reth19(i);

react(58,i) = rethyl_1(i) - rethyl_6(i) - rethyl_8(i) + rethyl_7(i) -
(2*rethyl_28(i)) ;

react(59,i) = rethyl_9(i) - rethyl_11(i) + (2*rethyl_26(i)) + rethyl_27(i);

react(60,i) = rethyl_6(i) - rethyl_7(i) - rethyl_9(i) - rethyl_10(i) -
(2*rethyl_26(i)) - rethyl_27(i);
```

```
react(61,i) = rethyl_2c(i) - rethyl_12(i) - rethyl_13a(i) - rethyl_13b(i) +
rethyl_20b(i) + rethyl_22(i);

react(62,i) = rethyl_2a(i) - rethyl_20a(i) - rethyl_20b(i) ;

react(63,i) = rethyl_5a(i) - rethyl_14(i) - rethyl_15(i) - rethyl_15(i) ;

react(64,i) = rethyl_15(i) - rethyl_16(i) - rethyl_17(i) + rethyl_25(i) -
rethylp1(i);

react(65,i) = rethyl_16(i) - rethyl_21a(i) - rethyl_21b(i) - rethyl_22(i);

react(66,i) = rethyl_17(i) - rethyl_18(i) - rethyl_19(i);

react(67,i) = rethyl_21a(i) - rethyl_23(i) - rethylp2a(i) - rethylp2b(i) -
rethylp2c(i) ;

react(68,i) = rethyl_23(i) - rethyl_24(i);

react(69,i) = rethylp1(i) - rethyl_25(i);


%% Assume velocity not homogeneous; laminar flow

    r(i) = r0 + dr*(i-1);
    denom = 2*r1*r1 - (r1*r1-r0*r0)/log(r1/r0) - (r1*r1-r0*r0);
    v(i) = 2*U*((r1*r1-r0*r0)*log(r(i)/r0)/log(r1/r0) - (r(i)*r(i)-
r0*r0))/denom;

    % Build the differential equations
    for j = 1:Ncomp
        dcdr(j,i) = (C(j,i+1) - C(j,i-1))/2/dr;
        d2cdr2(j,i) = (C(j,i-1) - 2*C(j,i) + C(j,i+1))/dr/dr;
        dcdL(j,i) = (D(j)*d2cdr2(j,i) + D(j)/r(i)*dcdr(j,i)+react(j,i))/v(i);
    end
end

for j = 1:Ncomp
    for i = 1:Nnodes
        dydz(i+Nnodes*(j-1)) = dcdL(j,i+1);
    end
end
%Calculation of concentrations in the intersections
for j = 1:Ncomp
            Clamp(j) = (4*C(j,1)-C(j,2))/3; % Concentrations on the lamp
(considering a parabolic equation for Conc.)
end
```

## C.3. Main Solver File

```
% main
clear all
clc
tic %start a timer
format long
data
options = odeset('RelTol', 1e-5, 'AbsTol', 1e-7, 'InitialStep', 0.0001);
[Z,Y] =
ode15s(@f,zspan,y0,options,dz,Nnodes,Ncomp,r0,r1,sig,E0,D,U,P,T,reflamp,phi,
phi_a, phi_b,phi_c);
[s1,s2] = size(Z);

%% C2H4 Plot and Outlet C
ncomp_C2H4=45; %Component number C2H4
plot(Z,Y(1:s1,(ncomp_C2H4-1)*Nnodes+1:ncomp_C2H4*Nnodes))
ylabel 'C2H4 Concentration(molecules/cm3)'
xlabel 'Reactor Length(cm)'
RS_C2H4=Y(1:s1,(ncomp_C2H4-1)*Nnodes+1:ncomp_C2H4*Nnodes);
%% C2H6 Plot and Outlet C
ncomp_C2H6=41; %Component number 1
plot(Z,Y(1:s1,(ncomp_C2H6-1)*Nnodes+1:ncomp_C2H6*Nnodes))
ylabel 'C2H6 Concentration(molecules/cm3)'
xlabel 'Reactor Length(cm)'
RS_C2H6=Y(1:s1,(ncomp_C2H6-1)*Nnodes+1:ncomp_C2H6*Nnodes);

%% CH4 Plot and Outlet C
ncomp_CH4=22; %Component number CH4
figure
plot(Z,Y(1:s1,(ncomp_CH4-1)*Nnodes+1:ncomp_CH4*Nnodes))
ylabel 'CH4 Concentration(molecules/cm3)'
xlabel 'Reactor Length(cm)'
Z;
RS_CH4=Y(1:s1,(ncomp_CH4-1)*Nnodes+1:ncomp_CH4*Nnodes);

%% O2 Plot
figure
plot(Z,Y(1:s1,Nnodes+1:2*Nnodes))
ylabel 'O2 Concentration(molecules/cm3)'
xlabel 'Reactor Length(cm)'

%% CH2O Plot and Outlet C
ncomp1=27; %Component number 1
figure
plot(Z,Y(1:s1,(ncomp1-1)*Nnodes+1:ncomp1*Nnodes))
ylabel 'CH2O Concentration(molecules/cm3)'
xlabel 'Reactor Length(cm)'
Z;
RS1=Y(1:s1,(ncomp1-1)*Nnodes+1:ncomp1*Nnodes);

%% CO2 Plot and Outlet C
ncomp3=25; %Component number 3
```

```
figure
plot(Z,Y(1:s1,(ncomp3-1)*Nnodes+1:ncomp3*Nnodes))
ylabel 'CO2 Concentration(molecules/cm3)'
xlabel 'Reactor Length(cm)'
Z;
RS3=Y(1:s1,(ncomp3-1)*Nnodes+1:ncomp3*Nnodes);
%% O3 Plot and Outlet C
ncomp4=9; %Component number 4
figure
plot(Z,Y(1:s1,(ncomp4-1)*Nnodes+1:ncomp4*Nnodes))
ylabel 'O3 Concentration(molecules/cm3)'
xlabel 'Reactor Length(cm)'
Z;
RS4=Y(1:s1,(ncomp4-1)*Nnodes+1:ncomp4*Nnodes);
%% H2O Plot and Outlet C
ncomp5=4; %Component number 5
figure
plot(Z,Y(1:s1,(ncomp5-1)*Nnodes+1:ncomp5*Nnodes))
ylabel 'H2O Concentration(molecules/cm3)'
xlabel 'Reactor Length(cm)'
Z;
RS5=Y(1:s1,(ncomp5-1)*Nnodes+1:ncomp5*Nnodes);
%% CH2CO (Ketene) Plot and Outlet C
ncomp7=61; %Component number 7
figure
plot(Z,Y(1:s1,(ncomp7-1)*Nnodes+1:ncomp7*Nnodes))
ylabel 'CH2CO Concentration(molecules/cm3)'
xlabel 'Reactor Length(cm)'
Z;
RS7=Y(1:s1,(ncomp7-1)*Nnodes+1:ncomp7*Nnodes);
%% CO Plot and Outlet C
ncomp8=24; %Component number 8
figure
plot(Z,Y(1:s1,(ncomp8-1)*Nnodes+1:ncomp8*Nnodes))
ylabel 'CO Concentration(molecules/cm3)'
xlabel 'Reactor Length(cm)'
Z;
RS8=Y(1:s1,(ncomp8-1)*Nnodes+1:ncomp8*Nnodes);

%% CH3OH Plot and Outlet C
ncomp9=30; %Component number 9
figure
plot(Z,Y(1:s1,(ncomp9-1)*Nnodes+1:ncomp9*Nnodes))
ylabel 'CH3OH Concentration(molecules/cm3)'
xlabel 'Reactor Length(cm)'
Z;
RS9=Y(1:s1,(ncomp9-1)*Nnodes+1:ncomp9*Nnodes);

%% CH3OOH Plot and Outlet C
ncomp10=32; %Component number 10
figure
plot(Z,Y(1:s1,(ncomp10-1)*Nnodes+1:ncomp10*Nnodes))
ylabel 'CH3OOH Concentration(molecules/cm3)'
xlabel 'Reactor Length(cm)'
Z;
```

```
RS10=Y(1:s1,(ncomp10-1)*Nnodes+1:ncomp10*Nnodes);
%%
Y(1:s1,1:Nnodes);

toc %read the timer

%% Efficiency Calculation
dr = (r1-r0)/(Nnodes+1);   % Node distance
for i = 2:Nnodes+1
    r(i) = r0 + dr*(i-1);
    denom = 2*r1*r1 - (r1*r1-r0*r0)/log(r1/r0) - (r1*r1-r0*r0);
    v(i) = 2*U*((r1*r1-r0*r0)*log(r(i)/r0)/log(r1/r0) - (r(i)*r(i)-
r0*r0))/denom;
end


%% Outlet Concentrations


% Concentration C2H4 at exit
F_mass_C2H4 = 0;
F_vol = 0;
for i = 1:(Nnodes-1)/2
    F_mass_C2H4 = F_mass_C2H4 + 2*pi*dr*(4*r(2*i)*v(2*i)*RS_C2H4(s1,2*i-
1)+2*r(2*i+1)*v(2*i+1)*RS_C2H4(s1,2*i));
    F_vol  = F_vol + 2*pi*dr*(4*r(2*i)*v(2*i)+2*r(2*i+1)*v(2*i+1));
end
C_exit_C2H4 = F_mass_C2H4 / F_vol;
C_C2H4_gm3 = C_exit_C2H4 * 28.054 * 1e6 / 6.0221412e23

F_mass_C2H6 = 0;
F_vol = 0;
for i = 1:(Nnodes-1)/2
    F_mass_C2H6 = F_mass_C2H6 + 2*pi*dr*(4*r(2*i)*v(2*i)*RS_C2H6(s1,2*i-
1)+2*r(2*i+1)*v(2*i+1)*RS_C2H6(s1,2*i));
    F_vol  = F_vol + 2*pi*dr*(4*r(2*i)*v(2*i)+2*r(2*i+1)*v(2*i+1));
end
C_exit_C2H6 = F_mass_C2H6 / F_vol;
C_C2H6_gm3 = C_exit_C2H6 * 30.07 * 1e6 / 6.0221412e23;

% Concentration CH4 at exit
F_mass_CH4 = 0;
F_vol = 0;
for i = 1:(Nnodes-1)/2
    F_mass_CH4 = F_mass_CH4 + 2*pi*dr*(4*r(2*i)*v(2*i)*RS_CH4(s1,2*i-
1)+2*r(2*i+1)*v(2*i+1)*RS_CH4(s1,2*i));
    F_vol  = F_vol + 2*pi*dr*(4*r(2*i)*v(2*i)+2*r(2*i+1)*v(2*i+1));
end
C_exit_CH4 = F_mass_CH4 / F_vol;
C_CH4_gm3 = C_exit_CH4 * 16.04 * 1e6 / 6.0221412e23;

% Concentration 1 at exit
F_mass1 = 0;
F_vol = 0;
```

```
for i = 1:(Nnodes-1)/2
    F_mass1 = F_mass1 + 2*pi*dr*(4*r(2*i)*v(2*i)*RS1(s1,2*i-
1)+2*r(2*i+1)*v(2*i+1)*RS1(s1,2*i));
    F_vol  = F_vol + 2*pi*dr*(4*r(2*i)*v(2*i)+2*r(2*i+1)*v(2*i+1));
end
C_exit1 = F_mass1 / F_vol;
C_CH2O_gm3 = C_exit1 * 30.027 * 1e6 / 6.0221412e23

%Concentration 3 at exit
F_mass3 = 0;
F_vol = 0;
for i = 1:(Nnodes-1)/2
    F_mass3 = F_mass3 + 2*pi*dr*(4*r(2*i)*v(2*i)*RS3(s1,2*i-
1)+2*r(2*i+1)*v(2*i+1)*RS3(s1,2*i));
    F_vol  = F_vol + 2*pi*dr*(4*r(2*i)*v(2*i)+2*r(2*i+1)*v(2*i+1));
end
C_exit3 = F_mass3 / F_vol;
C_CO2_gm3 = C_exit3 * 44.01 * 1e6 / 6.0221412e23

%Concentration 4 at exit
F_mass4 = 0;
F_vol = 0;
for i = 1:(Nnodes-1)/2
    F_mass4 = F_mass4 + 2*pi*dr*(4*r(2*i)*v(2*i)*RS4(s1,2*i-
1)+2*r(2*i+1)*v(2*i+1)*RS4(s1,2*i));
    F_vol  = F_vol + 2*pi*dr*(4*r(2*i)*v(2*i)+2*r(2*i+1)*v(2*i+1));
end
C_exit4 = F_mass4 / F_vol;
C_O3_gm3 = C_exit4 * 48.0 * 1e6 / 6.0221412e23

%Concentration 5 at exit
F_mass5 = 0;
F_vol = 0;
for i = 1:(Nnodes-1)/2
    F_mass5 = F_mass5 + 2*pi*dr*(4*r(2*i)*v(2*i)*RS5(s1,2*i-
1)+2*r(2*i+1)*v(2*i+1)*RS5(s1,2*i));
    F_vol  = F_vol + 2*pi*dr*(4*r(2*i)*v(2*i)+2*r(2*i+1)*v(2*i+1));
end
C_exit5 = F_mass5 / F_vol;
C_H2O_gm3 = C_exit5 * 18.02 * 1e6 / 6.0221412e23

%Concentration 7 at exit
F_mass7 = 0;
F_vol = 0;
for i = 1:(Nnodes-1)/2
    F_mass7 = F_mass7 + 2*pi*dr*(4*r(2*i)*v(2*i)*RS7(s1,2*i-
1)+2*r(2*i+1)*v(2*i+1)*RS7(s1,2*i));
    F_vol  = F_vol + 2*pi*dr*(4*r(2*i)*v(2*i)+2*r(2*i+1)*v(2*i+1));
end
C_exit7 = F_mass7 / F_vol;
C_CH2CO_gm3 = C_exit7 * 42.038 * 1e6 / 6.0221412e23

%Concentration 8 at exit
F_mass8 = 0;
F_vol = 0;
```

```
for i = 1:(Nnodes-1)/2
    F_mass8 = F_mass8 + 2*pi*dr*(4*r(2*i)*v(2*i)*RS8(s1,2*i-
1)+2*r(2*i+1)*v(2*i+1)*RS8(s1,2*i));
    F_vol  = F_vol + 2*pi*dr*(4*r(2*i)*v(2*i)+2*r(2*i+1)*v(2*i+1));
end
C_exit8 = F_mass8 / F_vol;
C_CO_gm3 = C_exit8 * 28.0110 * 1e6 / 6.0221412e23

%Concentration 9 at exit
F_mass9 = 0;
F_vol = 0;
for i = 1:(Nnodes-1)/2
    F_mass9 = F_mass9 + 2*pi*dr*(4*r(2*i)*v(2*i)*RS9(s1,2*i-
1)+2*r(2*i+1)*v(2*i+1)*RS9(s1,2*i));
    F_vol  = F_vol + 2*pi*dr*(4*r(2*i)*v(2*i)+2*r(2*i+1)*v(2*i+1));
end
C_exit9 = F_mass9 / F_vol;
C_CH3OH_gm3 = C_exit9 * 32.04 * 1e6 / 6.0221412e23

%Concentration 10 at exit
F_mass10 = 0;
F_vol = 0;
for i = 1:(Nnodes-1)/2
    F_mass10 = F_mass10 + 2*pi*dr*(4*r(2*i)*v(2*i)*RS10(s1,2*i-
1)+2*r(2*i+1)*v(2*i+1)*RS10(s1,2*i));
    F_vol  = F_vol + 2*pi*dr*(4*r(2*i)*v(2*i)+2*r(2*i+1)*v(2*i+1));
end
C_exit10 = F_mass10 / F_vol;
C_CH3OOH_gm3 = C_exit10 * 48.04 * 1e6 / 6.0221412e23

% Total flow rates at entrance and exit
Ft0 = 0;
Ft = 0;

for i = 1:(Nnodes-1)/2
    Ft0 = Ft0+2*pi*dr*(4*r(2*i)*v(2*i)*Y(1,2*i-
1)+2*r(2*i+1)*v(2*i+1)*Y(1,2*i));
    Ft = Ft+2*pi*dr*(4*r(2*i)*v(2*i)*Y(s1,2*i-
1)+2*r(2*i+1)*v(2*i+1)*Y(s1,2*i));
end
s1;
s2;
Efficiency = (1-(C_exit_C2H4/CC2H4))*100

Efficiency_CH4 = (1-(C_exit_CH4/CCH4))*100
Efficiency_C2H6 = (1-(C_exit_C2H6/CC2H6))*100
```

## C.4. Binary Gas Diffusivity Used in Data File

| | | | |
|---|---|---|---|
| mw N | 14.007 | mw O | 16 |
| mw H | 1.008 | mw C | 12.011 |

| | |
|---|---|
| mw Air | 29 |
| v Air | 19.7 |

| | | | |
|---|---|---|---|
| v N | 4.54 | v O | 6.11 |
| v H | 2.31 | v C | 15.9 |

| j | Species | # H | # O | # N | # C | mw Species | Σ v | M AB | Diffusivity Coefficient |
|---|---|---|---|---|---|---|---|---|---|
| 1 | H radical | 1 | 0 | 0 | 0 | 1.008 | 2.31 | 1.94828 | 6.4149 |
| 2 | $O_2$ | 0 | 2 | 0 | 0 | 32 | 16.3 | 30.42623 | 0.9580 |
| 3 | $N_2$ | 0 | 0 | 2 | 0 | 28.014 | 18.5 | 28.49847 | 0.9498 |
| 4 | $H_2O$ | 2 | 1 | 0 | 0 | 18.016 | 13.1 | 22.22494 | 1.2013 |
| 5 | $O(^3P)$ | 0 | 1 | 0 | 0 | 16 | 6.11 | 20.62222 | 1.5556 |
| 6 | OH | 1 | 1 | 0 | 0 | 17.008 | 8.42 | 21.44114 | 1.3956 |
| 7 | $HO_2$ | 1 | 2 | 0 | 0 | 33.008 | 14.53 | 30.87447 | 0.9867 |
| 8 | $O(^1D)$ | 0 | 1 | 0 | 0 | 16 | 6.11 | 20.62222 | 1.5556 |
| 9 | $O_3$ | 0 | 3 | 0 | 0 | 48 | 18.33 | 36.15584 | 0.8459 |
| 10 | $H_2O_2$ | 2 | 2 | 0 | 0 | 34.016 | 16.84 | 31.30837 | 0.9345 |
| 11 | $H_2$ | 2 | 0 | 0 | 0 | 2.016 | 6.12 | 3.769925 | 3.6367 |
| 12 | $N_2O$ | 0 | 1 | 2 | 0 | 44.014 | 35.9 | 34.96332 | 0.6808 |
| 13 | NO | 0 | 1 | 1 | 0 | 30.007 | 10.65 | 29.49491 | 1.1108 |
| 14 | $NO_2$ | 0 | 2 | 1 | 0 | 46.007 | 16.76 | 35.57543 | 0.8781 |
| 15 | $NO_3$ | 0 | 3 | 1 | 0 | 62.007 | 22.87 | 39.51791 | 0.7512 |
| 16 | $N_2O_4$ | 0 | 4 | 2 | 0 | 92.014 | 33.52 | 44.10078 | 0.6215 |
| 17 | $N_2O_3$ | 0 | 3 | 2 | 0 | 76.014 | 27.41 | 41.98309 | 0.6845 |
| 18 | $N_2O_5$ | 0 | 5 | 2 | 0 | 108.014 | 39.63 | 45.72388 | 0.5740 |
| 19 | $HNO_2$ | 1 | 2 | 1 | 0 | 47.015 | 19.07 | 35.87279 | 0.8382 |
| 20 | $HNO_3$ | 1 | 3 | 1 | 0 | 63.015 | 25.18 | 39.72037 | 0.7249 |
| 21 | $HO_2NO_2$ | 1 | 4 | 1 | 0 | 79.015 | 31.29 | 42.42809 | 0.6496 |
| 22 | $CH_4$ | 4 | 0 | 0 | 1 | 16.043 | 25.14 | 20.6579 | 1.0057 |
| 23 | $CH_3$ | 3 | 0 | 0 | 1 | 15.035 | 22.83 | 19.80311 | 1.0618 |
| 24 | CO | 0 | 1 | 0 | 1 | 28.011 | 18 | 28.49692 | 0.9585 |
| 25 | $CO_2$ | 0 | 2 | 0 | 1 | 44.011 | 26.7 | 34.96238 | 0.7570 |
| 26 | $CH_2OH$ | 3 | 1 | 0 | 1 | 31.035 | 28.94 | 29.98301 | 0.7945 |
| 27 | $CH_2O$ | 2 | 1 | 0 | 1 | 30.027 | 26.63 | 29.50457 | 0.8248 |
| 28 | $CH_3O_2$ | 3 | 2 | 0 | 1 | 47.035 | 35.05 | 35.87861 | 0.6779 |
| 29 | $CH_3O$ | 3 | 1 | 0 | 1 | 31.035 | 28.94 | 29.98301 | 0.7945 |
| 30 | $CH_3OH$ | 4 | 1 | 0 | 1 | 32.043 | 31.25 | 30.44565 | 0.7672 |
| 31 | HCO | 1 | 1 | 0 | 1 | 29.019 | 24.32 | 29.0095 | 0.8584 |
| 32 | $CH_3OOH$ | 4 | 2 | 0 | 1 | 48.043 | 37.36 | 36.16804 | 0.6596 |
| 33 | $CHO_2$ | 1 | 2 | 0 | 1 | 45.019 | 30.43 | 35.2761 | 0.7195 |

| | | | | | | | | | |
|---|---|---|---|---|---|---|---|---|---|
| 34 | $CH_2OOH$ | 3 | 2 | 0 | 1 | 47.035 | 35.05 | 35.87861 | 0.6779 |
| 35 | $HOCH_2OO$ | 3 | 3 | 0 | 1 | 63.035 | 41.16 | 39.72434 | 0.6071 |
| 36 | $CH_3ONO$ | 3 | 2 | 1 | 1 | 61.042 | 39.59 | 39.31983 | 0.6192 |
| 37 | $CH_3ONO_2$ | 3 | 3 | 1 | 1 | 77.042 | 45.7 | 42.13836 | 0.5667 |
| 38 | $CH_3O_2NO_2$ | 3 | 4 | 1 | 1 | 93.042 | 51.81 | 44.21786 | 0.5272 |
| 39 | $CH_2ONO_2$ | 2 | 3 | 1 | 1 | 76.034 | 43.39 | 41.98614 | 0.5790 |
| 40 | HNO | 1 | 1 | 1 | 0 | 31.015 | 12.96 | 29.97367 | 1.0379 |
| 41 | $C_2H_6$ | 6 | 0 | 0 | 2 | 30.07 | 45.66 | 29.52531 | 0.6772 |
| 42 | $C_2H_5$ | 5 | 0 | 0 | 2 | 29.062 | 43.35 | 29.03097 | 0.6965 |
| 43 | $C_2H_5O_2$ | 5 | 2 | 0 | 2 | 61.062 | 55.57 | 39.32398 | 0.5441 |
| 44 | $C_2H_5O$ | 5 | 1 | 0 | 2 | 45.062 | 49.46 | 35.2893 | 0.6008 |
| 45 | $C_2H_4$ | 4 | 0 | 0 | 2 | 28.054 | 41.04 | 28.51916 | 0.7173 |
| 46 | $C_2H_5OOH$ | 6 | 2 | 0 | 2 | 62.07 | 57.88 | 39.53069 | 0.5341 |
| 47 | $CH_3CHO$ | 4 | 1 | 0 | 2 | 44.054 | 47.15 | 34.97594 | 0.6147 |
| 48 | $C_2H_5OH$ | 6 | 1 | 0 | 2 | 46.07 | 51.77 | 35.59425 | 0.5878 |
| 49 | $CH_3CO$ | 3 | 1 | 0 | 2 | 43.046 | 44.84 | 34.6538 | 0.6294 |
| 50 | $C_2H_5ONO$ | 5 | 2 | 1 | 2 | 75.069 | 60.11 | 41.83765 | 0.5115 |
| 51 | $C_2H_5ONO_2$ | 5 | 3 | 1 | 2 | 91.069 | 66.22 | 43.99139 | 0.4800 |
| 52 | $C_2H_5O_2NO_2$ | 5 | 4 | 1 | 2 | 107.069 | 72.33 | 45.63862 | 0.4548 |
| 53 | $CH_3C(O)O_2$ | 3 | 3 | 0 | 2 | 75.046 | 57.06 | 41.83407 | 0.5221 |
| 54 | $CH_3C(O)OONO_2$ | 3 | 5 | 1 | 2 | 121.053 | 73.82 | 46.79063 | 0.4455 |
| 55 | $CH_3C(O)OH$ | 4 | 2 | 0 | 2 | 60.054 | 53.26 | 39.11258 | 0.5546 |
| 56 | $CH_3C(O)OOH$ | 4 | 3 | 0 | 2 | 76.054 | 59.37 | 41.98919 | 0.5130 |
| 57 | $CH_3CHOH$ | 5 | 1 | 0 | 2 | 45.062 | 49.46 | 35.2893 | 0.6008 |
| 58 | $C_2H_4OH$ | 5 | 1 | 0 | 2 | 45.062 | 49.46 | 35.2893 | 0.6008 |
| 59 | $OC_2H_4OH$ | 5 | 2 | 0 | 2 | 61.062 | 55.57 | 39.32398 | 0.5441 |
| 60 | $O_2C_2H_4OH$ | 5 | 3 | 0 | 2 | 77.062 | 61.68 | 42.14135 | 0.5044 |
| 61 | $CH_2CO$ | 2 | 1 | 0 | 2 | 42.038 | 42.53 | 34.32253 | 0.6452 |
| 62 | $CH_2CHO$ | 3 | 1 | 0 | 2 | 43.046 | 44.84 | 34.6538 | 0.6294 |
| 63 | $C_2H_3$ | 3 | 0 | 0 | 2 | 27.046 | 38.73 | 27.98894 | 0.7399 |
| 64 | $C_2H_2$ | 2 | 0 | 0 | 2 | 26.038 | 36.42 | 27.4393 | 0.7644 |
| 65 | $C_2H_2OH$ | 3 | 1 | 0 | 2 | 43.046 | 44.84 | 34.6538 | 0.6294 |
| 66 | HCCO | 1 | 1 | 0 | 2 | 41.03 | 40.22 | 33.98172 | 0.6621 |
| 67 | $(HCO)_2$ | 2 | 2 | 0 | 2 | 58.038 | 48.64 | 38.67511 | 0.5776 |
| 68 | HC(O)CO | 1 | 2 | 0 | 2 | 57.03 | 46.33 | 38.44868 | 0.5902 |
| 69 | $C_2H$ | 1 | 0 | 0 | 2 | 25.03 | 34.11 | 26.86915 | 0.7912 |

## Appendix D: Copyright Permission

Some of the simulation results presented in this thesis are already presented in a recently published journal paper, which presents only the methane and ethane models. This paper has been published at the Canadian Journal of Chemical Engineering, a Wiley journal, with the following information:

Asili, V. and De Visscher, A. (2018), *Modelling methane and ethane photolysis in waste gas: Optimization of reaction networks*. Can. J. Chem. Eng., 96: 1674-1683. doi:10.1002/cjce.23124

The permission of using published materials of the above-mentioned article in this thesis, has been granted by Wiley.

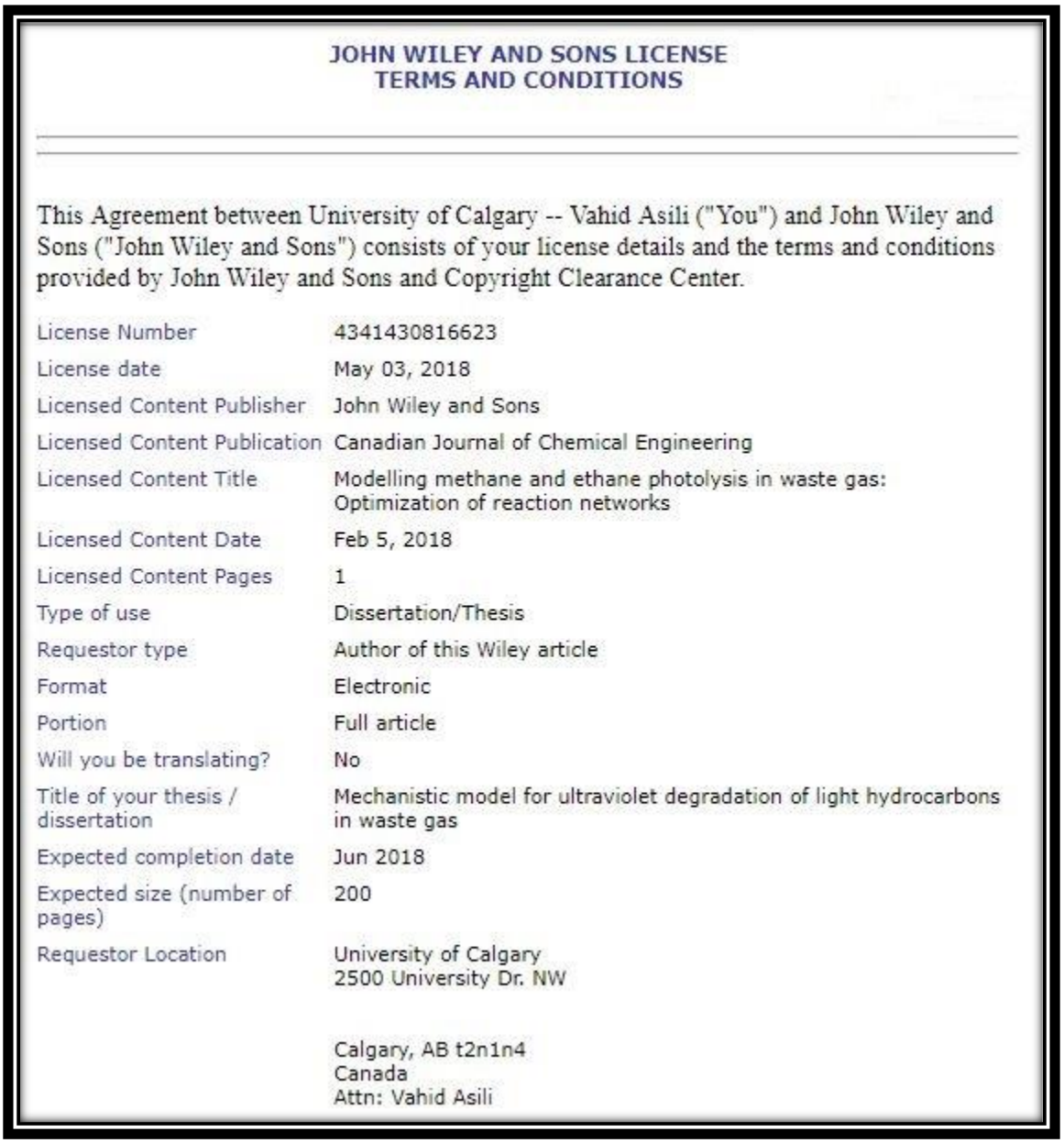

**JOHN WILEY AND SONS LICENSE TERMS AND CONDITIONS**

This Agreement between University of Calgary -- Vahid Asili ("You") and John Wiley and Sons ("John Wiley and Sons") consists of your license details and the terms and conditions provided by John Wiley and Sons and Copyright Clearance Center.

| | |
|---|---|
| License Number | 4341430816623 |
| License date | May 03, 2018 |
| Licensed Content Publisher | John Wiley and Sons |
| Licensed Content Publication | Canadian Journal of Chemical Engineering |
| Licensed Content Title | Modelling methane and ethane photolysis in waste gas: Optimization of reaction networks |
| Licensed Content Date | Feb 5, 2018 |
| Licensed Content Pages | 1 |
| Type of use | Dissertation/Thesis |
| Requestor type | Author of this Wiley article |
| Format | Electronic |
| Portion | Full article |
| Will you be translating? | No |
| Title of your thesis / dissertation | Mechanistic model for ultraviolet degradation of light hydrocarbons in waste gas |
| Expected completion date | Jun 2018 |
| Expected size (number of pages) | 200 |
| Requestor Location | University of Calgary<br>2500 University Dr. NW<br><br>Calgary, AB t2n1n4<br>Canada<br>Attn: Vahid Asili |